UNIVERSIDADE DE LISBOA
INSTITUTO SUPERIOR TÉCNICO

Nanoantennas and Biosensors: An Integrated Approach

Ricardo Alexandre Marques Lameirinhas

Supervisor: Doctor João Paulo Neto Torres
Co-Supervisors:
Doctor António Carlos de Campos Simões Baptista
Doctor Maria João Marques Martins

Thesis approved in public session to obtain the PhD Degree in Electrical and Computer Engineering

Jury final classification: Pass with Distinction and Honour

2024

UNIVERSIDADE DE LISBOA
INSTITUTO SUPERIOR TÉCNICO

Nanoantennas and Biosensors: An Integrated Approach

Ricardo Alexandre Marques Lameirinhas

Supervisor: Doctor João Paulo Neto Torres
Co-Supervisors:
Doctor António Carlos de Campos Simões Baptista
Doctor Maria João Marques Martins

Thesis approved in public session to obtain the PhD Degree in Electrical and Computer Engineering

Jury final classification: Pass with Distinction and Honour

Jury

Chairperson: Doctor Mário Alexandre Teles de Figueiredo, Instituto Superior Técnico, Universidade de Lisboa

Members of the Committee:
Doctor Pedro Manuel Brito da Silva Girão, Instituto Superior Técnico, Universidade de Lisboa
Doctor António Luís Jesus Teixeira, Departamento de Eletrónica, Telecomunicações e Informática da Universidade de Aveiro
Doctor Paulo Sérgio de Brito André, Instituto Superior Técnico, Universidade de Lisboa
Doctor Francisco André Corrêa Alegria, Instituto Superior Técnico, Universidade de Lisboa
Doctor Orlando José Reis Frazão, INESC TEC - Instituto de Engenharia de Sistemas e Computadores, Tecnologia e Ciência, Universidade do Porto
Doctor João Paulo Neto Torres, Departamento de Ciências Exatas e Engenharias (DCEE), Academia Militar

Funding Institutions
Fundação para a Ciência e a Tecnologia
Instituto de Telecomunicações

2024

I declare that this document is an original work of my own authorship and that it fulfills all the requirements of the Code of Conduct and Good Practices of the Universidade de Lisboa.

Declaro que o presente documento é um trabalho original da minha autoria e que cumpre todos os requisitos do Código de Conduta e Boas Práticas da Universidade de Lisboa.

Acknowledgements

A thesis, despite being an original result of a single author, is not the result of him alone. In fact, I would say that it would not be completed if it were up to him alone. It is the result of their scientific dedication and work combined with the effort and sacrifice of many other people.

It was an academic path that I never thought I would follow in my life. A lot is due to the support my family has always given me. If my choices never went wrong, it was largely due to them. I would like to thank my parents. To my father who instilled in me an interest in this area since I was a child. It might have started when he took me to his work and when he told me to sit next to him in the home workshop he built. There, he taught me how to assemble circuits while making me repeat that ”not in my mouth”, for fear that I would swallow the small devices. To my mother who always panicked when I was 5 whenever I picked up small components, but who felt and saw that it was something I do love. She always believes that something greater could be born from this interest. She always supported me and listened to me. She has always been able to seek strength (I do not know where) and to direct me in the right way. To my girlfriend whose support has always been inexhaustible, who has always listened to me and always understood my less regular schedules. She had a lot of patience, especially when I started to tell her my ideas and explain my results to her. I made a lot of progress with the doubts that arose in these conversations with her. Even today she may have nightmares about the precious help she gave me in getting the right angle references, which took many and long hours.

I would also like to express my deep gratitude to my supervisors. To Professor João Torres, Professor Baptista and Professor Maria João, for the patience they had in listening to my ideas and for the opportunities they gave me. The success of this work is also due to their guidance, advice, and support. I extend my gratitude to my colleague Catarina Bernardo, who has often listened to my outbursts and who has often contributed to the creation of a working environment conducive to scientific development without forgetting the personal side. I would also like to praise the support of the Instituto de Telecomunicações (under Project UIDB/50008/2020 supported in part by FCT/MCTES through national funds and in part by co-funded EU funds) and Instituto Superior Técnico, for hosting my research work, as well as of the Fundação para a Ciência e Tecnologia for awarding me the research grant UI/BD/151091/2021.

I am truly grateful to all of you. Thank you for being the ’light bulb’ that showed me the right path to follow. Without you, there would be neither motivation nor support to illuminate the still dark side of knowledge.

Let’s light it on...!

Abstract

Light-matter interactions have been studied since the XV century. However, novel phenomena as the Extraordinary Optical Transmission were only observed with the nanotechnology emergence. In 1998 Ebessen was conducting studies at metallic nanoarrays when observed more intense light peaks than classically predicted. The electromagnetic wave models of nanoantennas usually operate in the frequency domain. However, time domain results are just as important and more advantageous, for example, in light pulse propagation. A novel methodology is proposed based on Maxwell's equations, ray tracing and Fresnel Coefficients in absorbing media. A stochastic model is developed to obtain the response of optical devices based on wave-particle dualism. Recent literature shows that in the visible and near-infrared one may consider both approaches than using just the wave or the particle formalism. Although it is a time domain formulation, frequency domain results can also be obtained. Results show that some photons on the target are re-transmitted by the metal depending on the surrounding media. Refractive index with values spanning from 1.30 to 1.41, characteristic of some human tissues, DNA, or haemoglobin are considered for the application to biosensors. Ultrafast biosensors based on a gold nanoantenna are designed considering variations of the steady-state intensity (obtaining 10-40 %/RIU), settling time middle point (30-60 %/RIU) and its width around the maximum (600-800 nm/RIU). The response settling time is around 4.5-8 fs. The best wavelengths to exploit these indicators are 350 nm and 600 nm. However, the intensity sensitivity increases by stopping the emission before the response settles. These results suggest the design of an ultrafast and low-power biosensor at nanoscale.

Keywords

Nanoantennas; Biosensors; Nanostructures; Surface plasmons polaritons; Optoelectronic devices.

Resumo

As interações luz-matéria são estudadas desde o século XV. Contudo, fenómenos como a Transmissão Ótica Extraordinária só foram observados com o aparecimento da nanotecnologia. Em 1998, Ebessen realizava estudos em nano-estruturas metálicas quando observou uma maior intensidade luminosa do que a prevista classicamente. Os modelos eletromagnéticos para nanoantenas operam normalmente no domínio da frequência. Todavia, os resultados no domínio do tempo são igualmente importantes e mais vantajosos, por exemplo, na propagação de impulsos de luz. Propõe-se uma nova metodologia baseada nas equações de Maxwell, no traçado de raios e nos coeficientes de Fresnel em meios absorventes. Desenvolve-se um modelo estocástico para obter a resposta de dispositivos óticos baseado no dualismo onda-partícula. Literatura recente mostra que, no visível e infravermelho próximo, deve-se considerar ambos os comportamentos e não apenas o ondulatório ou corpuscular. Trata-se de uma formulação no domínio do tempo, mas podem também ser obtidos resultados no domínio da frequência. Mostra-se que alguns fotões no alvo são retransmitidos pelo metal dependendo dos meios envolventes. Varia-se o índice de refração entre 1,30 e 1,41, caraterizando tecidos humanos, ADN ou hemoglobina. Biossensores ultrarrápidos baseados numa nanoantena de ouro são propostos considerando variações da intensidade em regime estacionário (obtendo 10-40 %/RIU), o ponto médio de estabilização (30-60 %/RIU) e a sua largura em torno do máximo (600-800 nm/RIU). A estabilização da resposta varia entre 4,5-8 fs. Os melhores comprimentos de onda para operar são 350 nm e 600 nm. Porém, a sensibilidade da intensidade aumenta interrompendo-se a emissão antes da estabilização da resposta. Estes resultados sugerem a concetualização de um biossensor ultrarrápido e de baixa potência à escala nanométrica.

Palavras Chave

Nanoantenas; Biossensores; Nanoestruturas; Polaritões dos Plasmões Superfíciais; Dispositivos Optoeletrónicos.

Contents

Acronyms

EOT	Extraordinary Optical Transmission
FEM	Finite Element Method
FDM	Finite Differences Method
PDK	Process Design Kit
RIU	Refractive Index Unit
SPP	Surface Plasmon Polaritons
TE	Transverse Electric (modes)
TIR	Total Internal Reflection
TM	Transverse Magnetic (modes)

List of Symbols

A	Absorption Power Coefficient
I	Light Intensity
K	Imaginary Part of the Apparent Complex Refractive Index
L_e	Surface Power Loss Coefficient for a Transverse Electric Wave
L_p	Surface Power Loss Coefficient for a Transverse Magnetic Wave
M_e	Power Interference Coefficient for a Transverse Electric Wave
M_p	Power Interference Coefficient for a Transverse Magnetic Wave
N	Real Part of the Apparent Complex Refractive Index
P	Number of Photons
R_e	Electromagnetic Power Reflection Coefficient for a Transverse Electric Wave
R_p	Electromagnetic Power Reflection Coefficient for a Transverse Magnetic Wave
S	Sensitivity
T_e	Electromagnetic Power Transmission Coefficient for a Transverse Electric Wave
T_p	Electromagnetic Power Transmission Coefficient for a Transverse Magnetic Wave
c	Light Speed in Free Space
f	Frequency
$\bar{n}$	Complex Refractive Index
n	Real Part of the Complex Refractive Index

$\bar{r}_e$	Electromagnetic Field Reflection Coefficient for a Transverse Electric Wave
$\bar{r}_p$	Electromagnetic Field Reflection Coefficient for a Transverse Magnetic Wave
$\bar{t}_e$	Electromagnetic Field Transmission Coefficient for a Transverse Electric Wave
$\bar{t}_p$	Electromagnetic Field Transmission Coefficient for a Transverse Magnetic Wave
α	Angle between the Plane of Constant Phase and the Plane of Constant Amplitude
ϵ_0	Electric Permittivity of Free Space
$\bar{\epsilon}$	Complex Relative Electric Permittivity
ϵ'	Real Part of the Complex Relative Electric Permittivity
ϵ''	Imaginary Part of the Complex Relative Electric Permittivity
η	Propagation Angle
θ	Equi Phase Plane Angle
κ	Imaginary Part of the Complex Refractive Index
λ	Wavelength
μ_0	Magnetic Permeability of Free Space
μ	Relative Magnetic Permeability
ψ	Equi Amplitude Plane Angle
ω	Angular Frequency
$\hat{\boldsymbol{e}}$	Normal Vector to the Plane of Constant Phase
$\hat{\boldsymbol{g}}$	Normal Vector to the Plane of Constant Amplitude
$\hat{\boldsymbol{s}}$	Vector Perpendicular to the Interface
$\bar{\boldsymbol{E}}$	Complex Electric Field Vector
$\bar{\boldsymbol{H}}$	Complex Magnetic Field Vector
$\bar{\boldsymbol{k}}$	Complex Wavevector

1

Introduction

Contents

1.1 Motivation

The evolution of nanotechnologies has led to the discovery of some new phenomena and consequently to the design of new devices. In the last decades, massive progress in electronics and photonics associated with nanotechnologies allowed the design and fabrication of innovative devices in different application fields such as energy, medicine, information, defence, environment, and industry.

The priority of miniaturisation becomes increasingly important in assessing the needs of current projects. Even though the emergence of nanotechnology is contributing to this goal in different devices such as medical, chemical or biological sensors, antennas for a communication system and components to photonic integrated circuits, its accomplishment depends on several factors, such as the improvement of computational methods and the nanostructures techniques of synthesis and fabrication.

Light-matter interaction is a vast research field, captivating researchers by exciting their curiosity to find and explain new phenomena and develop new technological applications. In 1998, Ebbesen and his colleagues reported for the first time the Extraordinary Optical Transmission (EOT). They experimentally showed high transmission spectra when light is incident perpendicularly to a metallic nanoarray with nanometric holes periodically distributed in the metal. This phenomenon is due to optical transmission resonances, observed on nanoscale devices, mainly on the ultraviolet and visible spectral regions. These devices have the capability to concentrate, confine and locally amplify radiation, meaning that they are nanoantennas. The name EOT appears since this phenomenon can not be predicted by classical theories, meaning that the device might transmit in certain conditions more radiation than the classically predictable.

Ebbesen and his colleagues also advanced the hypothesis that surface plasmons are the main agents of this phenomenon, pointing out some evidence of it, namely comparing the results with others obtained previously by Kretschmann and Raether about the Surface Plasmon Polaritons (SPP) excitation in metallic thin films. Only in 2004 Lalanne and Hugonin presented a theoretical analysis based on Maxwell's equations, concluding that, at least in the ultraviolet and visible spectral regions the main agents in EOT are the SPP.

Nanoantennas might be used in several application areas and their performance may be improved by exploiting SPP optical resonances and some optical effects as EOT. EOT is not a necessary effect to design a device for an application, but it is certainly a novel freedom degree. For instance, it might be useful when designing sensors, because it depends on the characteristics of the used materials. To exploit optical phenomena, it is mandatory to understand light-matter interactions.

Light-matter interactions have been studied since the XVII century. It started with simple geometrical concepts, to which the electromagnetic theory brought a much more solid formalism. The excellent compromise between both allowed the evolution of the classical diffraction theories as well as some knowledge about wave-particle duality. Some phenomena are better characterised by particle formalism, others by wave formalism. For instance, it is rare to find quantum processes in the radio frequency spectrum and even rarer to hear someone refer to the frequency of a gamma ray, rather than the energy and momentum carried by a gamma ray photon. Although the whole range is governed by the same basic laws. It is in the optical range that we most often encounter wave-particle duality, which requires familiarity with both concepts. Then, the propagation of light is characterised both by the propagation of electromagnetic waves and by the propagation of photons.

Even that geometrical concepts were the base of this knowledge evolution, the discovery of high complex phenomena has been leaving these kinds of concepts aside. The goal is to develop a model based on Maxwell's equations. It is intended to obtain optical relations, from which it is possible to take advantage of the wave-particle dualism and the probabilistic character that radiation should have in smaller and low-power devices. For these reasons, the developed model is semi-classical and semi-analytic. It contributes to a more geometrical/visual perception of optical phenomena, such as the EOT. Also, since SPP are quasi-particle (not a physical entity, but a mathematical formalism quite useful to describe the overall effect) the model should not be strictly based on the SPP excitation and propagation, but it should reveal a tendency to it. This model will be the basis for the study of optical sensors.

1.2 Objectives

The main objectives of this research work are the modelling, simulation and design of sensors based on nanoantennas, mainly the slit ones.

It is intended to develop a novel semi-classical and semi-analytic model, both in time and frequency domains. For that propose, Maxwell's equations are used and one intends to take advantage of the wave-particle dualism and the probabilistic character of the electromagnetic radiation. It is expected to get a more geometrical/visual perception of high complex phenomena and effects, such as the propagation of SPP and the consequent EOT effect. The validation of the model is done using three different approaches: comparison with results directly from Maxwell's equations, comparison with other methodologies and models, and comparison with results obtained from COMSOL Multiphysics software (a Finite Element Method (FEM)).

The design of a sensor demands the knowledge of the control, geometrical and electrical parameters of the sensor structure. The modelling, simulation and design of sensors are held on the developed model. The main application is on biosensors, such that a refractive index change results in an optical response variation. It is intended to design these sensors based on power variations on the target, considering the possibility of changing EOT conditions, leading to variation in its shape as well as on the positions of the maxima and minima.

1.3 Outline

This document is divided into five main chapters, to which are attached three appendixes.

Chapter 1 (Introduction) is the introductory one, where the motivation is presented and the objectives are declared.

Chapter 2 (State-of-Art) begins with the presentation of state-of-the-art biosensors based on nanoantennas. Considering it, a theoretical review is presented, covering the classical diffraction theories, the discovery of the Extraordinary Optical Transmission effect and the Surface Plasmon Polaritons theory. Moreover, a revision of the refractive index of some biological samples as well as its variations with some diseases is presented.

Chapter 3 (Development and Validation of a Semi-Classical and Time-Domain Model) presents the performed research work to develop the proposed model, as well as a comparison with other methodologies and its validation.

The proposed model is used to design a biosensor, which work is presented in Chapter 4 (Biosensors based on Nanoantennas). It starts with the characterisation of the proposed emitter and by comparing the performance of different metallic nanoantennas. The work of the device as a biosensor is tested under different conditions, namely for different wavelengths, analytes and pulse duration. Also, a tilt angle sensor capable of being included in biosensor systems is proposed. The layout of a sensor based on a nanoantenna is also proposed. The Chapter ends with a comparison with other technologies and by defining how the device is sensible for different variations exemplified in the State-of-the-Art Chapter.

Finally, on chapter 5 (Conclusion) the overall conclusions are taken. In addition, suggestions are made for future work, in order to point out a vision of the near future for the further progress of the research.

There are also three appendixes: (i) A (Approach to Implement an Algorithm to Characterise the Wavevector at an Interface) to support the programming of the algorithm to detect interfaces; (ii) B (Metallic Nanostructures Inclusion to Improve Energy Harvesting in Silicon) describing another important application of nanoantennas in solar energy harvesting; (iii) C (The Impact of Nanoantennas on Ring Resonators' Performance) reporting progresses in Ring Resonators technology by the inclusion of nanoantennas.

2

State-of-the-Art

Contents

This chapter begins with the presentation of some state-of-the-art biosensors based on metallic nanoantennas. This review aims to identify not only the device to analyse but also which tools may be used or developed. After that, a brief review of some topics needed in our work is introduced. It includes a theoretical review of classical diffraction theories is presented, covering the advances since the XVII century. Extraordinary Optical Transmission (EOT) effect and, the Surface Plasmon Polaritons (SPP) theory and the electrical permittivity model are studied in order to give some background for the sensor modelling and design. Finally, several biosamples are introduced and optically characterised.

2.1 Review of State-of-the-Art Sensors based on Nanoantennas

Nanoantennas have a significant role in photonic nanodevices. This kind of device has a wide range of applications due to its different capabilities. For instance, the capability to increase radiation intensity in a small space region will allow the miniaturisation of solar cells. On the other hand, by incorporating the nanoantenna into the solar cell, the electromagnetic field that passes through the metal to a semiconductor may decay faster than if it passes directly to it. Thus, the cell thickness (and volume) may be reduced. These principles are the basis of the study of the incorporation of nanoantennas in solar cells [1–3].

Another application field is in optical communications, where nanoantennas are an important device to concentrate the LASER and LED radiation as well as to increase light absorption in photodetectors. In both emission and detection cases, they are used to improve the system's sensitivity and selectivity, amplifying a certain spectral region and attenuating others both in the near and far field [4, 5]. Some optical devices, such as multiplexers, ring resonators or filters, work based on evanescent waves. Consequently, the nanoantennas incorporation aims to tune this evanescent field, leading to a variation of the systems' optical response [6].

However, the focus of this research work is on biosensing. Sensors based on nanoantennas are a type of SPP-based sensors that, together with Kretschmann's sensors and fibre-optics sensors, are being both theoretically and experimentally studied. The use of these types of sensors is not limited to biological events. However, the interest in this kind of stimulus stands out among the others and arouses huge interest due to the possibility of real-time measuring in vivo, the use of non-ionising radiation and the sensitivity for very small stimuli. These are pointed out as the main advantages for detecting diseases or human conditions in a non-invasive way. Detection is performed by analysing the possible shift in the output optical response spectrum concerning the stimuli mentioned. Below are some examples of the values of this variation, in the form of the device's sensitivity.

The sensors based on Kretschmann's dielectric-metal structure typically present response variations per Refractive Index Unit (RIU) (sensitivities) around 100-300 deg/RIU [7]. The sensor is based on determining reflectance as a function of the angle of incidence of the light beam on the structure. The more collimated the beam, the greater the sensitivity of the device and the lower its detection limit. There are currently LED and LASER emitters with a very interesting degree of collimation for these applications. However, as recent technology their reproducibility and manufacturing processes still affect costs. Another solution is to use a collimator for this purpose, which not only affects costs but also the system dimensions. Also, a technique used but with significant disadvantages is to move the emitter away from the structure. Thus, the incident beam tends to be more collimated the further away it is. The visible disadvantage is the loss of a lot of emitted energy and the inability to miniaturise the system.

Similar problems are verified for fibre-optics sensors based on SPP resonances. Sensitivities around 2000-5000 nm/RIU are obtained. However, there are problems in reducing the systems' dimensions due to the size of the optical fibres. Also, some proposed devices increase the evanescent field by bending the optical fibre or by using multiple fibres. Then, on top of the dimension problem, some structural issues may come up. Furthermore, optical fibres have a limited acceptance angle and consequently, some emitted energy is also lost even before reaching the device. These issues directly affect the possibility of measuring based on non-invasive and in vivo methods.

The use of a nanoantenna in sensing applications can be divided into two different cases: one where the structure is used to improve an existing sensor or measurement system and another where the structure is itself the active device of the measurement system.

An electromagnetic wave can be locally amplified using nanoantennas, leading to the improvement of some instruments. In medical imaging or magnetic resonance imaging applications, they can be used to diminish the power needed per scan but also to focus radiation, such that, the maximum intensity of the field will be almost confined to the wound or illness area leading to a less intense radiation exposure on the healthy areas. In this way the radiation intensity in the healthy areas decreases, resulting in a decrease of the local heating and the risks of burning. Beyond that, in the case of higher ultraviolet radiation (ionising radiation), there is a minimisation of the damage risks to the healthy tissues, such as cell damage or radiation sickness [8–11].

On the other hand, their nano-size is a huge advantage of using a nanoantenna itself as the active device of a measurement system. It is possible to measure not only *in vitro* but also *in vivo*, to exploit real-time analysis, to have low limits of detection as well as to multiplex the sensing capability [5,12–14]. This last potential means that the system may be designed considering more than one sensor (different inputs) and there is the possibility of selecting the ones to be analysed. This is particularly useful for having a reference sample and for integrating more than one device into a system to increase measurement accuracy. Furthermore, if the emitter and detector are integrated into the photonic integrated circuit, autonomous and portable devices are obtained.

Researchers are trying to improve some figures of merit such as sensitivity, detection limits, selectivity, dynamic range, and power requirements [5, 12–14]. New antenna geometries and materials combinations are being proposed to accomplish that. The analysis of a spectral shift is by far the most used sensing principle in those proposes. However, other response variations may reveal the change in the SPP resonance caused by the stimulus, for instance, exploring time domain analysis and low-power applications [15, 16].

Some examples of nanoantennas working as biosensors are going to be presented to corroborate the previous paragraphs and present recent proposed devices.

Klinghammer et al. designed a gold nanoarray to detect variations in DNA (1.32-1.55 refractive index variations) [17]. They report spectral shifts from 1 to 8 nm, depending on the analysed DNA samples. These values lead to a sensitivity around 80-100 nm/RIU and it is measured in the red spectral region.

In [18] Jianye Guang presents a gold sensor with a sensitivity of 162.1 nm/RIU for monitoring refractive index variation between 1.33 and 1.38. Moreover, the authors report that it is possible to fabricate large-scale nanohole arrays at low cost for high-throughput on-chip plasmonic sensors.

Similarly, Alejandro Portela et al. proposed a nanogap antenna made of gold to detect the molecule miRNA-210 [19]. They suggest a sensitivity of 422 nm/RIU at a wavelength between 740 and 760 nm. The presence of this molecule varies the analyte's refractive index between 1.33 and 1.37.

In [20], Yu-Chun Lu et al. present a slit nanoantenna made of gold optimised with diamond particles serving to monitor serum albumin concentration. The structure is illustrated in figure 2.1 and the authors report sensitivities between 6 and 60 nm%.

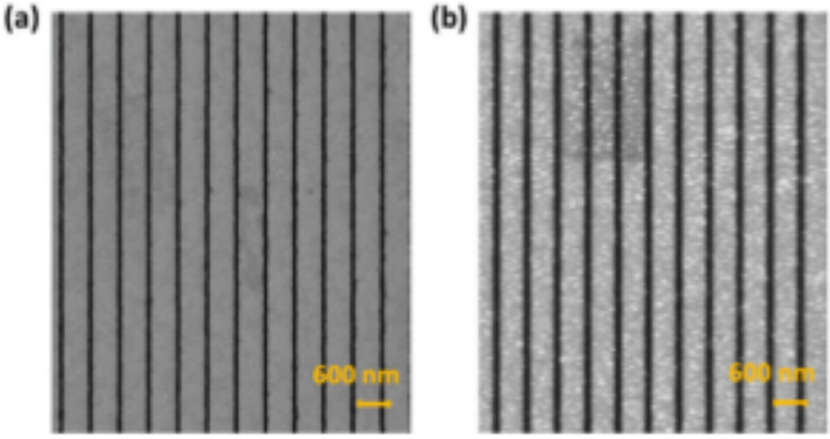

Figure 2.1: Slit nanoantenna proposed by Yu-Chun Lu et al. (from [20]): a) gold nanoantenna; b) diamond nanoparticles on the surface of the gold nano-slits.

Similarly to these two last works, Holger Fischer and Olivier Martin developed a study to analyse nanostructures as nanogaps/nanoslits and bowtie nanoantennas [21]. They verified that both geometries may work in visible and near-infrared spectral regions as illustrated in figure 2.2.

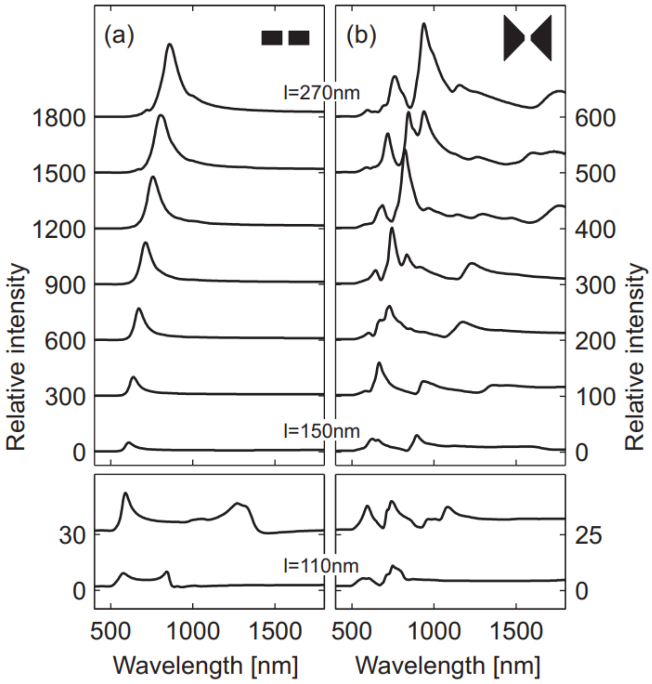

Figure 2.2: Comparison between nanoslits and bowtie nanoantennas spectra.

Yangyang Zhao et al. see the potential to use nanoantenna to monitor indoor and outdoor air quality as well as for the detection of breath biomarkers (e.g. acetone, ethanol, etc.) [22]. They designed a gas sensor based on a gold nanohole array, for refractive index variations around 1. Figure 2.3 shows the obtained spectra and the sensitivity in wavelength shift per acetone concentration.

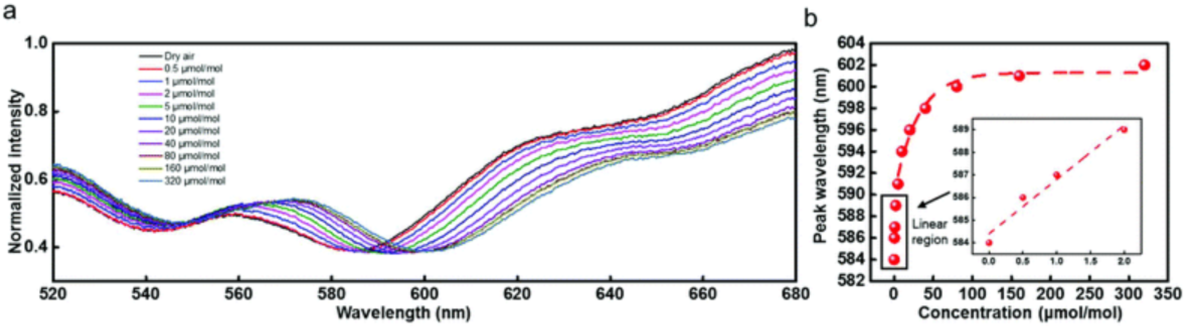

Figure 2.3: Sensor response for acetone monitoring: (a) Spectral response when the sensor is exposed to different concentrations; (b) Peak wavelength vs. concentration of acetone vapours. (from [22]).

Another interesting application is the blood group detection. Santosh Kumar Sahu et al. developed a Finite Element Method (FEM) model to analyse the sensitivity of a nanohole array [23]. The proposed device is illustrated in figure 2.4. The authors determine a sensitivity of 82 nm/RIU.

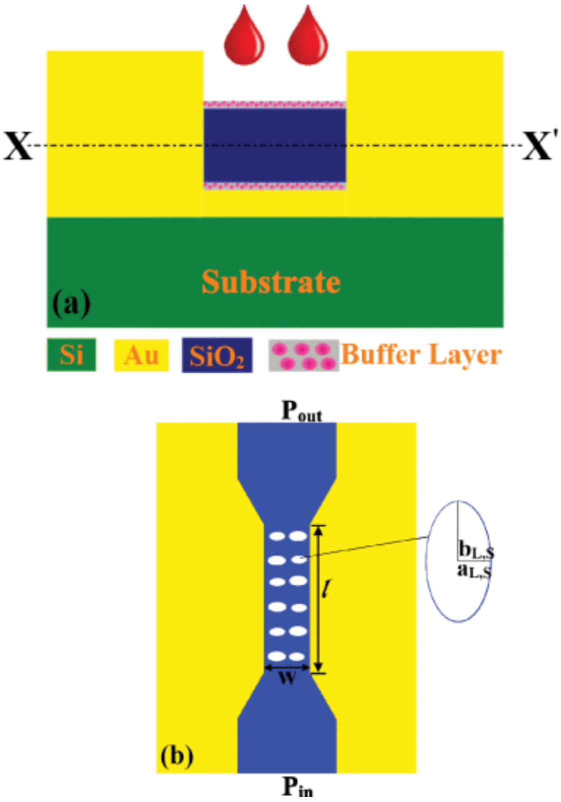

Figure 2.4: Santosh Kumar Sahu's nanoantenna design for human blood group detection: a) side view; b) top view (from [23]).

Fatma Kurul et al., in [24], suggest using gold nanoarrays to monitor several viruses (for instance SARS-COV-2). They emit light using a LED and a CMOS camera obtains light patterns after the sensor's active area. The same approach is used by Arif E. Cetin et al., whose works have the same goal [25]. Their proposed set-up is shown in figure 2.5 and the obtained results are in figure 2.6. Although this set-up is not miniaturised, authors report the opportunity it has to progress in that way since both LED and CMOS camera may be integrated in the same chip that the nanoantenna.

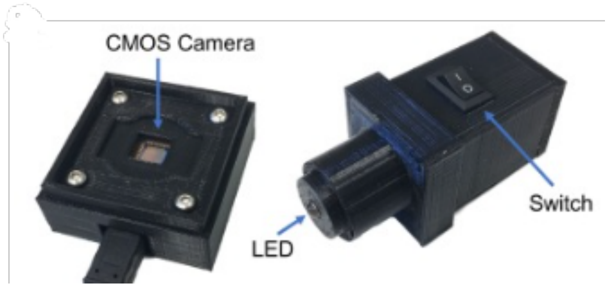

Figure 2.5: Arif E. Cetin proposed a set-up using a nanoantenna to detect viruses (from [25]).

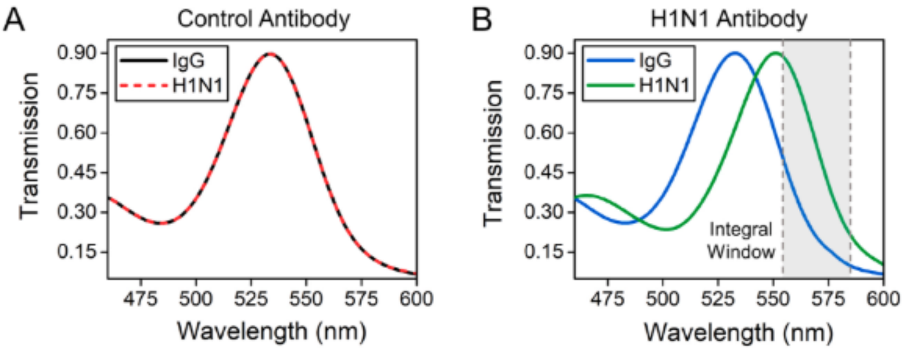

Figure 2.6: Spectral response of the proposed device: a) control analyte; b) after the addition of viruses molecules (from [25]).

Yanting Liu and Xuming Zhang have a book chapter about microfluidic-based plasmonic biosensors, where they mention several advantages of plasmonic nanostructures [26]. Authors spotlight the ultra-sensitive label-free and real-time biomolecular analysis of nanoantennas. Furthermore, they report that high-throughput chip platforms may be designed considering this kind of sensor, demonstrating the enormous potential for integration and excellent capabilities for biomedical applications [26].

Hasan Kurt et al. present in [27] a review of the sensitivities other researchers reported about different gold nanostructures to detect biological events. They suggest three main working principles to exploit SPP resonances as the base of a sensor's working principle. Figure 2.7 suggests some differences between these sensing techniques. One may want to explore directly the surface plasmon resonance and the sensing is based on the variation of the structure's reflection in the function of the incidence angle. This is the case of the Kretschmann's working principle. Moreover, it is also possible to analyse the field extinction ratio near a nanoparticle, which is a strategy known as localised surface plasmon resonance variation. The electromagnetic field near the nanoparticle reveals standing waves, whose extinction ratio may vary with the dielectric (analyte). This strategy is also exploited using metallic nanoantennas in the infrared region, where the metal reflects all the radiation but the reflected field phase depends on the surrounding media. Then, the standing wave condition changes with the media. The third strategy is based on the EOT phenomenon at nanoarrays and the analyte's variation leads to the variation of the transmission spectral. Furthermore, they report sensitivities between 100 and 400 nm/RIU in the visible range for different geometries.

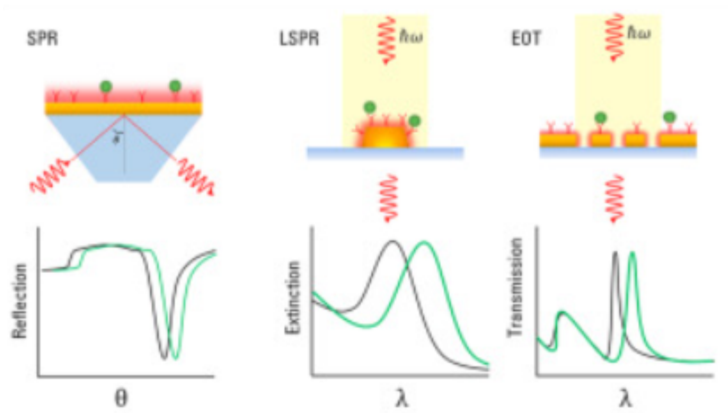

Figure 2.7: Surface Plasmon Polariton resonances and Extraordinary Optical Transmission sensors (from [27]).

Antonio Minopoli et al. also conducted a review analysis to compare different nanostructured plasmonic surfaces acting as biosensors [28]. They analysed the performance of silver and gold structures as nanorods and nanoslits. These analysed structures at the visible and near-infrared spectral regions present sensitivities from 10 to 400 nm/RIU [28].

Other literature reviews point out that periodic metallic arrays present typical sensitivities around 300-400 nm/RIU in the visible region [29,30].

In general, for a refractive index variation between 1.3 and 1.4, the sensitivities between 100 and 400 nm/RIU suggest a spectral shift in the order of dozens of nanometers.

There is a huge opportunity to create new sensors based on EOT. However, to design a sensor that could enter into the market, it is necessary to guarantee an acceptable fabrication cost and good reproducibility [12–14]. For that purpose, the project quality must be as high as possible. A proper project has to include the definition of the desired specifications, taking into account the trade-off between cost and performance, as well as a very accurate design. Nowadays, there are several proposed fluxes and some foundries also suggest step-by-step processes to ensure that all the excellent ideas lead to the pretended devices. The order of these processes may suffer some changes depending on the following design flux. However, they have to include hand calculations, numerical simulations, circuit layout design and parasitic simulations after the circuit fabrication and test to adjust further simulation and manufacturing processes.

The most common fabrication techniques to produce nanoantennas are based on lithography (mainly electron-beam lithography) although in some situations ion beam milling or bottom-up self-assembly might be used. These are top-down methods however, to integrate other devices in the same chip one may take into consideration other hybrid processes, for instance, to suspend the emitter. Figure 2.8 illustrates some lithography methods used to produce nanoantennas. These methods allow us to fabricate metal-made nanostructures ensuring their chemical stability, long-duration endurance against ultraviolet (and consequently visible and infrared) radiation and a high-temperature working range [31].

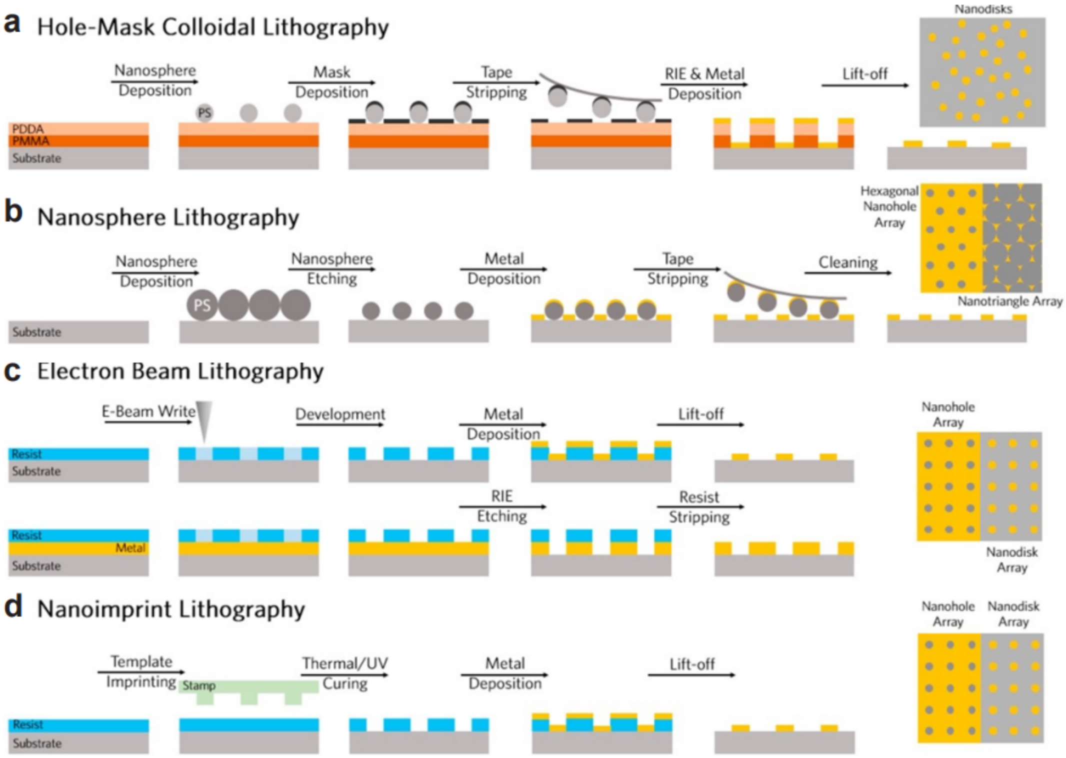

Figure 2.8: Fabrication methods to produce nanoantennas.

The importance of the simulation processes implies the development of computational methods and the use of powerful simulation software. The fabrication of the integrated circuits, namely with dimensions in the nano order, is only possible with advanced techniques of synthesis of semiconductors and nanomaterials.

Considering the presented state-of-the-art, it is concluded not only that aperture nanoantennas are definitely an interesting topic to research, presenting some innovative perspectives where it is intended to work. In those concepts, one may highlight two fascinating ideas.

The first is the possibility of designing sensors exploring time-domain figures of merit, namely the possibility of designing ultrafast sensors (at femtoseconds). This is not well covered in the literature since most of the results are taken from the steady-state light intensity results.

The other is the thought of quantifying radiation exploiting wave-particle dualism. Thus, SPP and EOT-based sensors may be better analysed and there is the possibility of thinking in low-power devices.

These ideas are in the device perspective. However, one may also think of the available designing tools, for instance, the computational tools used to simulate devices. In this field, most authors use or FEM or Finite Differences Method (FDM) based tools, namely *COMSOL Multiphysics* and *Ansys Lumerical*. Both are commercialised software characterised by a wave formalism from the application of Maxwell's equations.

However, recent literature suggests that complex phenomena at the visible and near-infrared spectral ranges may be explained by considering not only the wave formalism or the particle but also taking advantage of the wave-particle dualism [32, 33].

Radiation is both wave and particle however, low-frequencies (low-wavelengths) phenomena are better explained/simplified considering the wave postulates whereas for low-wavelengths (high-frequencies) it is useful to use particle perspective [32, 33]. The visible and near-infrared regions are the spectral transition. For that reason, optical phenomena such as EOT and the propagation of SPP may also be analysed using a dual point of view.

Considering the analysed state-of-the-art regarding the developed devices and used simulation tools, it is intended to develop a novel model considering what is mentioned in the previous paragraph as well as to apply it in the design of biosensors based on slit nanoantennas working at the visible range. The idea is to model the nanoantennas' behaviour at time-domain, exploring novel figures of merit from the light pulse propagation. Slit nanoantennas are chosen because literature reviews suggest that there is not enough difference between them and more complex structures in the visible range to think of applying to them a novel model (with all the necessary validation stages). They are also the structures for which EOT was first observed.

With these objectives in mind, the next step is to review classical diffraction theories in slit arrays. The idea is to present the chronological evolution that led to the discovery of EOT. Then, the EOT effect is analysed followed by theoretical concepts of the optical excitation and propagation of SPP. A review of several biosamples is also presented at the end of this chapter to complement the state-of-the-art presentation.

The models' state-of-the-art is connected to the development of the novel model and for that reason, it is only presented in the next chapter, which is only focused on models and their validations.

2.2 Classical Diffraction Theories

2.2.1 Huygens' Principle and Young's Experiment

In the XVII century, Huygens stated that every unobstructed point of a wavefront behaves as a punctual source of a new spherical wave with the same characteristics as the incident one, as illustrated in figure 2.9 [34–36]. One century later, Fresnel reformulated this principle for any cylindrical wave. The discussion about the existence of plane waves started. A plane wave is a utopia, used when the light source is quite distant from the analysed object. In those conditions, the direction of almost all the points of the cylindrical wave is perpendicular to the analysed object. This scenario is used for instance to characterise the sunlight waves that reach the Earth's surface. The source is so distant that it is possible to characterise all these waves as planes.

In addition, a plane wave may be emulated using a huge number of punctual and periodic cylindrical sources as illustrated in figure 2.10. For instance, on a Transverse Magnetic (modes) (TM) wave, the electric field will oscillate only in one direction, because every point on the wavelets that are not on the wavefront will be the superposition of different sources, which cancel the other directions' components. This scenario is important because of the wave-particle duality: a plane wave is characterised by particles in all the different directions. It is very difficult to obtain particles propagating with parallel directions. In this case, it is necessary to have a collimator.

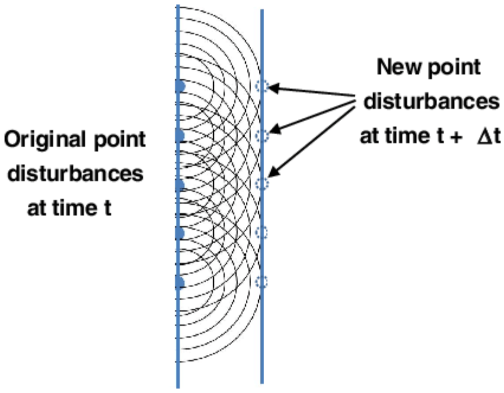

Figure 2.9: Huygens-Fresnel principle (adapted from [36]).

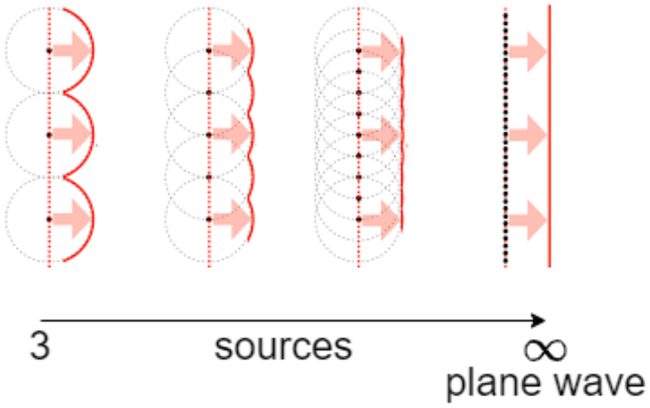

Figure 2.10: Plane wave emulation based on multiple cylindrical waves.

The wave-particle duality has been quite an important concept in proving some phenomena. This approach reveals that light might be characterised as either a wave or a particle. Some phenomena are better characterised by particle formalism, others by wave formalism. However, both always coexist. Thomas Young, in 1803, experimentally proved the wave characteristic of light. The famous Young's experiment, illustrated in figure 2.11, also known as the double slit experiment, allowed Young to prove light interference, which is a wave phenomenon [34, 35]. The experiment is nothing more than a light beam (plane wave) incident on a perfectly conducting plane, where there are two slits of width a and spaced by d. A target is placed at a distance of D and parallel to the conducting plane.

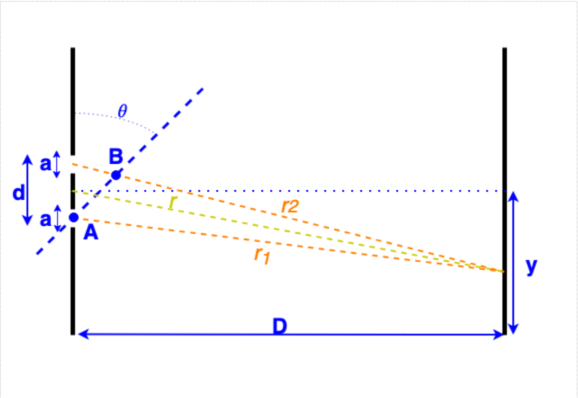

Figure 2.11: Young's experiments geometry (Adapted from [34]).

Based on Huygens-Fresnel's principle, the wavefront before the conducting plane will be composed of obstructed points except on the slits. Then, only the slits will transmit light. Assuming the small angle approximation and $D \gg d$, meaning that $\tan(\theta) = \frac{y}{D} \approx \sin(\theta) \approx \theta$. Consequently, each slit transmits one ray and both rays can be considered parallels near the array. Within these premises, the difference between both optical paths is determined by the expression 2.1.

$$r_2 - r_1 = x = d\,sin(\theta) \approx d\,\theta \tag{2.1}$$

If the optical path length difference of the two rays is a multiple, m, of $\lambda/2$, they interfere destructively, as they are in phase-opposition, expression 2.2 [34]. On the other hand, constructive interference, meaning that waves will be in-phase, is determined by the maxima positions, using expression 2.3, in the way that the optical path length difference of the two rays is a multiple m of the wavelength λ [34].

$$m\lambda + \frac{\lambda}{2} = d\,sin(\theta) \rightarrow m\lambda + \frac{\lambda}{2} \approx d\,\theta \rightarrow y_{min} \approx (2m+1)\,\frac{\lambda D}{2d} \tag{2.2}$$

$$m\lambda = d\,sin(\theta) \rightarrow m\lambda \approx \theta\,d \rightarrow y_{max} \approx \frac{m\lambda D}{d} \tag{2.3}$$

On top of that, it is possible to extrapolate the double slit for a $N+1$ slit experiment. In this case, expressions 2.2 and 2.3 might be respectively rewritten into expressions 2.4 and 2.5 [34, 35].

$$Nm\lambda + \lambda = Nd\,sin(\theta) \iff Nm\lambda + \lambda \approx Nd\,\theta \tag{2.4}$$

$$Nm\lambda = Nd\,sin(\theta) \iff Nm\lambda \approx Nd\,\theta \tag{2.5}$$

Another important quantity, sometimes used as a figure of merit, is the angular resolution, $\Delta\theta$. This is the smallest angular distance between the maximum and the minimum of the pattern on the target. Expression 2.6 is used to determine the angular resolution and it is deduced from expressions 2.4 and 2.5, determining the difference between θ_{max} and θ_{min} [34, 35].

$$\Delta\theta = \frac{\lambda}{Nd\,cos(\theta)} \tag{2.6}$$

Similarly, the resolution power might be defined as the capability to differentiate two different wavelengths at the same angle. This is commonly known as the Rayleigh criterion, described by expression 2.7. Expression 2.7 is obtained using minima and maxima conditions 2.4 and 2.5, for $\Delta\lambda = \lambda_{max} - \lambda_{min}$ and λ as the midpoint of this interval [34, 35]. This deduction is based on the fact that the best way to differentiate two wavelengths is when one is the maximum and the other is the minimum.

$$\frac{\Delta\lambda}{\lambda} = \frac{1}{Nm} \tag{2.7}$$

2.2.2 Fraunhofer's Diffraction Theory

Fraunhofer's Diffraction Theory unifies the aforementioned rationale about plane waves to obtain the light pattern on the target, namely to compute the maxima and minima position. On top of it, Fraunhofer also established a method to relate intensities on the pattern.

As illustrated in figure 2.12, and assuming a monochromatic plane wave with normal incidence on a perfect conductive metal, the slit of size a might be replaced by a collection of punctual sources uniformly distributed. Considering a certain wavelength λ, the wavevector $k = \frac{2\pi}{\lambda}$ and $\beta = \frac{ka}{2} sin(\theta)$, Fraunhofer mathematically proved the relation presented on expression 2.8, as the ratio between the irradiance at a certain angle of diffraction θ and the main lobe one [4, 34, 35]. The light pattern on the target will be similar to *sinc* functions of β, as revealed on expression 2.8.

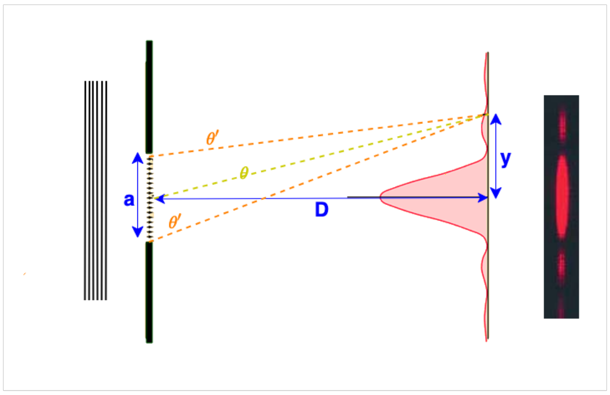

Figure 2.12: Fraunhofer's diffraction theory illustration.

The deduction is similar to Young's empirical idea. For a certain angle θ, the electric field on the pattern will have the contribution of each slit's punctual source. Considering r as the optical path between the target point and the slit's middle point, it is possible to compose the electric field varying the punctual source, *i.e.*, the optical path, denoted by r_1. Being I the distance between punctual sources and A the fields magnitude, expression 2.9 describes that difference among electric fields, where ω is the angular frequency. For $\theta = 0$ the variable β is also null. Consequently, $E(0) = 1$ and expression 2.8 is revealed, since $I \propto E^2$.

$$\frac{I(\theta)}{I(0)} = \left(\frac{sin(\beta)}{\beta}\right)^2 \tag{2.8}$$

$$dE = \frac{A}{r} e^{j(\omega t - kr_1)} dl \rightarrow E = \frac{A e^{j(\omega t - kr)}}{r_1} \int_{-a/2}^{a/2} e^{jklsin\theta} dl \iff E = \frac{sin(\beta)}{\beta} \tag{2.9}$$

In addition, Fraunhofer's theory might be generalised for an N slits array, where slits are spaced by d, using the same idea, composing the electric field not only in the slit width a but along all the array (points over the metal do not contribute). This is formulated in expression 2.10, considering the relations 2.11 and 2.12. The term I_0 in expression 2.10 is the contribution of each equal slit, such as for $N = 1$ (and consequently $d = 0$) this expression becomes expression 2.8.

$$I(\theta) = I_0 \left(\frac{sin(\beta)}{\beta}\right)^2 \left(\frac{sin(N\alpha)}{\alpha}\right)^2 = I_0 N^2 \left(\frac{sin(\beta)}{\beta}\right)^2 \left(\frac{sin(N\alpha)}{N\alpha}\right)^2 \tag{2.10}$$

$$\beta = \frac{ka}{2} sin(\theta) = \frac{\pi a}{\lambda} sin(\theta) = \frac{\pi a y}{\lambda D} \tag{2.11}$$

$$\alpha = \frac{kd}{2} sin(\theta) = \frac{\pi d}{\lambda} sin(\theta) = \frac{\pi d y}{\lambda D} \tag{2.12}$$

2.2.3 Fresnel's Diffraction Theory

As previously referred, Fresnel's Diffraction Theory assumes that the slit dimensions are greater than the incident wavelength. Figure 2.13 illustrates a scenario to analyse this theory, where the aperture has an area S, distanced from ρ_0 to a punctual source S and from r_0 to an observation point, P.

The field disturbance on P will be composed using expression 2.13, where ρ and r are the aforementioned distances source-slit and slit-observation point passing on an arbitrary point (y,z) on the slit area, A. In this expression, ω is the angular frequency, as well as ϵ_0 is the vacuum electrical permittivity (assuming the vacuum as the propagation medium).

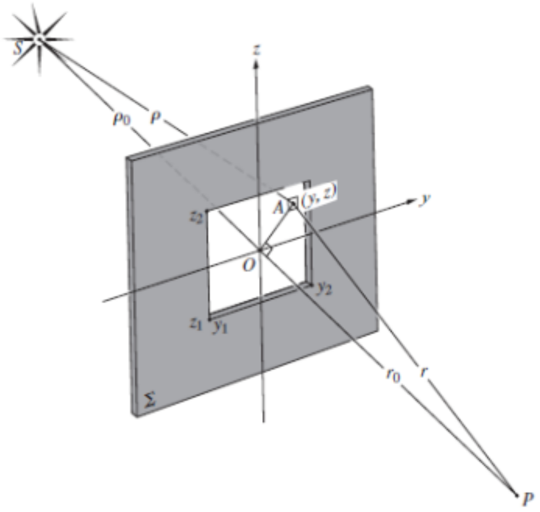

Figure 2.13: Fresnel's diffraction theory illustration.

$$dE_p = \frac{\epsilon_0}{2\rho r\lambda}(1 + cos(\theta))cos[k(\rho + r) - \omega t] \tag{2.13}$$

For a slit shorter than ρ and r, it is possible to verify that $\frac{1}{2}(1+cos(\theta)) \approx 1$ and that $\frac{1}{\rho r} \approx \frac{1}{\rho_0 r_0}$, meaning that the optical paths difference is negligible. Consequently, $\rho = \sqrt{\rho_0^2 + y^2 + z^2}$ and $r = \sqrt{r_0^2 + y^2 + z^2}$. Then, $\rho + r = \rho_0 + r_0 + (y^2 + z^2)\frac{\rho_0 + r_0}{2\rho_0 r_0}$. Based on these relations, expression 2.14 is obtained from expression 2.13.

$$\bar{E}_p = \frac{\epsilon_0 e^{-j\omega t}}{\rho_0 r_0 \lambda} \int_{y_1}^{y_2} \int_{z_1}^{z_2} e^{jk(\rho + r)} dydz \tag{2.14}$$

Considering $u = y(\frac{2}{\lambda r_0})^{\frac{1}{2}}$ and $v = z(\frac{2}{\lambda r_0})^{\frac{1}{2}}$, expression 2.15 is obtainable for $\frac{\bar{E}_u}{2} = \frac{\epsilon_0}{2(\rho_0 + r_0)} e^{j[(k(\rho_0 + r_0)) - \omega t]}$.

$$\bar{E}_p = \frac{\bar{E}_u}{2} \int_{u_1}^{u_2} e^{\frac{j\pi u^2}{2}} du \int_{v_1}^{v_2} e^{\frac{j\pi v^2}{2}} dv \tag{2.15}$$

There are two functions, also known as Fresnel functions, from which the integral on expression 2.15 is most easily calculated. These functions are presented on expressions 2.16 and 2.17. Nowadays, the functions $C(h)$ and $S(h)$ are tabulated simplifying the calculation of the integral in expression 2.15, with $h = u, v$.

$$C(h) = \int_0^h cos(\frac{\pi h'^2}{2}) dh' \tag{2.16}$$

$$S(h) = \int_0^h sin(\frac{\pi h'^2}{2}) dh' \tag{2.17}$$

Expression 2.18 relates both expressions 2.16 and 2.17. Usually, it is used to have only one look-up table in memory.

$$C(h) + jS(h) = \int_0^h e^{\frac{j\pi h'^2}{2}} dh' \tag{2.18}$$

Finally, the electric field at a certain observation point P is given by expression 2.19.

$$\bar{E}_p = \frac{\bar{E}_u}{2} [C(u) + jS(u)]_{u_1}^{u_2} [C(v) + jS(v)]_{v_1}^{v_2} \tag{2.19}$$

Based on this expression it is possible to compute the intensity on P by $I = \frac{\bar{E}_p \bar{E}_p^*}{2}$, where * denotes the complex conjugate.

For a multiple slit array, it is possible to obtain the overall contribution by adding the electric field's contributions of each slit, each one determined by expression 2.19, possibly with a more suitable referential for the array (not on the centre for a slit, but on the centre of the array).

2.2.4 Kirchhoff's Diffraction Theory

Kirchhoff's Diffraction Theory considers a plane wave, $\bar{u}(\boldsymbol{r})$, incident on an opaque plane. The wave propagates along the x-axis. After reaching a slit or aperture, the transmitted wave might be determined by expression 2.20 [4,37], where the integration is based on the surface coordinates y' and z', being x', y' and z' the coordinates of a point $\boldsymbol{r'}$ before or over the metal surface and $\boldsymbol{\phi}$ is the Green's function, for a monochromatic wave at a point $\boldsymbol{r}$ after the plane, given by $r^2 = x^2 + y^2 + z^2$ [4,37].

The assumptions established by Kirchhoff to derive this formulation are that the wave must be scalar ($\bar{u}(\boldsymbol{r}) = u(\boldsymbol{r})$) and its derivative $\frac{\partial \bar{u}}{\partial x'}$ is null after the surface. Then, close to the slit or aperture, there are no disturbances and, consequently, the wave intensity (u) is equal to the incident one u_0 $(u = u_0)$ [4,37].

$$u(\boldsymbol{r}) = \frac{1}{4\pi} \int \left[-\frac{\partial u}{\partial x'}(\boldsymbol{r'})\, \boldsymbol{\phi}(|\boldsymbol{r} - \boldsymbol{r'}|) + u(\boldsymbol{r'}) \frac{\partial \boldsymbol{\phi}}{\partial x'} \right] d\sigma \tag{2.20}$$

When considering dimensions higher than the wave wavelength, Kirchhoff's Diffraction Theory might have Fraunhofer's Diffraction Theory as a limit case. On top of that, another theory known as Fresnel's Diffraction Theory is obtained and valid for the Near-Field region ($D \ll \lambda$ and $a > \lambda$) in contrast with Fraunhofer's one that is valid for the Far-Field region ($D \gg a > \lambda$).

Most of all, the previous results are the base for analysing wave propagation for a slit dimension greater than the incident wavelength. Then, the theory extension for subwavelength slits is expressed in 2.21, only valid for $ka \ll 1$ where a is the slit or aperture diameter and A its area [4,37].

$$u(\boldsymbol{r}) = -A \left[\frac{\partial u_0}{\partial x'} \boldsymbol{\phi}(\boldsymbol{r}) + u_0 \frac{\partial \boldsymbol{\phi}(\boldsymbol{r})}{\partial x} \right] \tag{2.21}$$

2.2.5 Bethe-Bouwkamp's Diffraction Theory

In Kirchhoff's Diffraction Theory, the incident and reflected waves did not exist over the metal surface, leading to the non-verification of the boundary conditions imposed by Maxwell's equations. Also, the developed theory is valid for radiation wavelengths equal to or greater than the slit dimension.

In 1944, Bethe proposed a new theory that allowed the diffracted field to be obtained for slits smaller than the wavelength of the radiation and that verified the boundary conditions. Bethe assumes a plane wave normally incident to an infinite, perfect conductive metal surface, propagating along z and polarised along the x direction. The Bethe's aperture is not a rectangular slit but it is a subwavelength circular hole, which is studied as a cavity upon oscillation. There are mainly three different assumptions regarding the light-matter interaction [37]: (1) incident and reflected waves coexist over the metal surface; (2) the electromagnetic wave does not penetrate the surface, due to the infinite metal conductivity; (3) The complex electric field vector, $\bar{\boldsymbol{E}}$, is tangential to the surface.

Due to the new aperture geometry, Bethe's theory is presented in cylindrical coordinates, considering $\boldsymbol{r}$ as the analysed point after the metal surface ($r^2 = x^2 + y^2 + z^2$), $\boldsymbol{r'}$ a point before the surface ($(r')^2 = (x')^2 + (y')^2 + (z')^2$) and $\boldsymbol{r'} = \boldsymbol{0}$ is the source coordinates. Moreover, a is the hole radius, $\boldsymbol{\kappa}$ is the unity vector pointed to $\boldsymbol{r}$, as well as $\bar{\boldsymbol{E}}_{\boldsymbol{0}}$ and $\bar{\boldsymbol{H}}_{\boldsymbol{0}}$ the electric and magnetic field complex vectors before the metal surface if there is no hole [37].

Since Maxwell's equations and their consequent boundary conditions are satisfied, Bethe stated that his theory is valid for the Far-Field region, $kr \gg 1$, where k is the wave vector given by expression 2.22 [37]. Considering a punctual source, the approximation in expression 2.23 and the Green's function in expression 2.24 are used. Based on that, the complex electric and magnetic fields might be computed using expressions 2.25 and 2.26, respectively [37].

$$k = \frac{\omega}{c} = \frac{2\pi}{\lambda} \tag{2.22}$$

$$\nabla\boldsymbol{\phi} = ik\boldsymbol{\kappa r} \xrightarrow{linear\ aproximation} \boldsymbol{\phi} = \boldsymbol{\phi_0}\left(1 - ik\boldsymbol{\kappa r'}\right) \tag{2.23}$$

$$\phi_0 = \phi(\boldsymbol{r'} = \boldsymbol{0}) = \frac{e^{ikr}}{r} \tag{2.24}$$

$$\boldsymbol{\bar{E}} = \frac{1}{3\pi}k^2a^3\boldsymbol{\phi_0\kappa} \times \left(2\boldsymbol{\bar{H}_0} + \boldsymbol{\bar{E}_0} \times \boldsymbol{\kappa}\right) \tag{2.25}$$

$$\boldsymbol{\bar{H}} = -\frac{1}{3\pi}k^2a^3\boldsymbol{\phi_0\kappa} \times \left(2\boldsymbol{\bar{H}_0} \times \boldsymbol{\kappa} - \boldsymbol{\bar{E}_0}\right) \tag{2.26}$$

Also, Bethe applied Poynting's theorem to obtain the time-average complex radiation power per squared meter as presented in expression 2.27, based on expressions 2.25 and 2.26 [37]. Furthermore, it is possible to estimate the aperture's total transmitted power by integrating expression 2.27 among all the diffracted angles, equivalent to all $\boldsymbol{\kappa}$ directions, resulting in expression 2.28.

$$\boldsymbol{\bar{S}} = \frac{c}{4\pi}\boldsymbol{\bar{E}} \times \boldsymbol{\bar{H}} = \frac{c}{36\pi^3}\frac{k^4a^6}{\boldsymbol{r}^2}\boldsymbol{\kappa}\left(2\boldsymbol{\kappa} \times \boldsymbol{\bar{H}_0} - \boldsymbol{\kappa} \times \boldsymbol{\kappa} \times \boldsymbol{\bar{E}_0}\right)^2 \tag{2.27}$$

$$\boldsymbol{\bar{S}_{tot}} = \frac{c}{27\pi^2}k^2a^6\boldsymbol{\kappa}\left(4\boldsymbol{\bar{H}_0}^2 + \boldsymbol{\bar{E}_0}^2\right) \tag{2.28}$$

Therefore, the electric and magnetic fields are proportional to k^2a^3 and, consequently, the radiation power is proportional to k^4a^6. However, if it is considered a subwavelength hole, such as $ka \ll 1$, the radiation power is going to be proportional to $\left(^a/_\lambda\right)^4$ [37]. Comparing Bethe's theory with Kirchhoff's one, it can be shown that Kirchhoff's intensity drops with λ^{-2}, compared to the λ^{-4} deduced by Bethe.

On top of that, Bethe was also capable of proving that the aperture can be modelled as an electric and a magnetic dipole, respectively denoted by $\boldsymbol{P}$ and $\boldsymbol{M}$. Expressions 2.29 and 2.30 relate the electric and magnetic fields with the electric dipole. Similar relations, 2.32 and 2.30, can be used to relate the magnetic dipole to the electric and magnetic fields [37–39].

$$\bar{\boldsymbol{E}} = k^2 \boldsymbol{\phi_0} \boldsymbol{\kappa} \times \left(\bar{\boldsymbol{P}} \times \boldsymbol{\kappa}\right) \tag{2.29}$$

$$\bar{\boldsymbol{H}} = k^2 \boldsymbol{\phi_0} \boldsymbol{\kappa} \times \bar{\boldsymbol{P}} \tag{2.30}$$

$$\bar{\boldsymbol{H}} = k^2 \boldsymbol{\phi_0} \boldsymbol{\kappa} \times \left(\bar{\boldsymbol{M}} \times \boldsymbol{\kappa}\right) \tag{2.31}$$

$$\bar{\boldsymbol{E}} = -k^2 \boldsymbol{\phi_0} \boldsymbol{\kappa} \times \bar{\boldsymbol{M}} \tag{2.32}$$

Replacing the electromagnetic field expressions 2.25 and 2.26 on expressions 2.29 to 2.32, expressions 2.33 and 2.34 are deduced to obtain the electric and magnetic dipoles in terms of the incident field as well as on the aperture radius.

$$\bar{\boldsymbol{P}} = -\frac{1}{3\pi} a^3 \bar{\boldsymbol{E}}_{\boldsymbol{0}} \tag{2.33}$$

$$\bar{\boldsymbol{M}} = -\frac{2}{3\pi} a^3 \bar{\boldsymbol{H}}_{\boldsymbol{0}} \tag{2.34}$$

After that, Bethe analysed the electromagnetic field close to the aperture to present his theory on the region where he stated that Kirchhoff's failed. It is presented (in cartesian coordinates) in expressions 2.35 and 2.36, which are only valid up to a distance of the same order than the wavelength (Near-Field region) [37–39].

$$\bar{\boldsymbol{E}}(\boldsymbol{r}) \Rightarrow \begin{cases} \bar{E}_x = -\frac{4}{\pi} jk\sqrt{a^2 - x^2 - y^2} \\ \bar{E}_y = 0 \\ \bar{E}_z = jkx \end{cases} \tag{2.35}$$

$$\bar{\boldsymbol{H}}(\boldsymbol{r}) \Rightarrow \begin{cases} \bar{H}_x = 0 \\ \bar{H}_y = \frac{1}{\mu_0 c} \\ \bar{H}_z = -\frac{4}{\mu_0 c \pi} \frac{y}{\sqrt{a^2 - x^2 - y^2}} \end{cases} \tag{2.36}$$

However, analysing expressions 2.35 and 2.36, it is possible to observe that boundary conditions are not satisfied, since $\bar{E}_z \neq 0$. Bethe neglected a term of the same order as ka with a non-valid assumption, giving rise to this inconsistency [38, 39].

Years later, in 1950, Bouwkamp proposed the rectification of Bethe's theory, to guarantee the satisfaction of the boundary conditions [38, 39].

Bouwkamp's approach is based on Babinet's principle. Bouwkamp assumed a disk, instead of an aperture or a hole, to obtain the magnetic currents for the disk's hole and to deduce the electromagnetic field relations presented on expressions 2.37 and 2.38 [38, 39]. Comparing these expressions with Bethe's ones, it is possible to observe that the magnetic field expression did not change.

$$\bar{\boldsymbol{E}}(\boldsymbol{r}) \Rightarrow \begin{cases} \bar{E}_x = -\dfrac{4ik}{3\pi}\dfrac{2a^2 - x^2 - 2y^2}{\sqrt{a^2 - x^2 - y^2}} \\ \bar{E}_y = -\dfrac{4ik}{3\pi}\dfrac{xy}{\sqrt{a^2 - x^2 - y^2}} \\ \bar{E}_z = 0 \end{cases} \tag{2.37}$$

$$\bar{\boldsymbol{H}}(\boldsymbol{r}) \Rightarrow \begin{cases} \bar{H}_x = 0 \\ \bar{H}_y = \dfrac{1}{\mu_0 c} \\ \bar{H}_z = -\dfrac{4}{\mu_0 c\pi}\dfrac{y}{\sqrt{a^2 - x^2 - y^2}} \end{cases} \tag{2.38}$$

Due to differences in the electric field the total radiation power transmitted by the hole, determined by Bouwkamp and presented on expression 2.39, is different from the determined by Bethe [38, 39].

$$\bar{\boldsymbol{S}}_{\boldsymbol{tot}} = \frac{64}{27\pi}k^4 a^6 \bar{\boldsymbol{S}}_{\boldsymbol{0}} = \frac{64}{27\pi}k^4 a^6 \frac{1}{2}c\epsilon_0 \bar{\boldsymbol{E}}_{\boldsymbol{0}}{}^2 \tag{2.39}$$

As Bethe stated, results for the electromagnetic field may be explained due to the simultaneous existence of an electric dipole and a magnetic dipole. The expression for the field of the magnetic dipole is the same as Bethe, but the expression for the field of the electric dipole is of course different, as it is possible to observe on expressions 2.40 and 2.41, respectively for the electric and magnetic dipole [38, 39].

$$\bar{\boldsymbol{P}} = \frac{1}{3\pi}a^3 \bar{\boldsymbol{E}}_{\boldsymbol{0}} \tag{2.40}$$

$$\bar{\boldsymbol{M}} = -\frac{2}{3\pi}a^3 \bar{\boldsymbol{H}}_{\boldsymbol{0}} \tag{2.41}$$

2.3 Extraordinary Optical Transmission

Still in the last century, in 1998, Ebbesen and his colleagues reported an unusual transmission spectrum for a nanostructure where light has normal incidence [40]. Their study was carried out with a metallic and periodic hole array of subwavelength hole diameter and thickness. They present evidence of a huge transmission peak such that none of the classical theories previously described that.

They defined absolute transmission efficiency as the ratio between the fraction of transmitted light intensity by the fraction of surface area occupied by the holes, *i.e.*, the ratio between the transmitted and the incident light intensity divided by the holes' fraction area. They reveal that, in some conditions, it is possible to achieve values greater than 2, meaning that ”more than twice as much light is transmitted as impinges directly on the holes” [40]. At that time, they considered the array as a locally active element, whose response might be tuned in the designing stage by adjusting the hole diameter, the periodicity of the holes, the structure thickness and by changing the material dielectric function [40]. Also, they analysed some experimental evidence regarding Wood's Anomaly. It is an effect observed in the transmission spectrum of optical diffraction gratings, where there is a predictable minimum (dependent on the gratings' periodicity).

Ebbesen and his colleagues soon suggested that the main responsible agents for this remarkable phenomenon are surface plasmons polaritons. They compared their results with the theoretical and experimental studies, performed decades ago, by Kretschmann and Raether about the excitation of SPP in metal films.

Ebbesen and his colleagues suggested the name Extraordinary Optical Transmission since it is an optical phenomenon characterised by an unusual transmission, *i.e.* more than predicted until that time by classical theories. Thus, nanoarrays are a powerful device to concentrate and locally amplify electromagnetic radiation.

Since then, several researchers have been developing studies to better understand this phenomenon. Only in 2006, a research group led by Lalanne and Hugonin developed a study based on Maxwell's equations, proving that the interaction between light and the structures results from two contributions, one from the surface plasmons polaritons and the other from a creeping wave [41]. They were also able to demonstrate that SPP are the main agents of this interaction on the visible spectral region [41]. This research work was a colossal advance in scientific knowledge since until then there had been a big question mark raised by Lezec, Thio and Gay, in 2004. Lezec and Thio proposed one model confronting the SPP theory, named composite diffracted evanescent waves - CDEW -, in which the resonant behaviour is not due to the SPP mechanism, but is due to the interference of diffracted evanescent waves [42]. In the same year, Gay intensified the experimental studies and he obtained results that corroborated the CDEW model [43]. While Lezec and Thio used tungsten structures Gay used one of silver [42,43]. However, Lalanne and Hugonin's demonstration leaves no doubts about the SPP's role in phenomena such as EOT. Their report refuted the CDEW model since the evidence from Maxwell's equations reveals similar results to the SPP theory and huge differences in comparison to the CDEW model [41]. One possible justification, suggested by Lalanne and Hugonin, for the CDEW corroboration with experimental results, is that the metal samples used to perform these studies were spoiled by impurities. On top of that, they referred that the CDEW model has identical limitations as Kirchhoff Diffraction theory [41].

There are many references to the use of EOT in several areas, such as energy, medicine, information, defence, environment and industry. Without underestimating the importance of other application areas and the research works developed by researchers associated with them, these are some examples of the application of EOT: increasing energy harvesting and the efficiency of solar cells, designing miniaturised biosensors, and improving the optical responses of LED and LASER in communications.

2.4 Surface Plasmons Polaritons

In the middle of the XX century, Pines and Bohm's research aroused a general interest in plasmons. In 1956, Fano introduced the concept of polariton and one year later Ritchie established the first surface plasmons theory. The work carried out by Ritchie on SPP allows a better understanding of the anomalous behaviour of dielectric-metal interfaces and metal gratings [44–47].

Kretschmann and Raether made important contributions to the advancement of knowledge on SPP with their theoretical explanation of SPP´s optical excitation in metal films [44–47]. Raether's book on SPP published in 1988 is one of the most interesting and important documents to understand the excitation and propagation of this kind of wave [44].

Figure 2.14 sums up this theoretical evolution.

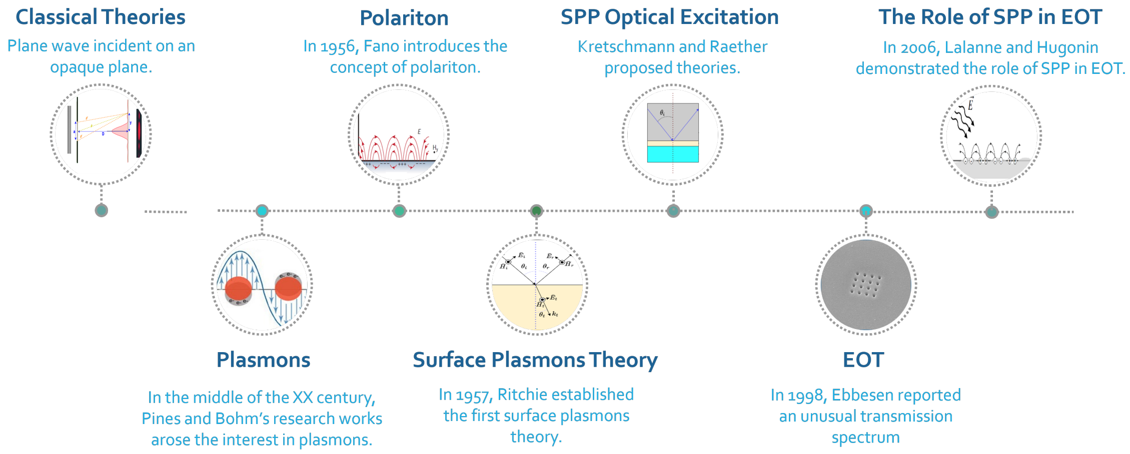

Figure 2.14: Timeline of theoretical evolution.

A plasmon, considered a quasiparticle, is a quantum of a plasma oscillation (the redistribution of plasma's free electrons), just as light is the optical oscillations of photons. Plasmons can be coupled with photons, creating another quasiparticle called a plasmon polariton. Thus, a surface plasmon and a surface plasmon polariton are not the same entity, even though they have a straight relationship [4, 6, 47, 48].

SPP are electromagnetic waves, excited at the interface, between a metal/plasma and a dielectric as illustrated in figure 2.15. Both media are non-magnetic and semi-unlimited. However, only TM waves can excite SPP, and TE waves cannot because they do not verify the boundary conditions at the interface.

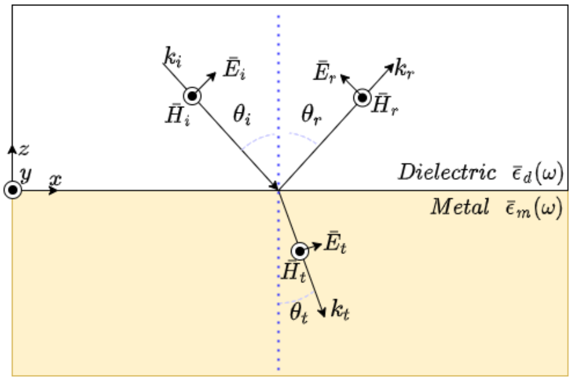

Figure 2.15: Dielectric-Metal Interface (TM wave representation).

The TM wave is described by a wavevector $\bar{\boldsymbol{k}} = [\bar{k}_x, 0, \bar{k}_z]$, with an electromagnetic field that obeys expression 2.42, where p is m or d, respectively for the metal or dielectric [4,41,47,49].

$$\begin{cases} \bar{E}_{x,p}(x,y,z,t) = E_0 e^{j(\bar{k}_x x + \bar{k}_{z,p}|z| - \omega t)} \\ \bar{E}_{z,p}(x,y,z,t) = \pm \dfrac{\bar{k}_x}{\bar{k}_{z,p}} E_0 e^{j(\bar{k}_x x + \bar{k}_{z,p}|z| - \omega t)} \\ \bar{H}_{y,p}(x,y,z,t) = H_0 e^{j(\bar{k}_x x + \bar{k}_{z,p}|z| - \omega t)} \end{cases} \tag{2.42}$$

In the absence of surface free charges, boundary conditions imply that $\bar{E}_{x,d} = \bar{E}_{x,m}$ and $\bar{H}_{y,d} = \bar{H}_{y,m}$. Then, deduction of expression 2.43 is valid and consequently, it is possible to obtain expression 2.44, where k_0 is the incident wavevector, and $\bar{\epsilon}_m$ and $\bar{\epsilon}_d$ are respectively the metal and the dielectric relative electric permittivity [4,41,49].

$$\boldsymbol{\nabla} \times \boldsymbol{H} = \bar{\epsilon} \frac{\partial \boldsymbol{E}}{\partial t} \Rightarrow \begin{cases} \dfrac{\bar{E}_0}{\bar{H}_0} = -\dfrac{\bar{k}_{z,1} c_0}{\bar{\epsilon}_m \omega} \\ \dfrac{\bar{E}_0}{\bar{H}_0} = \dfrac{\bar{k}_{z,d} c_0}{\bar{\epsilon}_d \omega} \\ \bar{k}^2 = \bar{k}_x^2 + \bar{k}_z^2 \end{cases} \Rightarrow \begin{cases} \dfrac{\bar{k}_{z,m}}{\bar{\epsilon}_m} + \dfrac{\bar{k}_{z,d}}{\bar{\epsilon}_d} = 0 \\ \bar{k}_x^2 + \bar{k}_{z,p}^2 = \bar{\epsilon}_p \left(\dfrac{\omega}{c_0}\right)^2 \end{cases} \tag{2.43}$$

$$\bar{k}_x = k_0 \sqrt{\frac{\bar{\epsilon}_m(\omega)\bar{\epsilon}_d(\omega)}{\bar{\epsilon}_m(\omega) + \bar{\epsilon}_d(\omega)}} \tag{2.44}$$

On the top of that, a perpendicular wavevector component $\bar{k}_z$ appears, such as $\bar{k}_{z,p} = \left(\bar{\epsilon}_p k_0^2 - \bar{k}_x^2\right)^{1/2}$.

Some examples of the SPP dispersion relation curves, $\omega(Re\{k_x\})$, are presented in chapter 3 to validate the proposed methodology. However, it is important to highlight at this point that SPP have an evanescent decay, since its curves are on the right side of the light one ($\omega = c_0 \frac{Re\{k_x\}}{n\sqrt{\bar{\epsilon}_d(\omega)}}$, where c_0 is the vacuum light speed and n is the dielectric refractive index) [4,6,40,41,50,51].

EOT is only verified at the nano-scale, due to the propagation distance of the SPP and the resonances of the materials in question. This fact is perfect as it leads to the miniaturisation of devices and the use of lower energies. Also, it depends on the propagation media, leading to a perfect scenario to design sensors, since it is its working principle.

However, even though devices based on SPP and also on EOT are already being proposed and fabricated, the search for models is not closed and much effort and dedication have been put into it since none of the classical diffraction theories describes EOT. The electromagnetism theory describes the phenomena and it is possible to study it using sophisticated tools based on Maxwell's equations. The main reason the classical diffraction theories fail to predict and describe EOT is that all of them completely ignore the light-matter interaction on the dielectric-metal interface. It is suggested that metal will reflect all radiation. It is not true in the near-infrared, visible and ultraviolet spectral regions of metals. In these regions there are surface plasmon resonances, leading to its polaritons propagation on the metal and to the light transmission throughout the metal. Also, metal should be thinner to guarantee that the SPP (an evanescent wave) is not absorbed in it, in other words, the radiation should be transmitted on the dielectric-metal interface, propagate in the metal, reach the metal-dielectric interface and reach the target.

2.5 Radiation Zones

From the analysis in the previous subsections, it is possible to understand that the slits' responses might be distinct at different target distances. In other words, maxima and minima positions, as well as intensities and the shape of the patterns, will vary not only if the slits array geometry changes but also accordingly to the source-target distance.

Thus, it is possible to divide the radiation zone as suggested in figures 2.16 and 2.17.

In the Far-Field region, the electromagnetic field and consequently the radiation profile follow Fraunhofer's Diffraction Theory. For that reason, this region is also known as the Fraunhofer region. It is usually defined from a distance of twice the wavelength to infinity. In this region, the pattern shape remains the same if the target moves. The further away the target is from the source, the less intense the peaks will be. At infinity, the pattern will tend to be uniform (a constant step), keeping its shape.

The biggest difference between the patterns of this region and the Fresnel region is that in the Fresnel region, changing the source-target distance changes the shape of the light pattern. The Fresnel region lies between a distance of $\lambda/2\pi$ and λ and the electromagnetic field follows Fresnel-Kirchhoff's Diffraction Theory (an approximation of Kirchhoff's Diffraction Theory at the near-field).

Even though the Fresnel region is the majority of the Near-Field region, they are not the same. The Near-Field region is divided into two different regions. Apart from the Fresnel region, which is the radiative Near-Field region, there is also the reactive Near-Field region, defined from the slits array to $\lambda/2\pi$. In this region, one should take into account other electromagnetic contributions, such as the propagation of evanescent waves on the array's material. These evanescent waves will appear whenever the material of the array is not opaque. If the material is perfectly conductor, then it is opaque and the region is also called Shadow Zone since all the radiation comes from the slit and consequently, the pattern is the perfect shadow (replica) of the array. Otherwise, radiation might also pass through the material and its contribution to the patterns should be considered.

The definition of the regions' cut-off numbers/distances is based on the relative strengths of the field component amplitudes. Since it is an empirical definition, mostly based on experimental results, it is commonly defined as a transition region between the Fresnel and the Fraunhofer ones. However, there are some assumptions regarding these divisions, namely regarding the device dimensions. In this case, it is assumed that the antenna (since the slits array behaves as an antenna) dimension is at least smaller than half the wavelength (short-antennas). Otherwise, the antenna is defined as a long antenna and the region's characterisation will depend on the source-target distance. Nevertheless, due to the scope of this research work (characterisation and design of nanoantennas), the short-antenna assumption will be used. Notwithstanding that this assumption will not interfere with the obtained results but only with their categorisation.

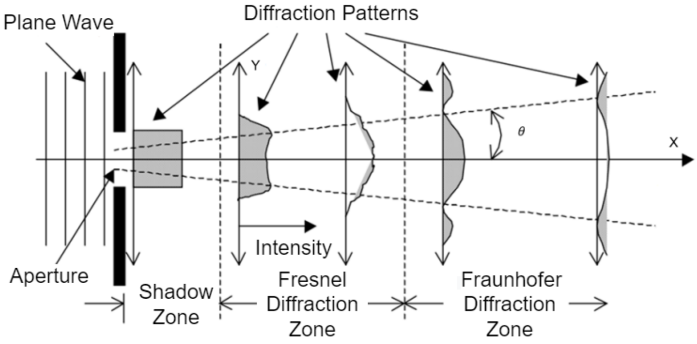

Figure 2.16: Diffraction patterns in different diffraction regions.

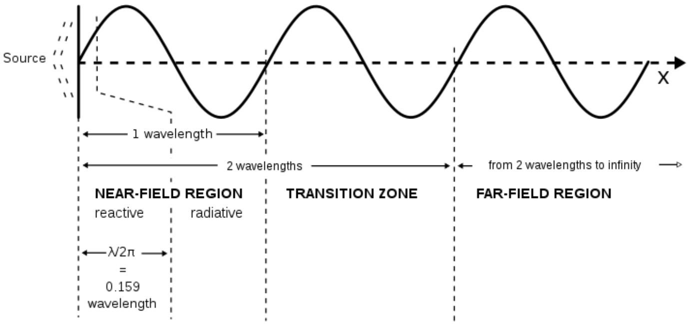

Figure 2.17: Radiation regions' cut-off distances.

2.6 Characterisation of Metals' Electrical Permittivity

In this section, the used model to characterise the metals' electrical permittivity is analysed.

Light-metal interaction might be characterised mainly due to the movement of the free electrons in the metal. According to Drude's model, the oscillations of those electrons and the electric field are in phase opposition. Consequently, most of the metals have a negative electrical permittivity leading to their high reflection coefficient [4].

Surface Plasmons are oscillations of the metals' free electrons that can couple with the incident radiation, leading to SPP [4, 5, 47].

Thus, these phenomena are especially dependent on the metals' electrical behaviour at different frequencies. For this reason, the metals' models should be adapted for the optical frequencies and for nano-scale structures.

The first approach to modelling the materials' optical properties is based on the electron movement equation, which describes the movement of metal's free electrons in the metal in the absence of a magnetic field and consequently the generated electrical current for the incident radiation. This equation is presented on expression 2.45, for a position vector r where $\bar{\boldsymbol{E}}_{\mathbf{0}}$ is the sinusoidal amplitude of the incident electrical field with angular frequency ω, q and m_e are respectively the electron's modulus of charge and its effective mass and Γ is the damping factor that is related to the electrons' Fermi velocity v_F and average propagation distance l by $\Gamma = v_F/l$. This factor relates to the energy loss due to electron collisions [4, 48].

From expression 2.45 is possible to obtain the relative electrical permittivity, which is presented in expression 2.46. In this expression, ω_p is the plasma frequency, which is electrically described as $\omega_p = \sqrt{\tilde{n}q^2/(m_e\epsilon_0)}$ where $\tilde{n}$ is the free electrons density and ϵ_0 the vacuum electrical permittivity [4, 48].

$$m_e \frac{\partial^2 \boldsymbol{r}}{\partial t^2} + m_e \Gamma \frac{\partial \boldsymbol{r}}{\partial t} = q\boldsymbol{E}_{\mathbf{0}} \tag{2.45}$$

$$\bar{\epsilon}_{Drude}\left(\omega\right) = 1 - \frac{\omega_p^2}{\omega^2 + \Gamma^2} + j\frac{\Gamma\omega_p^2}{\omega\left(\omega^2 + \Gamma^2\right)} \tag{2.46}$$

This model is sufficient to characterise metals' behaviour at frequencies below the near-infrared region. In the near-infrared and visible regions, the model must change to include the influence of bound electrons due to intraband transitions.

Expression 2.47 describes the movement of bound electrons, where γ is the radiation damping factor for the case of bound electrons, α is the potential force restitution coefficient and m is the bound electrons' effective mass.

Based on expression 2.47 it is possible to establish the contribution of bound electrons to the relative electrical permittivity, presented in expression 2.48 [4, 48]. In this case, $\tilde{\omega} = \sqrt{\tilde{\tilde{n}}q^2/(m\epsilon_0)}$ and $\omega_i =$

$\sqrt{\alpha/m}$ for $\tilde{n}$ bound electrons density.

$$m\frac{\partial^2 \boldsymbol{r}}{\partial t^2} + m\gamma\frac{\partial \boldsymbol{r}}{\partial t} + \alpha\boldsymbol{r} = q\boldsymbol{E_0} \tag{2.47}$$

$$\bar{\epsilon}_{be}\left(\omega\right) = 1 + \frac{\tilde{\omega}_p^2(\omega_i^2 - \omega^2)}{(\omega_i^2 - \omega^2)^2 + \gamma^2\omega^2} + j\frac{\gamma\tilde{\omega}_p^2\omega}{(\omega_i^2 - \omega^2)^2 + \gamma^2\omega^2} \tag{2.48}$$

Thus, it is possible to consider that the relative dielectric function results from the sum of different contributions regarding free and bound electrons, leading to more precise models. This is the base of the Drude-Lorentz model, in which the permittivity function is presented on expression 2.49 [4,6,48,52].

$$\bar{\epsilon}(\omega) = 1 - \frac{\Omega_p^2}{\omega(\omega + j\Gamma_0)} + \sum_{n=1}^{N}\frac{f_n\omega_p^2}{(\omega_n^2 - \omega^2) - j\omega\Gamma_n} \tag{2.49}$$

The most used metals are Gold, Silver, Aluminium and Copper due to their optical properties that are analysed in the following sections. In table 2.1 are presented the constant values for these metals, according to models and fitting made by Rakic [52,53]. Here, the plasma angular frequency ω_p is given by ω_0 and $\Omega_p = f_0^{1/2}\omega_p$, for each of the N considered oscillations.

Table 2.1: Rakic's Drude-Lorentz Parameters.

	Gold			Silver		
n	f_n	$\omega_n\,[eV]$	$\Gamma_n\,[eV]$	f_n	$\omega_n\,[eV]$	$\Gamma_n\,[eV]$
0	0.760	9.030	0.053	0.845	9.010	0.048
1	0.024	0.415	0.241	0.065	0.816	3.886
2	0.010	0.830	0.345	0.124	4.481	0.452
3	0.071	2.969	0.870	0.011	8.185	0.065
4	0.601	4.304	2.494	0.840	9.083	0.840
5	4.384	2.214	13.32	5.646	20.290	2.419

	Aluminium			Copper		
n	f_n	$\omega_n\,[eV]$	$\Gamma_n\,[eV]$	f_n	$\omega_n\,[eV]$	$\Gamma_n\,[eV]$
0	0.523	14.98	0.047	0.575	10.830	0.030
1	0.227	0.162	0.333	0.061	0.291	0.378
2	0.050	1.544	0.312	0.104	2.957	1.056
3	0.166	1.808	1.351	0.723	5.300	3.213
4	0.030	3.473	3.382	0.638	11.180	4.305
5	-	-	-	-	-	-

2.7 Complex Refractive Index of Different Biosamples

In this section, some samples' refractive indices are presented. Before analysing biosamples more closely, figure 2.18 shows the values for common samples, which can both be analytes or even serve as a reference [53]. As verified, these analytes' refractive indices are real, meaning they do not absorb radiation within this wavelength range.

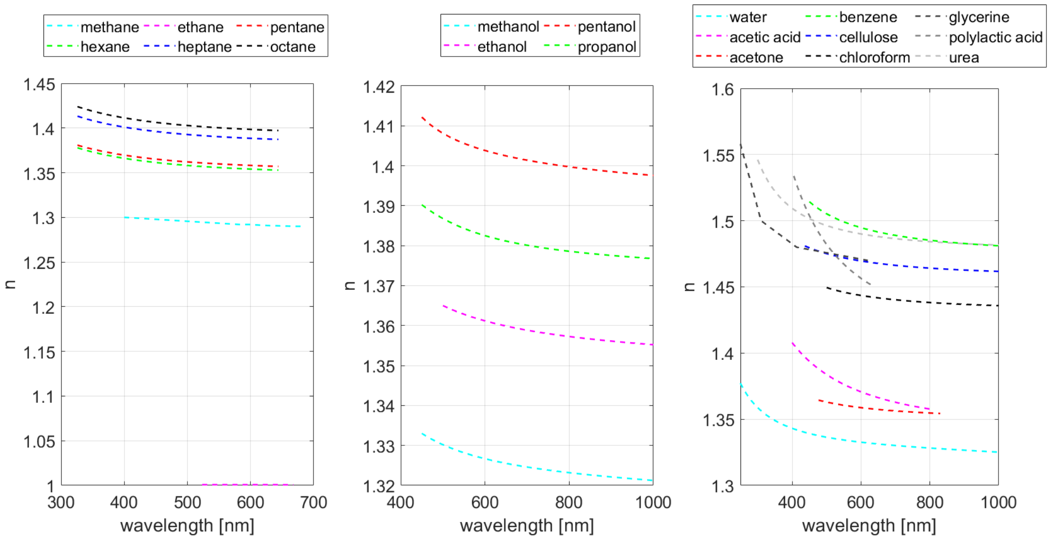

Figure 2.18: Refractive index of common analytes that can act as reference (obtained from [53]).

In table 2.2 (from [54]) is the refractive index of urine considering sugar concentration in blood since both are related. Similarly, in figure 2.19 is the refractive index of water for different glucose (sugar) concentrations [55, 56]. It is possible to verify that the higher the glucose concentration the higher the refractive index. Also, the variation has a linear trend for the different analysed refractive indices.

Table 2.2: Refractive index of urine for different glucose concentrations in blood.

Concentration	n
0-15 mg/dl	1.335 $\pm$ 0.001
1.25 mg/dl	1.337 $\pm$ 0.001
2.5 mg/dl	1.338 $\pm$ 0.001
5 mg/dl	1.341 $\pm$ 0.001

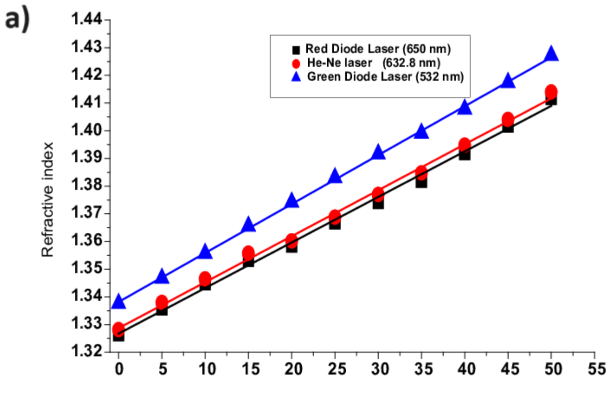

b)

concentration (%)	*n* λ=455 nm	*n* λ=525 nm	n λ=633 nm	n* λ=633 nm
0	1.3322	1.3320	1.3318	1.3282
5	1.3379	13377	1.3375	1.3380
10	1.3424	13421	1.3419	1.3465
15	1.3521	13516	1.3512	1.3558
20	1.3583	13579	1.3576	1.3602
25	1.3645	13642	1.3639	1.3688
30	1.3715	13712	1.3709	1.3770
35	1.3753	13748	1.3745	1.3848
40	1.3849	1.3844	1.3838	1.3948

Figure 2.19: Refractive index of sugar/glucose aqueous solution: a) from [55]; b) from [56].

Focusing even more on biological samples, figure 2.20 presents the refractive index of haemoglobin (Hb) and oxygenated haemoglobin (HbO_2) in water. The results are experimentally obtained considering 150 g_{Hb}/l, which is a typical concentration in blood. It is used as a molar coefficient database and for that reason, one may determine the extinction factor (refractive index's imaginary part, κ) based on it. After that, Kramers–Kronig relations are applied to determine the refractive index's real part. Both are presented in figure 2.20 and these results are validated with [57].

Blood is made up of plasma (55%) and cellular elements (45%). Plasma is the liquid part of blood and is largely composed of water ($> 90\%$) and various dissolved substances. On the other hand, cellular elements are mainly divided into two types of cells (red blood cells/erythrocytes and white blood cells/leucocytes) and cell fragments known as platelets. Haemoglobin is the element that exists in the greatest quantity among the red blood cells. Haemoglobin is the protein that transports oxygen.

The blood refractive index is computed as $\bar{n}_{blood} = \bar{n}_e V_e + \bar{n}_p V_p$, where V is volume and $\bar{n}$ the complex refractive index as well as e denotes erythrocytes and p the plasma. Since plasma is mainly water and the erythrocytes are mainly composed of haemoglobin, the blood can be seen as a haemoglobin-aqueous solution.

The results in figure 2.20 suggest that the real part of the refractive index (n) varies between 300 and 500 nm and its imaginary part (κ) has a wide variation range. Considering the κ variation it is possible to design sensors mainly analysing the optical power that is absorbed in a certain optical path. In contrast, the real refractive index can be used to design sensors based on reflectance variations.

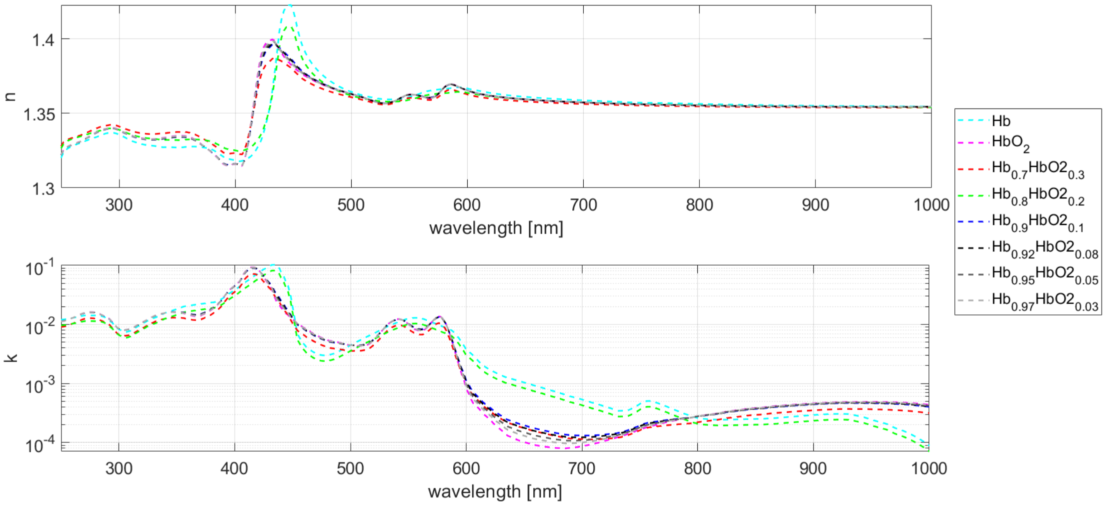

Figure 2.20: Refractive index of haemoglobin (Hb) and oxygenated haemoglobin (HbO_2) in water.

For wavelengths in the red and near-infrared, the blood refractive index does not vary with the haemoglobin (oxygen percentage). Then, it is possible to analyse other markers, mainly the ones associated with other blood functions. Besides transporting oxygen to cells, blood also transports glucose which gives them energy to operate (glycation). Insulin is produced in the pancreas and helps our body to control and regulate the glucose levels in blood. If the pancreas does not produce enough insulin to adjust the glucose concentration in blood or if it is not used properly by our body, cells will not operate correctly and one develops diabetes.

It is possible to analyse glucose levels in blood considering its refractive index, as observed in figure 2.19. Since haemoglobin is highly dependent on oxygen levels, to measure glucose one may operate at wavelengths where haemoglobin has a small influence, namely at red and near-infrared, as characterised by the variation in figure 2.20. Thus, the solution is defined as haemoglobin in sugar water, where the glucose level varies. The analysed concentration levels allow us to design diabetes markers, since some entities as the American Diabetes Association established glucose concentration levels for the disease behaviour. For this entity, glucose levels for a healthy person are limited to 5.7%. Also, the prediabetes stage is defined between 5.7% and 6.4%, being diabetes for values higher than 6.4%. These relations are shown in figure 2.21, where other sub-levels are used to categorise the severity of the diseases and the risks of complications [58, 59].

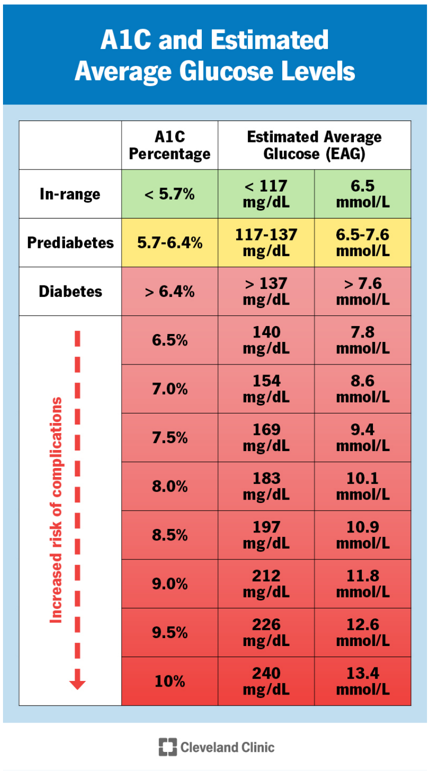

A1C and Estimated Average Glucose Levels

	A1C Percentage	Estimated Average Glucose (EAG)	
In-range	< 5.7%	< 117 mg/dL	6.5 mmol/L
Prediabetes	5.7-6.4%	117-137 mg/dL	6.5-7.6 mmol/L
Diabetes	> 6.4%	> 137 mg/dL	> 7.6 mmol/L
Increased risk of complications	6.5%	140 mg/dL	7.8 mmol/L
	7.0%	154 mg/dL	8.6 mmol/L
	7.5%	169 mg/dL	9.4 mmol/L
	8.0%	183 mg/dL	10.1 mmol/L
	8.5%	197 mg/dL	10.9 mmol/L
	9.0%	212 mg/dL	11.8 mmol/L
	9.5%	226 mg/dL	12.6 mmol/L
	10%	240 mg/dL	13.4 mmol/L

Cleveland Clinic

Figure 2.21: Average glucose levels in blood (from [58]).

Other diseases also have interesting marks on the refractive index. This is the case with breast cancer and fibroadenoma (benign lumps in the breast). Figure 2.22 presents the results of a study carried out to analyse the complex refractive index variation with the cell's type [60].

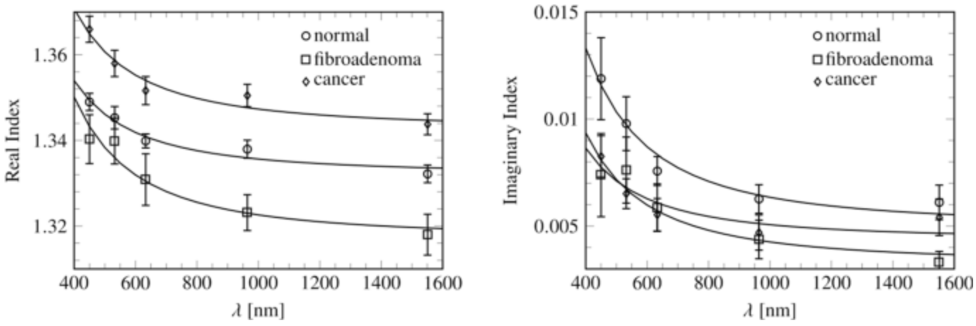

Figure 2.22: Refractive index of human breast tissues: normal, fibroadenoma and cancer cells (from [60]).

Another disease that is affecting the population in the XXI century is liver cancer. The refractive index of liver cells is also influenced by their type, as illustrated in figure 2.23 [61]. In this study, the authors analysed different individuals with different stages and cancer types. They tested normal liver tissue (N), liver metastases and hepatocellular carcinoma. In specimens with liver metastases, they characterise metastatic tissue (MET) and non-cancerous tissue (NMET). The same is performed in hepatocellular carcinoma for primary liver tumour (HCC) and non-cancerous tissue (NHCC). From the results presented in figure 2.23, it is possible to verify that the cancerous tissues are characterised by a lower real part of their refractive index. Considering the real part of the refractive index, the MET cells may be differentiated from normal cells or NMET. Also, NHCC and HCC differ from normal cells but their refractive index is not different between them.

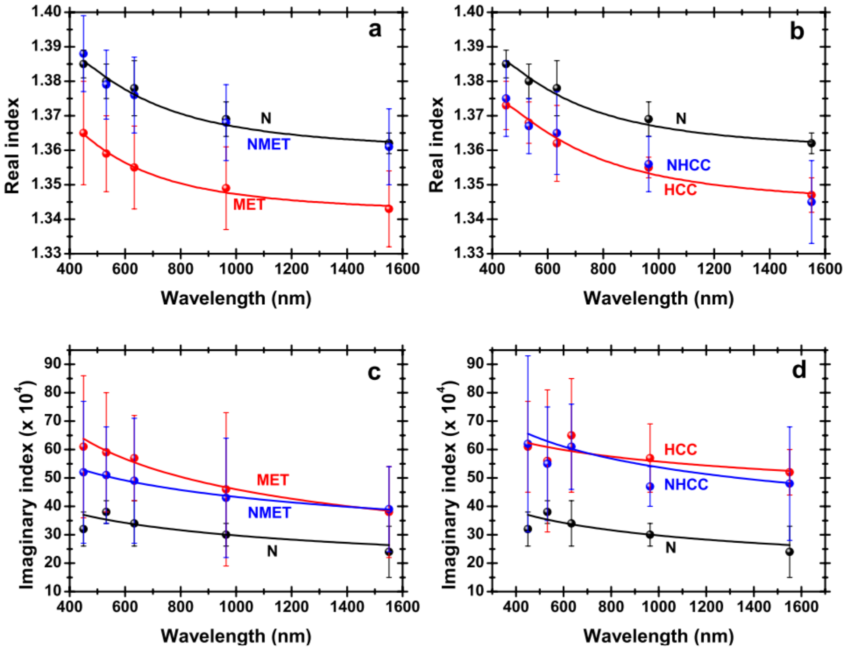

Figure 2.23: Refractive index of human liver tissues: normal (N), metastatic tissue (MET), non-metastatic tissue (NMET), hepatocellular carcinoma (HCC) and non-hepatocellular carcinoma tissue (NHCC).

To get a better idea of the variation in the refractive index (real part) for different diseases in the visible spectral range, the authors of [62] have compiled different samples as presented in figure 2.24. As biology is not just about human beings, they also present samples of other animals as a means of comparison (H: Human, Ho: Horse, C: Canine; M: Mouse, P: Porcine, R: Rat; F: Frog, Rb: Rabbit, T: Trout, B: Bovine, O: Ovine). In figure 2.24a is the refractive index of skin and its components as well as in 2.24b is the eye characteristics. In 2.24c is presented the results for adipose tissues and in 2.24d is the refractive index of central nervous system's tissues. Figure 2.24e shows liver and blood results, in 2.24f are other tissues such as cartilage, heart, lungs, thyroid, breast, and neck as well as kidney, spleen, stomach, esophagus, pancreas and colon in figure 2.24g.

From these results, it is possible to conclude that several diseases, including cancer, influence the tissues' refractive index. Once the living bodies are mostly made of water, the tissues' refractive index is around 1.33-1.35, thus optical sensors that cover this value range can detect the tissue's illness. Also, observing that the refractive index range between 1.30 and 1.41 covers many diseases, optical sensors may be designed to mark them considering these limits.

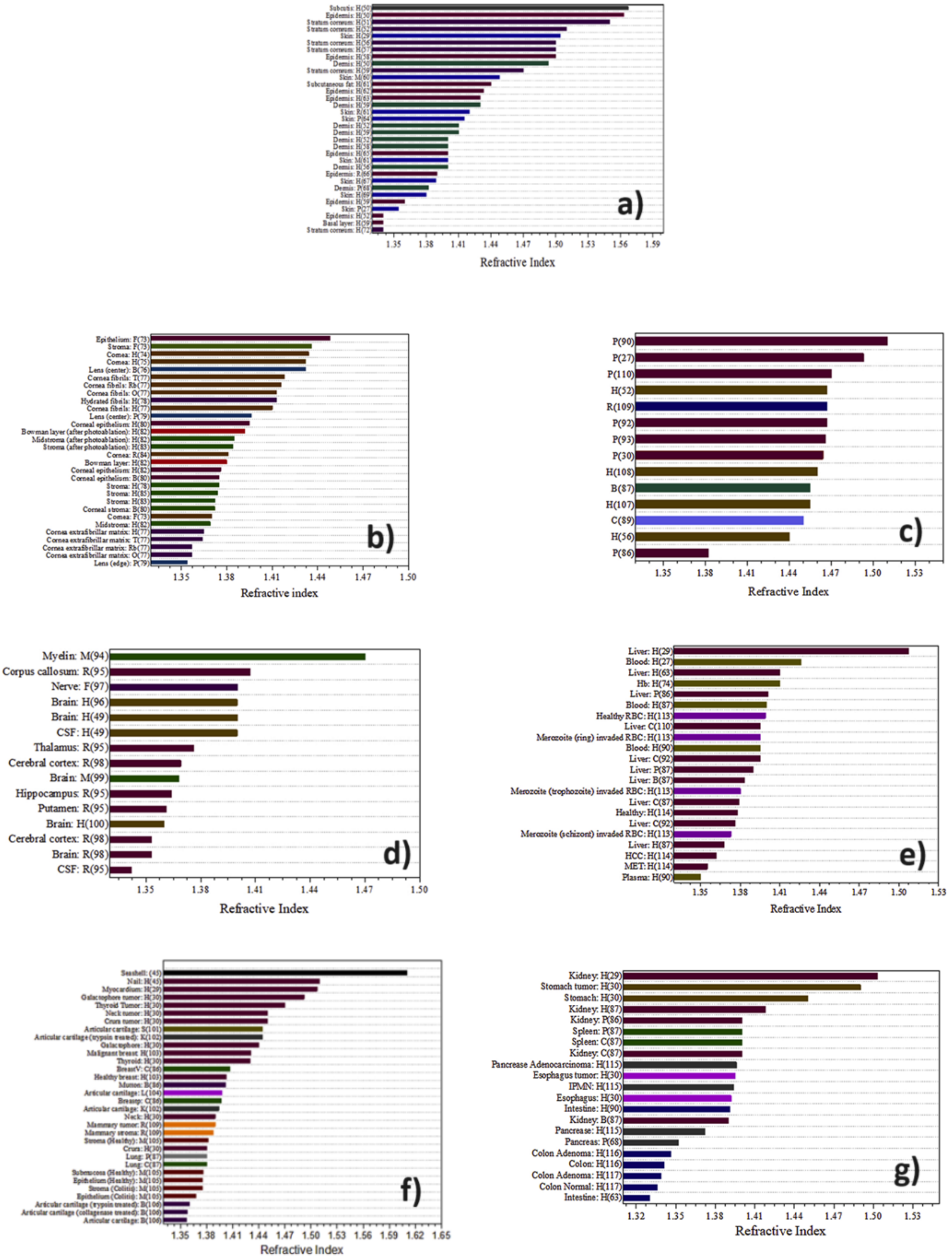

Figure 2.24: Refractive index of different biological tissues in the visible spectral range. H: Human, Ho: Horse, C: Canine; M: Mouse, P: Porcine, R: Rat; F: Frog, Rb: Rabbit, T: Trout, B: Bovine, O: Ovine. Age is within parenthesis. (e.g.: H(27) is a 27-year-old human being)

3

Development and Validation of a Semi-Classical and Time-Domain Model

Contents

In this chapter, a new methodology and a novel model are proposed, and validated, aimed at analysing the Extraordinary Optical Transmission effect in slit nanoantennas. The methodology is based on optical concepts such as Fresnel Coefficients and Snell's law. At the end of this chapter, both methodology (mathematical formalism) and model (implementation covering wave-particle duality) are validated and prepared to be used to characterise the nanaoantennas' behaviour at different biological stimuli. The innovative model recognizes the trend towards miniaturization of this type of device, in particular considering the stochastic nature of light and its quantization.

A photon is described both as a particle and an electromagnetic wave. Then, the wave methodology is applied in the particles' propagation. The implemented model is stochastic since the Fresnel Coefficients describe the probability of a certain event at an interface. Photons follow the average power direction (wave propagation direction), and their electromagnetic characteristics are connected to the wavevector, which is computed according to the reflection and refraction laws. This methodology allows the analysis of wave phenomena, such as diffraction and interference, even with many photons in the simulation environment or when the results are an average of an immense set of runs. On the other hand, the model allows us to obtain results for low-power devices.

During the validation process, some important analyses are performed. First, the method (mathematical expressions) is validated accordingly to Maxwell's equations and their prediction about surface plasmon resonances. This leads to the study of the role of surface plasmon polaritons in the dielectric-metal interface. After that, Kretschmann structures are analysed in a validation stage whose results demonstrate that the variables of the proposed method have physical significance whereas other methods are purely mathematical. Until there, it is a ray tracing tool based on wave formalism. After that, algorithms are implemented to obtain a semi-classical model on the time-domain, focus on wave-particle duality. Then, results are obtained and they are compared with results from commercial software, called COMSOL Multiphysics, which is a Finite Element Method tool. The developed model is implemented in Python.

3.1 Methodology

3.1.1 Proposed Approach

The propagation of a plane wave characterised by an angular frequency ω follows Maxwell's equations that can take the expression 3.1 form. This form is valid for homogeneous, isotropic, linear media without external charge or current sources. Also, it is assumed $e^{-j\omega t}$ as the wave oscillation notation. The propagation media are defined by a certain magnetic permeability μ and a given complex electric permittivity $\bar{\epsilon}$, which are relative properties referenced to the universal constants μ_0 and ϵ_0, respectively.

$$\begin{cases} \nabla \cdot \bar{\boldsymbol{E}}(\boldsymbol{r}) = 0 \\ \nabla \cdot \bar{\boldsymbol{H}}(\boldsymbol{r}) = 0 \\ \nabla \times \bar{\boldsymbol{E}}(\boldsymbol{r}) = j\omega\mu_0\mu\bar{\boldsymbol{H}}(\boldsymbol{r}) \\ \nabla \times \bar{\boldsymbol{H}}(\boldsymbol{r}) = -j\omega\epsilon_0\bar{\epsilon}\bar{\boldsymbol{E}}(\boldsymbol{r}) \end{cases} \tag{3.1}$$

Helmholtz wave equation for a Transverse Magnetic (modes) (TM) wave is in expression 3.2, which is obtained from the previous expression 3.1, where k is the intrinsic complex propagation constant [63,64]. The solution of the Helmholtz wave equations has the form $\bar{\boldsymbol{H}}(\boldsymbol{r}) = \boldsymbol{H}e^{j\bar{\boldsymbol{k}}\cdot\boldsymbol{r}}$, where $\bar{\boldsymbol{k}}$ is the complex wavevector defined in 3.3.

$$\left(\nabla^2 + k^2\right)\bar{\boldsymbol{H}}(\boldsymbol{r}) = 0 \tag{3.2}$$

The proposed methodology is based on inhomogeneous plane waves on absorbing media. A wave is defined as inhomogeneous when there is no coincidence between the normal to the plane of constant phase, $\hat{e}$, and the normal to the plane of constant amplitude, $\hat{\boldsymbol{g}}$ [63–66]. It is also known that the incident planes of $\hat{e}$ and $\hat{\boldsymbol{g}}$ may be different and distanced by an angle ϕ [7,16,67]. There is an angle θ representative of the real component of the wavevector (normal to the equi phase planes) and a different angle ψ responsible for its imaginary part (normal to the equi amplitude planes). Both angles are referenced with the surface normal vector.

For media characterised by a complex refractive index, the wavevector is also complex and then these media may support inhomogeneous waves, as presented on expressions 3.3 and 3.4, being $\hat{s}$ a vector perpendicular to the interface. The apparent refractive index components, *N* and *K*, can be defined using expressions 3.5, where n and k are respectively the real and imaginary parts of the complex refractive index. Expression 3.5 is obtained from the equalities in expression set 3.3. Based on that, expression 3.6 is obtained, considering $cos(\alpha) = \hat{\boldsymbol{e}} \cdot \hat{\boldsymbol{g}}$. The value of *K* may be determined using one of the expressions of 3.5, based on the already determined *N* [7,16,63–65,67].

$$\begin{cases} \bar{\boldsymbol{k}} = k_0\left(N\hat{\boldsymbol{e}} + jK\hat{\boldsymbol{g}}\right) \\ \bar{\boldsymbol{k}} \cdot \bar{\boldsymbol{k}} = k^2 \\ k = \omega\sqrt{\mu\bar{\epsilon}\mu_0\epsilon_0} = k_0\sqrt{\mu\bar{\epsilon}} \end{cases} \tag{3.3}$$

$$\bar{\boldsymbol{k}} \cdot \hat{\boldsymbol{s}} = \bar{k} = k_0\left(N\,cos\,(\theta) + j\,K\,cos\,(\psi)\right) \tag{3.4}$$

$$\begin{cases} N^2 - K^2 = n^2 - \kappa^2 \iff N^2 - K^2 = \mu\epsilon' \\ NK\hat{\boldsymbol{e}} \cdot \hat{\boldsymbol{g}} = n\kappa \iff NK\hat{\boldsymbol{e}} \cdot \hat{\boldsymbol{g}} = \dfrac{\mu\epsilon''}{2} \end{cases} \tag{3.5}$$

$$N^2 = \frac{1}{2}\left(n^2 - \kappa^2 + \sqrt{(n^2-\kappa^2)^2 + 4\left(n\kappa/cos\left(\alpha\right)\right)^2}\right) \tag{3.6}$$

On the interface between two media, radiation will interact with the interface, and its directions may change. That interaction leads to the reflection and refraction of radiation. In both cases the complex components of $\boldsymbol{k}$ must be conserved, due to boundary conditions presented in expression 3.7, leading to expression 3.8 [64, 65].

$$\begin{cases} \epsilon_0[\bar{\epsilon}_2\bar{\boldsymbol{E}}_{\boldsymbol{2}}(\boldsymbol{r},\boldsymbol{t}) - \bar{\epsilon}_1\bar{\boldsymbol{E}}_{\boldsymbol{1}}(\boldsymbol{r},\boldsymbol{t})] \cdot \hat{\boldsymbol{s}} = 0 \\ \mu_0[\mu_2\bar{\boldsymbol{H}}_{\boldsymbol{2}}(\boldsymbol{r},\boldsymbol{t}) - \mu_1\bar{\boldsymbol{H}}_{\boldsymbol{1}}(\boldsymbol{r},\boldsymbol{t})] \cdot \hat{\boldsymbol{s}} = 0 \\ \hat{\boldsymbol{s}} \times [\bar{\boldsymbol{E}}_{\boldsymbol{2}}(\boldsymbol{r},\boldsymbol{t}) - \bar{\boldsymbol{E}}_{\boldsymbol{1}}(\boldsymbol{r},\boldsymbol{t})] = 0 \\ \hat{\boldsymbol{s}} \times [\bar{\boldsymbol{H}}_{\boldsymbol{2}}(\boldsymbol{r},\boldsymbol{t}) - \bar{\boldsymbol{H}}_{\boldsymbol{1}}(\boldsymbol{r},\boldsymbol{t})] = 0 \end{cases} \tag{3.7}$$

$$\bar{\boldsymbol{k}}_{\boldsymbol{i}} \cdot \boldsymbol{r} = \bar{\boldsymbol{k}}_{\boldsymbol{r}} \cdot \boldsymbol{r} = \bar{\boldsymbol{k}}_{\boldsymbol{t}} \cdot \boldsymbol{r} \tag{3.8}$$

From this relation it is also determined the relation for the angles ϕ (angle between the incident planes of $\hat{e}$ and $\hat{\boldsymbol{g}}$), such that $\phi_i = \phi_r = \phi_t$ [7, 16, 64, 65, 67].

Thus, if the incident wave is a homogeneous wave, where the planes of constant phase and amplitude coincide, $\phi_i = 0 \rightarrow \alpha = \theta - \psi$. Then, this relation will be valid along all the simulations since ϕ will be null in every interface [7, 64, 65, 67]. In other words, if the emission medium is homogeneous, then $\phi = 0$ and since $\phi_i = \phi_r = \phi_t$ it is possible to neglect ϕ because it will be always null.

Decomposing $\boldsymbol{r}$ into parallel and perpendicular components to the interface expression 3.8 leads to expression 3.9. These conditions reveal that the parallel component (to the interface) of the wavevector must be continuous at the interface. Also, the perpendicular component of the incident and the reflected wavevectors must be anti-parallel.

$$\begin{cases} \hat{\boldsymbol{s}} \times \bar{\boldsymbol{k}}_{\boldsymbol{i}} = \hat{\boldsymbol{s}} \times \bar{\boldsymbol{k}}_{\boldsymbol{r}} = \hat{\boldsymbol{s}} \times \bar{\boldsymbol{k}}_{\boldsymbol{t}} \\ \hat{\boldsymbol{s}} \cdot \bar{\boldsymbol{k}}_{\boldsymbol{i}} = -\hat{\boldsymbol{s}} \cdot \bar{\boldsymbol{k}}_{\boldsymbol{r}} \end{cases} \tag{3.9}$$

Relation in expression 3.9 leads to $\theta_r = \theta_i$ and $\psi_r = \psi_i$, for the reflection case. For the refraction scenario, the complex Snell's law should be used, as presented on expression 3.11 [7, 16, 63–68].

$$\begin{cases} sin(\theta) = \hat{\boldsymbol{s}} \times \hat{\boldsymbol{g}} \\ cos(\theta) = \hat{\boldsymbol{s}} \cdot \hat{\boldsymbol{g}} \\ sin(\psi) = \hat{\boldsymbol{s}} \times \hat{\boldsymbol{e}} \\ cos(\psi) = \hat{\boldsymbol{s}} \cdot \hat{\boldsymbol{e}} \end{cases} \tag{3.10}$$

$$\begin{cases} N_i \sin(\theta_i) = N_t \sin(\theta_t) \\ K_i \sin(\psi_i) = K_t \sin(\psi_t) \end{cases} \tag{3.11}$$

However, N_t and K_t are unknown parameters that must be determined to compute θ_t and ψ_t. Expression 3.12 may be obtained to compute N_t from the incident wave parameters [65], where $N_s = N_i \sin(\theta_i)$, $K_s = K_i \sin(\psi_i)$ and ϕ_i will be null. After obtaining N_t, K_t must be calculated from expression 3.5 [7, 16, 64, 65, 67].

$$\begin{aligned} N_t^4 - N_t^2 \left(N_s^2 + K_s^2 + \left(n_t^2 - \kappa_t^2 \right) \right) + N_s^2 K_s^2 + \\ N_s^2 \left(n_t^2 - k_t^2 \right) - \left(n_t \kappa_t - N_s K_s \cos(\phi_i) \right)^2 = 0 \end{aligned} \tag{3.12}$$

Fresnel reflection and transmission coefficients are also obtained from the boundary conditions. Using Fresnel coefficients it is possible to calculate the wave percentage that is reflected or refracted. Other, since the final goal is to obtain a semi-classical model, this point of view should be also analysed, *i.e.* not only the wave but also the photon characterisation. Since photons represent a quantum of light, they can not be divided and consequently on the interface they will be either reflected or refracted and Fresnel coefficients represent their probabilities.

In expression 3.13 are presented the electromagnetic field coefficient for TM and Transverse Electric (modes) (TE) waves [7, 16, 64–67]. Furthermore, on expression 3.14 the reflection power coefficients are presented. It is denoted $\bar{k}_h = \hat{\boldsymbol{s}} \cdot \hat{\boldsymbol{k}}_{\boldsymbol{h}} = k_0(N_h cos(\theta_h) + K_h cos(\psi_h))$, where $h = i, r, t$.

$$\begin{cases} \bar{r}_p = \dfrac{\bar{n}_t^2 \bar{k}_i - \bar{n}_i^2 \bar{k}_t}{\bar{n}_t^2 \bar{k}_i + \bar{n}_i^2 \bar{k}_t} \\ \bar{r}_e = \dfrac{\mu_t \bar{k}_i - \mu_i \bar{k}_t}{\mu_t \bar{k}_i + \mu_i \bar{k}_t} \end{cases} \tag{3.13}$$

$$\begin{cases} R_p = |\bar{r}_p|^2 \\ R_e = |\bar{r}_e|^2 \end{cases} \tag{3.14}$$

The transmission field coefficient may be determined by expression 3.15, as well as the transmission power coefficients by expression 3.16.

$$\begin{cases} \bar{t}_p = \dfrac{2\bar{k}_i / \bar{n}_i^2}{\bar{k}_i / \bar{n}_i^2 + \bar{k}_t / \bar{n}_t^2} \\ \bar{t}_e = \dfrac{2\mu_t \bar{k}_i}{\mu_t \bar{k}_i + \mu_i \bar{k}_t} \end{cases} \tag{3.15}$$

$$\begin{cases} T_p = |\bar{t}_p|^2 \dfrac{Re\{\bar{k}_t/\bar{n}_t^2\}}{Re\{\bar{k}_i/\bar{n}_i^2\}} \\ T_e = |\bar{t}_e|^2 \dfrac{\mu_i Re\{\bar{k}_t\}}{\mu_t Re\{\bar{k}_i\}} \end{cases} \tag{3.16}$$

Usually, the determination of *R* and *T* is enough to understand what happens at an interface. However, in absorbing media (namely high absorbing media), other coefficients might be necessary to account for the phenomena. The correct expression is $R + T = 1 + M$, where *M* is the interference coefficient defined by expression 3.17. Surface conductivity is neglected in this analysis, and consequently, there is no surface Joule-heat-loss (surface absorption) [7,16,64,67].

$$\begin{cases} M_p = Im\{\bar{r}_p\} \dfrac{Im\{2\bar{k}_i/\bar{n}_i^2\}}{Re\{\bar{k}_i/\bar{n}_i^2\}} \\ M_e = Im\{\bar{r}_e\} \dfrac{Im\{2\bar{k}_i\}}{Re\{\bar{k}_i\}} \end{cases} \tag{3.17}$$

Then, the reflection probability/percentage at the interface is $P_{reflected} = R$ and the refraction one $P_{refracted} = T - M$. The value $R + T$ must be higher than 1, depending on the *M* coefficient values. However, they are complementary phenomena, since $P_{reflected} + P_{refracted} = 1$, meaning that M acts as a correction term [7,16,67,68]. $M > 0$ in absorbing media and $M < 0$ in media with gain.

For a charged interface, with $\bar{\sigma}_s$ being the complex surface charge, the Fresnel coefficients might also be determined based on boundary conditions in expression 3.18, leading to even more generalised expressions, as presented from expression 3.19 to 3.23. The new boundary conditions have included the $\bar{\boldsymbol{J}}_{\boldsymbol{s}}(\boldsymbol{r},\boldsymbol{t})$, η_0 and η terms all associated to $\bar{\sigma}_s$ and representative of the surface current density, the external and oscillatory surface charge density, respectively. Once again, it is denoted $\bar{k}_h = \hat{\boldsymbol{s}} \cdot \hat{\boldsymbol{k}}_{\boldsymbol{h}} = k_0(N_h cos(\theta_h) + K_h cos(\psi_h))$, where $h = i, r, t$.

$$\begin{cases} \epsilon_0[\bar{\epsilon}_2 \bar{\boldsymbol{E}}_{\boldsymbol{2}}(\boldsymbol{r},\boldsymbol{t}) - \bar{\epsilon}_1 \bar{\boldsymbol{E}}_{\boldsymbol{1}}(\boldsymbol{r},\boldsymbol{t})] \cdot \hat{\boldsymbol{s}} = \eta_0 + \eta(\boldsymbol{r}, t) \\ \mu_0[\mu_2 \bar{\boldsymbol{H}}_{\boldsymbol{2}}(\boldsymbol{r},\boldsymbol{t}) - \mu_1 \bar{\boldsymbol{H}}_{\boldsymbol{1}}(\boldsymbol{r},\boldsymbol{t})] \cdot \hat{\boldsymbol{s}} = 0 \\ \hat{\boldsymbol{s}} \times [\bar{\boldsymbol{E}}_{\boldsymbol{2}}(\boldsymbol{r},\boldsymbol{t}) - \bar{\boldsymbol{E}}_{\boldsymbol{1}}(\boldsymbol{r},\boldsymbol{t})] = 0 \\ \hat{\boldsymbol{s}} \times [\bar{\boldsymbol{H}}_{\boldsymbol{2}}(\boldsymbol{r},\boldsymbol{t}) - \bar{\boldsymbol{H}}_{\boldsymbol{1}}(\boldsymbol{r},\boldsymbol{t})] = \bar{\boldsymbol{J}}_{\boldsymbol{s}}(\boldsymbol{r},\boldsymbol{t}) \end{cases} \tag{3.18}$$

$$\begin{cases} \bar{r}_p = \dfrac{\bar{n}_t^2 \bar{k}_i - \bar{n}_i^2 \bar{k}_t + \sigma_s \bar{k}_i \bar{k}_t/(\omega\epsilon_0)}{\bar{n}_t^2 \bar{k}_i + \bar{n}_i^2 \bar{k}_t + \sigma_s \bar{k}_i \bar{k}_t/(\omega\epsilon_0)} \\ \bar{r}_e = \dfrac{\mu_t \bar{k}_i - \mu_i \bar{k}_t - \sigma_s \omega \mu_t \mu_i}{\mu_t \bar{k}_i + \mu_i \bar{k}_t + \sigma_s \omega \mu_t \mu_i} \end{cases} \tag{3.19}$$

$$\begin{cases} R_p = |\bar{r}_p|^2 \\ R_e = |\bar{r}_e|^2 \end{cases} \tag{3.20}$$

$$\begin{cases} \bar{t}_p = \dfrac{2\bar{k}_i/\bar{n}_i^2}{\bar{k}_i/\bar{n}_i^2 + \bar{k}_t/\bar{n}_t^2 + \sigma_s\bar{k}_i\bar{k}_t/(\omega\epsilon_0)} \\ \bar{t}_e = \dfrac{2\mu_t\bar{k}_i}{\mu_t\bar{k}_i + \mu_i\bar{k}_t + \sigma_s\omega\mu_t\mu_i} \end{cases} \tag{3.21}$$

$$\begin{cases} T_p = |\bar{t}_p|^2 \dfrac{Re\{\bar{k}_t/\bar{n}_t^2\}}{Re\{\bar{k}_i/\bar{n}_i^2\}} \\ T_e = |\bar{t}_e|^2 \dfrac{\mu_i Re\{\bar{k}_t\}}{\mu_t Re\{\bar{k}_i\}} \end{cases} \tag{3.22}$$

$$\begin{cases} M_p = Im\{\bar{r}_p\} \dfrac{Im\{2\bar{k}_i/\bar{n}_i^2\}}{Re\{\bar{k}_i/\bar{n}_i^2\}} \\ M_e = Im\{\bar{r}_e\} \dfrac{Im\{2\bar{k}_i\}}{Re\{\bar{k}_i\}} \end{cases} \tag{3.23}$$

The reflection and transmission angles remain the same, but there is surface absorption due to the complex surface conductivity. Then, R, T and M values are re-calculated and there is the appearance of a new term L, associated with $\bar{\sigma}_s$, described by expression 3.24. L is the average surface power loss and the new interface power balance equation is $R + T - M + L = 1$.

$$\begin{cases} L_p = \dfrac{1}{2\epsilon_0\omega Re\{\bar{k}_i/\bar{n}_i^2\}} \left[Re\left\{ \dfrac{\bar{\sigma}_s^*\bar{t}_p^*\bar{k}_t^*\bar{k}_i}{\bar{\epsilon}_t^*\bar{\epsilon}_i} \right\} - Re\left\{ \dfrac{\bar{\sigma}_s^*\bar{r}_p\bar{t}_p^*\bar{k}_t^*\bar{k}_i}{\bar{\epsilon}_t^*\bar{\epsilon}_i} \right\} + \dfrac{|\bar{t}_p|^2\bar{k}_t^2}{|\bar{\epsilon}_t|^2} Re\{\bar{\sigma}\} \right] \\ L_e = |\bar{t}_e|^2 \dfrac{\omega\mu_0\mu_i Re\{\bar{\sigma}_s\}}{Re\{\bar{k}_i\}} \end{cases} \tag{3.24}$$

Another aspect to implement is the wave absorption in a certain media, *i.e.* for the wave propagation and not at the interface. The absorption ratio might be obtained using the Lambert-Beer law, however, it is known that the absorption coefficient is dependent on the wave parameters, namely on the transmitted angles and the incident angles [7,16,65,67]. This statement reveals that Lambert-Beer's law is only valid for homogeneous waves, *i.e.* when the propagated wave has its plane of constant phase coincident with its plane of constant amplitude. Also, Lambert-Beer's law is only valid for perpendicular incidence and it is not generalised for an oblique incidence.

Since the field attenuation is associated with the decay verified between two equi phase planes, it is possible to describe it as the decay in a path $\boldsymbol{r_d} = d\hat{e}$, where d is its path length, as presented in expression 3.25.

$$\bar{\boldsymbol{H}}(\boldsymbol{r_p}, \boldsymbol{t_1}) = \boldsymbol{H}e^{jd\bar{\boldsymbol{k}}\cdot\hat{\boldsymbol{e}}} = \boldsymbol{H}e^{-k_0Kcos(\alpha)d}e^{jk_0Nd} \tag{3.25}$$

Thus, it is possible to compute absorption according to expression 3.26, where *d* is the propagated distance. This expression is similar to Lambert-Beer law and expression 3.26 tends to that law for $\alpha = 0 \rightarrow K = \kappa$ [7,67].

$$A = 1 - e^{-k_0 K cos(\alpha) d} \tag{3.26}$$

Another important step is to clarify the wave/photons propagation direction, *i.e.*, the average power might have a different direction in comparison with the wavevector. In the case of TE waves the propagation direction, η_{TE} coincides with the direction given by θ. On the other hand, the TM waves propagation direction will be dependent on the electrical permittivity phase, δ_ϵ, and on the phase of the wavevector component perpendicular to the surface, δ_k. The relation is presented on expression 3.27 [7, 16, 69].

$$tan(\eta_{TM}) = \frac{tan(\theta)}{1 + tan(\delta_\epsilon)tan(\delta_k)} \tag{3.27}$$

Although the propagation direction might be different, the angles of the wavevector remain the same. The boundary conditions are always be dependent on θ and ψ, even that $\eta \neq \theta$ [7, 16, 69]. For non absorbing media ($\delta_\epsilon = 0$) $\eta_{TM} = \theta$.

Thus, according to this scenario, materials may be divided into four different groups as illustrated in figure 3.1, with a special focus on the epsilon-negative materials since the analysis is going to be done in dielectric-metal interfaces. Since the electrical permittivity is a complex quantity, its phases are considered for this categorisation.

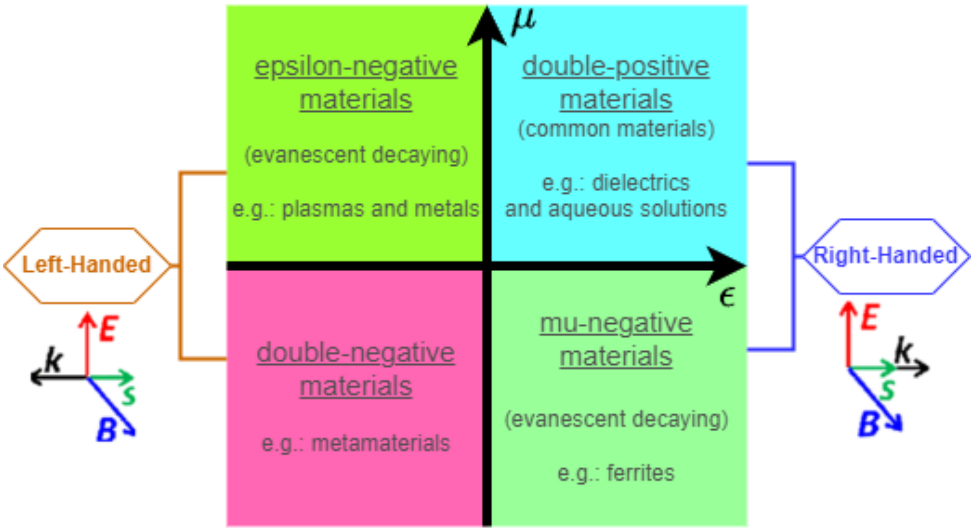

Figure 3.1: Materials division based on their electromagnetic properties.

3.1.2 Comparison with Other Methodologies

The usual methodology is based on Snell's law but already assumes the possibility of complex angles, as presented in expression 3.28 obtained from the Helmholtz equation. The complex Snell's law is in expression 3.29 and the angle between the complex wavevector and the surface normal is complex and it is determined by expression 3.30 [7, 70–73].

Since the emission is on a lossless medium and with a real incidence angle, the first complex angle will appear at an interface with a complex transmission medium. Instead of having two different real angles, this approach has only one angle with all the wavevector information, but with no immediate physical significance [7, 63, 64].

$$\begin{cases} \bar{\boldsymbol{k}} = k_0 \bar{n} \hat{\boldsymbol{u}}_{\boldsymbol{k}} \\ \bar{\boldsymbol{k}} \cdot \bar{\boldsymbol{k}} = k^2 \\ k = \omega \sqrt{\mu \bar{\epsilon} \mu_0 \epsilon_0} = k_0 \sqrt{\mu \bar{\epsilon}} \end{cases} \tag{3.28}$$

$$\bar{n}_i sin\left(\bar{\theta}_i\right) = \bar{n}_t sin\left(\bar{\theta}_t\right) \tag{3.29}$$

$$\bar{\boldsymbol{k}} \cdot \hat{\boldsymbol{s}} = \bar{k} = k_0 \bar{n}\, cos\left(\bar{\theta}\right) \tag{3.30}$$

The field and power Fresnel coefficients remain the same as the ones presented before however, $\bar{k}_i$ and $\bar{k}_t$ are obtained from expression 3.30 [7, 70–73].

This method´s limitations rely on the validation of expressions 3.29 and 3.30.

There are equivalences between the complex angle $\bar{\theta}$ from this methodology and the angles θ and ψ from the proposed one [63, 64]. However, even though the equivalence between these methods is demonstrated, the method with real-angles is more physically meaningful than the complex-angles method [7, 63, 64, 67]. Consequently, expressions 3.29 and 3.30 might be used, even though there is no immediate significance of those angles, or in other words, although the wavevector is mathematically corrected, its angles have no physical representation.

For non-absorbing media or weakly absorbing media, the real part of $\bar{\theta}$ is approximately the angle between the equi phase normal vector and the surface and the extinction factor is sufficiently low to neglect the imaginary wavevector component in both methodologies. Thus, this method tends to the proposed one whenever expression 3.31 is not verified (meaning that media are not strongly absorbing ones) [68, 69, 74]. The other methodology should be preferred, for instance, for metals in spectral regions of the ultraviolet, visible, or near-infrared (near surface plasmon resonances).

$$\frac{\kappa_i}{n_i} > \frac{\kappa_t}{n_t} > 0.1 \tag{3.31}$$

3.2 Validation

In this section, the methodology validation is performed, starting from a single dielectric-metal interface, followed by an n-layer stack structure, until the semi-classical and time-domain model validation stage.

3.2.1 Single Dielectric-Metal Interface

This validation process is performed to compare the proposed methodology results with others directly from Maxwell's equations. The main goal is to verify that the resonances are as expected by the Electromagnetism and by Surface Plasmon Polaritons (SPP) dispersion relations. Finally, based on the presented results, the role of SPP at a dielectric-metal interface is demonstrated.

As previously referred on section 2.6, SPP has evanescent decay and consequently, their dispersion relation is on the right side of the line curve. The real and imaginary part of $k_x = k_{SPP}$ at the air-metal interface are presented in figures 3.2 and 3.3, for the four metals already characterised by the Drude-Lorentz model in that section.

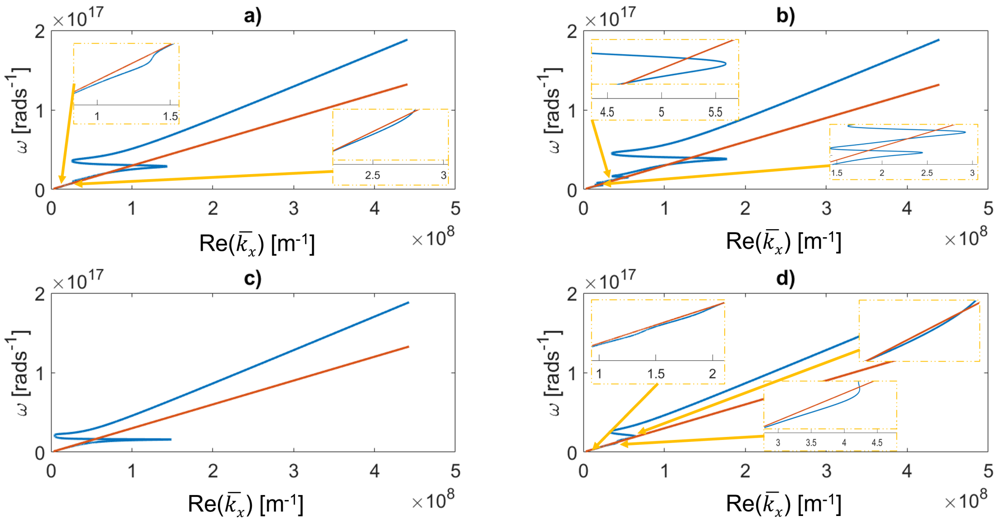

Figure 3.2: Wavevector surface component ($\bar{k}_x$) real part of an air-metal interface: a) gold; b) silver; c) aluminium; d) copper. Zoom on SPP frequencies.

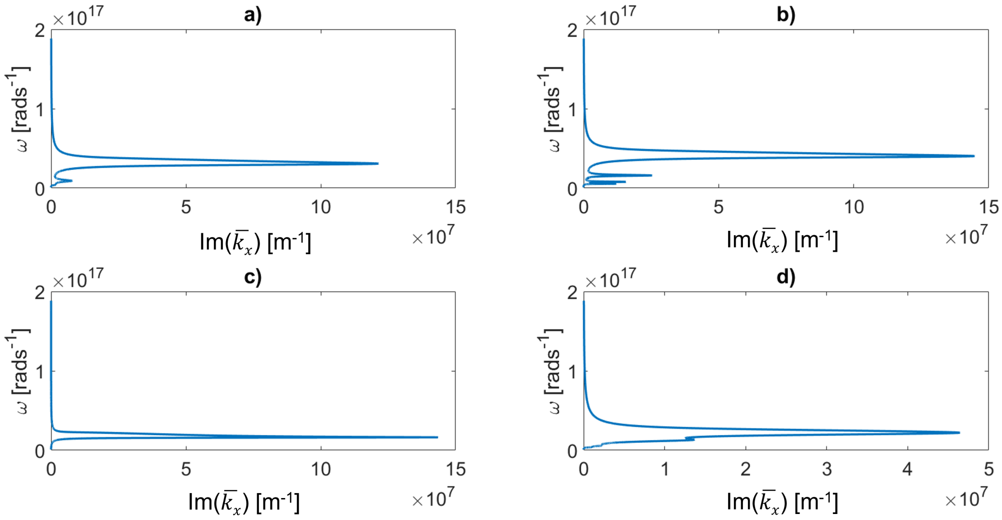

Figure 3.3: Wavevector surface component ($\bar{k}_x$) imaginary part of an air-metal interface: a) gold; b) silver; c) aluminium; d) copper.

Denoting ϵ' and ϵ'' as respectively the real and imaginary part of the complex electrical permittivity, and assuming that the dielectric has a real permittivity, it is verified that for $\epsilon'_m > 0$, both x and z components of the wavevector are purely real, leading to radiative modes. However, for $-\epsilon_d < \epsilon'_m < 0$ the imaginary part of $\bar{k}_x$ is much higher than its real part, meaning that there are quasi-bound modes of propagation. Also, for $\epsilon'_m < -\epsilon_d$ the x component of the wavevector is mainly real in contrast with the z component which is mostly imaginary, leading to bound modes [4].

Moreover, the real part of $\bar{k}_x$ tends asymptotically to $\frac{\omega_p}{\sqrt{1+\epsilon_d}}$, as the limit between the quasi-bound and bound modes region (maximum of k_x values on figure 3.2 below the light curve). Radiative modes are on the left side of the light curve for angular frequencies higher than ω_p. Between $\frac{\omega_p}{\sqrt{1+\epsilon_d}}$ and ω_p are the quasi-bound modes as well as below $\frac{\omega_p}{\sqrt{1+\epsilon_d}}$ are the bound ones [4].

Based on figures 3.2 and 3.3 it is possible to extrapolate the resonance wavelengths for the air-metal interfaces. These resonance wavelengths are presented in table 3.1. They are calculated by analysing those figures and determining the transition wavelengths for which the imaginary part of $\bar{k}_x$ becomes from much greater to much smaller than its real part.

Table 3.1: Wavelengths with expected resonance.

Metal	Gold	Silver	Aluminium	Copper
λ	64 nm 238 nm 536 nm	49 nm 123 nm 249 nm 355 nm	118 nm	85 nm 158 nm 360 nm 550 nm

3.2.1.A Transmission Probability - Transmission Angle Analysis

It starts with the analysis of the transmission angle θ_t and the transmission percentage of an incident wave by sweeping both the incidence angle and wavelength. Since $n_i = N_i = 0 \Rightarrow \psi_t = 0$, meaning that the waves on the metal are evanescent as predicted. For that reason, charts about Ψ_t are not presented, because they are null. This means that the plane of constant amplitude is parallel to the interface.

The figures in this section should be analysed as maps or charts since not all the transmission angles are allowed. Only the ones with a non-null transmission probability(particle)/percentage(wave). Furthermore, since an electromagnetic wave might be composed of several rays with different directions (incidence angles), the transmitted wave will also be composed of different transmitted rays, once again with different angles. Some of these angles or transmission directions are affected by the SPP phenomenon.

The charts for the air-gold interface are in figures 3.4 and 3.5. As expected, and presented in previous sections, this interface should have an SPP resonance at 64 nm, 238 nm and 536 nm. Analysing these figures, it is possible to verify that the transmission angle (propagation direction of $\bar{k}_t$) achieves high values. Near these resonance wavelengths, a particular behaviour is obtained, namely, there is an abrupt appearance of higher transmission angles. On top of that, it is possible to verify that the transmission percentage is not null, and its value is quite considerable and impressive when compared with its null value on microwave regimes.

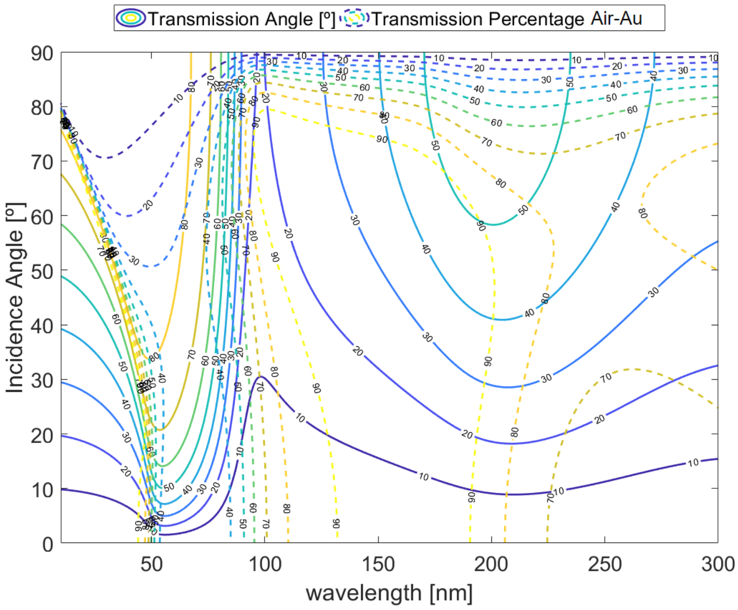

Figure 3.4: Transmission angle and transmission percentage/probability in function of the incident wavelength and angle for the air-gold interface on the wavelength range 10-300 nm (SPP resonance near 64 nm and 238 nm).

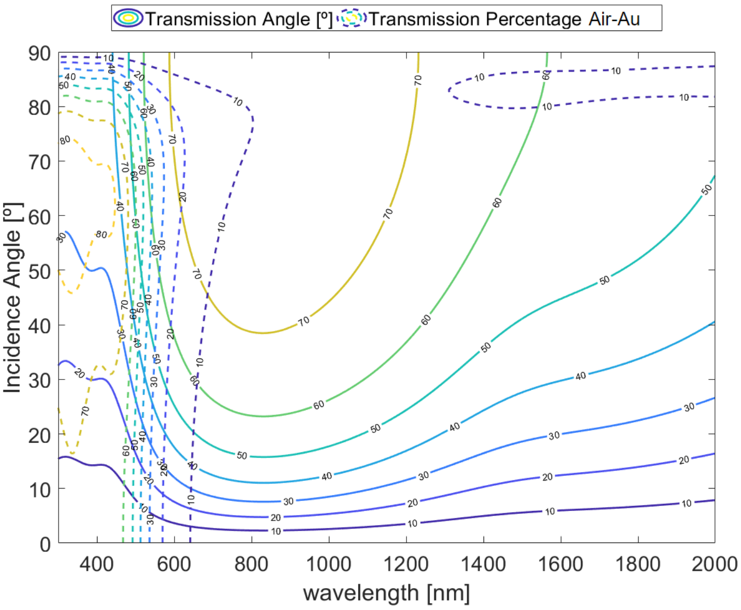

Figure 3.5: Transmission angle and transmission percentage/probability in function of the incident wavelength and angle for the air-gold interface on the wavelength range 300-2000 nm (SPP resonance near 536 nm).

It is also noticeable a different resonance at 97 nm. It is a resonance of the gold electrical permittivity, and the obtained value is quite huge in comparison with the resonance value at the dielectric-metal interface. Thus, small transmission angles dominate in contrast with the ample transmission angles (transmission closer to the surface) obtained on SPP resonance. This is also detectable on the dispersion relation curves, since at this wavelength there is a peak on the imaginary part of $\bar{k}_x$, being its real part practically null.

Silver resonances are near 49 nm, 123 nm, 249 nm and 355 nm as previously predicted. In figures 3.6 and 3.7 is noticeable that their behaviour is identical to the gold ones. However, since the higher resonance wavelength in the silver predictions is 355 nm and in the gold interface is 536 nm, it is possible to verify in figure 3.7 that in the visible region, the silver-air interface has a smaller transmission percentage. In other words, the air-gold interface has transmissions along almost all the visible parts of the spectrum in contrast with the air-silver interface.

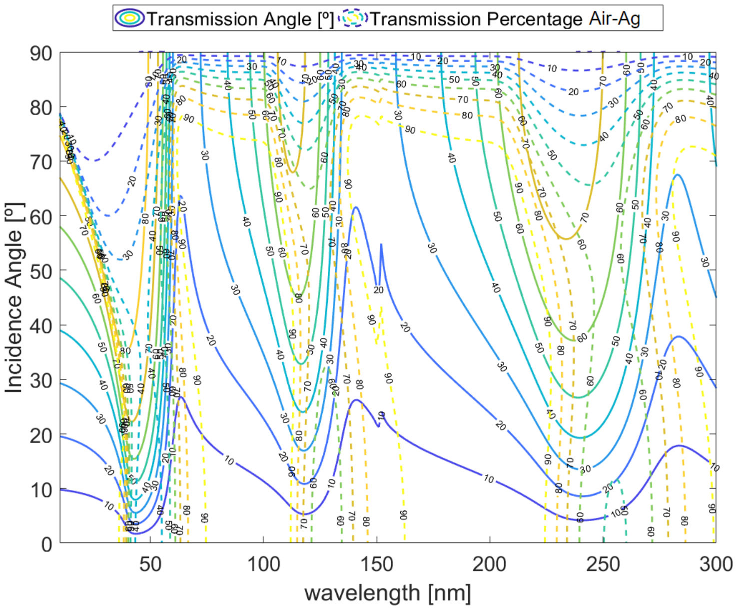

Figure 3.6: Transmission angle and transmission percentage/probability in function of the incident wavelength and angle for the air-silver interface on the wavelength range 10-300 nm (SPP resonance near 49 nm, 123 nm and 249 nm).

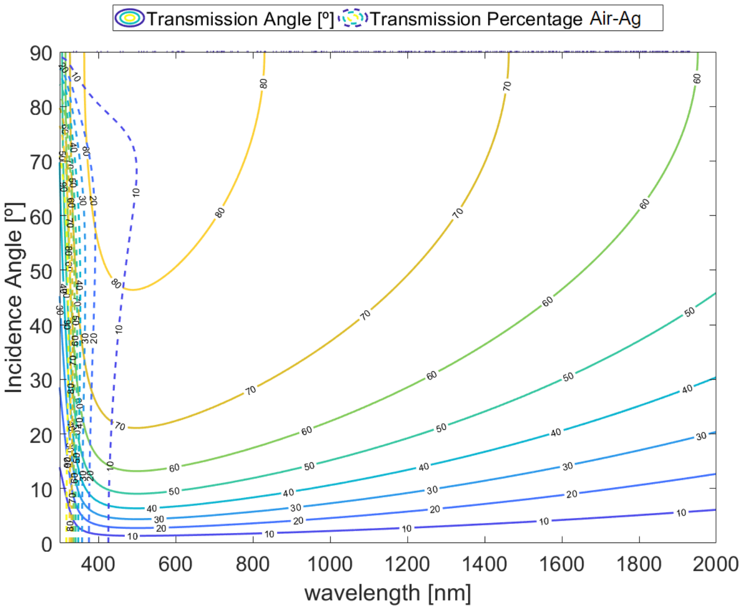

Figure 3.7: Transmission angle and transmission percentage/probability in function of the incident wavelength and angle for the air-silver interface on the wavelength range 300-2000 nm (SPP resonance near 355 nm).

The aluminium behaviour is different from gold and silver ones. The aluminium's resonance is at 118 nm and it is visible in figure 3.8. However, near 800 nm the imaginary part of $\bar{k}_x$ has a small peak that leads to the general increase of the transmission percentage as well as the decrease of transmission angles. This means that the wave is more evanescent and it will decay/be absorbed closer to the interface. The angle $\alpha = \theta - \psi$ tends to zero, leading to the increase in the absorption ratio of expression 3.26. This effect will also be observed in the propagation length figures, in the following section.

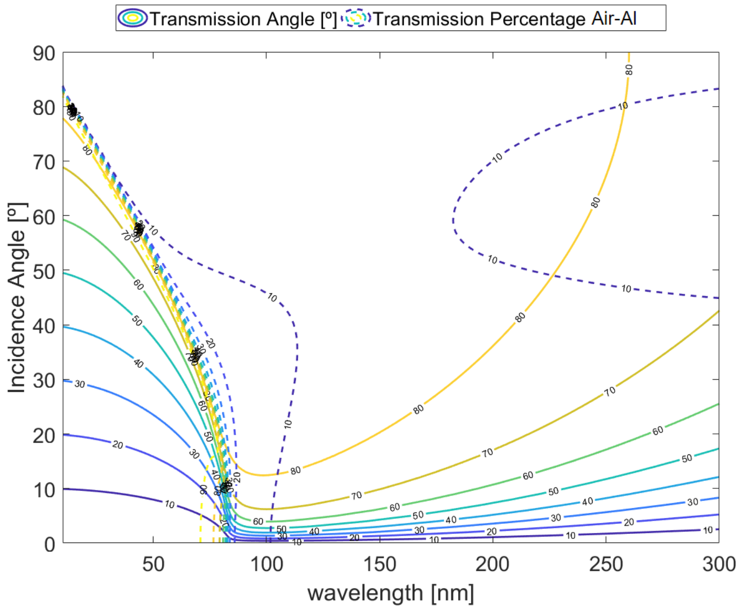

Figure 3.8: Transmission angle and transmission percentage/probability in function of the incident wavelength and angle for the air-aluminium interface on the wavelength range 10-300 nm (SPP resonance near 118 nm).

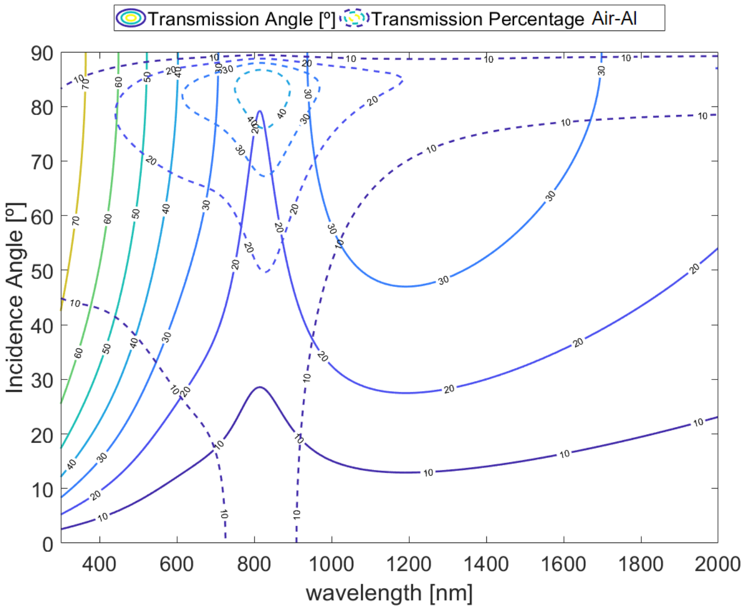

Figure 3.9: Transmission angle and transmission percentage/probability in function of the incident wavelength and angle for the air-aluminium interface on the wavelength range 300-2000 nm.

The last metal is copper, whose charts are presented in figures 3.10 and 3.11. The resonances are near 85 nm, 158 nm, 360 nm and 550 nm as predictable. The importance of analysing a metal such as copper is because there is a double resonance on the visible spectral region. The cleaner resonance appears on aluminium since there is mostly one plasma frequency, which is visible in figures 3.2 and 3.3. Zooming in the copper's dispersion relation it is possible to verify a region where there are two peaks of $\bar{k}_x$. These peaks are so close that there is no room to treat them independently. This means that the visible region is influenced by a superposition of two different resonances. In figure 3.11 is possible to verify this behaviour, where generally the transmission angles increase in this region.

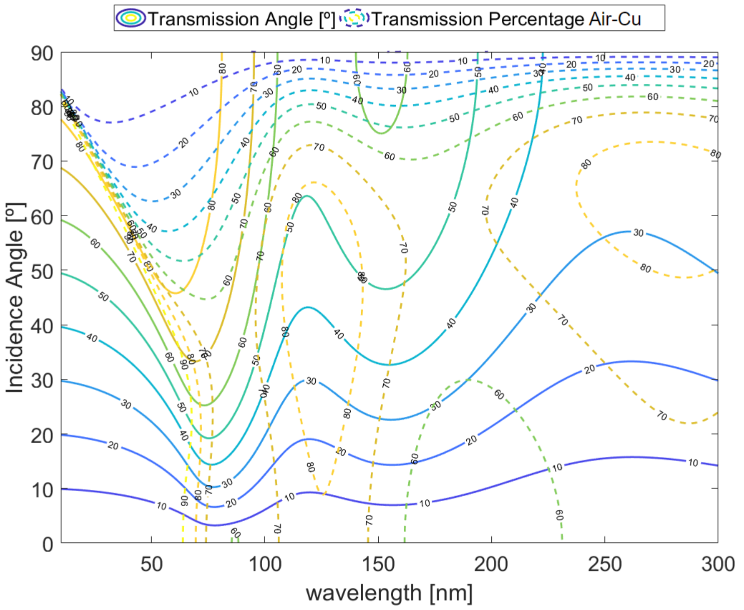

Figure 3.10: Transmission angle and transmission percentage/probability in function of the incident wavelength and angle for the air-copper interface on the wavelength range 10-300 nm (SPP resonance near 85 nm and 158 nm).

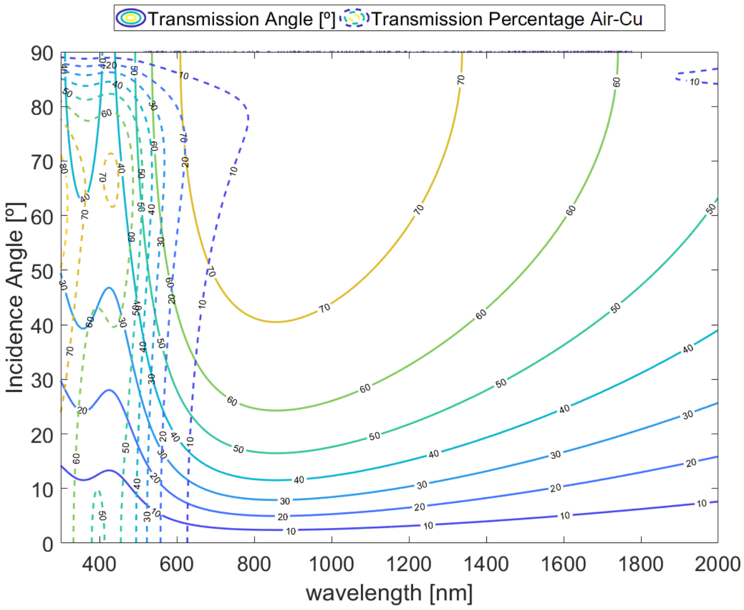

Figure 3.11: Transmission angle and transmission percentage/probability in function of the incident wavelength and angle for the air-copper interface on the wavelength range 300-2000 nm (SPP resonance near 360 nm and 550 nm).

3.2.1.B Transmission Probability - Propagation Length Analysis

After analysing the transmission percentage and angle, it is also quite interesting to investigate and observe the behaviour of the propagation length.

Propagation length is defined as the distance for which the electromagnetic field decays $1/e$. From the particle point of view, it is the photons' average travelling distance, before being absorbed. This means that the propagation length might be computed using expression 3.26, determining the distance d, for which the power absorption is $1/e^2$.

It is already known that this kind of wave has a propagation length in the nanometres range. This is the justification for which phenomena such as Extraordinary Optical Transmission (EOT) are only observable at nanostructures. The transmitted wave might come out from the metal however, it cannot be absorbed before. For this reason, new nano-scale phenomena appear.

In figures 3.12 and 3.13 are presented the propagation length in gold. It is possible to corroborate the above paragraph statements. Also, it is observed that the propagation length is dependent not only on the wavelength but also on the incident angle, as predictable from expression 3.26. The propagation length in the infrared region might reach more than twice the values in the visible and ultraviolet regions. The near-infrared is the region with higher values, but there is also a smaller transmission percentage.

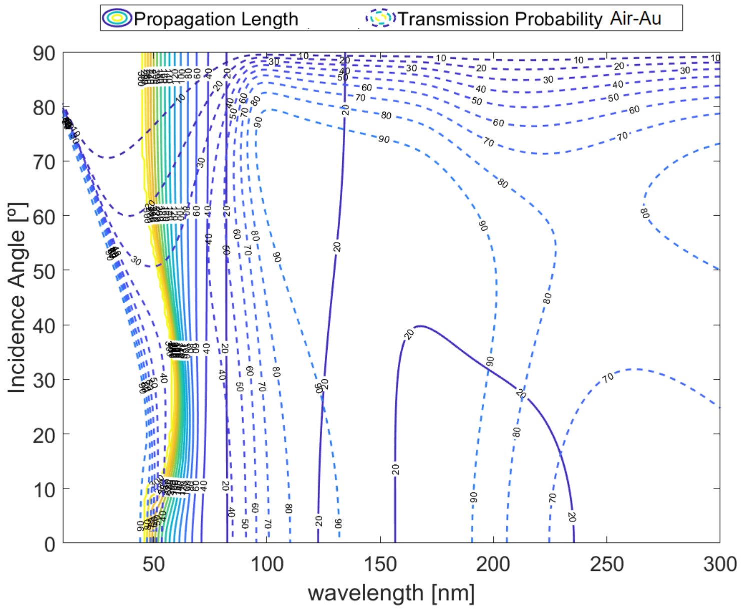

Figure 3.12: Propagation length and transmission percentage/probability in function of the incident wavelength and angle for the air-gold interface on the wavelength range 10-300 nm (SPP resonance near 64 nm and 238 nm).

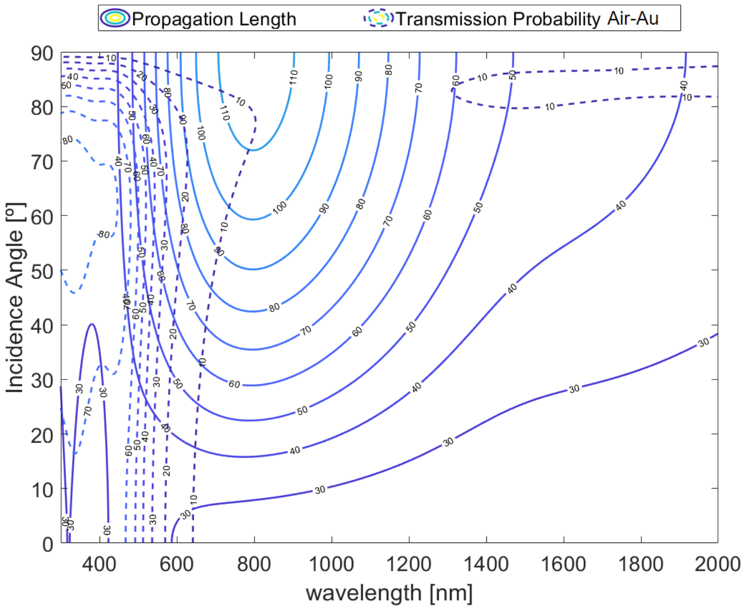

Figure 3.13: Propagation length and transmission percentage/probability in function of the incident wavelength and angle for the air-gold interface on the wavelength range 300-2000 nm (SPP resonance near 536 nm).

Figures 3.14 and 3.15 present the propagation length of silver. Comparing these results with gold ones, it is possible to verify that on surface plasma polaritons resonances the behaviour of the propagation length curves is different. First, it is possible to divide these charts into two different regions plus a transition one. Above the resonance frequencies, the propagation length tends to have a linear behaviour with the incident wavelength. It is visible the tendency to horizontal lines, meaning it is almost independent of the incident wavelength. On top of that, for small incident wavelengths, it is observed vertical lines, meaning that the propagation length is not dependent on the incident angle. The transition between both regions occurs on the resonances.

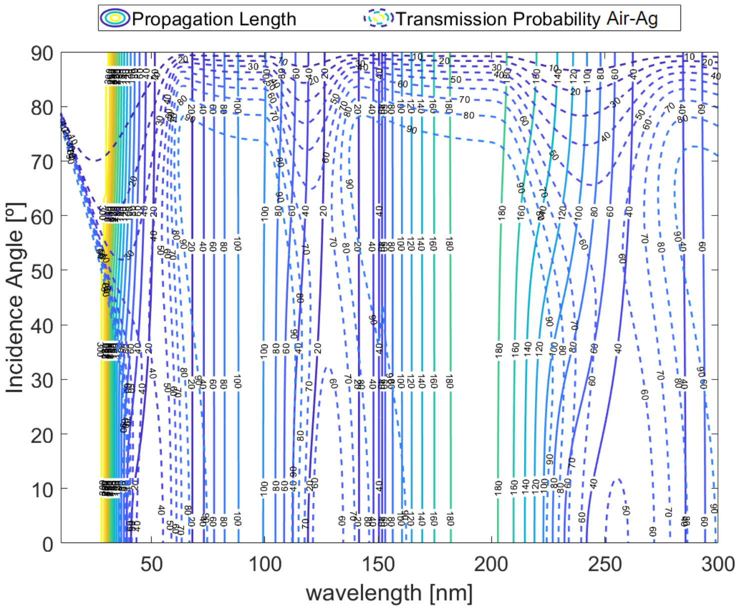

Figure 3.14: Propagation length and transmission percentage/probability in function of the incident wavelength and angle for the air-silver interface on the wavelength range 10-300 nm (SPP resonance near 49 nm, 123 nm and 249 nm).

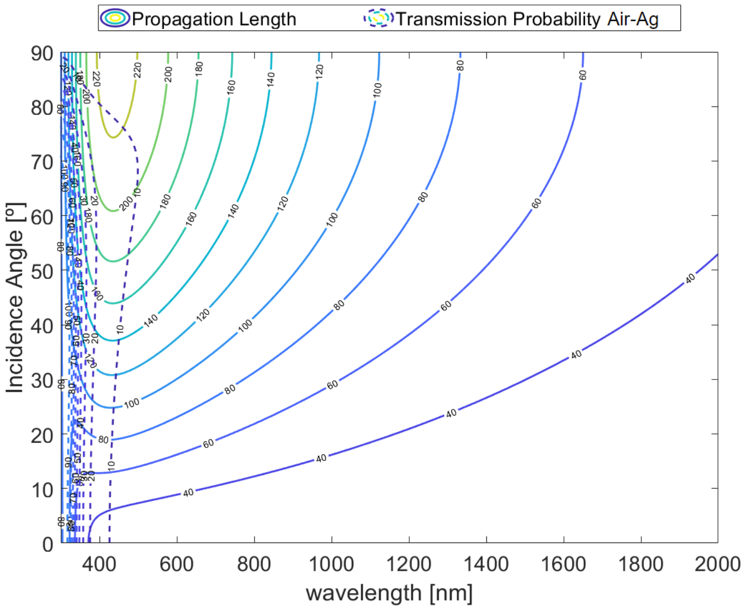

Figure 3.15: Propagation length and transmission percentage/probability in function of the incident wavelength and angle for the air-silver interface on the wavelength range 300-2000 nm (SPP resonance near 355 nm).

The aluminium propagation length results are illustrated in figures 3.16 and 3.17. These results also confirm the previous analysis. Once again, it is visible that aluminium's response has different properties than the other three analysed metals. At 800 nm there is a peak of $\bar{k}_x$ imaginary part, meaning that the propagation length decreases.

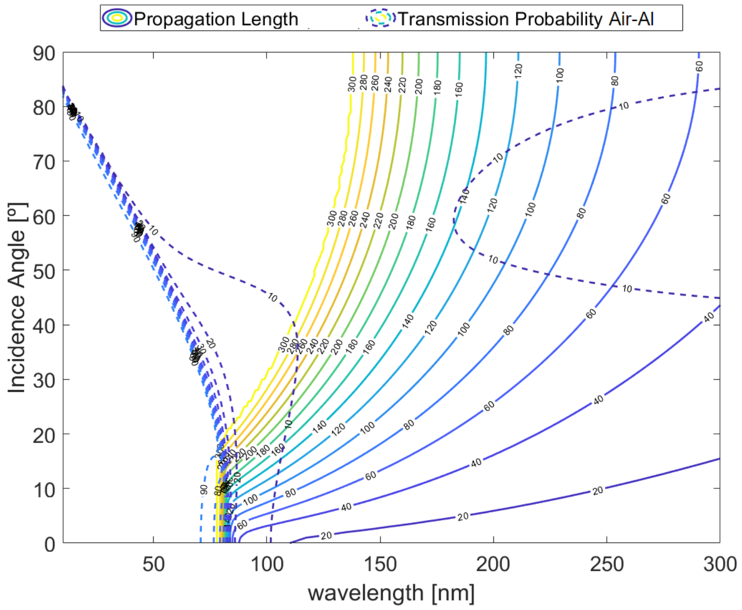

Figure 3.16: Propagation length and transmission percentage/probability in function of the incident wavelength and angle for the air-aluminium interface on the wavelength range 10-300 nm (SPP resonance near 118 nm).

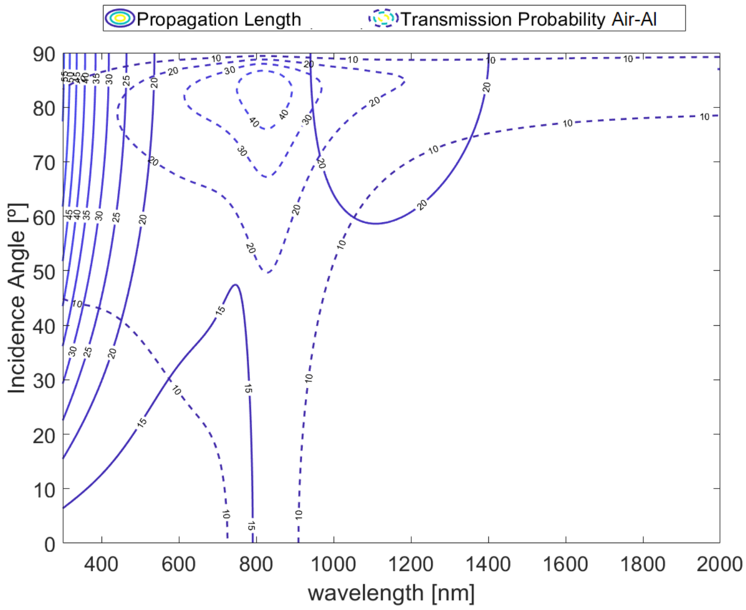

Figure 3.17: Propagation length and transmission percentage/probability in function of the incident wavelength and angle for the air-aluminium interface on the wavelength range 300-2000 nm.

As already verified, copper presents a similar behaviour to gold, despite having different resonance frequencies. In the same way, the results in figures 3.18 and 3.19 allow us to divide them into mainly two different regions. In this case, due to the double resonance, it is possible to verify a different pattern on the propagation length curve, where there is a double curvature near 400 nm.

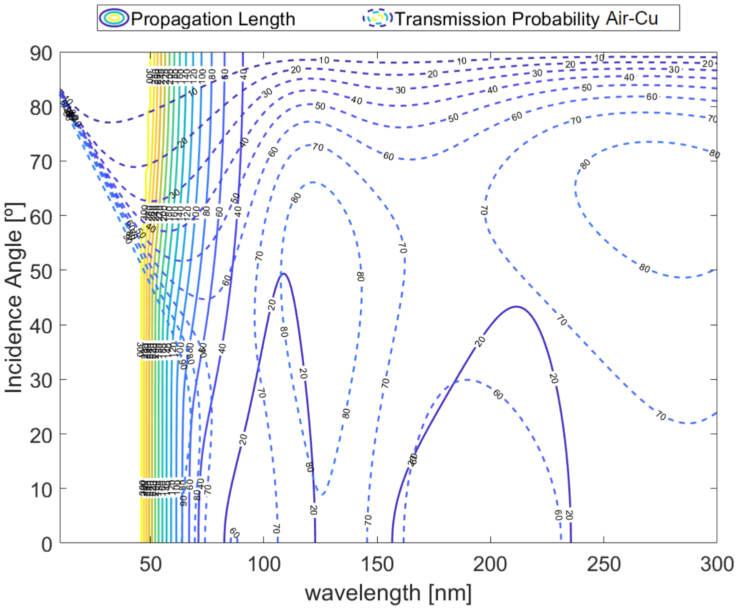

Figure 3.18: Propagation length and transmission percentage/probability in function of the incident wavelength and angle for the air-copper interface on the wavelength range 10-300 nm (SPP resonance near 85 nm and 158 nm).

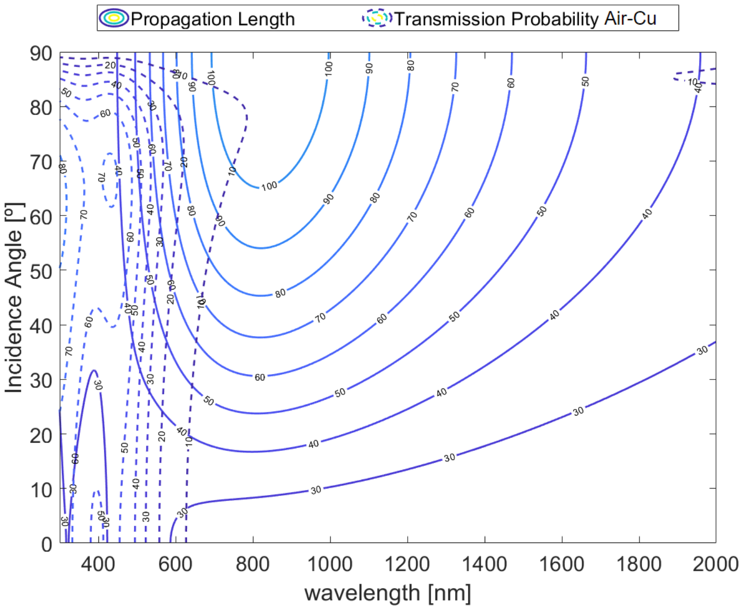

Figure 3.19: Propagation length and transmission percentage/probability in function of the incident wavelength and angle for the air-copper interface on the wavelength range 300-2000 nm (SPP resonance near 360 nm and 550 nm).

Thus, it is observed that near resonance wavelengths the propagation length is highly dependent on both incident wavelength and angle. Below it, there is only wavelength influence and above it, there is only angle dependence.

3.2.1.C Discussion

The proposed methodology allows us to have a different perception of what are the phenomena and their implications on dielectric-metal interfaces at optical frequencies. The proposed method allows us to focus more attention on the interface. It is oriented for plane waves. However, at the nano-scale where sources might be near the interfaces, there are no plane waves but a composition of different plane waves at several angles (cylindrical waves).

Based on the obtained results it is possible to point out some important and novel conclusions. First, the transmission percentage has important local maxima and minima near resonance frequencies. However, it is possible to verify that the transmission percentage has impressive high values (in comparison with the null percentage at microwave regimes). Additionally, these non-null probabilities are combined with also high transmission angles, meaning that power must be transmitted closer to the surface. Analysing this fact and the charts' behaviour (resonances on the predictable wavelengths) it is possible to conclude that surface plasmon polaritons are the main agents on the transmission peaks in ultraviolet and visible regions. Furthermore, propagation length is analysed, and the results show us this kind of phenomenon is only observable at the nano-scale since the transmitted waves/particles only propagate orders of 50-100 nm. This is quite relevant since it is not only important to have a sub-wavelength structure but also to work at optical frequencies. The work on optical frequencies allows the transmission and propagation in the metal. The subwavelength dimensions allow the appearance of these waves/particles at other interfaces, meaning that it is possible to use them before being absorbed and in certain cases, re-transmit them for non or less absorbing media (for instance EOT).

The illustrated charts obtained using the proposed methodology, allow us to have a better idea about SPP resonances. For instance, it is quite useful when choosing the correct materials for a certain application, since it is possible to verify in which conditions radiation is reflected or transmitted by the interface. Also, the proposed methodology based on Maxwell's equations, gives us a grounded understanding of surface plasmon polaritons' role and wave propagation, throughout the interface. This approach is based on optical concepts, such as Fresnel Coefficients and Generalised Snell's law.

3.2.2 Kretschmann Configuration

The next validation stage is also based on the SPP excitation in a metal thin film. However, an n-layer stack structure is analysed. This structure is known as the Kretschmann structure, in honour of Kretschmann, one of the forerunners and most respected researchers in this research field, whose most important milestone was the study of this type of structure as a way to excite SPP (as stated on the beginning of section 2.4) [7].

On the Kretschmann structure, illustrated in figure 3.20 light rays will propagate on a prism until a prism-metal interface. They will be transmitted if their angle of incidence, θ_i, is lower than the critical angle, determined by expression 3.32. For higher angles, the light would be totally reflected (Total Internal Reflection (TIR)) [7, 70–73]. However, it is not totally right since, in certain conditions, a certain light percentage will be transmitted as evanescent waves. Expression 3.32 is deduced assuming only real refractive indexes. For angles above this critical one, the transmitted radiation will have a huge attenuation such that the transmitted power will only be near the interface [70, 71]. Using nanostructures (for example, layers with tens or hundreds of nanometres) it is possible to re-transmit light over a nanolayer. The that will be transmitted to the metal will be evanescent, meaning that the metal should be thin. After that, a similar principle is used to analyse the metal-analyte interface (or any other subsequent interface). This kind of structure works as biosensors since the optical response will vary regarding the analyte refractive index. The optical response will be dependent on the light wavelength and incidence angle [7, 70–73].

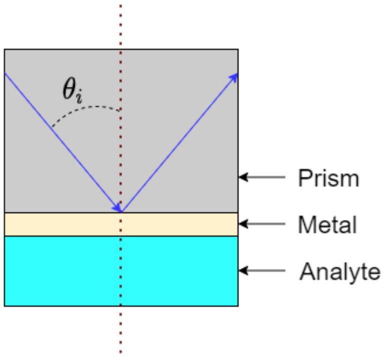

Figure 3.20: Kretschmann configuration.

For a certain wavelength and assuming TM polarisation, there is an angle $\theta_i = \theta_{rps}$, for which the system's reflectance has a resonant peak [70,71,73]. This angle is deduced from Maxwell's equations and its boundary conditions and its expression is presented on 3.33. It is possible to verify it using Snell's law, where p, m and a are used as indexes for the prism, metal and analyte, respectively. Since $Re\{\bar{k}_{x_p}\} = Re\{\bar{k}_{x_m}\} = Re\{\bar{k}_{x_s}\}$ and $Re\{\bar{k}_x\} = k_0 n\, sin(\theta)$ then, $k_0 n_p sin(\theta_i) = k_0 n_m sin(\theta_m)$ and that in turn $Re\{\bar{k}_{x_s}\} = Re\left\{k_0\sqrt{\frac{\bar{\epsilon}_m(\omega)\bar{\epsilon}_a(\omega)}{\bar{\epsilon}_m(\omega)+\bar{\epsilon}_a(\omega)}}\right\}$, leading to expression 3.33 [7,47,70,71,75].

$$\theta_c = asin\left(\frac{n_t}{n_i}\right) \tag{3.32}$$

$$\theta_{rps} = asin\left(\sqrt{\frac{1}{\epsilon_p}\frac{\epsilon_m \epsilon_s}{\epsilon_m + \epsilon_s}}\right) = asin\left(\frac{1}{n_p}\sqrt{\frac{\epsilon_m \epsilon_s}{\epsilon_m + \epsilon_s}}\right) \tag{3.33}$$

In this case, for angles near θ_{rps} the transmission at the interface metal-analyte will be higher (since the wavevectors are more matched), meaning that its reflectivity will be lower, and consequently, there is less power on the detector.

Several articles from several authors were used as references to compare results. Their methodology is not the one proposed in this research work (in subsection 3.1.1), but it is based on the one presented to compare with (in subsection 3.1.2).

These authors determine recursively the wavevector in each layer, starting from the first and using expressions 3.11 and 3.30.

Then, also in a recursive way, it is possible to compute the total field reflection coefficient, r_p in each layer. As explained before, the r and R formulas are equal for both methodologies and then, to obtain the total field reflection coefficient for the three layers case, it is necessary to sum every light ray contribution and impose phase difference and attenuation due to the ray propagation inside the middle medium, given by the propagation function β. That sum will be a geometric series, and it will originate expression 3.34 without any assumption. The phase term is dependent on the effective wavevector, which is computed by expression 3.35, where d is the medium depth. On top of that, the structure reflectance is $R_{p_{012}} = |r_{p_{012}}|^2$ [75].

$$\bar{r}_{p_{012}} = \frac{r_{01} + r_{12}e^{2j\beta_1}}{1 + r_{01}r_{12}e^{2j\beta_1}} \tag{3.34}$$

$$\bar{\beta} = \frac{2\pi}{\lambda}\bar{k}d \tag{3.35}$$

Moreover, it is possible to obtain a similar expression for an N-layers structure. However, since the higher N value in this research work is 4, it is presented the 4-layer structure expression. Similar processes should be performed to obtain the successive expressions. It is noticeable from expression 3.34 that is possible to obtain r_p values for groups of 2 interfaces (3 layers). Then, for instance, with 3 interfaces (4 layers), it is necessary to start the process through the lower interfaces. Having media numbered from 0 to 3, the $r_{p_{123}}$ (last 2 interfaces) is the first to be computed, using expression 3.36. Therefore, $r_{p_{123}}$ represents the response of the two bottom interfaces. Using an identical expression, it is possible to determine $r_{p_{0123}}$, based on two interfaces: $r_{p_{01}}$ and $r_{p_{123}}$ [7, 75].

This methodology is valid for N-layers and independently of the N value, $R_p = |r_p|^2$ [7, 75].

$$\bar{r}_{p_{123}} = \frac{r_{12} + r_{23}e^{2j\beta_2}}{1 + r_{12}r_{23}e^{2j\beta_2}} \tag{3.36}$$

$$\bar{r}_{p_{0123}} = \frac{r_{01} + r_{123}e^{2j\beta_1}}{1 + r_{01}r_{123}e^{2j\beta_1}} \tag{3.37}$$

3.2.2.A Results

The first analysis is done from [71] for a BK7-Au-Analyte Kretschmann structure. The analysis is done for 633 nm, where the BK7 prism has a refractive index of 1.52, the gold is characterised by 0.18344+j3.4332 and the analyte varies from 1.33 (water) to 1.35 (for example, representative of 80 mg/ml concentration of bovine serum albumin protein water solution [71]). Both prism and analyte are considered semi-limited media, as presented in figure 3.20, and the gold thickness is 40 nm.

Figure 3.21, extracted from [71], illustrates the structure's reflectance for the considered sample refractive indexes. Although there is no exact value of the reflectance minimum and its θ_{rps}, it is possible to verify that the responses presented in figure 3.21 are similar to the ones presented on 3.22, obtained using the proposed methodology. Even though, for $n_a = 1.33$, it is obtained a $\theta_{rps} = 71.00°$ with a reflectance of $R = 0.084 = 8.4\%$ as well as for $n_a = 1.35$, $\theta_{rps} = 73.78°$ and $R = 0.070 = 7\%$. These values are corroborated with the ones in figure 3.21. It is noticeable a quite small decrease of the reflectance with the increase of the analyte refractive index from 1.33 to 1.35 as well as a shift on θ, especially on θ_{rps}. In this case, the variation of 0.02 on the refractive index leads to a variation of about $2.78\,°$, meaning that there is a sensitivity of $139\,°/\mathrm{RIU}$.

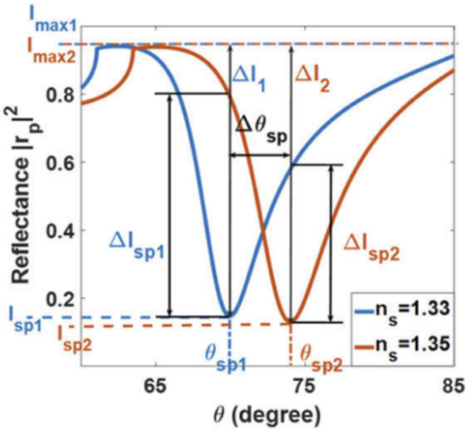

Figure 3.21: Reflectance of a BK7-Au(40nm)-Analyte Krestchmann structure for two different analyte refractive indices (from [71] to validate the proposed method).

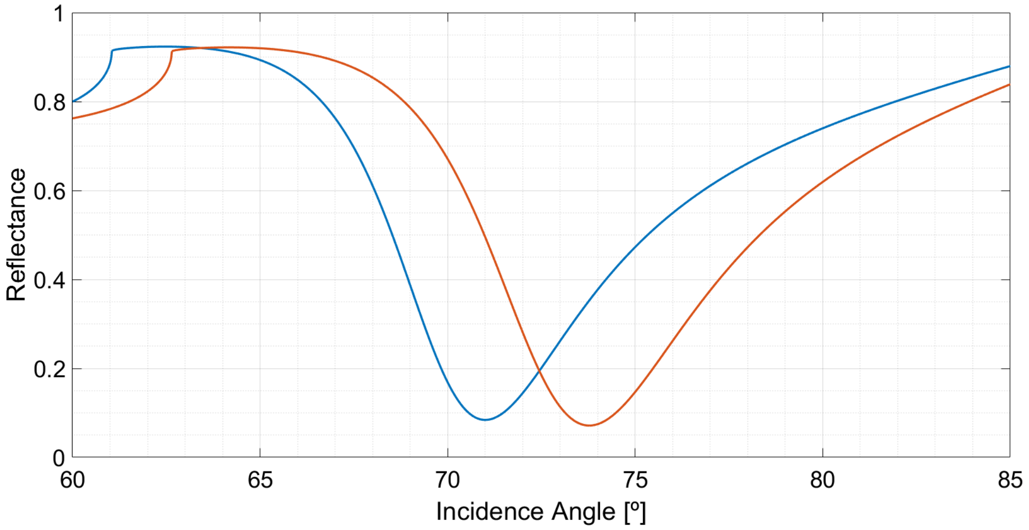

Figure 3.22: Reflectance of a BK7-Au(40nm)-Analyte Krestchmann structure, for a 1.33 (blue) and a 1.35 (red) analyte refractive index, obtained from the proposed method.

After that, the already existing methodology, from other authors, is implemented to compare with the proposed one.

In this case, a SF10-Au-Graphene-Analyte Kretschmann structure is analysed at 633 nm [76]. The SF10 refractive index is 1.723, gold and graphene are characterised by complex refractive indexes of 0.1726+j3.4218 and 3+j1.149, respectively, and the analyte only has a refractive index of 1.33. The gold thickness is 50 nm, and the graphene one is given by 0.34L nm, where L is an integer. Graphene is used to improve the analyte adhesion on metals such as gold. However, its influence on the sensor's performance should be analysed, which is a goal of this research work.

In figure 3.23 is presented the results from both methods, both corroborating the ones presented in [76]. The results confirm the validity of the proposed methodology since all curves are precisely superposed, even when $L \neq 0$.

The results are interesting since there is no reflectance variation between the methods. It is already known that if expression 3.31 is valid, the limitations of the already existing method should negatively influence the results [68]. Since the reference angle is the incident one (equal for both methods), curves are superposed. If one looks into the internal angles, for instance, the transmission angle between gold and graphene, there will be huge discrepancies. It means that the real part of $\bar{\theta}$ is not the same as the value of θ (from the proposed methodology, which is the precise angle). However, $\bar{\theta}$ has the minimal information to perform the reflectance computation, even though it has no immediate physical significance. It means that the limitation influences the incident, reflected and transmitted wavevectors in the same way, which might be cancelled when computing the reflectance.

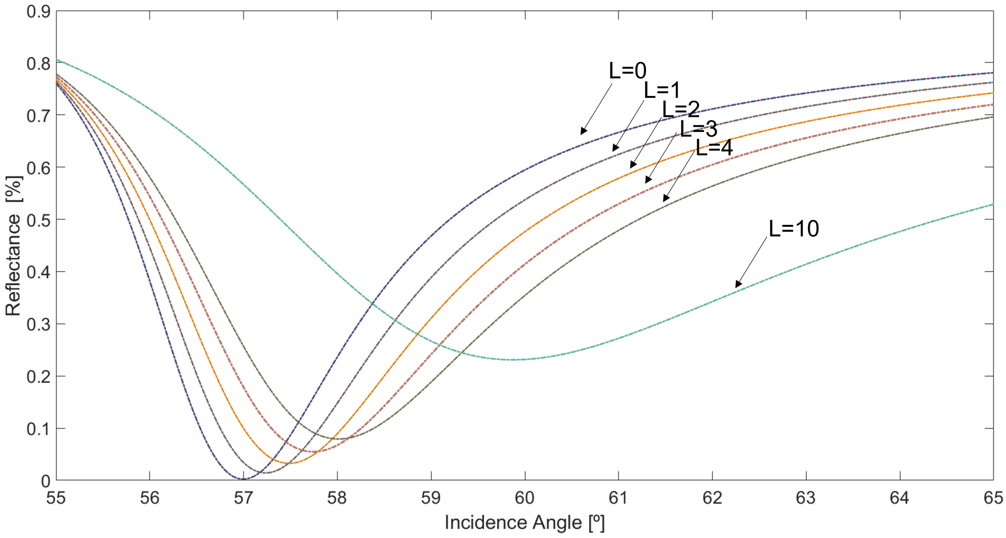

Figure 3.23: Reflectance of an SF10-Au(50nm)-Graphene(0.34L nm)-Analyte Krestchmann structure, for a 1.33 analyte refractive index, obtained from the proposed method.

To finish the validation process, an experimental scenario is presented. A set of experimental results from [77] is used to corroborate the proposed methodology, using the data from this reference. In this set of results are gold-based structures, namely a BK7-Au-Air structure with a gold thickness of 50 nm, a BK7-Cr-Au-Air structure where chromium and gold have respective thicknesses of 0.5 nm and 50 nm, as well as another BK7-Cr-Au-Air structure where chromium and gold have thicknesses of 1 nm and 50 nm, respectively.

The experimental results from [77] are illustrated in figure 3.24. Accordingly to figure 3.24 and to the authors, there is a reflectance minimum at $42.6\,°$ due to the SPP resonance, for all the analysed structures. The results from the proposed methodology are in figure 3.25, where the minimum is at $42.61\,°$, corroborating the proposed approach.

Also, comparing both results it is possible to observe that the obtained curves from the proposed methodology follow the experimental results from [77], preserving the same shape and tending to the same values.

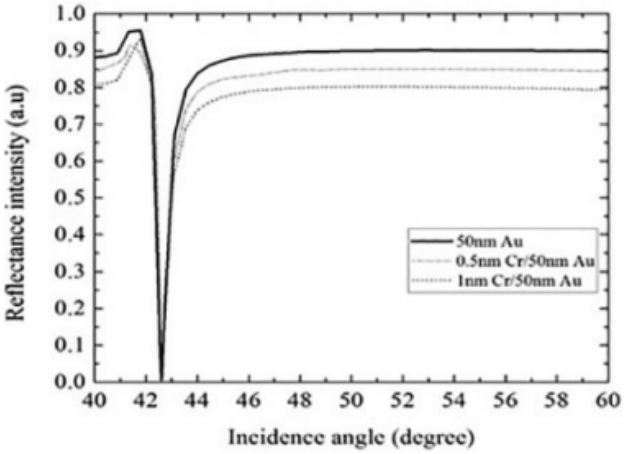

Figure 3.24: Experimental results for gold-based Kretschmann structures (from [77] to validate the proposed method).

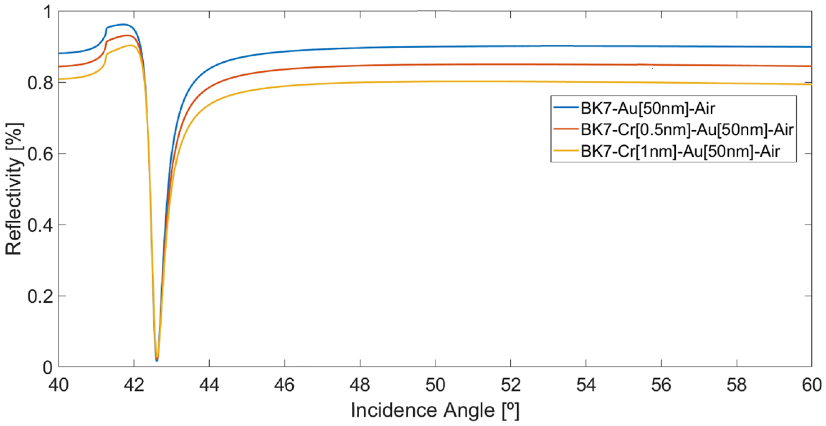

Figure 3.25: Results for gold-based Kretschmann structures to compare with experimental results.

After that, using the proposed approach, the SF10-Au-Graphene-Analyte Kretschmann optical sensor is analysed using the proposed method. The main goals are the verification of θ_{rps} for the 1.33 and 1.35 analyte's refractive index, the advantages and disadvantages of adding the graphene layer and analysing the working regions where this structure works as a sensor. The following results are obtained for a rigorous sweep on the incidence angle, θ,($0\,°$ to $90\,°$, with resolution of $0.01\,°$) as well as on the wavelength, λ, (250 nm to 2000 nm, with 1 nm of resolution). For that reason, the materials' refractive index models should be more appropriate, mainly on the plasmon resonances. Then, the N-SF10 from the SCHOTT database is used for the SF10 refractive index, and for the gold characterisation is used the Rakic's Drude-Lorentz model [52, 53]. When applicable, graphene is characterised by the expression $3 + j\frac{5.446\times10^{-6}}{3}\lambda$ [53, 73]. In the following figures, there are presented reflectance contour plots within those aforementioned ranges. Responses such as the ones presented in the validation subsection are under vertical lines in the following figures.

First, in figure 3.26 are presented the reflectance for each wavelength and incidence angle for $L = 0$ and a 1.33 refractive index analyte. In this case, the gold thickness is 30 nm. Thicknesses values are chosen using a previously published study [67], which gives us some perception about what is the SPP propagation distance and consequently, what are the thickness values for SPP to propagate between interfaces. It is possible to verify that the transition between the maximum and minimum reflectance (that minimum is obtained for θ_{rps}) is between $50°$ and $60°$. Moreover, it is visible that this transition is more abrupt on higher wavelengths (already in the infrared spectral region) and smoother for small wavelengths (in visible and ultraviolet regions).

Increasing it to 50 nm, which results are illustrated in figure 3.27, it is visible that the transition between the maximum and minimum reflectance is smoother in the infrared region, being identical in the visible and ultraviolet regions. However, in these cases, the structure is not already working as a sensor.

However, these two figures and their analysis are not related to sensing. To develop the sensor, it is necessary to characterise the variation of the structure's response to a particular stimulus, in this case on the analyte refractive index variation from 1.33 to 1.35 or vice-versa, which is uniquely a subtraction of figures identical to the above ones. Using this structure without this variation may be suitable as an optical filter, for instance, in this case, to suppress the reflectance of certain angles/wavelengths or to eliminate the transmission of angles/wavelengths.

Thus, in figure 3.28 are presented the obtained results for the sensor when the analyte medium varies from a 1.33 refractive index to 1.35, for $L = 0$. In figure 3.29 are identical results when $L = 4$. Both figures are achieved for a gold thickness of 30 nm. These figures allow us to have a perception of the sensor sensitivity. Since they are the difference between the two responses, the sensor has a better sensitivity where the reflectance variation is higher. In these cases, there are variations of approximately 90%, meaning that it is almost ”everything or nothing”, *i.e.*, for 1.33, there is no reflected radiation, and for 1.35, there is almost total reflection, or vice-versa.

Furthermore, it is noticeable that this graphene layer's introduction allows us to increase the reflectance variation near the plasmon resonance. For that reason, it should be analysed if it is necessary to have a narrow or a wide variation. The main conclusion to sum up here is that this kind of optical sensor should work properly above 1000 nm, and its resonance angles θ_{rps} are between $50°$ and $56°$. Moreover, it is visible that although the optical response for a certain analyte refractive index has just one resonance, the sensor optical response regarding the variation of that refractive index may have more than one resonance. In this case, there are wavelengths for which this response presents two possible detectable regions. For instance, in figure 3.29 at 1500 nm, there are two different angles for which the reflectance variation has local maxima, meaning that they are possible working regions. Even though only one of those angles represents the global maximum, there are two different regions with high sensibility.

Also, the same methodology is used to analyse the structure behaviour for the gold thickness of 50 nm. As expected from the previous results for the 633 nm (figure 3.27), the sensor working regions are narrower, as shown in figures 3.30 and 3.31, respectively, for $L = 0$ and $L = 4$.

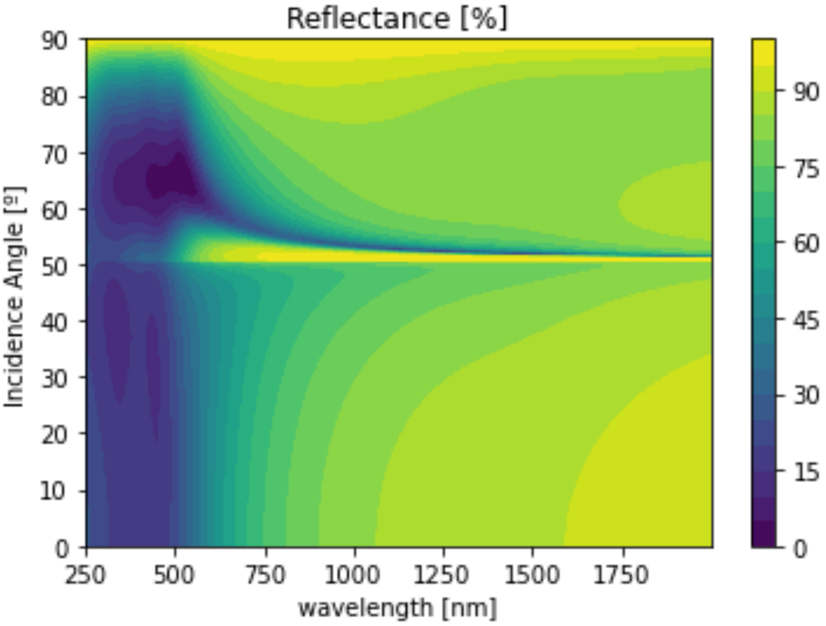

Figure 3.26: Reflectance of an SF10-Au(30nm)-Analyte Krestchmann structure, for a 1.33 analyte refractive index, obtained from a rigorous sweep on the incidence angle and wavelength using the proposed method.

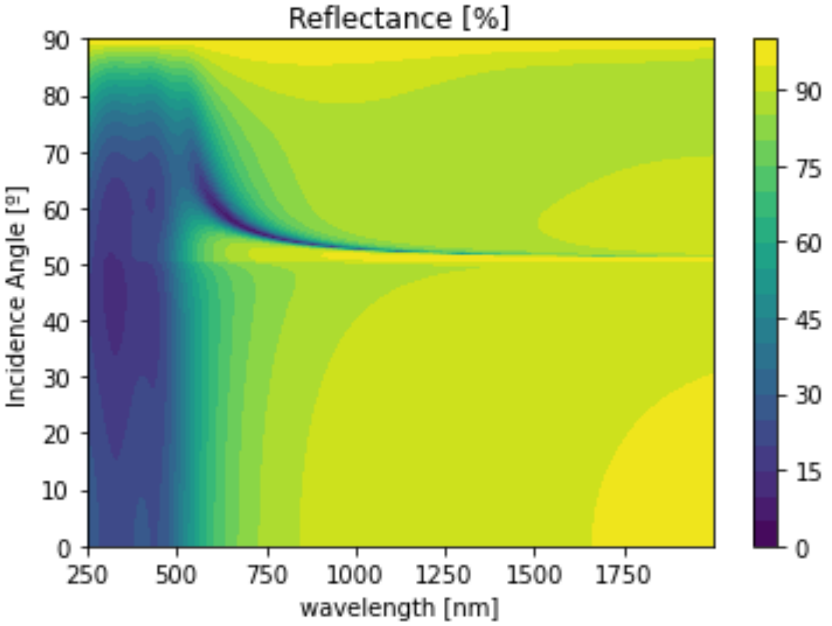

Figure 3.27: Reflectance of an SF10-Au(50nm)-Analyte Krestchmann structure, for a 1.33 analyte refractive index, obtained from a rigorous sweep on the incidence angle and wavelength using the proposed method.

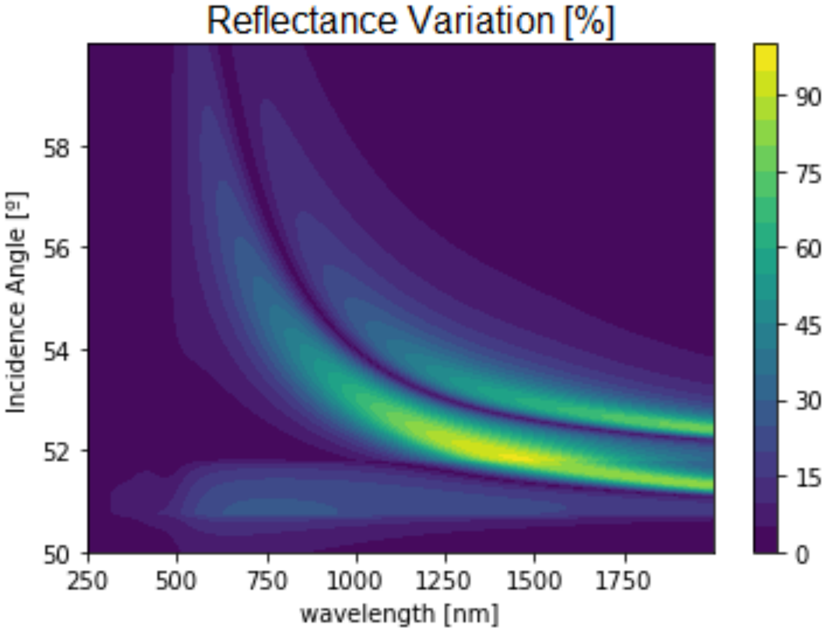

Figure 3.28: Reflectance variation of an SF10-Au(30nm)-Analyte Krestchmann structure, when the analyte refractive index varies from 1.33 to 1.35 (or vice-versa), obtained from a rigorous sweep on the incidence angle and wavelength using the proposed method.

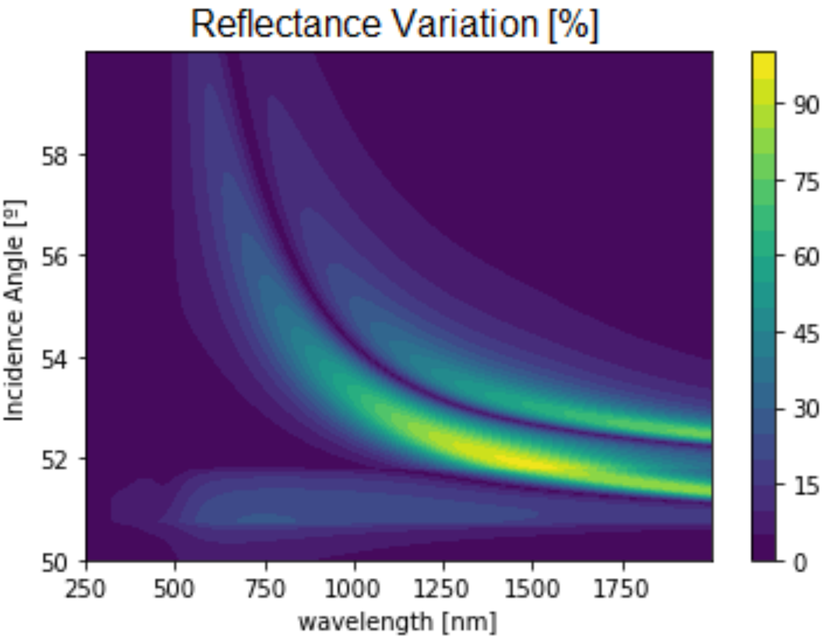

Figure 3.29: Reflectance variation of an SF10-Au(30nm)-Graphene(1.36nm,$L = 4$)-Analyte Krestchmann structure, when the analyte refractive index varies from 1.33 to 1.35 (or vice-versa), obtained from a rigorous sweep on the incidence angle and wavelength using the proposed method.

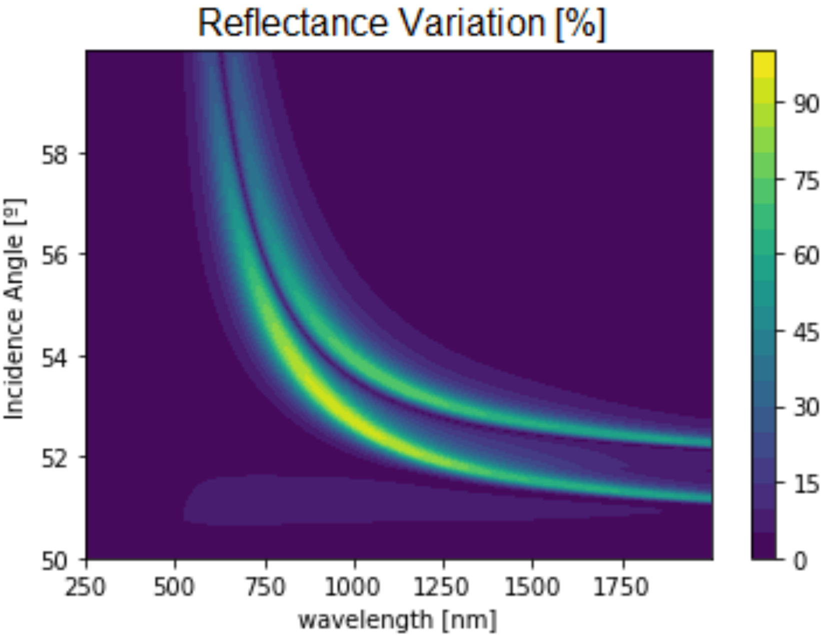

Figure 3.30: Reflectance variation of an SF10-Au(50nm)-Analyte Krestchmann structure, when the analyte refractive index varies from 1.33 to 1.35 (or vice-versa), obtained from a rigorous sweep on the incidence angle and wavelength using the proposed method.

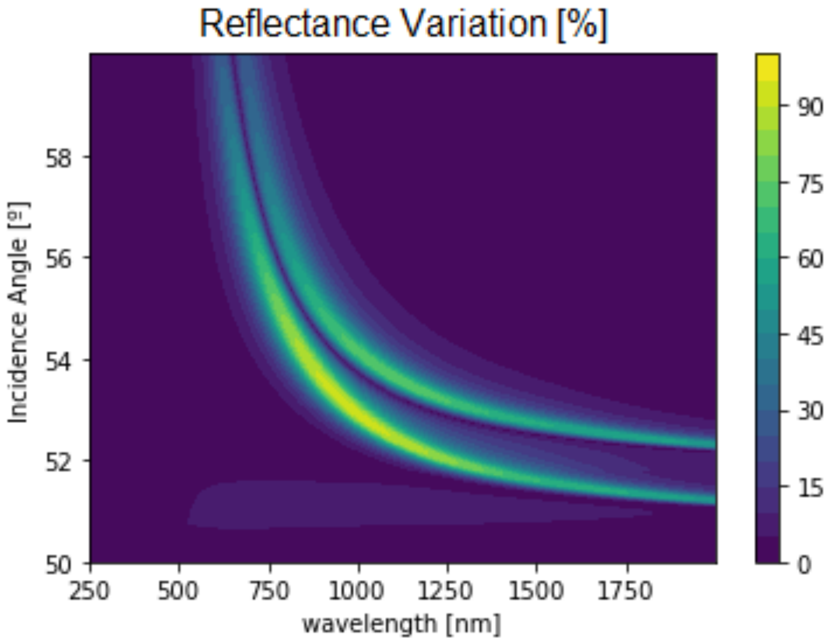

Figure 3.31: Reflectance variation of an SF10-Au(50nm)-Graphene(1.36nm,$L = 4$)-Analyte Krestchmann structure, when the analyte refractive index varies from 1.33 to 1.35 (or vice-versa), obtained from a rigorous sweep on the incidence angle and wavelength using the proposed method.

To summarise and present the quantitative results of this optimisation, table 3.2 is presented, with the results from figures 3.28 to 3.31. It is observed that the structure with the lowest gold thickness has the highest reflectance variations. This was expected, since the larger the absorbing layers, the higher the absorption and therefore the lower the reflectance of the structure. On the other hand, it is also found that by changing the thickness of gold, the optimum operating region is changed. At 30 nm the optimum point is at approximately 1400-1450 nm while for 50 nm it is at 900-950 nm. The placement of the graphene layer may help the adhesion of the analyte to the structure, but it has no major consequences for its optical response, especially in terms of the optimal operating point. However, the introduction of this graphene layer leads to an increase in the resonance angle and the optimal wavelength.

Table 3.2: Optima operating points of the structures as sensors for measuring the analyte's refractive index variation from 1.33 to 1.35.

Test	$(\Delta R_p)_{max}$ [%]	Wavelength [nm]	Incidence Angle [º]
Figure 3.28	95.5	1412	51.83
Figure 3.29	96.2	1452	51.86
Figure 3.30	92.4	914	52.89
Figure 3.31	92.1	928	53.04

3.2.2.B Discussion

The methodology is validated by comparing its results with experimental ones in the literature and other simulation results. The proposed method overcomes some limitations of the previous methods, allowing a simple physical interpretation of the whole process.

Kretschmann sensors are quite sensitive, simple to design and fabricate, presenting huge reproducibility and reliability and low production costs. Furthermore, they have several possible working regions, which is useful in diverse experimental setups.

BK7-Au-Analyte, SF10-Au-Analyte and SF10-Au-Graphene-Analyte Kretschmann structures are evaluated as optical sensors to detect an analyte refractive index variation from 1.33 to 1.35, or vice-versa.

On the BK7-Au-Analyte structure, the analyte refractive index variation leads to a sensitivity of $139\,°/\mathrm{RIU}$.

The sensing response of SF10-Au-Analyte and SF10-Au-Graphene-Analyte structures is optimised on a wide wavelength interval from 250 nm to 2000 nm. Although the inclusion of graphene layers between the metal and the analyte is crucial to improve analyte adhesion on metals such as gold, its effect on the sensors' optimal working regions is not significant.

The sensor sensitivity is higher in the infrared spectral region. For a gold thickness of 30 nm, the maximum sensitivity is 95.5% at 1412 nm (without the graphene layer) and 96.2% at 1452 nm (with the graphene layer), meaning the graphene inclusion led to a small increase in the sensitivity. On the other hand, for a gold thickness of 50 nm, the maximum sensitivity is 92.4% at 914 nm (without the graphene layer) and 92.1% at 928 nm (with the graphene layer), meaning that the graphene layer led to a small decrease of the sensitivity. In both cases, when including the graphene layer, it is observed a small increase in the optimal wavelength. Also, the impact of the graphene layer on the 30 nm gold structure is quite visible above 500 nm and less perceptible for the 50 nm gold structure (figures 3.28 to 3.31).

The proposed methodology proved to be very effective and it was successfully validated through the comparison with experimental and simulation results. The successive steps of the new method allow a simple physical interpretation and perception of the whole process.

3.2.3 Semi-Classical Approach on Time-Domain

To implement this model, a Python script is developed using the above methodology and expressions for a 2D analysis.

The implementation is in Python. The *Start* is illustrated in figure 3.32 by a green rounded rectangle.

In Python a *Photon* class is created with all the useful information to describe it, namely its direction of propagation, the angles of the representative wave vector and the wavelength. We then start by generating a certain number of photons, developing an algorithm called *Photon Generation* that cycles through the positions of the emitter and generates the photons in the required directions, creating an element of the *Photon* class and placing it on a stack.

A cycle is defined as a complete iteration of all active photons in the stack. A photon changes from active to inactive when absorbed or when it leaves the boundaries of the programmed environment. With the data structure used, you can not eliminate elements from the middle of the stack. For this reason, photons are not eliminated. It is useful to make the final calculations and to know in which coordinates they became inactive.

To make space and time uniform in the simulation environment, it is defined Δt as the time that elapses between cycles. The spatial increments were defined as 1 nm in Δt seconds in vacuum. Since time and space are universal, then the space travelled will be proportional to the real part of the wave vector.

If in its motion the photon passes through an interface, then the probabilities of it being absorbed, reflected or transmitted at that interface are calculated. A random number is generated from 0 to 100 and it is compared to the probability values. These results generate the action that the photon takes, being calculated the new direction and angles of the photon wave vector.

If, on the other hand, no interface is found, then the probability that the photon was absorbed in that path is calculated. A random number between 0 and 100 is generated and the values are compared.

Having gone through all the active photons in the stack, a new cycle begins, that is, the simulation clock advances one tick (corresponding to Δt seconds). However, the new cycle only starts if there are or there will be active photons in the stack. In each cycle new photons can be generated, adding them to the stack in the active state. The program ends when all photons in the stack are in the inactive state.

The end of the programme is illustrated with a red rounded rectangle, called *Terminator*. However, before the program ends, some counts are made, such as the number of absorbed photons or the number of photons at certain coordinates (for instance, the target) that have passed through the metal.

The program is designed so that throughout the cycles, as well as at the end of the cycle, an Excel output file is written with the necessary counts. These files are then analysed and converted into more elucidated ways of presenting the results, such as graphs or tables.

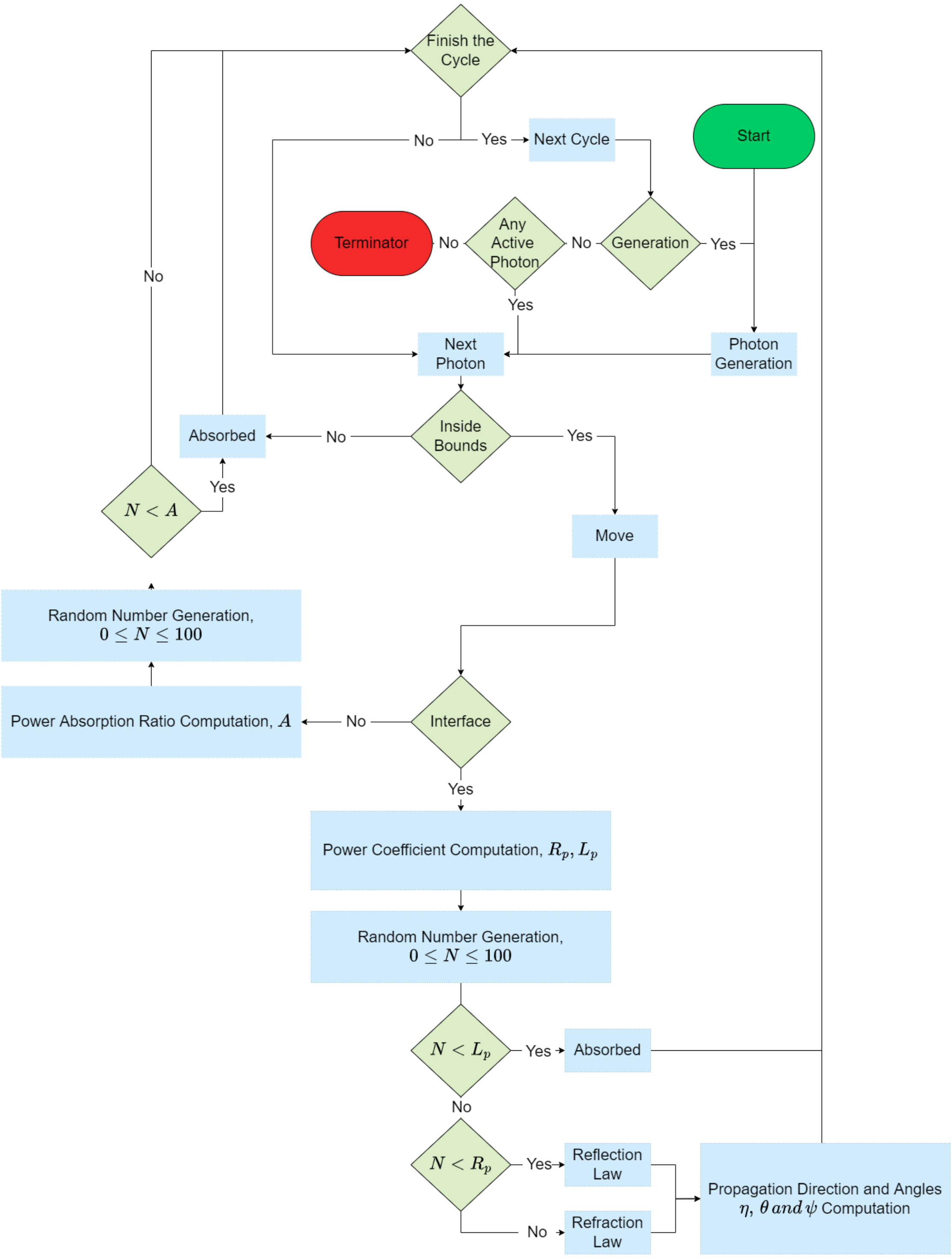

Figure 3.32: Developed model flowchart: the start is illustrated in a green rounded rectangle; the implemented function/algorithms are in the light blue rectangles; the light green rhombuses express conditions or decisions; the program ends in the terminator task illustrated with a red rounded rectangle.

On a metal film of thickness t, there are two equal slits of width d, spaced by s, as illustrated in figure 3.33. This is identical to Young's experiment (presented in subsection 2.2.1), which was the beginning of the knowledge line. To have a more complex model, N emitters are placed distanced by d_e to the metal surface. Each emitter generates a particle in each δ degree, each of them characterised as an inhomogeneous plane wave for a given direction and in a time interval Δt_e. Then, each emitter generates a cylindrical wave (all particles are emitted at the same time). It is intended to emulate a TM wave as in figure 2.10. A target is placed at a distance D from the metal.

This is a stochastic method since particles' movement is characterised by its representative wavevector, which may change whenever the particle reaches an interface, and their actions at the interface are randomly obtained from the power coefficients (obtained from Maxwell's equation). The model is based on the methodology previously presented in section 3.1.1. Furthermore, it is also assumed a non-magnetic media $\mu = 1$ as well as no surface charge density $\sigma_s = 0$ [16].

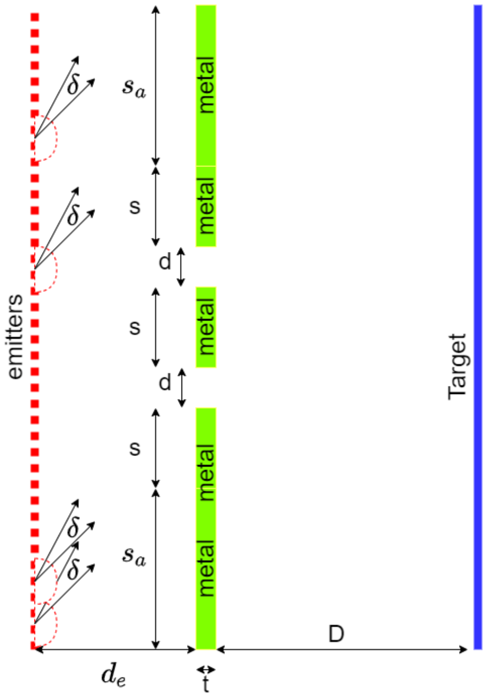

Figure 3.33: A double slit experiment scheme.

The proposed approach is based on the wave-particle dualism. Both wave and particle behaviours coexist, but it is rare to find quantum processes in the radio frequency spectrum and even rarer to hear someone refer to the frequency of a gamma ray, rather than the energy and momentum carried by a gamma ray photon. Although the wave aspects dominate the behaviour of longer wavelengths and the particle aspects dominate the behaviour of shorter wavelengths, the whole range is governed by the same basic laws. It is in the optical range that we most often encounter wave-particle duality, which requires familiarity with both concepts [32,33].

The photons probabilities of being reflected or refracted in an interfaced are computed based on the Fresnel Coefficients, which are deduced from Maxwell's equations. The same expressions deduced as Fresnel Coefficients can be deduced from Schrödinger equation [78,79]. In fact, both Maxwell and Schrödinger equations lead to the Helmholtz equation. In the first case, the entity that reach the interface is a electromagnetic wave whereas in the second it is a particle and its probabilities are given by a wave function. In fact, the wave from Maxwell's equations and the wave function from Schrödinger equation represent the same: the average response for a certain electromagnetic excitation. Based on the Fresnel Coefficients movement probabilities may be obtained in the same way from the ones obtained from wave function. Fluctuations are going to appear in the optical response, which are related to noise and uncertainty associated to the stochastic behaviour of light. The less photons are in the environment, the higher the influence it has on the optical response.

3.2.3.A Results

The method validation includes a set of experiments designed to validate the methodology proposed.

The first experiment starts with a double slit set-up, with slits widths of the order of the incident wavelength. The second experiment refers also to the same two-slit configuration, but, the slit widths are ten times smaller than the incident wavelength. On both tests, the used wavelength is 1550nm quite far from the plasma resonances, as presented on [16,67]. The third test is identical to the second one, except on the operating wavelength, which is 550nm (near the resonance). A huge increase in the number of photons on the target is expected due to the EOT phenomenon, although the pattern might be identical. For the fourth set-up, the number of slits is increased from two to four to assess the differences in results. The fourth test is also identical to the second one but with four slits instead of two. The fifth and last test allows us to confirm EOT phenomena since a four-slit structure is considered, for a wavelength of 550nm (near the resonance), and with a thickness of 30nm, expecting to have even more photons on the pattern [16,67]. Table 3.3 sums up the considerations for these five tests.

A space resolution of $1\,\text{nm}$ is defined which leads to a time resolution of $3.3\,\text{fs}$, considering propagation in free space. The particle propagation elsewhere is nonetheless affected by the refractive index value. For all the configurations, the emission angle δ is 0.1 ° and to introduce more complexity to the structure to test this new approach, a metal extension of $s_a = 1000\,\text{nm}$ is added in each side [16].

Table 3.3: Considered configurations.

	λ [nm]	Slits	d [nm]	t [nm]	D [nm]
1	1550	2	1550	300	1550/2π
2	1550	2	155	300	1550/2π
3	550	2	155	300	1550/2π
4	1550	4	155	300	1550/2π
5	550	4	155	30	1550/2π

This same structure is simulated using a Finite Element Tool, COMSOL Multiphysics. In this case, the results are obtained by applying a finite element method to Maxwell's equations in the time domain. A TM pulse emulates a plane wave with the same duration as on the developed tool. All the other external boundary conditions are defined as scattering boundary conditions to absorb wave components propagating perpendicular to them, being transparent only to their parallel components.

In the developed tool, a total of 250 cylindrical emitters are considered, each one emitting 720 particles (one every $\delta = 0.25\,°$). The convergence of both methods must improve when the number of emitters and the number of emitted particles per emitter increases, since the emission conditions will tend to the emission of a plane wave, under the Huygens–Fresnel principle.

The Rakic's Drude-Lorentz model for the gold electrical relative permittivity is assumed, whose parameters are obtained from [53]. At $\lambda = 1550\,\mathrm{nm}$ the gold electrical relative permittivity is characterised by $\epsilon_{gold} = -96.957 + j11.504$ while $\epsilon_{air} = 1 + j0$ is assumed for air [16].

In figure 3.34 the results from the developed tool on the first configuration are presented, in blue. In the same figure, the red curve represents the results taken from the Finite Element Tool analysis. Both results consider all the particles or waves that pass on that position in the same time interval. In the developed tool that time is defined so that there is no active particle, *i.e.* all photons were absorbed or are already out of boundaries. The results are normalised to the maximum intensity obtained for each tool. Similarly, in figure 3.35 are the results for the second configuration.

In both configurations 180000 photons are emitted (250 emitters, each one emitting 720 photons), being the maximum of figure 3.34 and 3.35 representative of 41 and 28 photons, respectively. Also, 92043 photons are on the pattern of figure 3.34, in contrast with 15885 photons in figure 3.35. Then, it is possible to conclude that small slits transmit less photons. However, the obtained results differ from those predicted by classical theories, *i.e.*, it does not follow the rule $(d/\lambda)^4$. On the other hand, it is also verified that some photons are transmitted and passed from the metal, 1 in the pattern of figure 3.34 and 2 in figure 3.35. In these conditions, metal might reflect almost all the radiation.

The differences between these methods are expected since our model is stochastic and presents discrete results. However, intensity profiles are identical and running the model it is possible to verify that by increasing the photon number (decreasing δ, or increasing the number of emitters) the particle profile will tend to the electromagnetic result. The spatial and time resolution of the developed model is also important to approximate both results and obtain more precise results. It is possible to recognise the electromagnetic profile on the obtained results, following the more stressed areas (as verified in figures 3.34 and 3.35).

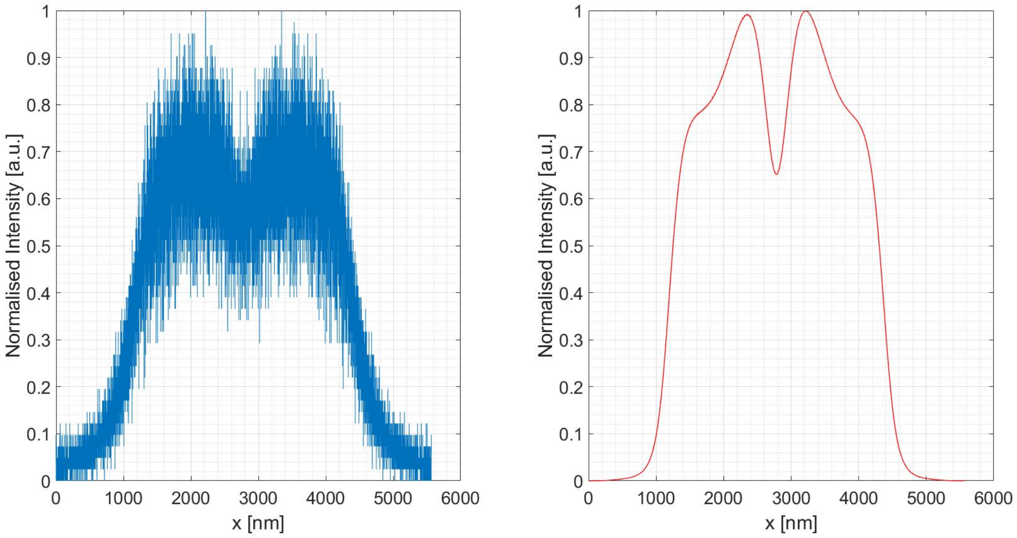

Figure 3.34: A double slit experiment at $\lambda = 1550\,\mathrm{nm}$ with $d = 1550\,\mathrm{nm}$, $s = 155\,\mathrm{nm}$ and $t = 300\,\mathrm{nm}$, $D = 1550/(2\pi)\,\mathrm{nm}$.

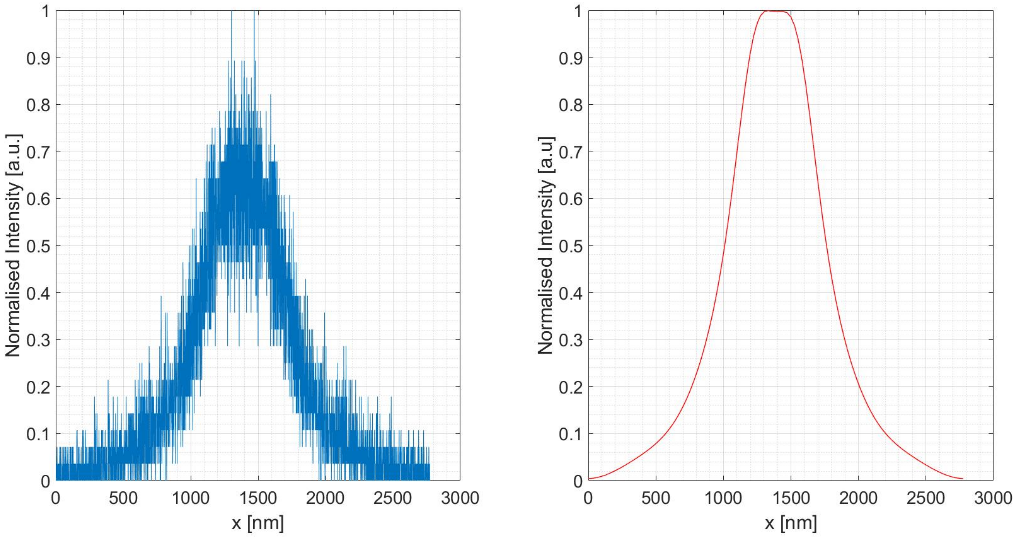

Figure 3.35: A double slit experiment at $\lambda = 1550\,\mathrm{nm}$ with $d = 155\,\mathrm{nm}$, $s = 155\,\mathrm{nm}$ and $t = 300\,\mathrm{nm}$, $D = 1550/(2\pi)\,\mathrm{nm}$.

Another configuration of interest is the same as the second one. However, the emission takes place at $\lambda = 550\,\mathrm{nm}$, where gold is characterised by $\epsilon_{gold} = -5.371 + j2.360$. Using this relative permittivity, the gold reflectivity is lower than the previous one. As a consequence, the pattern has fewer photons (12807 in total) and the maximum corresponds only to 27 photons. Nevertheless, as expected, the number of photons refracted by the metal increases, since the photons' wavelength is close to a resonance region. In this case, a total of 13 from 12807 incidents are transmitted by the metal. This configuration is equal to the second one, however, the photons' wavelength changes, leading to EOT photons on the target.

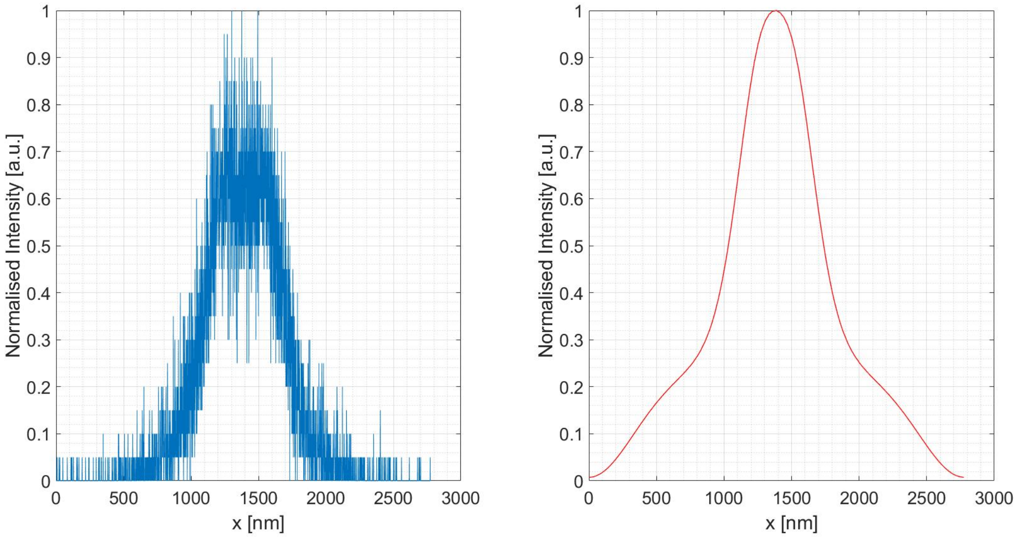

Figure 3.36: A double slit experiment at $\lambda = 550\,\mathrm{nm}$ with $d = 155\,\mathrm{nm}$, $s = 155\,\mathrm{nm}$ and $t = 300\,\mathrm{nm}$, $D = 1550/(2\pi)\,\mathrm{nm}$.

To better assess the validity of the developed method the next (fourth) configuration will be presented, which is identical to the second one. The pattern on the target is presented in 3.37, both for the developed tool (blue) and using the Finite Element Tool (red). Once again, the convergence of results from both tools is verified. The maximum number corresponds to 23 photons and the sum of photons on the pattern is 14986. Moreover, it is also observed that some photons pass through the metal, 14 of the previously mentioned 14986.

Also, for $\lambda = 550\,\mathrm{nm}$ the gold thickness is reduced to $30\mathrm{nm}$, since according to the previous results published on [67] it is an excellent thickness to increase the number of photons on the target. The propagation length computed on [67] for these conditions allows radiation/photons' propagation until other interfaces are reached, meaning that there will be a certain outcome probability. In figure 3.38 are the obtained results. In this case, there are 32744 photons on the target, of which 5929 (18.11%) come through the metal. The maximum of this pattern represents 32 photons, and consequently, the comparison with previous figures should be done carefully. Comparing both figures, it is possible to verify that the pattern has more peaks than the previous one and that the intensity will be higher almost everywhere, including on the edges (on the metal extension s_a).

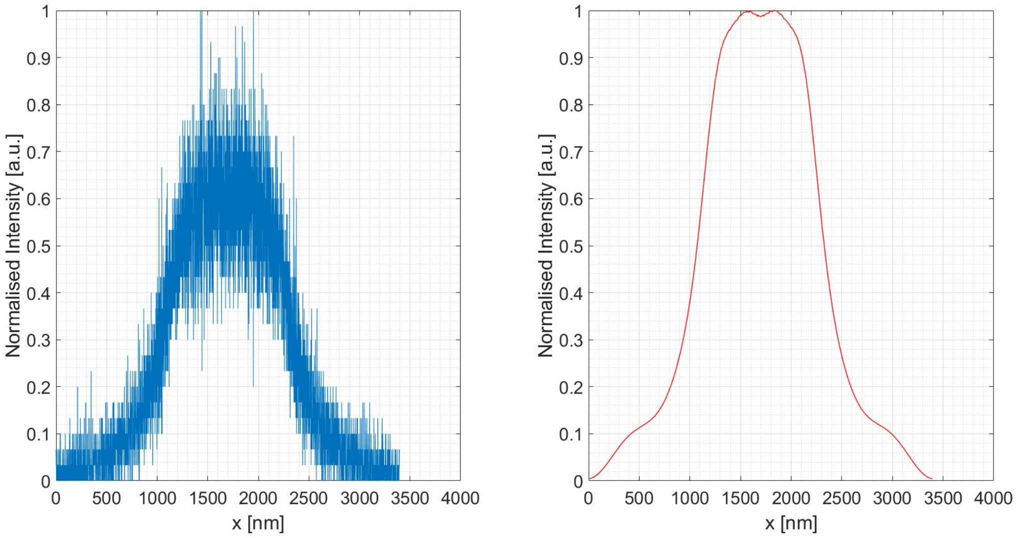

Figure 3.37: Four slits experiment at $\lambda = 1550\,\mathrm{nm}$ with $d = 155\,\mathrm{nm}$, $s = 155\,\mathrm{nm}$ and $t = 300\,\mathrm{nm}$, $D = 1550/(2\pi)\,\mathrm{nm}$.

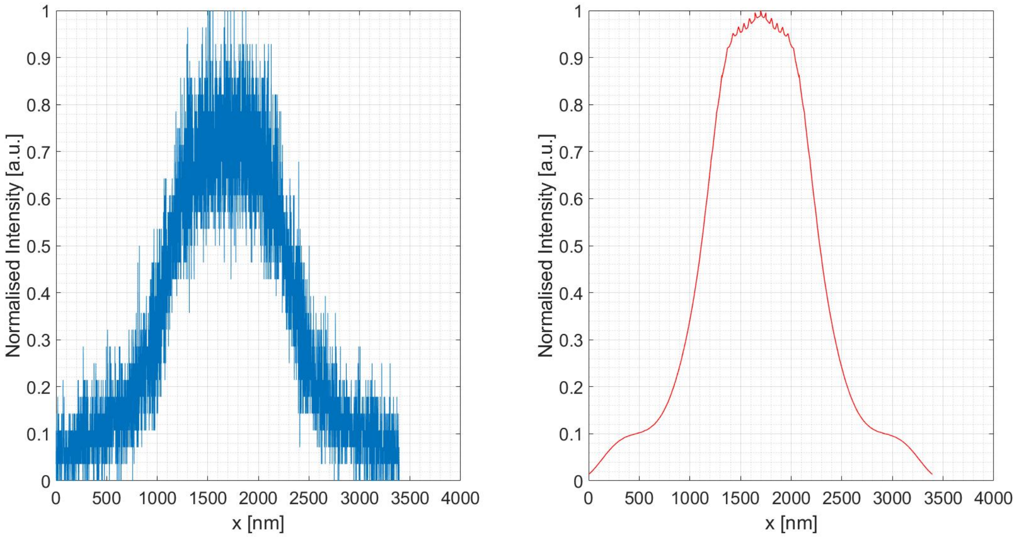

Figure 3.38: Four slits experiment at $\lambda = 550\,\mathrm{nm}$ with $d = 155\,\mathrm{nm}$, $s = 155\,\mathrm{nm}$ and $t = 30\,\mathrm{nm}$, $D = 1550/(2\pi)\,\mathrm{nm}$.

3.2.3.B Discussion

Geometry or ray optics assumes that rays propagate along a straight-line optical path in a homogeneous medium [16,65,66]. A usual ray optics model cannot predict interference and diffraction scenarios. However, by analysing not the ray but particles, and including phase variation by using a complex refractive index on the calculations, it is possible to overcome the interference and diffraction problems. Different photons can be in the same spatial coordinate since they are bosons. When the number of involved particles is high enough, the response tends to be the one obtained by the wave approach. A single photon cannot produce a diffraction pattern or interfere with others and for that reason, it is impossible to extrapolate a pattern using a small set of photons. For that reason, the pattern will be improved when the number of photons increases, *i.e.*, decreasing the angle δ leading to a more continuous cylindrical wavefront or increasing the number of emitters [16].

Another important aspect to be referred to is that this method allows us to obtain excellent results even for sub-wavelength structures. Since it is a single-particle methodology, the results are discrete and thus, the resolution of the patterns is an important parameter. For that reason, the results are not as smooth as the ones obtained using a more complete electromagnetic theory framework obtained from the Finite Element Tool. However, increasing the number of photons, the patterns tend to become identical. On the other hand, Maxwell's equations are verified for the average results. Analysing the more stressed areas of the obtained patterns it is possible to identify the pattern from the FEM tool [16].

Moreover, this method does not neglect the role of the metal in the observed pattern. First, the observed pattern and respective time response varies with the incident wavelength, influenced by variations in the metal electrical permittivity. Then, for specific wavelengths and incident angles, there is some probability of a certain photon to be transmitted by the metal, leading to an extraordinary transmission in comparison with what is expected by classical theories (Kirchhoff's, Bethe's or Bouwkamp's theories), which predict a decrease proportional to $(d/\lambda)^4$ [4, 6, 40]. It is verified that even at large wavelengths there is a certain non-null probability of having a transmitted photon from the metal [16].

The last test is the most complex one, since the incident wavelength is near the gold plasma resonance and the metal thickness is of the order of the propagation length of the air-metal interface, as previously presented on [16, 67]. The complexity of this test relies on the fact that the light pattern will be more influenced by photons passing through the metal. Using the proposed approach it is possible to quantify phenomena such as extraordinary optical transmission (EOT). In this case, it is possible to verify an increase in the number of photons passing through the metal from tens to thousands or tens of thousands, by adjusting the structure dimensions and by changing the incident wavelength [16].

The classical theories, assuming that metals reflect all incident light, can adequately represent light-metal interaction for radio and microwave frequencies. However, they no longer apply to optical frequencies; in this case, a new interaction model must be considered [16].

In this research work, a model based on ray tracing in absorbing media is presented, applied not only on waves but also on photons. For that reason, the developed tool is not deterministic, but it reveals stochastic processes. To validate the proposed model, time domain analysis with pulse excitation is performed, obtaining light patterns that can be compared with other published results [16].

The considered structures in this work include an emitter of photons or waves, a metal film with slits and a target. The obtained results suggest that some photons in the target pattern come from the metal and not from the aperture. This reveals the phenomenon of extraordinary optical transmission (EOT) in the time domain, i.e., on the pattern, there are more photons than the photons transmitted by the aperture. This effect is due to the surface plasmon resonances in the illuminated metal, resulting from the variation of the metal's permittivity with the light wavelength and its incident angles [16].

It is also verified that different structural configurations result in patterns of various shapes and intensities. Thus, a methodology to design structures like optical sensors, photodetectors, and optical filters might be developed. The reduced computational effort is the most significant advantage of employing this tool instead of a finite element one. With a finite element tool, one must sum all the waves that pass on a certain plane in a given time interval. The sum of processing influences the pattern, i.e., smaller time steps generate better results but demand more computational effort. The proposed methodology and developed tool represent an excellent alternative, returning quite interesting and suitable results for small light intensities. This novel approach is useful to quantify phenomena as EOT [16].

3.3 Summary

The proposed methodology allows us to have a different perception of what are the phenomena and their implications on dielectric-metal interfaces at optical frequencies. The proposed method allows us to focus more attention on the interface. It is oriented for plane waves. However, at the nano-scale where sources might be near the interfaces, there are no plane waves but a composition of different plane waves at several angles (cylindrical waves).

Based on the obtained results it is possible to point out some important and novel conclusions. First, the transmission percentage has important local maxima and minima near resonance frequencies. However, it is possible to verify that the transmission percentage has impressive high values (in comparison with the null percentage at microwave regimes). Additionally, these non-null probabilities are combined with also high transmission angles, meaning that power must be transmitted closer to the surface. Analysing this fact and the charts' behaviour (resonances on the predictable wavelengths) it is possible to conclude that surface plasmon polaritons are the main agents on the transmission peaks in ultraviolet and visible regions. Furthermore, propagation length is analysed, and the results show us this kind of phenomenon is only observable at the nano-scale since the transmitted waves/particles only propagate orders of 50-100 nm. This is quite relevant since it is not only important to have a subwavelength structure but also to work at optical frequencies. The work on optical frequencies allows the transmission and propagation in the metal. The subwavelength dimensions allow the appearance of these waves/particles at other interfaces, meaning that it is possible to use them before being absorbed and in certain cases, re-transmit them for non or less absorbing media (for instance EOT).

The illustrated charts obtained using the proposed methodology, allow us to have a better idea about SPP resonances. For instance, it is quite useful when choosing the correct materials for a certain application, since it is possible to verify in which conditions radiation is reflected or transmitted by the interface. Also, the proposed methodology based on Maxwell's equations, gives us a grounded understanding of surface plasmon polaritons' role and wave propagation, throughout the interface. This approach is based on optical concepts, such as Fresnel Coefficients and Generalised Snell's law.

Thus, the developed computational programs (tools) are based on the same methodology, exploiting the advantages of it, but they are different: 1) Ray Tracing: The first two validations use the ray tracing programme. They allow structures with multiple parallel and semi-infinite interfaces to be analysed in the frequency domain (for instance: 1 interface - to analyse SPP excitation and propagation; 2+ interfaces - Kretschmann's structures). 2) Object-Oriented Programming: Allows any type of optical/photonic structure to be analysed. Photons are objects that move in a given environment and are characterised by a complex, physically well-defined wavevector. They can be analysed in both the time and frequency domains.

4

Biosensors based on Nanoantennas

Contents

This chapter focuses on the design of sensors based on nanoantennas, exploiting the Extraordinary Optical Transmission effect. As mentioned above, the aim is to focus on biosamples. However, since the sensor's direct measurement is the refractive index, it was decided to study the properties of several samples (see section 2.7) and select a range that would allow the monitoring/detection of a reasonable number of analytes. Thus, based on the results presented in section 2.7, the 1.30-1.41 refractive index range was selected as the study objective. Within it, the main focus is on the 1.30-1.33-1.35 sub-interval (related to water variations). The following study focuses on this interval without mentioning the actual sample that could be studied. In the end, the operation of the sensor will be associated with various monitoring methods.

4.1 Emitter Characterisation

Aiming the analysis of the available technology to realise the device, this chapter starts with the emitter characterisation and an innovative application in Kretschmann's structures.

As presented in section 3.2.3, in the semi-classical model, photons are generated in the emitter. A plane wave is emulated in the emission line, considering the Huygens-Fresnel principle and exploiting wave-particle dualism. However, since the model is semi-classical, photons may be generated according to a certain photon's distribution. Also, light intensity, *i.e.*, the number of photons, should be carefully selected to ensure the physical viability.

This section is divided into three different subsections. Photon distribution/statistics are presented in the first, followed by an application in Kretschmann's sensors. This application aims to validate the implementation of the presented equations however, it also introduces a novel scientific paradigm in analysing these structures with a semi-classical methodology. The used program is not the semi-classical and semi-analytical model, but it is the analytical (and now semi-classical) methodology, i.e. the ray tracing program is used instead of the object-oriented program. Finally, a discussion about the generated light intensity is added, aiming at the possibility of selecting a real emitter.

4.1.1 Photon Distribution

Poisson and Thermal (Super-Poisson) distributions are considered to characterise the light emission. From a classical perspective, the most stable type of light is a perfectly coherent beam. However, fluctuations occur and their influence might be important for low-power signals or for short time scales due to the discrete nature of light [15,16,80].

Poissonian light is a perfectly coherent light characterised by a constant intensity. The average number of photons in a beam segment is given by $n_{av} = \phi L/c$, where ϕ is the photon flux, L is the segment length and c is the light velocity in the propagation medium. The probability of having n photons in the light segment is given by expression 4.1, which describes a Poisson distribution. Furthermore, in this statistic, it is possible to deduce that the variance of the photon is equal to the photon's mean value [80].

$$P(n) = \frac{n_{av}^{n}}{n!} e^{-n_{av}} \tag{4.1}$$

When the flux variance is higher than the photons' average, one is observing Super-Poissonian light. Super-Poissonian emitters are easier to obtain than Poissonian ones since it is easier to develop unstable sources. Chaotic, Incoherent and Thermal light are the three classical types of Super-Poissonian sources. In this research work, one focuses on Thermal light, since it defines the emission of a black-body [80]. The photon distribution is presented in expression 4.2 and it can be deduced from statistical mechanics. Due to its origins, this distribution is also known as Bose-Einstein and its variance is given by $n_{av}+n_{av}^2$. Furthermore, the average value is related to the body's temperature, T, by Planck's formula presented in expression 4.3, where k_B is the Boltzmann's constant and ω is the mode's frequency [80].

$$P(n) = \frac{1}{n_{av}+1}\left(\frac{n_{av}}{n_{av}+1}\right)^{n} \tag{4.2}$$

$$n_{av} = \left(e^{\frac{\hbar\omega}{k_B T}} - 1\right)^{-1} \tag{4.3}$$

Sub-Poisson distributions occur from a photon variance lower than its mean value. The distribution is narrower in comparison with the previous ones. Sub-Poissonian light is somehow more stable than Poissonian ones and there is no classical equivalent. For that reason, the observation of this type of light reveals the quantum nature of light [80]. For that reason, this kind of distribution is not considered.

Figure 4.1 illustrates Poisson and Thermal distributions for 4 different n_{av}: 1, 5, 10 and 100.

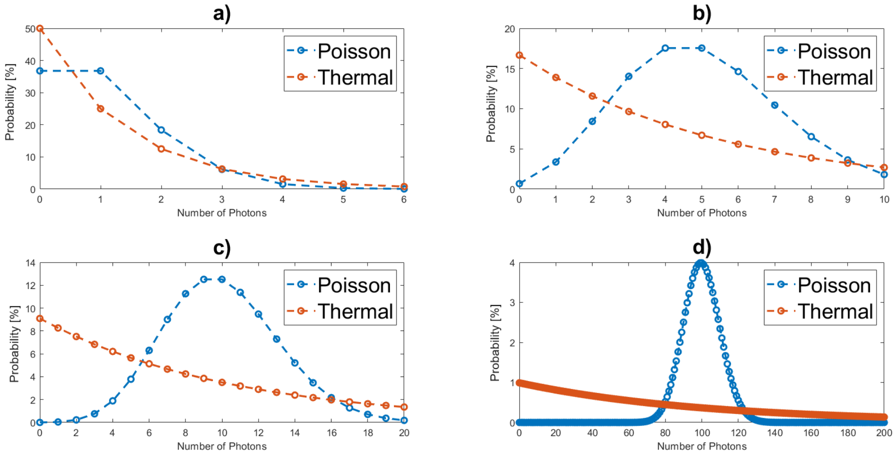

Figure 4.1: Emitter statistics (Poisson and Thermal) for the mean values, n_{av}: a) 1; b) 5; c) 10 and d) 100.

4.1.2 Application in Kretschmann's Sensors

In this section, results are divided into two subsections. The optimised Kretschmann's sensor of section 3.2.2 is firstly analysed for a Poissonian emitter, followed by the analysis for a Thermal one.

In both subsections, the simulated structure is an SF10-Au(30nm)-Graphene(1.36nm)-Analyte, whose results are presented in section 3.20. There, it is already concluded that the best incident wavelength to detect a refractive index variation between 1.33 and 1.35 is 1452 nm, with an incident angle of $\theta_{opt} = 51.86°$. Furthermore, the reflectance variation is 96.2%. Results are presented in an angle range between $50°$ and $60°$, with a resolution of $0.01°$.

4.1.2.A Poissonian Emitter

From the published literature, one should already know the output of a Kretschmann's structure, but how is the photons' distribution if one assumes a quantum or semi-classical behaviour? This is the question to be clarified, starting with the Poissonian emitter. This is implemented considering expression 4.1.

Firstly, in figure 4.2 are the results from the photons' distribution for a 1.33 analyte. As expected, the structure may reflect almost all the radiation, due to the metal behaviour. However, due to the metal and its interface with dielectrics, surface plasmon polaritons are excited on these interfaces, allowing the energy transmittance through the metal, within the wavevector match condition ($R_p \approx 0$). For this case, the reflectance minimum is at $\theta_{min} = 51.70°$, which is also verified from the performed simulations.

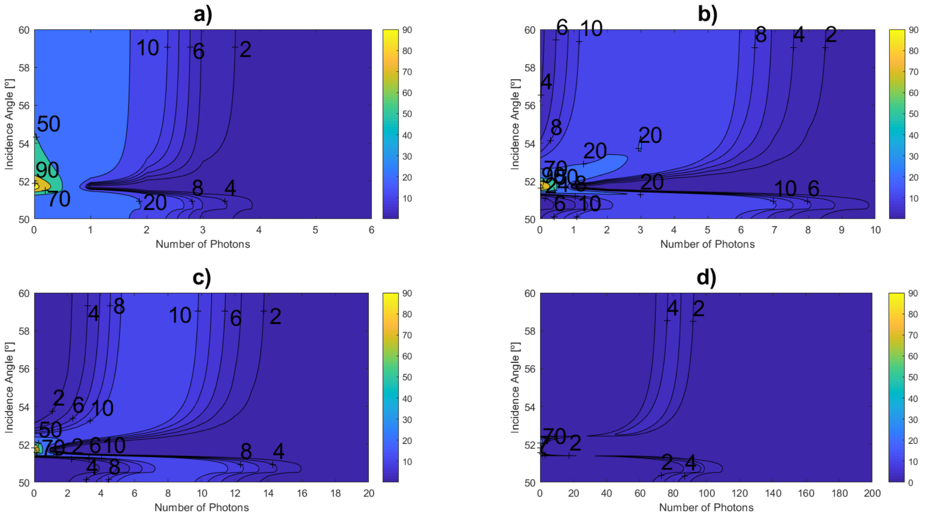

Figure 4.2: Photons probability as a function of the incident angle and number of emitted photons by a Poisson emitter, considering $n_a = 1.33$, for the mean values, n_{av}: a) 1; b) 5; c) 10 and d) 100.

Moreover, although the emission follows the Poisson expression, figure 4.2 reveals that the photons' distribution on the detector deviates from a Poissonian one. The photons' distribution (for a constant angle - horizontal lines) tends to have a lower mean value in comparison with the ones emitted and presented in figure 4.1. Furthermore, it can be seen also that it is quite dependent on the incident angle, and consequently, it is not possible to state that it might be a Poissonian distribution. The minimum reflectance values occur for an angle θ_{min}, meaning that it is most probable to obtain 0 photons on the detector and consequently, the distribution tends to the null average.

Similar scenarios occur for a 1.35 analyte, whose results are illustrated in figure 4.3. It is possible to verify variations on the distributions, namely around the photons' mean values and for the lower analysed angles, which are the cases where the structure itself has higher reflectance, and the angle θ_{min} presents a new value of 52.84°.

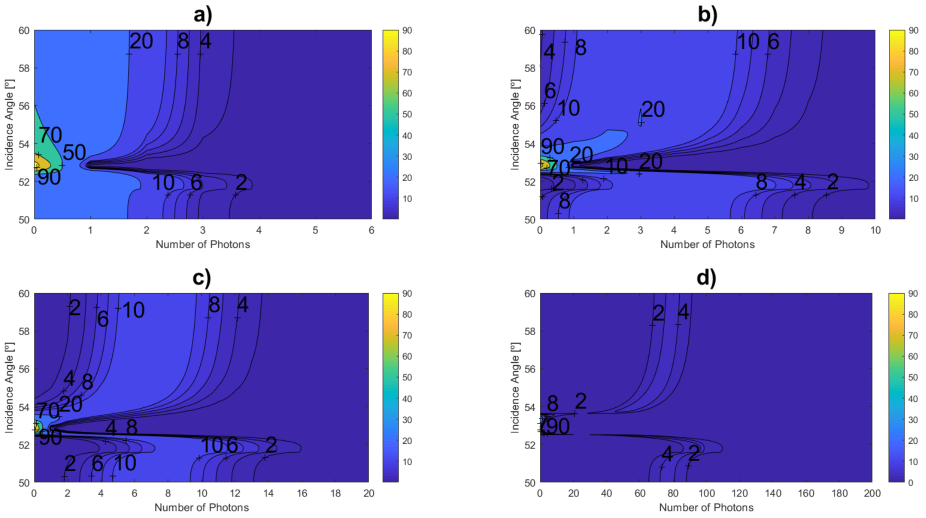

Figure 4.3: Photons probability as a function of the number of emitted photons by a Poisson emitter, considering $n_a = 1.33$ and three specific incident angles, for the mean values, n_{av}: a) 1; b) 5; c) 10 and d) 100.

The figures above allow a better understanding of the consequences of the refractive index variation on the reflectance, mainly on its minima. In figures 4.4 and 4.5, the reflected photons' distribution is presented for three different angles: θ_{min_1} (minimum reflectance for the 1.33 analyte refractive index), θ_{opt} (optimised sensor) and θ_{min_2} (minimum reflectance for the 1.35 analyte refractive index).

For the 1.33 analyte refractive index, it can be seen in figure 4.2 that the reflectance is null for $\theta_{min_1} = 51.70$°, and consequently one should obtain a maximum probability at 0 on the detected distribution. This is verified in figure 4.4, where θ_{min_1} and θ_{opt} (which is also near to θ_{min_1}) have identical distributions and all of them present an almost null reflection. Furthermore, the distribution corresponding to θ_{min_2} has a lower mean value and a lower probability in comparison with the emitted values presented in figure 4.1, as a consequence of being far from the wavevector matching condition at the interface.

When the analyte's refractive index varies to 1.35, the angle of minimum reflectance varies from $\theta_{min_1} = 51.70$° to $\theta_{min_2} = 52.84$°, meaning that the reflectance minimum will occur at θ_{min_2}. According to figure 4.5, it is possible to verify this effect, since the distribution at θ_{min_2} is identical to the distribution of θ_{min_1} in figure 4.4. On the other hand, the distribution at θ_{min_1} is almost the same as at θ_{opt}. The obtained distributions are equal to the emitted ones because this structure reflects almost all the radiation at this wavelength and incident angle.

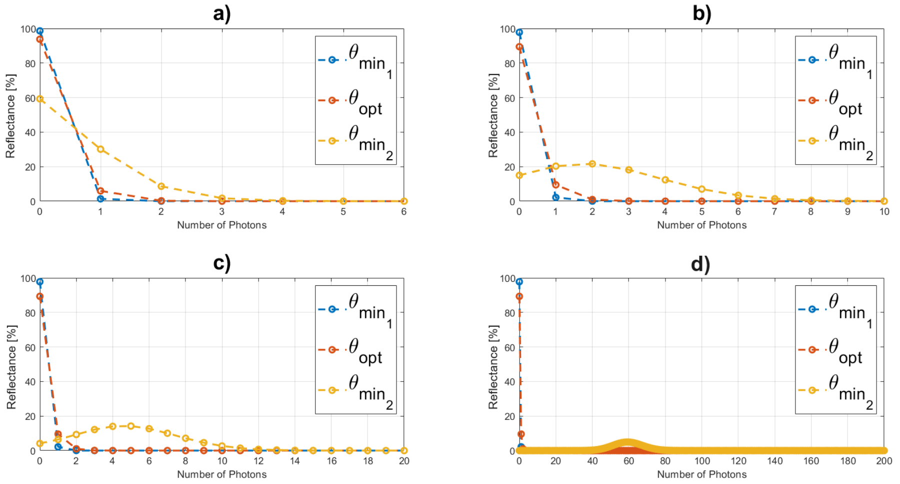

Figure 4.4: Photons probability as a function of the incident angle and number of emitted photons by a Poisson emitter, considering $n_a = 1.33$, for the mean values, n_{av}: a) 1; b) 5; c) 10 and d) 100.

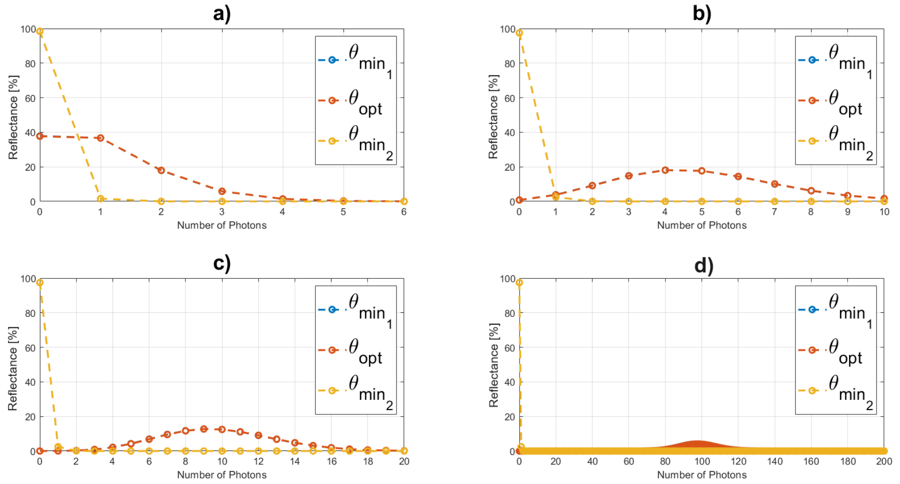

Figure 4.5: Photons probability as a function of the number of emitted photons by a Poisson emitter, considering $n_a = 1.35$ and three specific incident angles, for the mean values, n_{av}: a) 1; b) 5; c) 10 and d) 100.

The sensor's performance is then verified by the analysis from figures 4.4 and 4.5. At θ_{opt}, the device reflects almost all the radiation for a refractive index of 1.33 and transmits all the radiation for a refractive index of 1.35. For that reason, this sensor is quite effective in detecting refractive index variation, since the reflectance variation is higher than 90%.

4.1.2.B Thermal Emitter

Thermal emitters are quite different from the Poissonian ones since their distribution is monotone and the emission probability decreases by increasing the number of photons. Consequently, Thermal distributions have a maximum for 0 photons, which is shown in figures 4.6 and 4.7. Comparing both figures it is possible to verify the variation of the reflectance's minimum from $\theta_{min_1} = 51.70°$ to $\theta_{min_2} = 52.84°$.

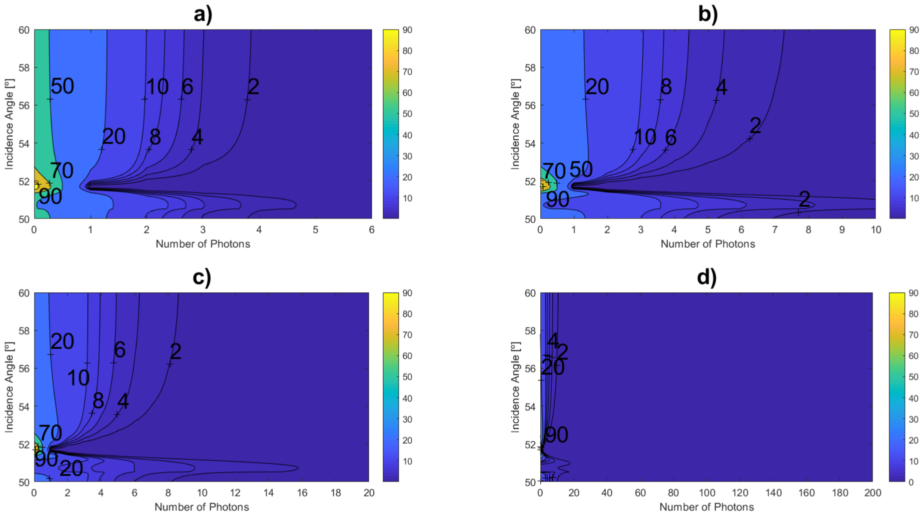

Figure 4.6: Photons probability as a function of the incident angle and number of emitted photons by a Thermal emitter, considering $n_a = 1.33$, for the mean values, n_{av}: a) 1; b) 5; c) 10 and d) 100.

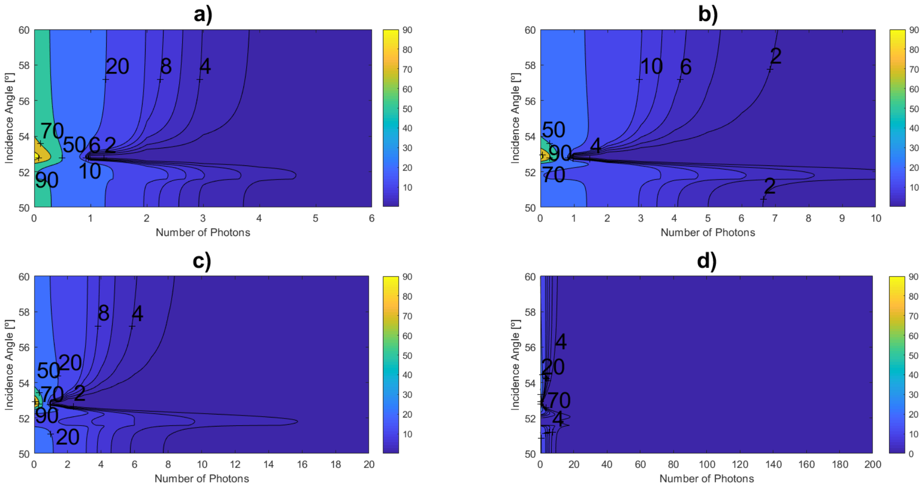

Figure 4.7: Photons probability as a function of the incident angle and number of emitted photons by a Thermal emitter, considering $n_a = 1.35$, for the mean values, n_{av}: a) 1; b) 5; c) 10 and d) 100.

In figures 4.8 and 4.9 the photons' distribution as a function of the incident angle on the detector is considered.

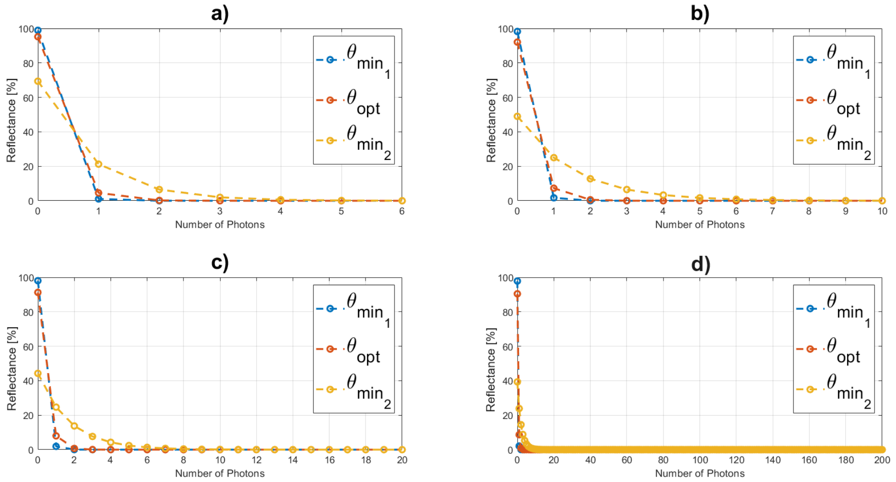

Figure 4.8: Photons probability as a function of the incident angle and number of emitted photons by a Thermal emitter, considering $n_a = 1.33$, for the mean values, n_{av}: a) 1; b) 5; c) 10 and d) 100.

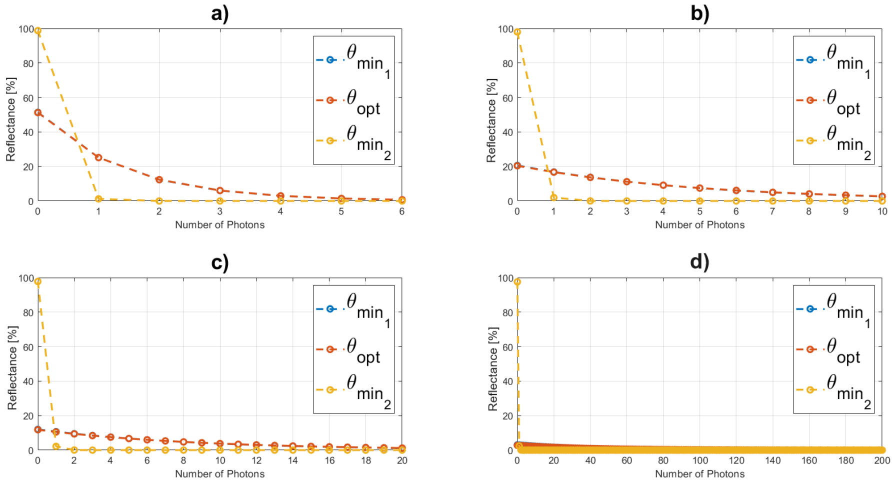

Figure 4.9: Photons probability as a function of the number of emitted photons by a Thermal emitter, considering $n_a = 1.35$ and three specific incident angles, for the mean values, n_{av}: a) 1; b) 5; c) 10 and d) 100.

In figure 4.8 the distributions for a 1.33 analyte refractive index are presented, and it can be seen that the distributions at θ_{min_1} and θ_{opt} are quite similar and they do not follow the emitted one, which is a consequence of the nonexistence of reflected signal. The distribution at θ_{min_2} is identical to the Thermal emitted one but with a lower mean value.

The results obtained for the 1.35 analyte are presented in figure 4.9. In this case, it is possible to verify that the distributions at both θ_{min_1} and θ_{opt} are equal (superposed in figure 4.9) and equal to the emission distribution presented in figure 4.1. On the other hand, at θ_{min_2}, the obtained distributions present an almost null probability of having photons on the detector since the wavevector matching condition is nearly verified.

4.1.3 Light Intensity

The simulations carried out consider between 175 and 250 cylindrical emitters, each emitting in 360 directions. Assuming 250 cylindrical emitters (the results with 175 differ practically nothing, as can be analysed by the orders of magnitude of the other variables under analysis), a total of 9×10^4 photons per 3.3×10^{-18} seconds. Then, 2.7×10^{22} photons/s is computed as the photons flux. This means that in the performed simulations the photon flux will be around 10^{22} photons/s. The device area rounds dozens of μm^2 (the 2D cut line has 3 μm), which is consistent with the several sources and optic fibres core diameters.

Classically, it is intended to emulate an electromagnetic plane wave. For that purpose, the Huygens-Fresnel principle is used to emulate the wave considering a huge number of cylindrical point sources. The wave power flux might be adjusted by considering that each optical path instead of representing 1 photon, counts as other numbers (either higher or lower than 1). Since all the results are normalised, it is possible to consider them in terms of the emitted power.

Quantumly or at least semi-classically, the wave power has more impact, since it is not totally correct to state that by multiplying the wave power, the optical response remains the same. For instance, it is not possible to divide photons and on the other hand, the assumption of having more than 1 always in the same space-time is not totally satisfied, since the group may be divided in the interfaces.

Thus, one must consider a photon flux density associated with real optical sources. For instance, the ones presented in the tables 4.1 and 4.2.

Table 4.1: Photon flux density for different commonly used light sources working at 100 mW/cm^2 (adapted from [81]).

Light Source	Photon Flux $[10^{17}/(cm^2 s)]$
G173	2.9
BB3k	1.7
LED - 635nm	3.2
LED - 850nm	4.3
LED - 950nm	4.8
LASER - 808nm	4.1
LASER - 1064nm	5.4

Table 4.2: Mean photon flux density for several optical sources.

Light Source	Photon Flux [$10^7/cm^2s$]
Starlight	0.1
Moonlight	1
Twilight	10^3
Indoor Light	10^5
Sunlight	10^7
10mW HeNe Laser - 633nm @ 20 μm radius spot	10^{15}

From these tables, it is possible to conclude that there are some LEDs and LASERs with optical power densities at 10^{17} to 10^{22} photons/(cm^2s).

The proposed emitter can be semi-classically visualised as a LED or a LASED with an optical lens to focus all the emitted power.

Considering the He:Ne LASER example: Its maximum power density is 10^{22} photons/(cm^2s), and the LASER is focused in a circular spot with a radius of 20 μm, leading to a focused density around 10^{28} photons/(μm^2s). Since the proposed emitter as 2.7×10^{22} photons/s, the He:Ne LASER is a possibility to produce our results if our device area stands around μm^2.

Considering LED sources: Their power density is at the 10^{17} photons/(cm^2s) which may be focused for 10^{23} photons/(μm^2s) orders, verifying our requirements if our device area stands around μm^2.

In both LASER and LED solutions, it is verified that in the emission pattern, the wave focused on the spot is considered plane and uniform.

4.1.4 Emulation of TM Plane Wave

The emitter is a TM wave emulated by the emission of photons in different directions at different cylindrical point sources, based on the Huygens principle (also named as Huygens-Fresnel principle). The implemented emitter is composed of 250 point sources, each one emitting in a total of 720 different optical paths. A Poissonian distribution is applied to each optical path, considering the emission of just one photon on average per time stamp. The time resolution is approximately 3.3×10^{-18} (the propagation time of a photon in vacuum to cross 1 nm).

4.2 Metal’s Apparent Refractive Index

The analytes are already settled, and the emitter is also characterised. Then, one may verify how SPP are excited at analyte-metals interfaces before analysing the optical response of complex structures as nanoantennas.

With this in mind, the apparent complex refractive index, the transmission angles and the reflectance of analyte-metal interfaces are analysed in this section. Due to the results’ similarity, it is focused on the analyte’s refractive index sub-interval among 1.30-1.33-1.35.

Four metals are analysed: gold, copper, silver and aluminium. However, just two are analysed in this section. Gold and copper have similar electrical permittivity values. Although copper is cheaper than gold, gold’s chemical stability is an advantage for sensing applications. This is the argument to exclude aluminium since its optical properties change a lot when in contact with other media. Also, aluminium resonances in this wavelength range and analyte’s range are weak in comparison with the other metals. Thus, gold and silver are analysed in this and the following section.

In figures 4.10a to 4.12c is the analyte-gold characterisation.

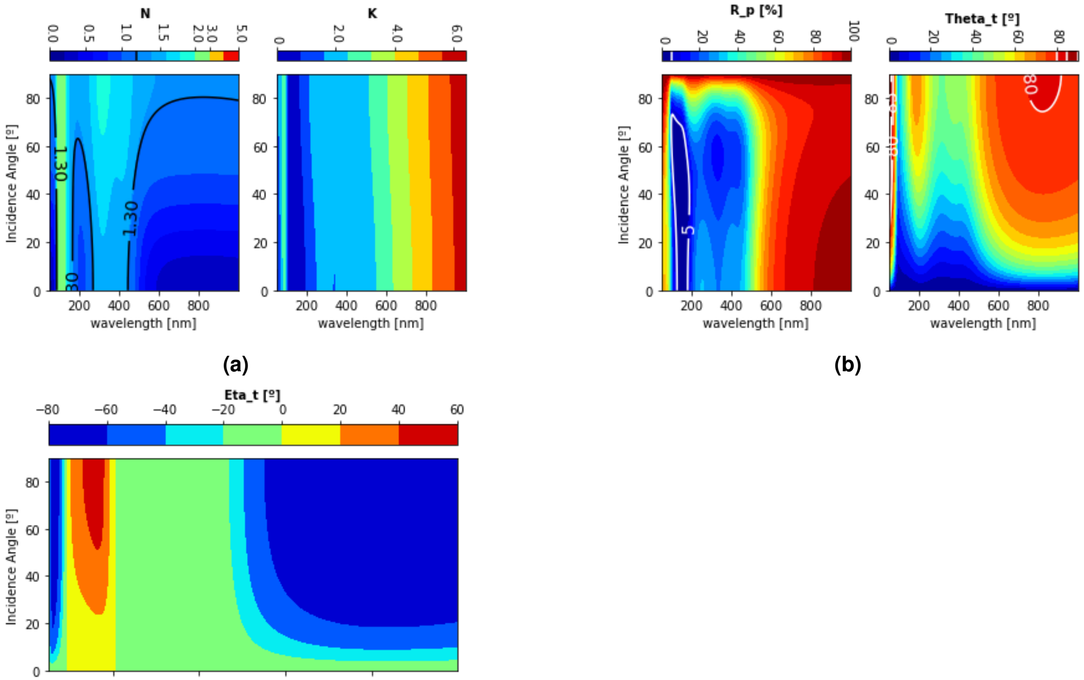

(a)

(b)

(c)

Figure 4.10: Characterisation of the analyte-gold interface for a 1.30 refractive index analyte.

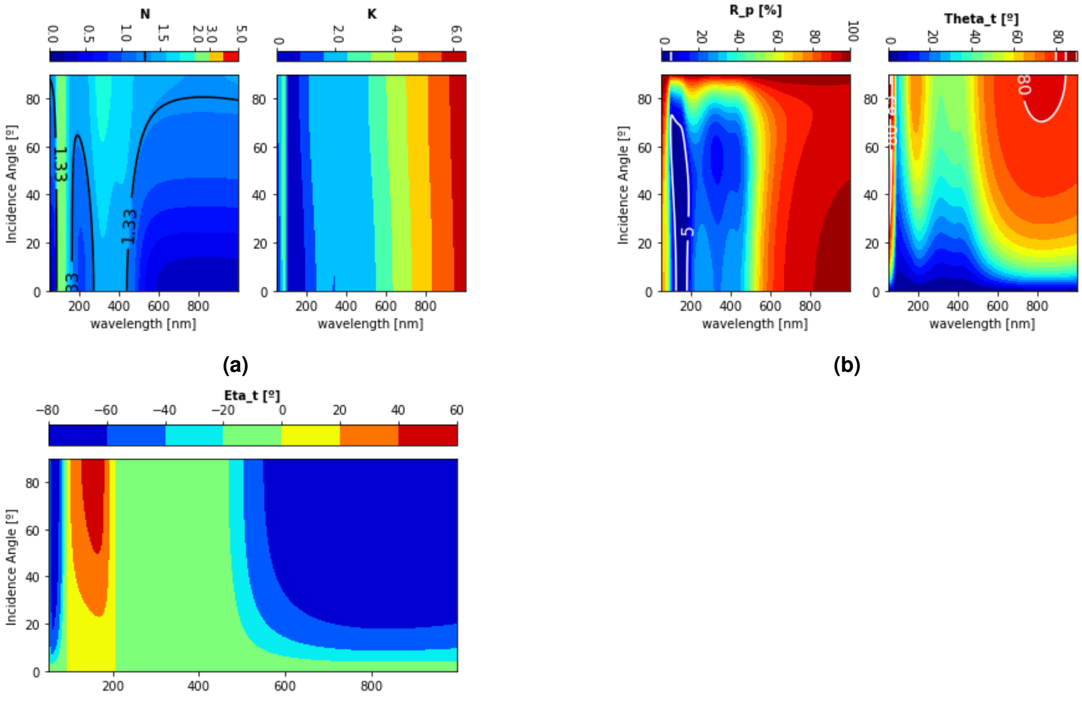

(a)

(b)

(c)

Figure 4.11: Characterisation of the analyte-gold interface for a 1.33 refractive index analyte.

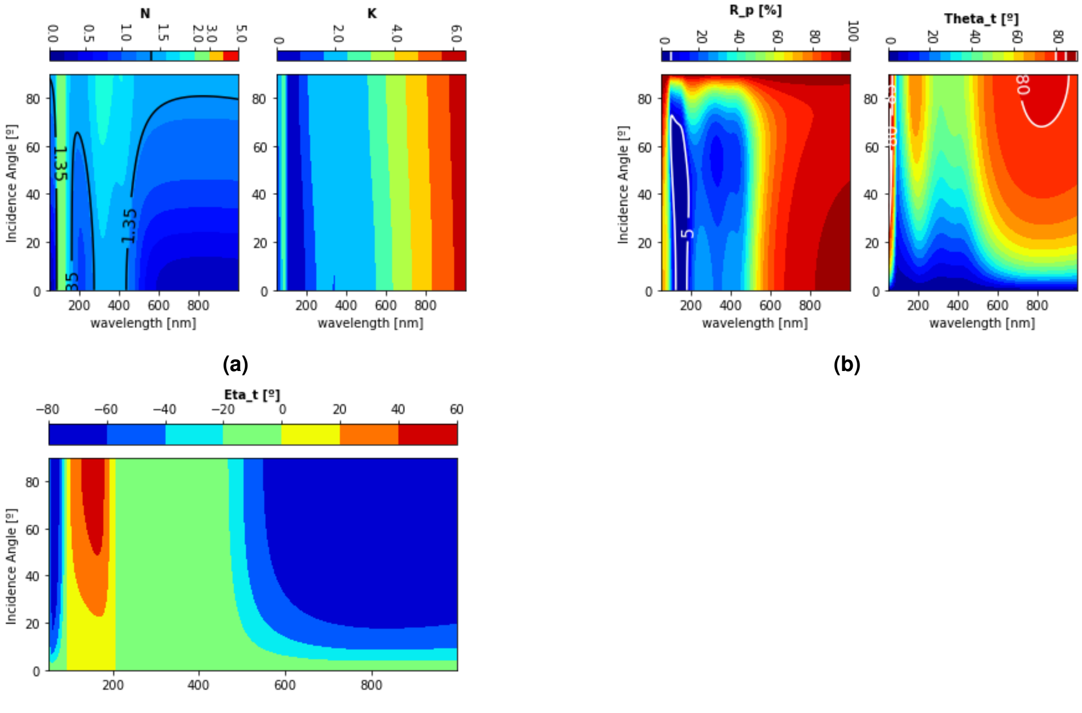

(a)

(b)

(c)

Figure 4.12: Characterisation of the analyte-gold interface for a 1.35 refractive index analyte.

By analysing the $R_p(\lambda, \theta_i)$ values, it is verified that by increasing the refractive index, the resonance influence region tends to a narrow wavelength range but within a certain wavelength the R_p values tend to increase.

Positive values of η correspond to regular transmission and in contrast, negative angles suggest that power is transmitted to the 3rd quadrant of the incident plane instead of the 4th one. In this case, the material behaves as a plasma and its real part of the complex electrical permittivity has a negative value. Also, the fields have typically a huge decay. This is verified in the figures below where the negative angular values are consistent with the negative phases of the electrical permittivity values for each metal considering Rakic's model [53].

For a dielectric-metal interface where the dielectric is lossless and since $k_x = Nsin(\theta) + jKsin(\psi)$ and $k_z = Ncos(\theta) + jKcos(\psi)$ (normalised to the vacuum's value) and as $K_i = 0 \rightarrow \psi_t = 0$°, it is verified that the transmitted wavevector (normalised to the vacuum's value) is defined as $k_x = Nsin(\theta) \xrightarrow{\theta=90°} N$ and $k_z = Ncos(\theta) + jK \xrightarrow{\theta=90°} jK$. Then, the huge K_t value leads to the decaying of the field mainly along the z-direction (the wavevector has only the imaginary component) and the field phase is directed mainly along the x-axis, revealing the SPP evanescent wave. This fact leads to excellent but not perfect resonances. If they were perfect, the transmission may be regular, but in this case, it will generate a SPP, *i.e.*, the wave is evanescent with a high parallel component.

Since $k_x = Nsin(\theta) + jKsin(\psi)$ and $k_z = Ncos(\theta) + jKcos(\psi)$ and $\psi = 0$°, it is verified that the transmitted wavevector is defined as $k_x = Nsin(\theta) \xrightarrow{\theta=90°} N$ and $k_z = Ncos(\theta) + jK \xrightarrow{\theta=90°} K$. Then, the phase of the wavevector component orthogonal to the surface, δ_{k_z}, is highly dependent on K. For low values of K, the phase of k_z tends to zero, otherwise, it increases for high K. If $\delta_{k_z}\delta_\epsilon < -1$, then η has negative value. Since δ_{k_z} is mostly a positive value, it acts just as a weight for the phase of the electrical permittivity δ_ϵ since the mathematical signal of this material property varies in the analysis range.

Similarly, in figures 4.13a to 4.15c are the silver values.

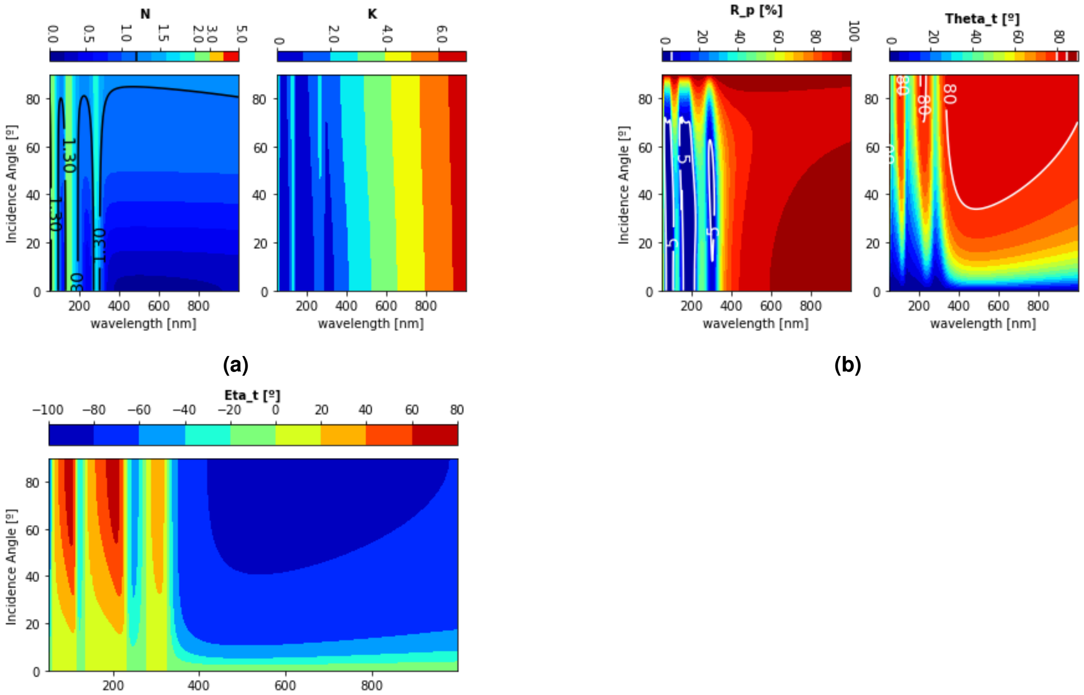

(a)

(b)

(c)

Figure 4.13: Characterisation of the analyte-silver interface for a 1.30 refractive index analyte.

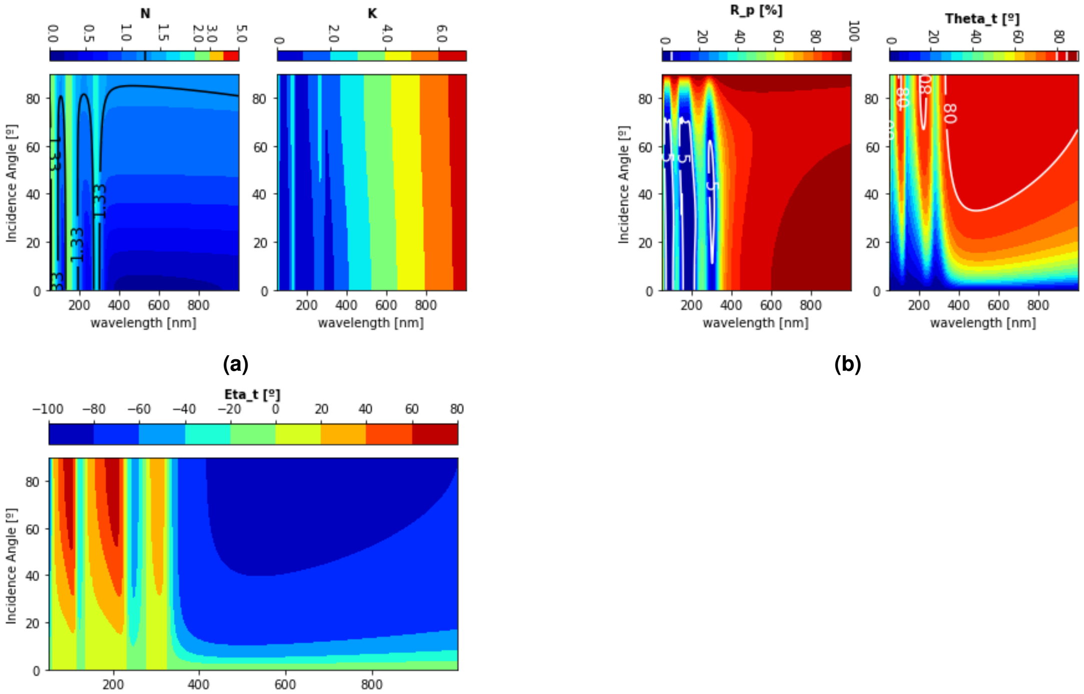

(a)

(b)

(c)

Figure 4.14: Characterisation of the analyte-silver interface for a 1.33 refractive index analyte.

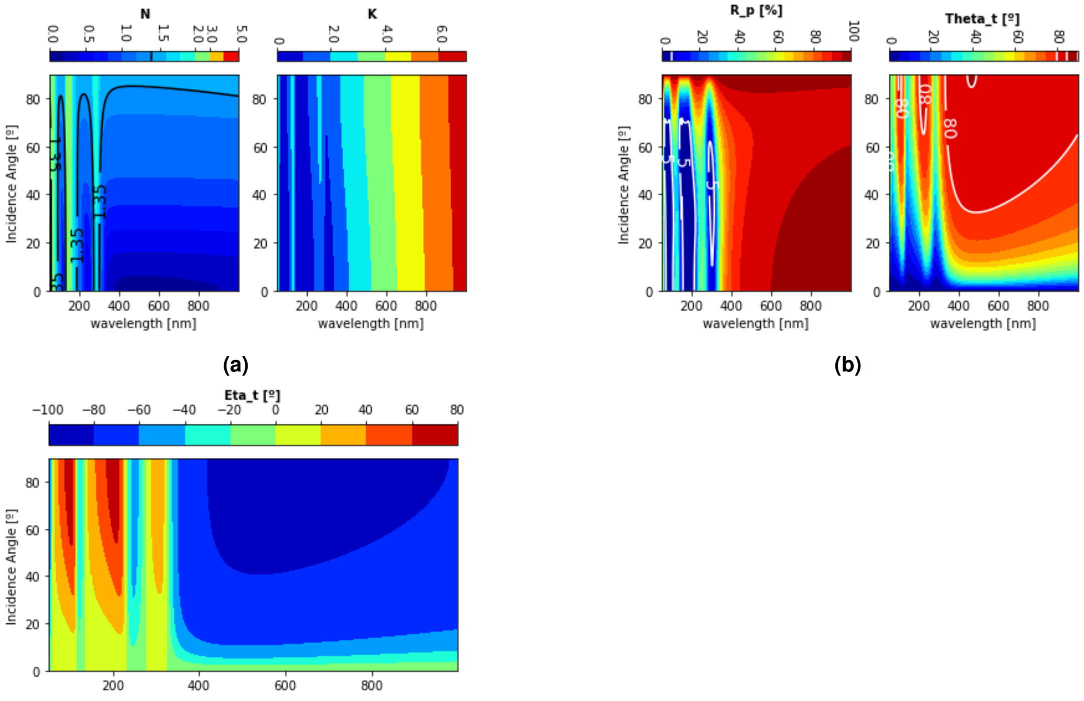

(a)

(b)

(c)

Figure 4.15: Characterisation of the analyte-silver interface for a 1.35 refractive index analyte.

4.3 Geometry Selection

The proposed device is a metallic nanoantenna on top of a quartz substrate. Also, the analyte is placed on top of it. Figure 4.16 illustrates it as well as the emitter and target positions. The quartz optical properties are modelled by Gao's model, where the metals' refractive index is characterised by Rakic's Drude-Lorentz model [53]. The geometric parameters of the device are presented in table 4.3.

According to recent studies, ”below 10–20 nm, the classical theory deteriorates progressively due to its neglect of quantum effects such as nonlocality, electronic spill-out, and Landau damping” [82]. Thus, the materials' characterisation by the complex electrical permittivity remains valid, since there are significant metal atoms. For instance, the gold atom has a dimension of 0.146 nm and silver's has 0.144 nm. Also, the metals' structures have a lattice constant of about 0.407 nm, and 0.409 nm, for gold and silver respectively.

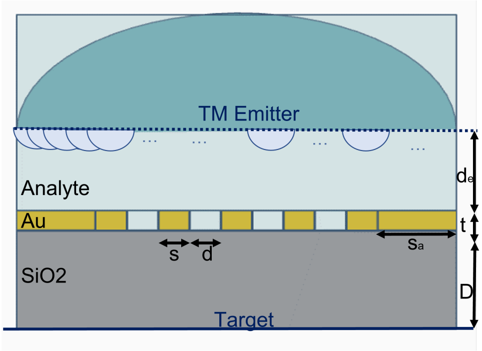

Figure 4.16: Nanoantenna illustration.

Table 4.3: Geometric parameters.

Symbol	Definition	Value [nm]
d_e	Emitter-Nanoantenna Distance	155
s	Slit Size	155
d	Metal Size	155
s_a	Metal extension	1000
t	Nanoantenna Thickness	30
D	Nanoantenna-Target Distance	1550

The results presented in chapter 3 are considered to size the nanoantennas thickness, due to the propagation depth of the evanescent waves excited in the metal. As presented in table 4.3 and ensuring the limitation stated in the previous paragraph, the nanoantenna's thickness is settled as 30 nm.

An intermediate study is performed to define the other dimensions. A gold nanoantenna without metal extension with 7 slits and 30 nm of thickness is considered on top of quartz. Also, one uses an analyte with a refractive index of 1.33 at 350 nm (within the gold's resonance). A slit size sweep is performed to evaluate the number of detected photons, the number of EOT photons and the number of photons absorbed in metal. Keeping the nanoantenna's periodicity at 310 nm, the slit size is varied, meaning that the larger the slit the narrow the metal.

As verified in figure 4.17, the number of detected photons increases by increasing the slit size. Since metal becomes smaller, the number of detected photons that pass through the metal decreases. The same is verified in the absorbed photons. Figure 4.18 presents the light patterns.

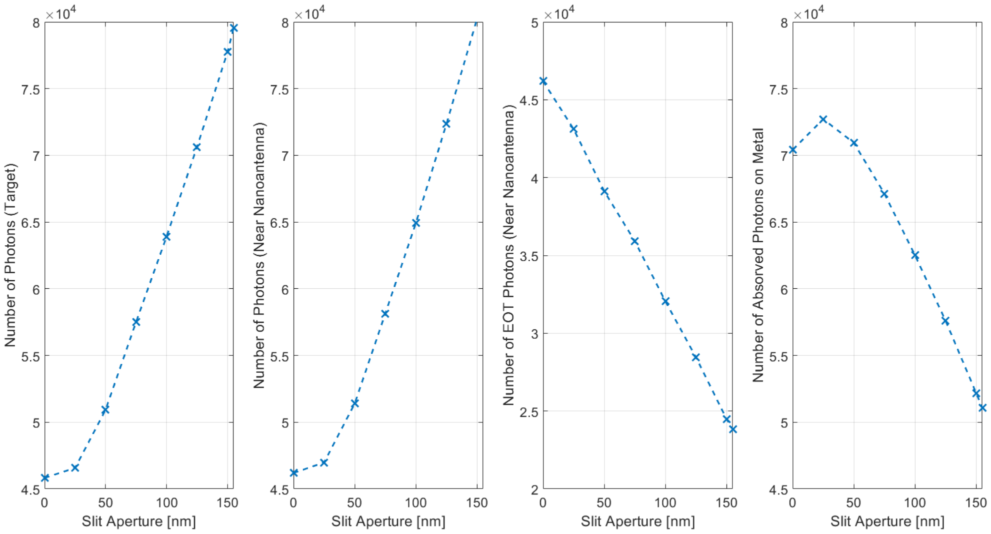

Figure 4.17: Detected photons in function of the size of the slits (considering $s_a = 0$ nm).

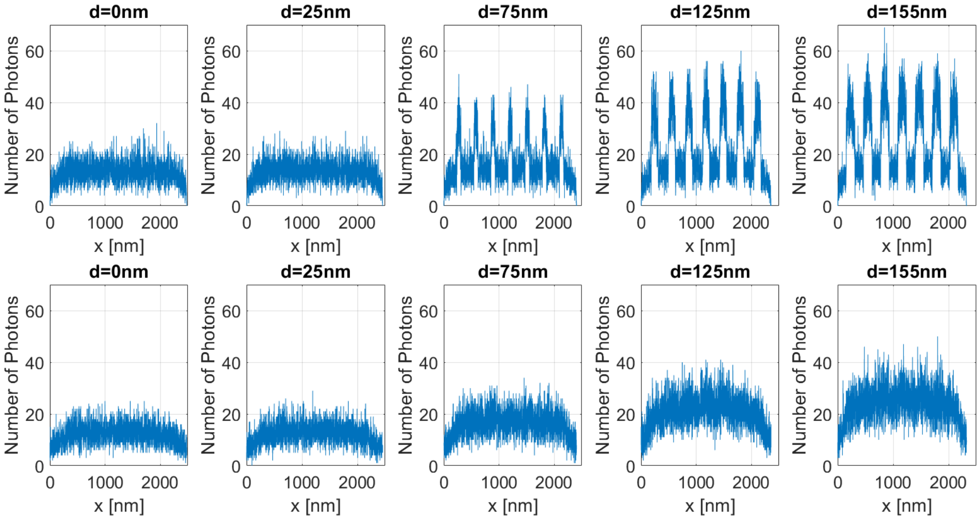

Figure 4.18: Light patterns in function of the size of the slits (considering $s_a = 0$ nm). In the first row are the patterns near the nanoantenna whereas in the second are the ones at D.

Although the periodicity and the metal extension are identical to Ebbesen's ones, the metal extension is added for four different proposes: (i) to increase the number of EOT photons for the same amount of photons that pass the slit; (ii) to create a "shadow zone" as discussed before; (iii) to ensure the physical realisation of the proposed device; (iv) to adjust light patterns on the target and increase concentration. Also, this periodicity value ensures that the analysed metal sizes are within the limitation imposed by the use of electrical permittivity to characterise metals.

Focusing on the first proposal, the increase of EOT photons allows to have an identical number of photons that passes by the slit and through the metal in regions where the resonance is weak (around 600 nm in the gold case). Thus, in this spectral region, there continue to be variations due to the EOT (the device may have a non-null sensitivity). Without this metal extension, the device sensitivity may be null at above 600 nm. An extension of 1000 nm is added to reach this goal. Furthermore, the 155 nm slit size is chosen to have a great trade-off between output optical power and obtained light pattern. The selection of a smaller slit leads also to the choice of a smaller metal extension to fulfil the previous objective. However, the final output optical power is lower than the proposed one, without improving sensitivities. Then, this option may lead to the possibility of having an output optical signal that should be amplified before being analysed, which is an expensive solution and a false device miniaturisation. On top of this, the slit size is also within the definition of short-antenna discussed in section 2.5. Also, according to the definitions in that section, the target distance and the number of slits (4) are settled to have photons concentration in Fresnel Diffraction Zone.

The emitter distance to the nanoantenna is settled in accordance with the average number of emitted photons to ensure the emulation of a TM plane wave.

Considering a gold nanoantenna, it is possible to prove the achievement of this geometry sizing goal based on figure 4.19. From this figure, it is possible to verify that the magnitude of the number of photons transmitted by the metal and by the slit is identical, considering the proposed metal extension. Also, it is concluded that the number of detected photons is highly dependent on the photons that pass through the metal, namely in the resonant wavelengths (between 250 nm and 500 nm).

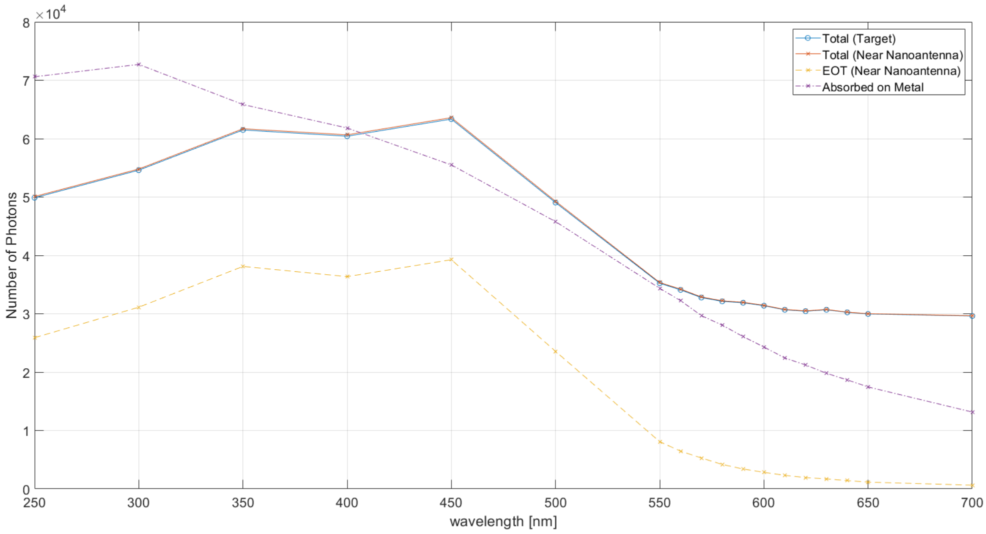

Figure 4.19: Number of detected and absorbed photons in function of the wavelength.

4.4 Metals' Influence on the Plasmonic Nanoantennas' Optical Response for Sensing Applications

The results are taken by emitting photons in just one time stamp, like a Dirac excitation in time. Shifting in time the device's optical response several times and summing them in the same temporal reference, the optical response for a long pulse is produced.

A new methodology approach is used to describe the steady-state response of the device. This regime is reached when emitting a long pulse. Since time is discrete in the implemented model, the pulse is generated as a Dirac comb, where the time distance between pulses is minimal compared with the time response of the material. Thus, the pulse response is the sum of time-domain responses shifted in time. For each emitted Dirac, the response is assumed to be the same and the long pulse response is the sum of all the Diracs' responses shifted accordingly to its emission time.

The device is tested considering a long pulse emission (33 fs) emulated by considering a Dirac comb. Then, one may consider the response for the Dirac excitation and sum each of the 10 000 shifts.

These processes are carried out for different wavelengths to perform spectral analysis. 10 different wavelengths are selected, between 250 nm and 700nm, with a step of 50 nm.

4.4.1 Results

First, the optical response for a Dirac is determined for each metal. Figures 4.20 and 4.21 show respectively the computed response for the gold and silver nanoantennas, respectively, for a subset of the considered wavelengths [83].

Analysing these responses, a first peak is observed due to the radiation that passes directly through the slit, meaning the metal has low influence. It occurs at different time stamps due to the propagation velocity in the analyte.

The main difference among these responses is observed after that, which is related to the photons that pass through the metal. The propagation velocity in the metal is lower in comparison with the analyte and substrate ones. Thus, after the first peak, a new one will appear. This peak corresponds to the radiation that passes on the metal and that reaches it with a small incident angle. The other incident angles will produce different optical paths that have different transmission probabilities and high optical lengths. Thus, the device response presents a kind of tail [83].

The silver response presents a lower number of photons that pass through the metal in comparison with the gold one. This is because the analyte-metal reflection coefficient is higher in silver than in gold. Furthermore, the first peak is more intense in silver, followed by the platinum and gold responses. Photons that pass directly through the slit may have different optical paths: reach the substrate interface or any vertical interface with the nanoantenna. The firsts have a similar influence in the analysed devices (metal does not influence), but the others that reach an interface may be reflected to the slit and substrate or be transmitted to the metal. Thus, the higher the analyte-metal reflection coefficient, the higher the first peak intensity. Considering the same analyses, the higher the analyte-metal reflection coefficient, the lower the number of photons that may be transmitted through the metal.

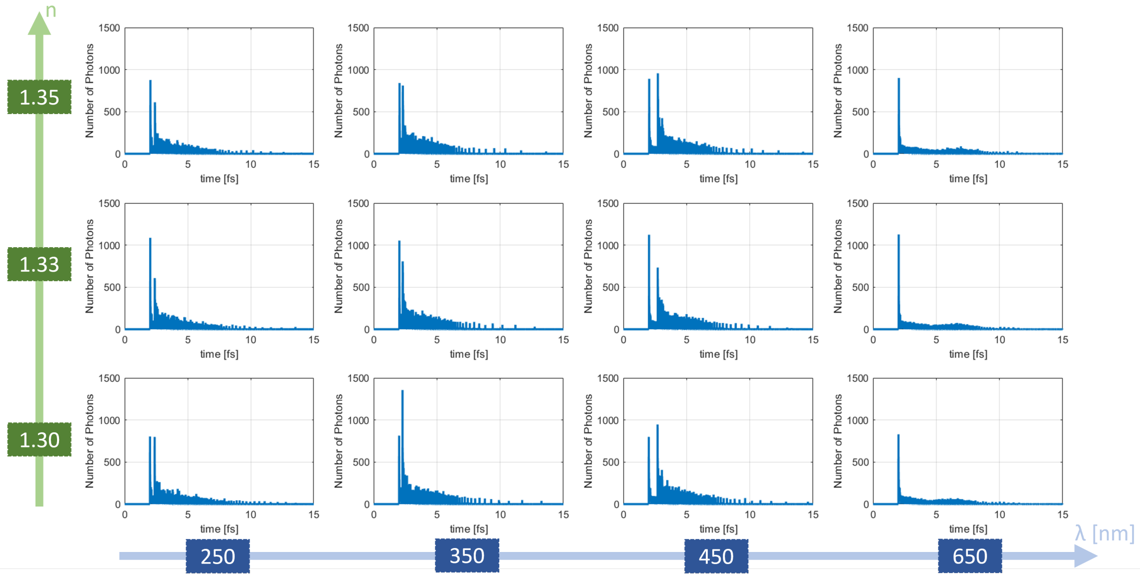

Figure 4.20: Time response of a gold nanoantenna for different analyte's refractive index and considering a Dirac excitation.

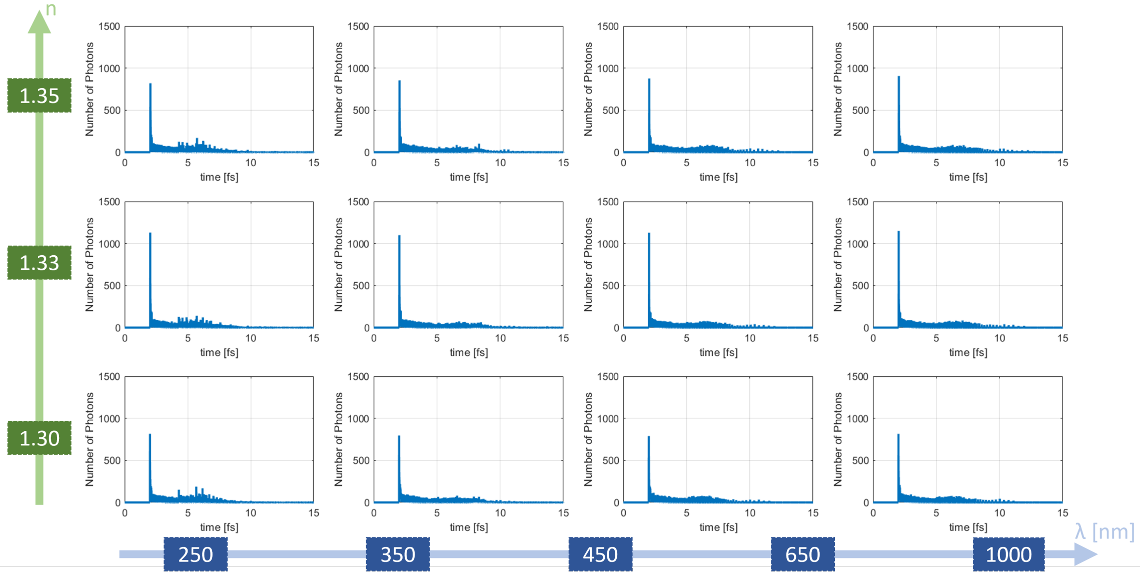

Figure 4.21: Time response of a silver nanoantenna for different analyte's refractive index and considering a Dirac excitation.

The used time scale for the Dirac excitation is at attoseconds orders. This is within the state-of-the-art devices. A perfect example is ‘The Nobel Prize in Physics 2023’, given to Pierre Agostini, Ferenc Krausz and Anne L’Huillier “for experimental methods that generate attosecond pulses of light for the study of electron dynamics in matter” [84]. In 2008, an 80 as pulse was reported [32]. However, today, this state-of-the-art technology may not be easily available. For that reason, a longer pulse emission must be considered: at femtoseconds orders. Then, the sensor can be designed manufactured, tested and commercialised. Since the discretisation of the long pulse is a Dirac comb, the results of the Dirac excitation are used to model the long pulse optical response.

In figure 4.22 are the obtained pulse responses for a 33 fs emission. It is verified that the number of photons that reach the target depends on the selected metal and incident wavelength. Although this figure is normalised to the maximum number of photons, which is obtained with silver at 300 nm, it is also observed that the number of photons at the target changes by varying the analyte’s refractive index. Although this variation is high considering the imposed stimuli, the curves’ normalisation to the silver’s maxima leads to the illusion that for each metal all are superposed [83].

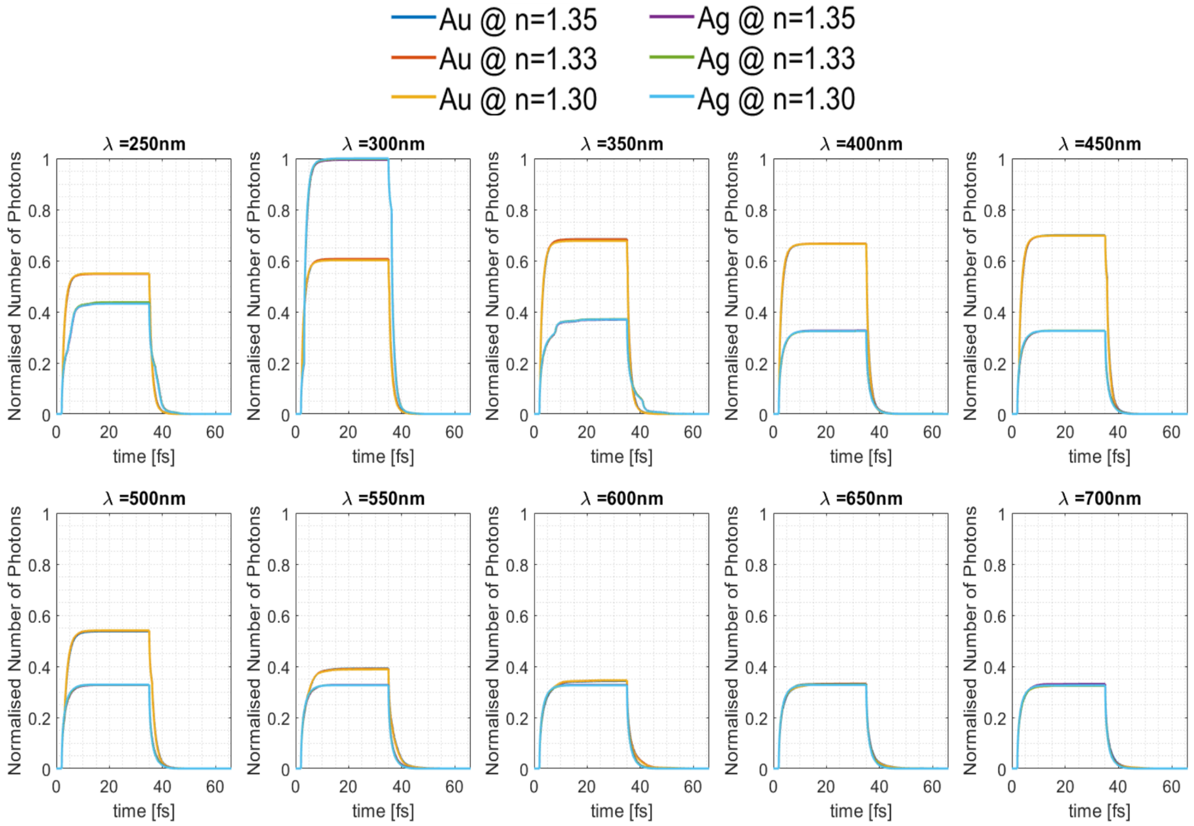

Figure 4.22: Step response for different metallic nanoantennas and considering different analyte’s refractive index.

The device’s optical response is a first-order system response. Although there are some fluctuations the response stabilises within a 10% band, without overshoots and after a certain time interval. The fluctuations are mainly due to the emission photon distribution (Poissonian distribution) and due to the different probabilities on dielectric-metal and metal-dielectric interfaces.

Since it is a first-order system response, the maximum intensity is considered as the steady-state value and the fluctuations are treated as noise. In this case, noise is mainly due to the stochastic photon distribution in the emitter as well as interface probabilities.

Thus, the settling time is defined as the time stamp for which the optical responses stabilise within a 10% band of the steady-state value. Also, the rise time is computed as the time interval between 10% and 90% of the steady-state value (rising period), whereas the fall time corresponds to the interval between 90% and 10% of that value (falling period). In these results, both present the same values and, consequently, they are merged in the same graphic. Moreover, it also presented the maximum intensity time, which is the first time stamp in which the optical response reaches its maximum value [83].

Figure 4.23 presents the results of these time quantities in function of the incident wavelength, for each metal-analyte combination. First, it is evident that each material has different time variations.

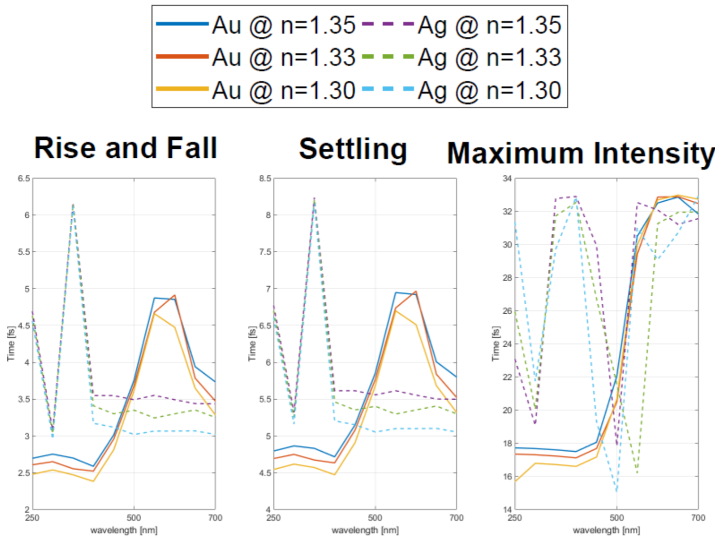

Figure 4.23: Rise, fall, settling and maximum time for different metallic nanoantennas and analytes.

Gold reveals fast rising and falling periods within the influence region of SPP resonances (250-500 nm). Also, in this region, the analyte's refractive index variation has a small influence on the rise and fall time. This is due to the propagation velocity inside gold, which is quite higher in comparison with the analyte's. Thus, since most of the photons that reach the target propagate in gold, the rise and fall time is highly dependent on that. In contrast, for higher wavelengths, the rise and fall time does not depend on the gold's propagation velocity, consequently, it varies with the analyte's refractive index. That variation is constant as shown for 650 nm and 700 nm. These causes also influence settling time. As the rise time is calculated from 10% to 90%, the response resembles that of a 1st order system and the settling time is determined between 90% and 100% of the maximum value, so the settling time is related to the rise and fall time. In other words, as soon as the response reaches 90% of its maximum value, it enters the 10% band and, consequently, the settling time is determined. It is also this instant that is used to determine the rise time. The same is true for the fall. So not only for gold, but for all the other metals tested, the shape of the graph is the same. There is only an offset of approximately 2 fs (the right value has a small variation with the wavelength and used metal). Based on the previously explained, this value is the time stamp for which the response reaches 10% of its maximum value. Moreover, the maximum intensity reached with the gold device is the time of Dirac's analysis, except in the resonance influence region, where the value is approximately half of it. The analysis of the Dirac excitation is done with a 33 fs frame, meaning that if some fluctuations appear at the end of this time interval (figure 4.20), they will influence the maximum intensity and the steady state. Even though, the response must reach the state-state has been verified in these results [83].

Similar results are obtained for silver. However, since the propagation velocity in silver is lower than the analytes' and gold's, the device has higher rise and fall times in the resonance region (near 300 nm).

Considering the steady-state values, spectra are traced. Figure 4.24 shows the obtained spectra for the different metallic devices, normalised to the maximum intensity value that is computed for the silver device at 300 nm. These results also corroborate the fact that in the influence region of SPP resonances, the intensity in the target can reach more than twice the intensity in the near-infrared region. Moreover, it is verified not only that gold is more sensible than silver but also that the sensing occurs for a wide range of wavelengths. Furthermore, the EOT effect allows us to have a stronger optical signal at the output. Then, for instance, a variation of 1% at the output in EOT wavelengths is more detectable than without EOT as well as it may require less extra equipment, such as optical amplifiers.

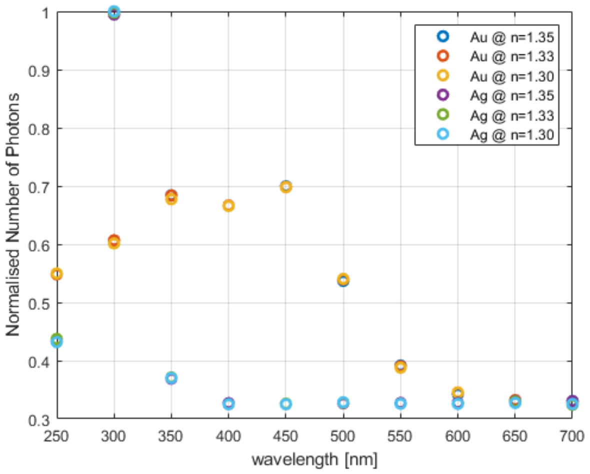

Figure 4.24: Metallic nanoantennas spectra for different analyte's refractive index.

4.4.2 Discussion

Table 4.4 presents the metal's complex refractive index, $\bar{n} = n + j\kappa$, for the considered wavelengths. It is verified that the real part of the gold's refractive index takes values near the range 1.30-1.35 from 250 nm to 450 nm, namely around 400-450 nm. Considering the generalised reflection coefficient, it is possible to verify that in these conditions, reflection decreases and radiation is transmitted in the dielectric-metal interface. Also, having a non-neglectable refractive index imaginary part, the radiation transmitted into the metal is evanescent and has an exponential decay. It is also verified in the silver device at 300 nm, which has a small contrast with the analysed analytes, meaning that the output power should be the highest [83].

Table 4.4: Metals' complex refractive index [53].

	Gold		Silver	
λ [nm]	n	κ	n	κ
250	1.1132	1.5658	0.46651	1.2453
300	1.5199	1.6783	1.3733	0.66320
350	1.4877	1.6008	0.27898	1.1458
400	1.4094	1.7448	0.15804	1.8270
450	1.2529	1.6787	0.13617	2.3280
500	0.78714	1.8971	0.13210	2.7657
550	0.49785	2.3703	0.13425	3.1722
600	0.36216	2.8493	0.13936	3.5604
650	0.29364	3.2964	0.14623	3.9367
700	0.25701	3.7175	0.15433	4.3046
1000	0.25573	5.9864	0.21961	6.4251

Although this analysis can be carried out considering the variables n and κ, it is only a first approach. The correct approach is to use the reflectance coefficient expressed in 3.14, as explained before since they take into account N and K which describe better the wavevector in the metal layer.

The metal with the best resonance is silver, near 300 nm. Gold is the one with a wider resonance range, in contrast with silver which is the most selective material [83].

It is also important to note that in performed simulations the emitted is composed of 250 point sources, each one emitting one photon on average, considering a Poissonian distribution, per degree. This means that a wide range of incident angles reach the nanoantenas's interfaces. Thus, it is also important to have a great wavevector match in a wide angular range (even if it does not lead to a perfect resonance).

These sensors mainly work at the visible spectral region (non-invasive radiation) and they can monitor in-vivo and in-vitro variations in femtoseconds and in real-time analysis, which is within the state-of-the-art technology. For these reasons, sensors based on nanoantennas have a very wide application range [83].

4.5 Gold Nanoantenna to Detect a Refractive Index Variation of 1.30-1.41

This work aims to verify the possibility of using visible radiation, which is non-invasive, to detect variations in biological analytes. To reach that, the research aims to analyse if the EOT effect allows better sensing. However, based on the analysis done for Kretschmann's structure, it is already verified that, in this spectral range, intensity variations are not high considering the proposed refractive index variations (around 1%). For that reason, the proposed methodology in the time domain will be used to characterise the analysed structure for biosensing [85].

Since the refractive index variations are around 1-2%, the intensity variations will also be around those values. Then, the first step is to characterise the stochastic variations of the proposed model. These variations reveal the expected fluctuations (noise) in experiments [85].

Considering the previous analysis on the gold resonances, it is possible to state that the highest fluctuations are for wavelengths as 350 nm. This is due to the fact that the resonance there is not high enough to pass all the photons through the metal (for instance at 450 nm) or to reflect all the photons [85]. Then, since the R_p coefficient takes intermediary values, the stochastic phenomena will be more evidenced and consequently, fluctuations will occur.

These fluctuations are not only verified at the interfaces. The emission fluctuations should also count for this analysis since the emitter is considered stochastic following a Poissonian distribution.

Figures 4.25 and 4.26 show the number of emitted and detected photons for 6 different runs, for 350 nm and 550 nm respectively and an analyte's refractive index of 1.33.

These figures suggest that fluctuations for 5 runs, one may verify a maximum deviation of around 0.4% referenced to the average value. This number of runs and the obtained deviation are going to be used for the subsequent analysis. Furthermore, this is a constraint to the limit of detection. In other words, this is the minimum limit of detection that these devices must have since it is determined by the stochastic behaviour of light that must be always considered [85].

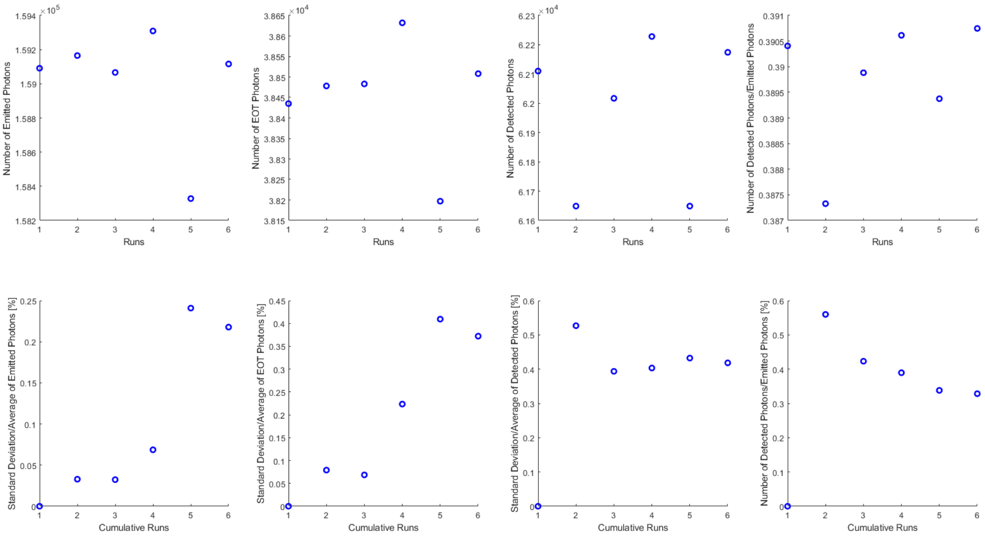

Figure 4.25: Fluctuations due to stochastic processes in the emitter and radiation-matter interactions for 350 nm.

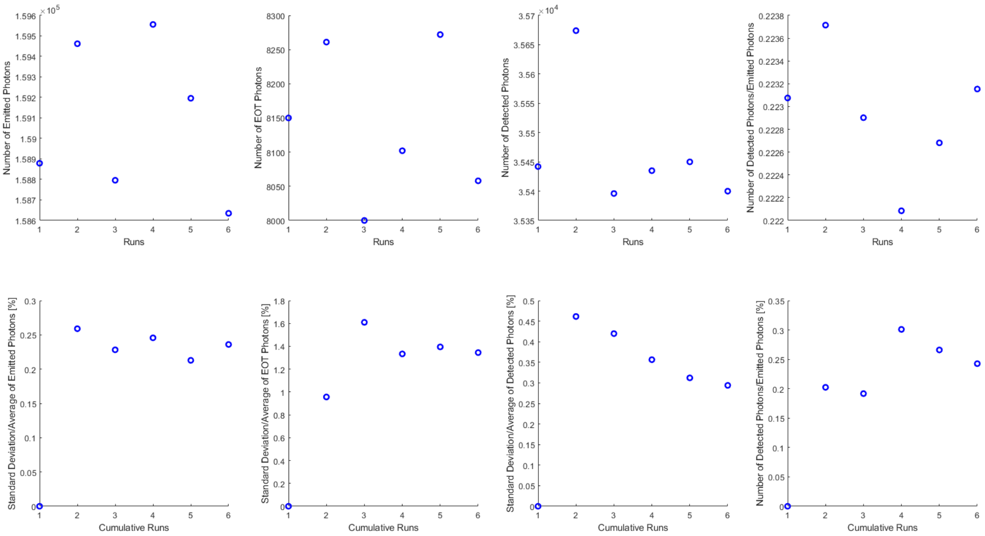

Figure 4.26: Fluctuations due to stochastic processes in the emitter and radiation-matter interactions for 550 nm.

For five runs, the average step response for different analytes and wavelengths is presented in figure 4.27.

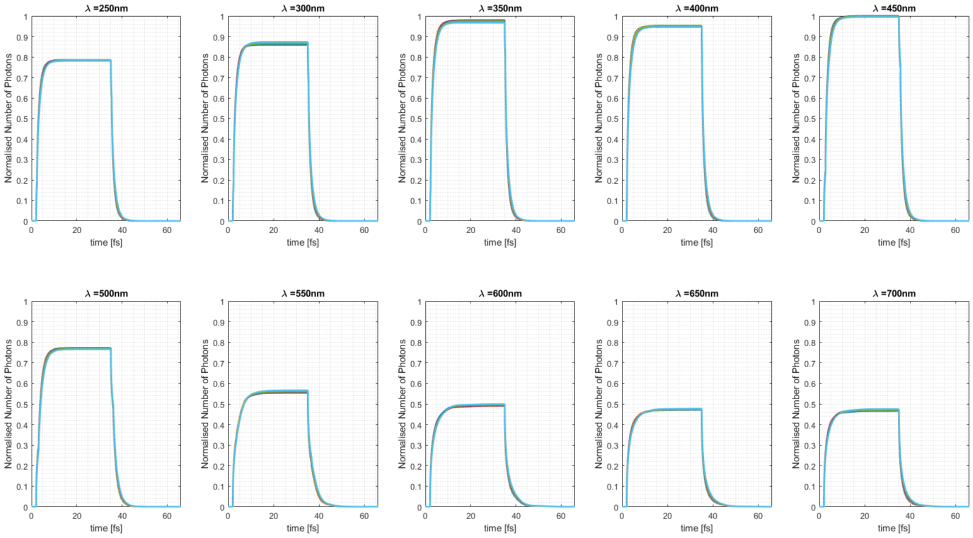

Figure 4.27: Step response for different analyte's refractive index and wavelengths.

From the previous figure, one may note variations in rise and fall, settling and maximum intensity times. As already discussed, and verified in figure 4.28 the rise and fall times take not only the same shape but also the same values. Also, settling time has the same shape as the rise and fall time, differing by around 2.05 fs, which is the time took till the response reached 10%.

High refractive index leads to low velocity in the analyte and substrate, whereas in metal it will depend on the incident angle and wavelength. Generally, the propagation velocity in metal rises with the wavelength [85].

As verified from this figure, analytes may be differentiated by analysing the results in figure 4.27, namely the rise, fall and settling time. Considering these quantities, it is verified that until around 400 nm, the response varies according to the radiation propagation time difference in the analyte. This is due to the fact that the metal transmits more photons than the slits [85].

After around 400 nm, there are three different regions. The first is where the response time has a linear relation to the wavelength (from 400 nm to 550 nm). This is due to the fact that the metal refractive index decreases and consequently, the number of photons that pass to the metal starts to decrease but they are also less absorbed by the metal and they have a low probability of being transmitted both for the analyte and the substrate. Then, the number of detected photons starts to decrease but they leave the metal in more high time stamps. This behaviour is verified until around 550 nm, when an inflection starts to occur. There, the number of photons transmitted through the metal starts to be equal to the one transmitted by the slit and consequently, the response times start to inflect. This is only due to the fact that one designed the structure to have similar values in this wavelength region, as stated in section 4.3. To increase precision, the number of wavelengths is increased near the maximum. A step of 10 nm (instead of 50 nm) is adopted between 500 nm and 600 nm. The results are presented in figure 4.29. After that, at 700 nm the response tends to the other region, where no photon is transmitted through the metal and consequently, the response time is only due to the analyte-substrate interfaces [85].

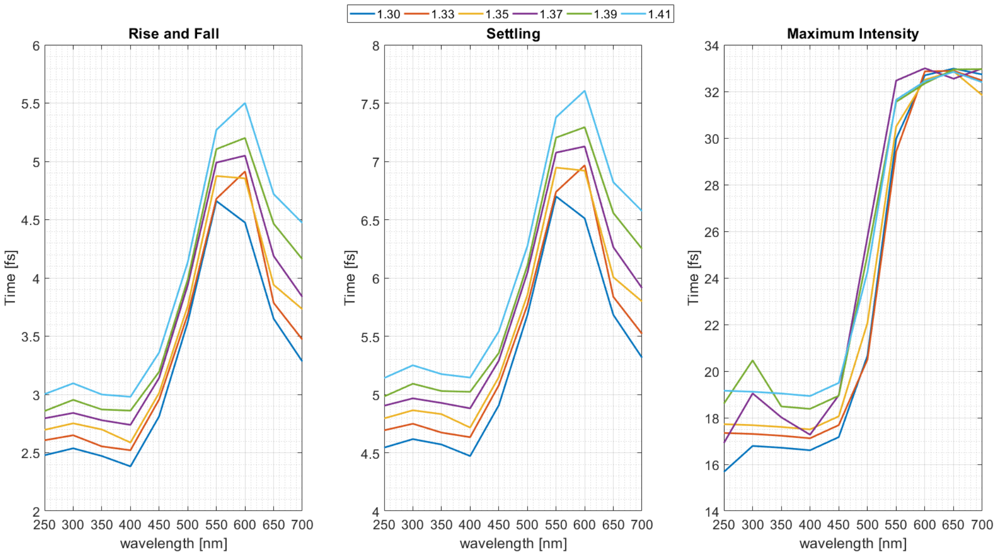

Figure 4.28: Rise, fall, settling and maximum time for analytes.

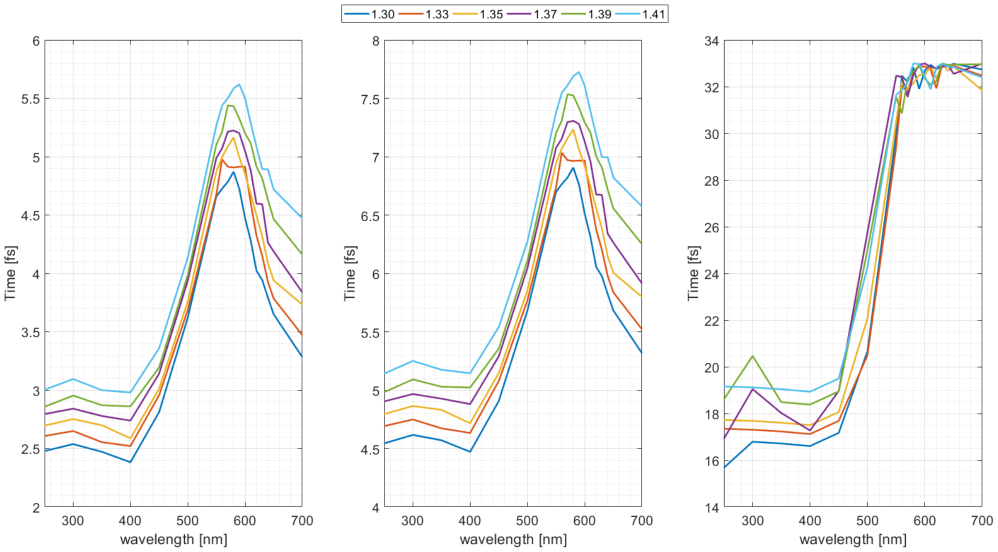

Figure 4.29: Rise, fall, settling and maximum time for analytes (increased precision near the maximum).

Looking at the previous figure, one may differentiate the analyte by just analysing the time and compare to the others.

For instance, considering a resonant wavelength it is possible to differentiate these analytes (variations around 1%) by a time variation around 3% at 500 nm and about 5% at 400 nm.

However, this direct measure may not be as accurate as wanted. Then, other options are added.

The first is the variation of the middle point on the time-wavelength linear region for each analyte. As already stated, this region depends on the analyte-gold resonances. Since they vary, the middle point will also vary. It is computed by analysing the wavelength for which the rise, fall or settling times are half the difference between the maximum and minimum. The minimum value differences depend mainly on the radiation propagation in the analyte. The maximum value depends on the propagation difference between the radiation propagation in the metal and the analyte in the slits [85].

Figure 4.30 presents the sensitivity of this middle-point time with the analyte's refractive index considering different samples as references. Based on this figure, it is possible to verify that the resonance influence region is decreasing with the increase of the analyte's refractive index. In other words, the analyte-gold reflection probability is increasing with the analyte's refractive index. This behaviour is corroborated by the analysis done in the analyte-gold interface analysis [85].

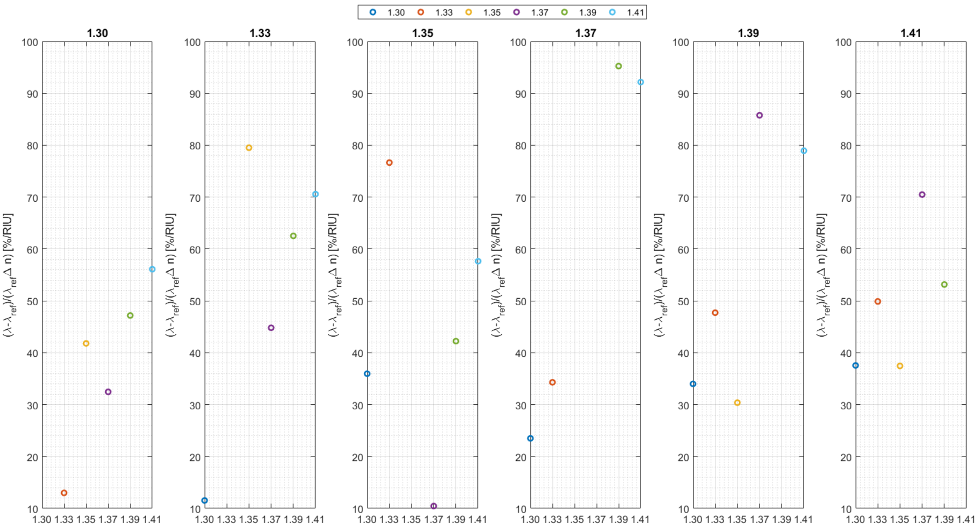

Figure 4.30: Device sensitivity considering the middle-point variation.

Also, it is verified that the higher the refractive index the wider is the region near the maximum rise, fall and settling time. This is due to the difference between the propagation velocity in the metal (that depends on the surrounding media) and the velocity in the analyte. Thus, a new figure of merit is defined considering the 90% width referenced to the time maxima. Sensitivities presented in the figure suggest an accurate work as a sensor, mainly for identical analytes [85].

The higher the refractive index the narrower the widths. This analysis reveals more sensible than the one from the middle point. This is due to the fact that the width depends on the number of photons that passes both by the slit and through the metal. This means that the lower the percentage reference the lower the sensitivity, before saturate [85].

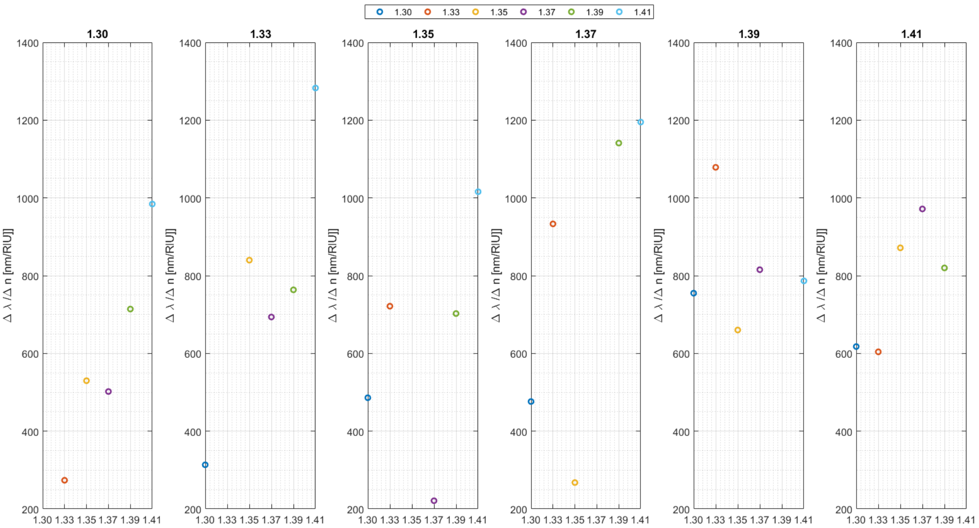

Figure 4.31: Values of the 90% width referenced to the time maxima.

Also, to complement this analysis one may also check the possibility of detecting variation based on the intensity variations. In figure 4.32 are the obtained sensitivities for 5 random runs. Once again, it is possible to state that it has a higher variation where the analyte-gold resonance varies more, namely around 350 nm and 600 nm [85].

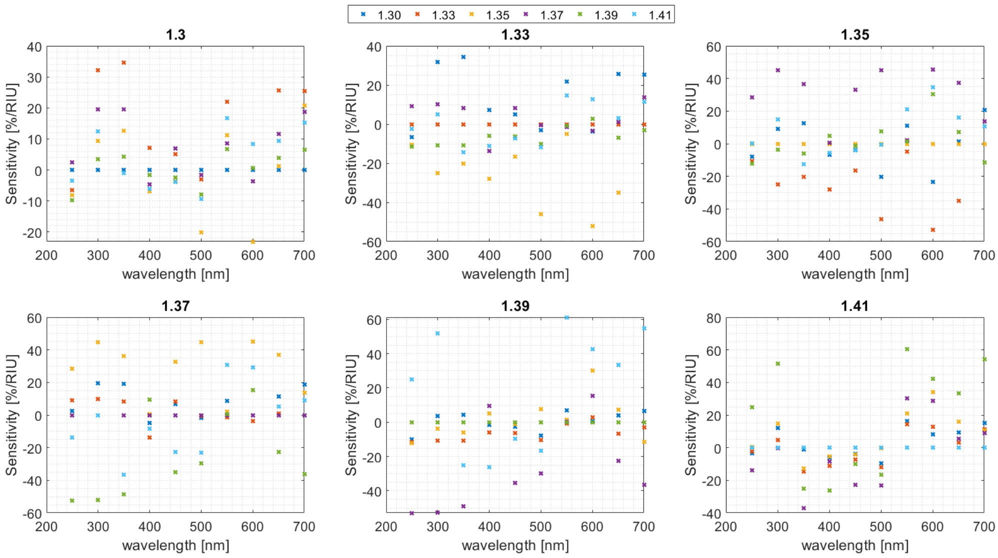

Figure 4.32: Obtained sensitivities for the different analytes' refractive index.

It is already expected that for low analyte-gold R_p and where it has a low variation the sensitivity decreases. Also, that variation should not be enough to verify enough variation in the output. Then, if one establishes as zero the sensitivities values that are within the standard deviation due to fluctuations, figure 4.33 is obtained. These are the stimuli that are definitely detectable, being above the limit of detection. There, it is possible to verify that near 350 nm and 600 nm the samples are differentiable by analysing the average output of only 5 pulses responses [85].

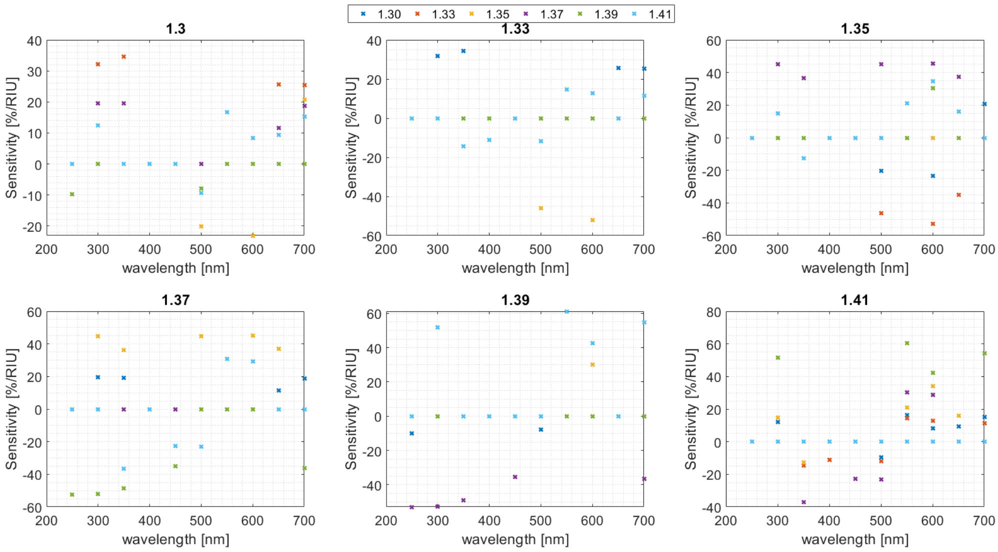

Figure 4.33: Obtained sensitivities for the different analytes' refractive index, considering the ones higher than the fluctuations.

This is an ultrafast sensor. Note that since the response denotes a first-order system and it is stabilised after 4.5 fs to 8 fs depending on the wavelength, one may use a 33fs emission as presented, but one also may use for instance an emission of seconds. For example, if one excites 10^{21} photons per second, considering these sensitivities, it is possible to obtain a difference signal between samples of $10^{18} - 10^{19}$ photons per second. These magnitudes are both possible to be emitted and detected with commercial devices as previously stated. On top of that, the femtoseconds analysis has been the subject of many studies and prototypes. Innovative technology in this time scale is being proposed nowadays worldwide [85].

Since the analyte-gold and gold-substrate probabilities are different as well as the optical paths and velocities namely within the gold layer, the decaying of the "EOT tail" will be different considering different analytes. This means that although the number of detected photons is similar but differentiable in many cases, the time stamps they leave the metal differ more. Then, if one stops the emission before the responses are settled but after some EOT photons leave the metal, the intensity variations may increase [85].

Figure shows the cases where the output variation is higher than the double of the fluctuations, to have a detectable difference signal. By comparing figure 4.33 to figures 4.34 and 4.35, it is concluded not only that more analytes can be analysed but also that the output signal variation is higher. Furthermore, all the values are negative, meaning that the higher the refractive index, the higher the output intensity [85].

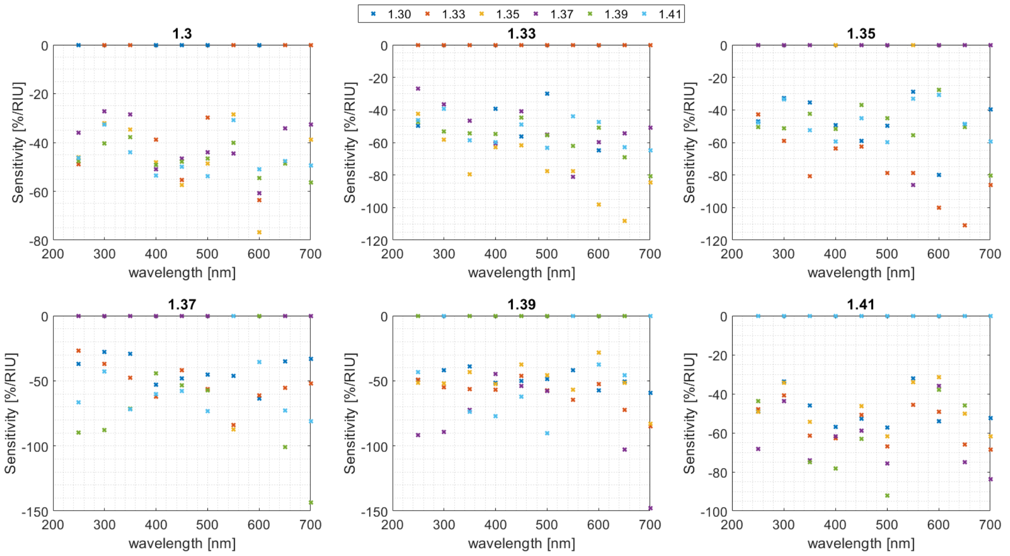

Figure 4.34: Obtained sensitivities for the different analytes' refractive index, considering the ones higher than the fluctuations for a pulse excitation of 2.3 fs.

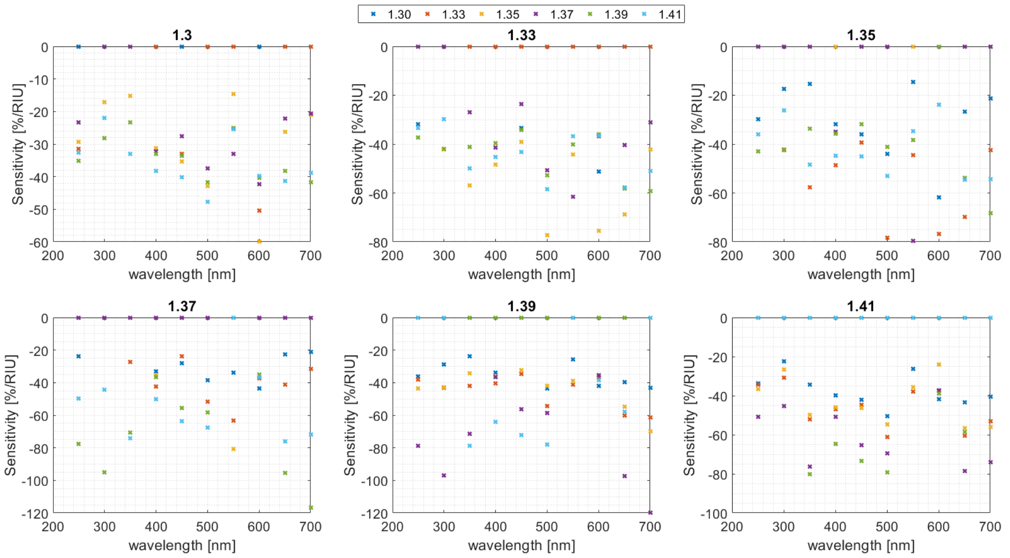

Figure 4.35: Obtained sensitivities for the different analytes' refractive index, considering the ones higher than the fluctuations for a pulse excitation of 3.3 fs.

Another important consideration is that by making combinations of the 18 tested wavelengths (from pairs until a group of 18) the device's sensitivity may increase. For these tests, all the combinations among the 18 wavelengths are tested. For each combination the Dirac responses of the selected wavelengths are sum. The pulse algorithm runs considering that new Dirac response. Output optical intensities are analysed as for a regular pulse excitation. Figure 4.36 shows the maximum sensitivity obtained to monitor the different refractive index variations considering different combinations [85].

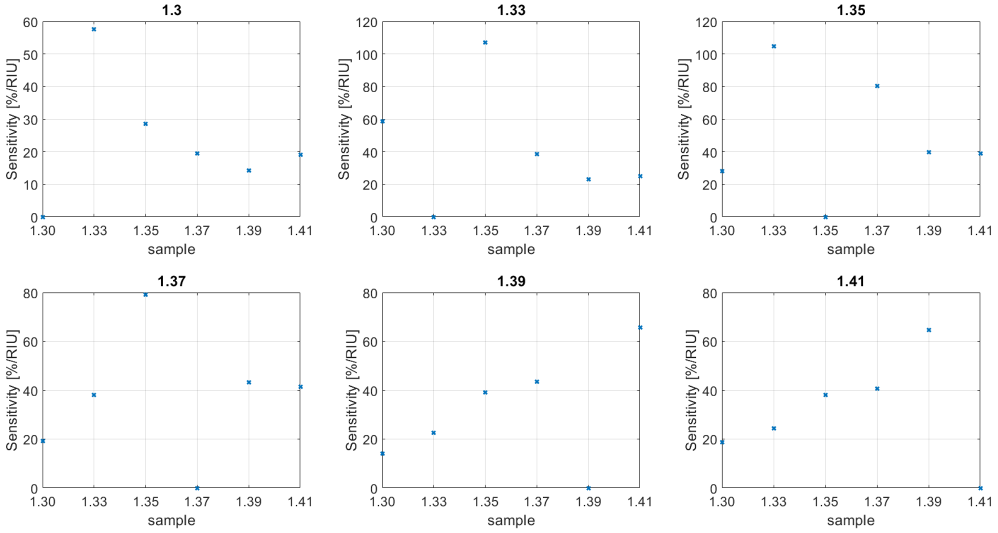

Figure 4.36: Maximum sensitivities for the different analytes' refractive index, considering the ones higher than the fluctuations for a pulse excitation of 33 fs.

4.6 Plasmonic Slit Nanoantenna as a High Sensitivity Tilt Sensor

Analysing the applications of nanoantennas, one verified that they may also work as tilt angle sensors. This kind of sensor is also important to have in some biosensor systems, mainly to obtain rotation data of the main system [15,83].

Figure 4.37 presents the new architecture of the designed model with the inclusion of the input variable m which is the inclination between the emitter and the nanoantenna. Referring to the figure, the greater the inclination the more all the cylindrical emitters tend to come together on the left side. By tilting the emitter, the cylindrical emitters keep the same distance among themselves but their horizontal coordinate tends to the same value [15,83].

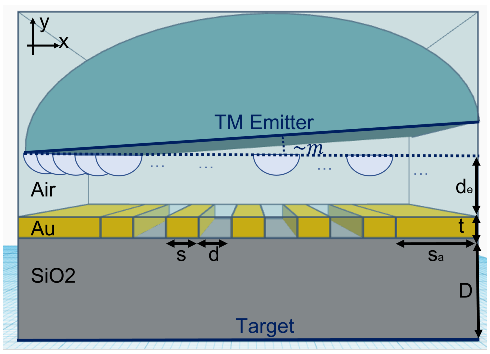

Figure 4.37: Scheme of the proposed nanostructure.

4.6.1 Results

The main aim of this research work is to analyse the pulse response of a four-slit nanoantenna, characterised in the above section. It is done in two different ways. First, the number of photons that reach the target is presented over time. After, the light pattern in the target is illustrated on two different time stamps [15,83].

The emitter tilt varies, assuming angles of $m = \{0; 0.5\pi/100; \pi/100; 2\pi/100; 4\pi/100; 10\pi/100\}\,rad = \{0; 0.9; 1.8; 3.6; 7.2; 18\}$ °. Two wavelengths (frequencies) are used: one at SPP resonances, 450 nm (visible spectral region), and the other at 1000 nm (near-infrared). The optical signal is computed on the target as illustrated in figure 3.33.

4.6.1.A Pulse Response

A huge Dirac pulse is expected as the result of the photons that pass directly through the slits with optical paths similar to the direct straight line between the emitter and the target. Moreover, other optical paths' directions reach directly the target, but at different time stamps. Some of them reach an interface having some probability of being transmitted or reflected [15,83].

At 1000 nm, it is expected that the metal reflects almost all the radiation, meaning that there is that huge Dirac pulse and others from the reflections of the photons in the vertical interfaces of the slits, illustrated in figure 3.33. These last ones have larger optical paths than the ones that reach directly the target and consequently, the result appears at high time stamps [15,83]. This is observed in figure 4.38, presented in blue for this incident wavelength.

On the other hand, at 450 nm there are optical resonances in the dielectric-metal interface, meaning that the photons have some probability of being transmitted to the metal. This probability is dependent on the incident angle [67], and at this wavelength, it has a large value. The main Dirac pulse at the response as well as some time stamps around it are equal to the ones obtained at 1000 nm since the photons do not interact with the metal. After a certain time interval associated with those optical paths, the extraordinary optical transmission effect is revealed. Many optical paths with a non-null probability of reaching the target appear, since there is a non-null probability of a certain photon being transmitted to the metal and re-transmitted to the dielectric after propagating on the metal without being absorbed. Consequently, an exponential tail appears on the response, as observed in figure 4.38 [15, 83].

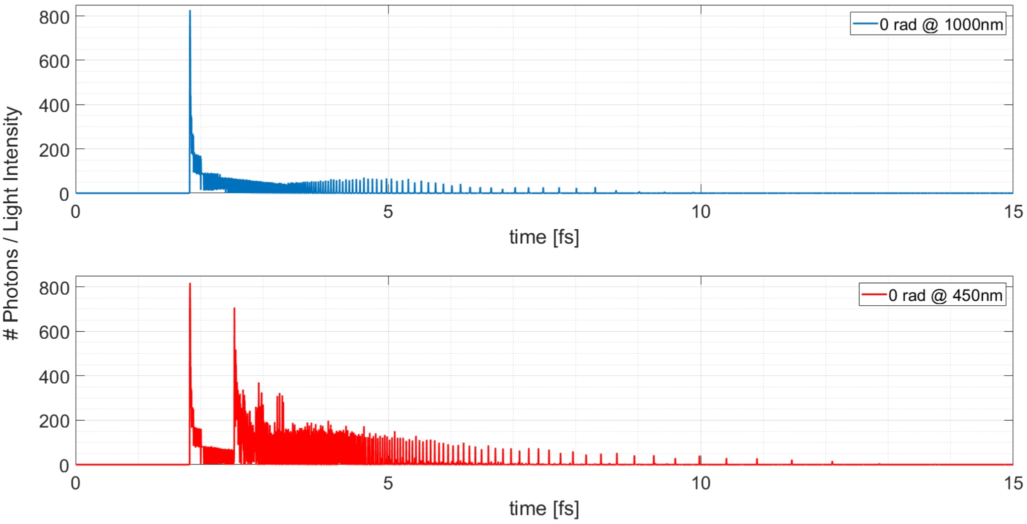

Figure 4.38: Pulse response at 1000 nm (blue) and 450 nm (red) of a four-slit nanoantenna.

By tilting the emitter, different optical paths will reach the interfaces and consequently, the metal. Thus, it is expected that the optical response varies with that tilt angle.

Figure 4.39a presents the pulse response at 1000 nm, for the previously referred tilt angles. Not only the main Dirac pulse but also the consequent exponential tail (even that smaller than the one obtained at 450 nm) varies with the tilt angle. When the emitter is perfectly parallel to the nanoantenna, the photon distribution in the environment tends to be symmetric.

By tilting, that distribution changes because the point sources coordinate varied. Although the distance between point sources remains the same, the horizontal and vertical coordinates vary and the point sources tend to have the same horizontal coordinate by increasing the angle. For that reason, photons' optical paths vary as well as the time response [15, 83]. As m increases, it is possible to observe the appearance of four different maxima instead of the huge Dirac pulse. Each maximum is related to the optical paths that pass directly to the slit (and some near them), which is four in this scenario. It is because the point sources tend to be more at one side of the nanoantenna and consequently, the response of each individual slit is different. There are more photons on one side of the device and, on the side with fewer photons the optical paths between the emitter and the nanoantenna are larger. Furthermore, the higher the tilt angle the fewer photons are in the target, mainly because more photons are reflected back on the metal interface and propagate to the target's opposite side. It happens because there is a metal extension on both sides, and more photons reach those interfaces, due to the tilt angle [15,83].

From figure 4.39a is possible to conclude that the optical response of these devices varies with the tilt angle m and consequently, there is the possibility to use it as a tilt sensor.

On the other hand, the device is simulated at 450 nm, a wavelength inside the dielectric-metal resonances, and the response is presented in figure 4.39b. Once again, response differences are found when varying the tilt angle m. The big question is if the extraordinary optical transmission effect allows us to obtain a better sensitivity of the tilt angle. This question is going to be answered below numerically, but it is already possible to conclude that the pulse response has different characteristics, namely the appearance of a second peak and a longer response tail [15,83].

Comparing figure 4.39b to figure 4.39a it is possible to observe that without extraordinary optical transmission, one should obtain a clearer response. As the light-matter interaction at low intensities is a stochastic process, more fluctuations are in the time response. However, they might be useful to miniaturise devices and reduce power consumption without losing or even increasing, sensitivity or any other important figure of merit.

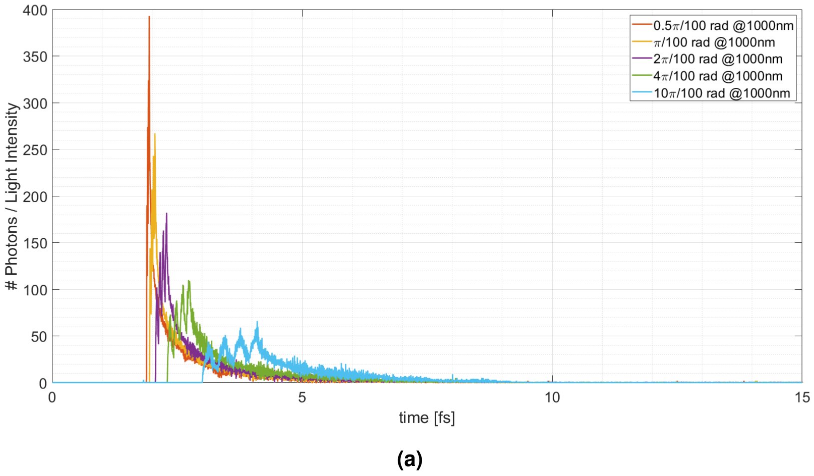

(a)

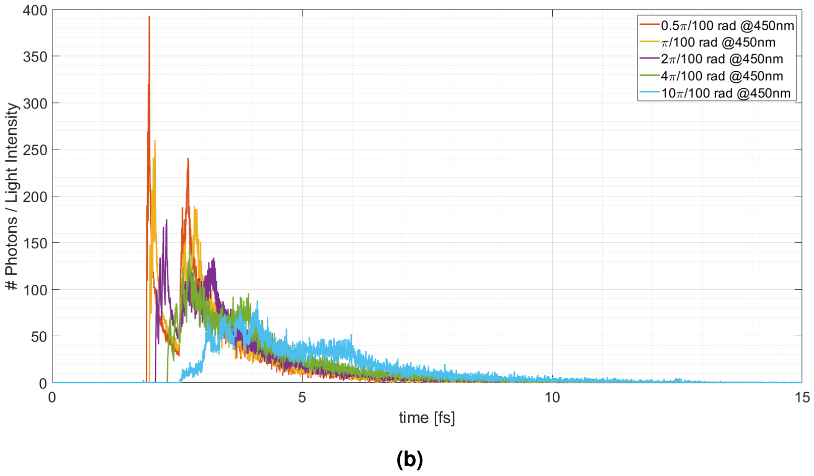

(b)

Figure 4.39: Pulse responses at different tilt angles of a four-slit nanoantenna at: a) 1000 nm; b) 450 nm.

The aforementioned question is not already answered or at least, completely answered. To do so, one should verify the values presented in table 4.5 and figures 4.40 and 4.41. The summing of all photons at different timestamps converge to the number of photons in steady-state.

The number of photons that passed through the metal, P_{EOT}, is impressive. It is obtained by summing all the photons that pass through the metal near the nanoantenna. The obtained values are expected based on the previous studies [7,16,67]. Moreover, near metal resonances this research work shows that the number of photons that pass through the metal decays when increasing the emitter tilt angle. In the infrared region, the number of photons that pass through the metal is reduced in comparison with the number of photons that reach the target.

The output signal is the optical signal at the target, as explained previously. Even when one has a huge number of extraordinary photons, P_{EOT}, their origin is not easily detectable. Then, the number of photons on the target is computed for all the analysed tilt angles m [15,83].

Once again, by comparing the values at 450 nm and 1000 nm the extraordinary optical transmission phenomenon is observed. At the visible resonant wavelength, the light intensity obtained is double of that obtained at the infrared wavelength [15,83].

The tilt angle variation leads to a monotone change in the number of photons at the target, P_{Target}. Since these intensity values are experimentally measurable, the device's sensitivity is computed based on them. By sensitivity one has the output variation (P_{Target}) divided by the input/parameter variation (tilt angle m). Two indicators are used: one the sensitivity referred to the null inclination, S_{ref}, and the other associated with the incremental increase of the tilt angle (two consecutive values), S.

As expected, both are negative due to the obtained decay tendency, as illustrated in figure 4.41. It is also concluded that at the resonant wavelength, both sensitivities are higher, meaning that the extraordinary optical transmission brought huge improvements. Moreover, at 450 nm, when the inclination increases the sensitivity referred to the null inclination decays, as suggested in both figures and table. Although it is not monotone, at 1000 nm, it is observed an increasing trend. Considering the incremental sensitivity, it is not monotone and there is no trend in both wavelengths [15,83].

Figure 4.40 has also another indicator, defined as P_{ABS}, which is the number of photons absorbed in the metal. This variable allows us to clarify geometrically the extraordinary optical transmission phenomenon. The extraordinary photons (the ones that passed through the metal) have to reach any nanoantenna dielectric-metal interface, be transmitted to the metal, reach any metal-dielectric interface and be re-transmitted to the dielectric in the direction of the target. Also, in this path, the photon has some probability of being absorbed and, it should not be if it is intended to get it on the target. Thus, the designer can geometrically visualise the photon propagation and choose media considering the probabilities at the different interfaces and the absorption probability in the media.

Furthermore, the propagation cycle related before should have loops, since photons can be reflected or transmitted multiple times at different interfaces until being absorbed or leave the test environment. Also, there are other optical paths but only the ones derived from this are considered extraordinary optical transmission optical paths since they are the ones that pass through the metal.

As suggested in figure 4.40, at 450 nm the number of absorbed photons, P_{ABS}, is also high in comparison with the obtained at 1000 nm. This is due to the fact that more photons are transmitted to the metal, as expected from [67], but none of them leave the metal. Then, they are absorbed. Based on the information in this figure, the probability of leaving the metal (metal-dielectric interface) might be increased (by choosing another dielectric) to increase the number of photons in the target [15,83].

Table 4.5: Number of extraordinary photons and number of photons on the target for different tilt angles. Sensibilities determination.

m [rad]	P_{EOT}		P_{Target}					
	450 nm	1000 nm	450 nm	$S_{ref}[rad^{-1}]$	$S[rad^{-1}]$	1000 nm	$S_{ref}[rad^{-1}]$	$S[rad^{-1}]$
0	41454	148	67065	—	—	29112	—	—
0.5 $\pi/100$	32671	104	65962	-70219	-70219	28927	-11777	-11777
$\pi/100$	41942	151	65316	-55672	-20563	28802	-9868	-3979
2 $\pi/100$	43024	128	63869	-50866	-23030	28185	-14754	-9820
4 $\pi/100$	40066	127	61195	-46712	-21279	27084	-16138	-8761
10 $\pi/100$	37969	103	53294	-43834	-25150	23180	-18882	-12427

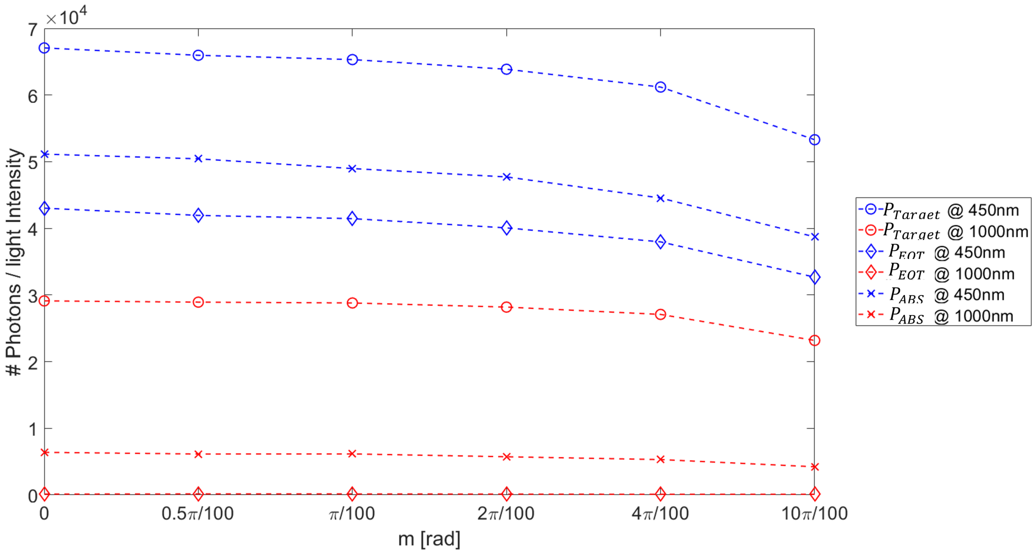

Figure 4.40: Number of photons at the target, number of photons that pass through the metal and number of absorbed photons in the metal.

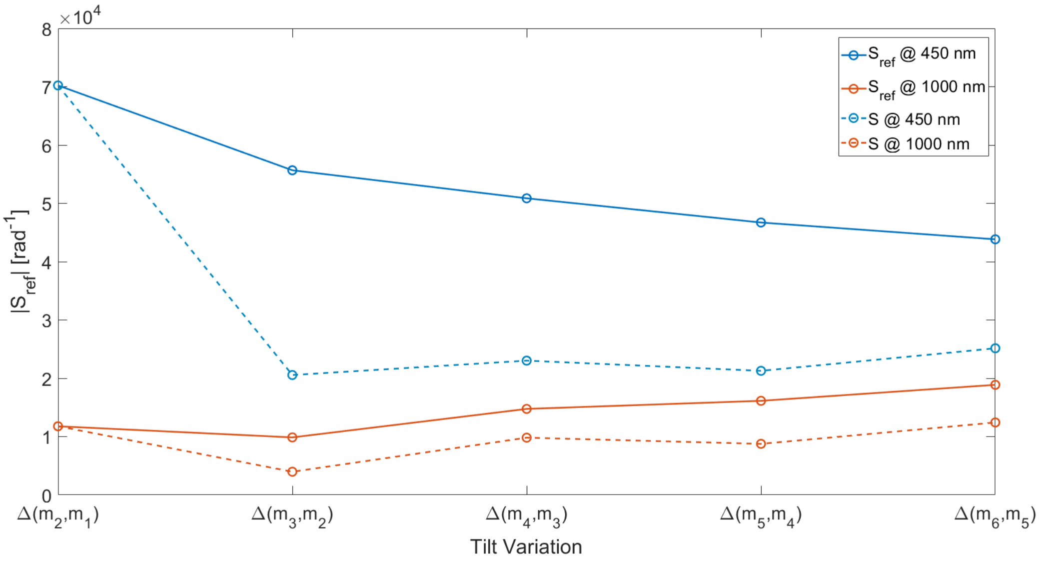

Figure 4.41: Sensitivities in function of the tilt angle, where the x-axis is referred to the tilt variations presented in figure 4.40.

In general, the extraordinary optical transmission phenomenon allows us to design the tilt sensor with improved sensitivity. Their trend is visualised in figure 4.40. Besides the detection of the tilt angle using the number of photons on the target (light intensity) it is also possible to perform it in two other forms.

First, it is also possible to establish relations with the peak values illustrated in figures 4.38 to 4.39b. In table 4.6 are the values at different tilt angles for the intensity peaks and their time stamps. These intensity peaks are the maximum (global) and not the first peak [15, 83]. The maximum is only the first peak at a null inclination. Also, in table 4.6 are the sensitivity values using the peak. It is concluded that the more tilted the emitter the less sensitive the device is. Also, the incremental sensitivity is in the same order as the referenced one [15, 83].

Another possibility to measure the emitter tilt angle is using the maximum time stamp. In this case, the sensitivity has other units, but it is also presented in table 4.6, where it is verified that the time sensitivity values are more identical. For that reason, only the sensitivity is determined, avoiding the presentation of the small values of the incremental one. Based on the time sensitivity, it is possible to conclude that a few fs (1 to 4) are enough to register a pattern with information about the emitter tilt angle. The recovery time (time until a new measure) is also at the fs orders. In these scenarios, two to three tens of fs are acceptable definitions, based on the observation of figures 4.38 to 4.39b. From these values, sensitivities around 7 $fs\,rad^{-1}$ are obtained. These time values are equal for both wavelengths, since the peak is at the same time stamp, and it only varies its value [15, 83].

Based on the figures and tables presented in this section it is possible to conclude that a device based on a 4-slit nanoantenna can act as a tilt sensor, namely detecting small angular variations at orders of $0.5\pi/100$ rad ($0.9°$).

Table 4.6: Light peak values on the target for different tilt angles. Sensitivities determination.

m [rad]	Peak @ 1000 nm	Peak @ 450 nm	t [fs]	$S_{p_{ref}}$ $[rad^{-1}]$	S_p $[rad^{-1}]$	$S_{t_{ref}}$ $[fs\,rad^{-1}]$
0	827	818	1.83	—	—	—
0.5 $\pi/100$	393	393	1.94	-27629	-27056	7.003
$\pi/100$	267	260	2.06	-17825	-17762	7.321
2 $\pi/100$	182	175	2.29	-10265	-10234	7.321
4 $\pi/100$	110	145	2.73	-5706	-5356	7.162
10 $\pi/100$	66	88	4.10	-2422	-2324	7.226

4.6.1.B Light Patterns

Besides analysing the time response, it is also possible to analyse the influence of the emitter tilt angle on the light pattern obtained on the target. This is a continuation of the research work published in [16], but in this case, aiming the collection of information to detect that angle. Two time stamps are selected observing figures 4.38 to 4.39b. The obtained patterns are as in [16], which are the number of photons (light intensity) that reached the target at a certain horizontal coordinate (1 nm resolution) until that time stamp.

After 3.3 fs as well as after 13.2 the patterns are obtained. Based on figure 4.38 it is possible to verify that at the first instant differences regarding patterns at 1000 nm and 450 nm are observable since the number of photons is quite huge. At 13.2 fs the target is already receiving no more photons and consequently, it is the final pattern. Furthermore, regarding the tilt angle variation, it should be possible to observe the same differences at least at 3.3 fs, the number of photons and their optical paths on the target differs [15,83].

In Figures 4.42a and 4.42b are the patterns obtained at 3.3 fs, for different tilt angles. As expected, there are clear differences among them. First, it is observed that there are more photons at lower x, which denotes the horizontal coordinate. It is because there are more point sources on that side of the device. Moreover, photons are observed at the devices' boundaries, even at 1000 nm, because it has already had some spatial dispersion. However, the number of photons at 450 nm is quite higher than at 1000 nm. Furthermore, at 450 nm it is possible to visualise a more uniform pattern since more photons have already reached the target at different coordinates. Also, by observing patterns it is possible to verify the emitter inclination: the patterns are not symmetric (or tending to it) [15,83].

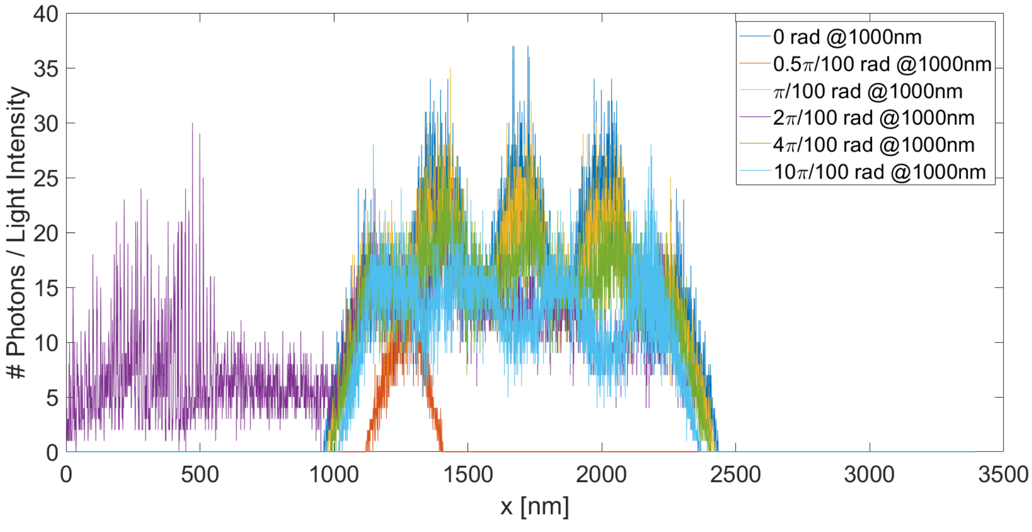

(a)

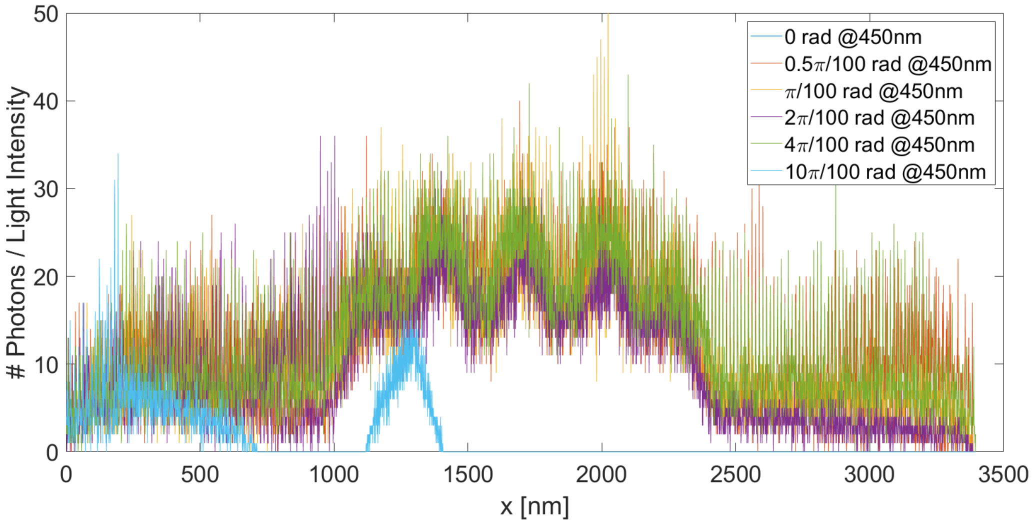

(b)

Figure 4.42: Light pattern of a four-slit nanoantenna after 3.3 fs for different tilt angles at: a) 1000 nm; b) 450 nm.

Analysing them at 13.2 fs, it is possible to observe the final patterns at the target at different tilt angles. Comparing figures 4.43a and 4.43b to figures 4.42a and 4.42b, it is concluded that some angles must be detected, but generically one will obtain worse sensitivities at 13.2 fs than at 3.3 fs. Nonetheless, these figures are presented at least to rule out the hypothesis of detecting tilt variations.

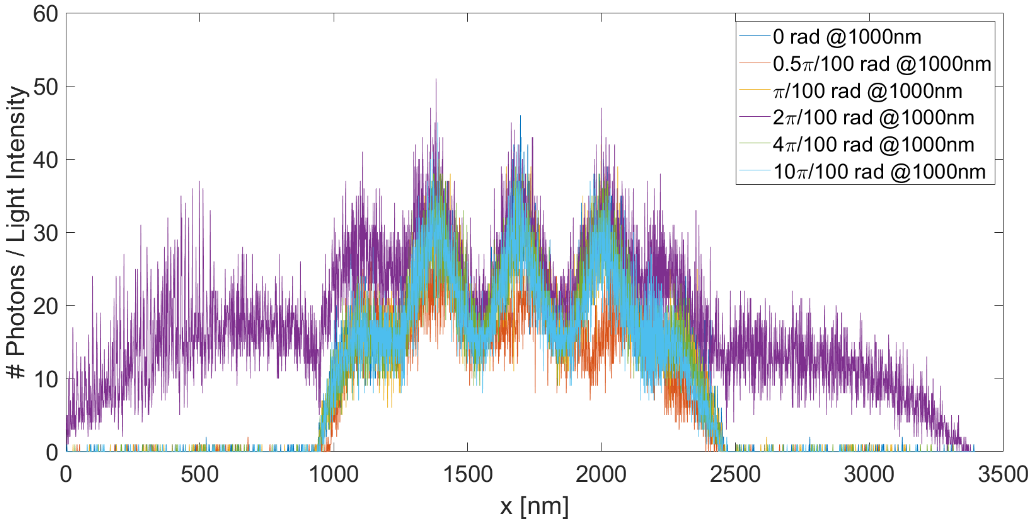

(a)

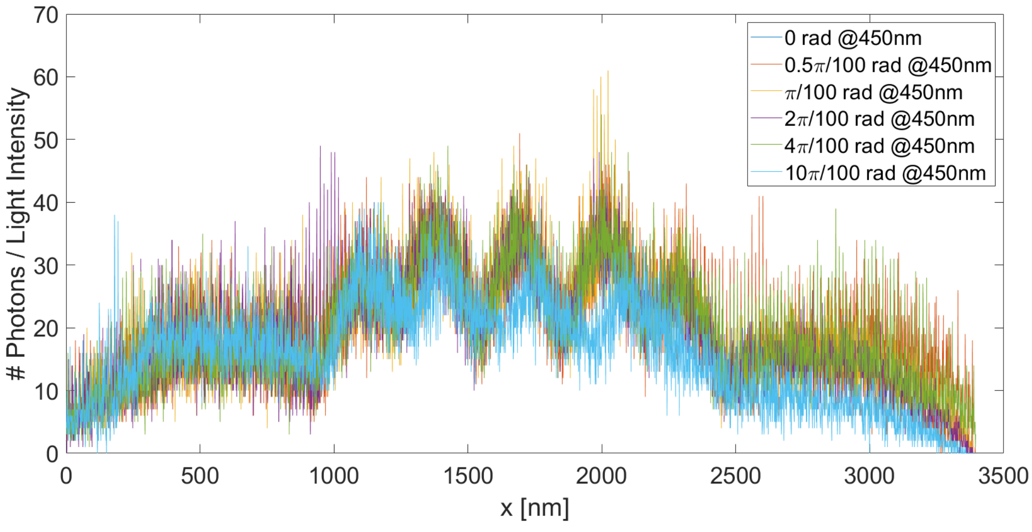

(b)

Figure 4.43: Light pattern of a four-slit nanoantenna after 13.2 fs for different tilt angles at: a) 1000 nm; b) 450 nm.

It is verified that different angles have different patterns on the target, meaning that the response is sensible to the tilt angle. Furthermore, besides near the resonance, the optical power of the detected signal is higher, different patterns will also be obtained since other optical paths are allowed (the ones that pass through the metal).

4.6.2 Discussion

The aim is to verify if the extraordinary optical transmission phenomenon improves the sensor response. The proposed structure presents some advantages in sensing, in this case in the emitter tilt angle detection. It allows us to miniaturise devices, namely reducing their dimensions to nano-scale, reducing also the power necessity. The obtained results suggest that this device acts as a tilt sensor at femtoseconds, being capable of detecting tilt angles of at least $0.5\pi/100$ rad (0.9°) at nano-scale [15, 83].

The results suggest that the analysis of the photons (light intensity) on the target in a certain time interval leads to higher sensitivity values than in comparison with the pattern analysis after the time interval. A sensitivity of 70219 rad^{-1} is obtained as a maximum at 450 nm, a resonant wavelength when analysing the total output optical power. Outside the dielectric-metal resonances, at 1000 nm, the maximum sensitivity is 18882 rad^{-1}. This fact suggests that the extraordinary optical transmission phenomenon allows the design of even more sensitive devices. Also, if an ultra-fast tilt sensor is necessary, the tilt angle information is possible to be obtained at less than 4 fs, with a resolution around 7 $fsrad^{-1}$, by analysing the appearance of the first transmission peak [15, 83].

4.7 Layout Proposal

Several technologies may be used to manufacture the proposed device. The most indicated are the ones based on photonic integrated circuits since they rely on the same used materials for similar applications. However, this kind of technology is yet mainly designed for the infrared spectral region (for instance 1310 nm and 1550 nm), due to the applications in optical communications.

Several foundries have equipment to manufacture the proposed device. Searching in the EUROPRATICE services, 8 foundries are presented: AMF, CEA-LETI / IRT Nanoelec, CORNERSTONE, GlobalFoundries, IHP, imec, LioniX and Teem Photonics. They work mainly in SOI technology (Silicon on Insulator) as illustrated in figure 4.44, where the insulator is denoted as BOX (Buried Oxide), which is usually made with SiO_2.

Each foundry has its Process Design Kit (PDK) available, where all the useful information about the physical processes to manufacture the device is presented, namely the available masks, dimensions and tolerances.

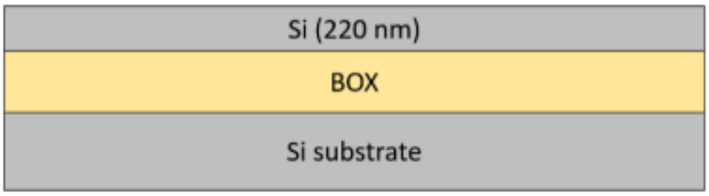

Figure 4.44: SOI substrate.

Besides this SOI technology, there are two other important possibilities.

First, finding foundries that can substitute Si with SiN, silicon nitride is possible. SiN presents a lower refractive index in comparison with Si. It allows for some applications in the visible range as well as to reduce the fabrication tolerances and some fluctuations (noise), since the contrast between SiN-SiO$_2$ is lower than Si-SiO$_2$.

On the other hand, there is a problem for longer wavelengths since SiO$_2$ becomes a highly absorbing material above 3.8 $\mu\mathrm{m}$. Then, some foundries have the suspended-Si technology available. This means that in some conditions the SiO$_2$ layer may be removed locally, leading to high transparencies up to 8 $\mu\mathrm{m}$. This is usually done under some special waveguides for optical communications. However, the proposed device focuses on gold-SiO$_2$ technologies. With some creativity, it can be made with SOI technology, leading to cost reduction due to the use of common fabrication techniques.

The proposed designed layout is based on the fabrication rules for the 37th call of the CORNERSTONE foundry. Figure 4.45 presents the proposed nanoantenna layout. The device fabrication process starts with the structure presented in figure 4.44. The SiO$_2$ layer has thicknesses that may range between 1 um and 3 um. This call is done for a thickness of 2 um.

The layout of figure 4.45 is obtained starting by removing all the Si layers. This means that one may use the mask Silicon Etch 2 (120 nm $\pm$ 10 nm) to obtain a 100 nm Si layer and after that the mask Silicon Etch 3 (100 nm to BOX). Furthermore, a Resist Patterning with a thickness of 500 um may be used to etch directly the BOX layer. After that, a metal layer is deposited with the desired thickness supported by a group of four 155 nm masks to define the slits. This value is within the capabilities presented by CORNERSTONE in 2020 [86] as well as described in their PDK. Since the usual metal deposition rate is at Å$\,\mathrm{s}^{-1}$ orders, it is possible to lift off the desired thickness with excellent tolerance.

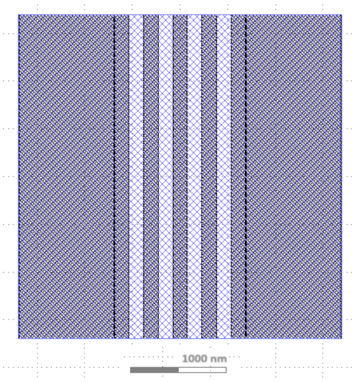

Figure 4.45: Proposed nanoantenna layout.

The proposed device has a silicon substrate. This substrate may be used as the detector that converts the optical radiation into an electrical signal. Also, since the top layer is metallic, it is possible to ask the foundry to remove the substrate by recursive use of Silicon Etch 2/3 masks.

However, since one may think in systems integration in the same photonic or opto-electronic chip, the emitter and the detector are also in the same chip. Then, the proposed solution is to design the detector between the BOX and the Si substrate and the emitter on top of the metallic layers, as illustrated in figure 4.46 [87–89]. In the same way, instead of using a detector under the device, one may also include, for instance, other circuits as optical amplifiers before the conversion to an electrical signal. The substrate is also used as external shield. One side of the device has an opening, that serves to place the analyte.

The distance between the nanoantenna and the emitter may be adjust according to the size of the sample. The emitter is suspended (with or without the use of waveguides) or it may be considered as the input of a optic fibre or waveguide. It may not illuminate all the nanoantenna in order to neglect the boundary effects [87–89]. Then, all the planes have the same response as the ones analysed before.

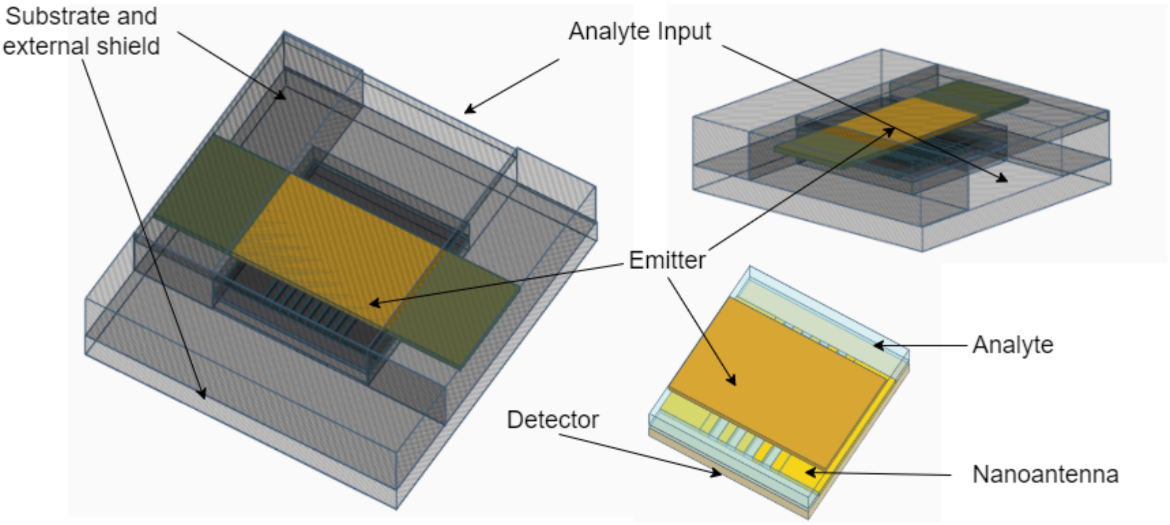

Figure 4.46: Photonic integrated circuit scheme.

The size of the whole device may be adjust according to its application but it must be done without changing the nanoantenna dimensions. Also, other option is to manufacture several devices in parallel. Then, the dimension increases and one may obtain at the same time the response of several devices. It allow us to perform the averages using the same time and increase redundancy.

The analyte to be analysed (be it liquid, solid or gas) is introduced through the opening, which size is adjusted to the sensor's application. The sensor can be reused as many times as is chemically possible to clean the residues of the analyte and ensure the chemical stability of the gold. Calibrations may be done between different analyte's tests, using known samples.

4.8 Comparison with other Technologies

In this section, the performance of the proposed device as a biosensor is compared with other devices, namely others whose working principle is also based on the propagation of SPP. As reviewed in Chapter 2, there are two other types of SPP-based sensors: Kretschmann's structures and sensors based on optical fibres.

The first is also analysed in this work. Kretschmann's structures may be used as biosensors considering angular variations (sensitivities are defined in $°/RIU$). The obtained values for this structure sensors are within the ones presented in Chapter 2. To perform the test one may have a lot of expensive and extra devices. For instance, one may have a collimator between the emitter and the structure to have only photons with a certain incidence angle. This is a huge step back to reproducing the system, reducing the costs and to miniaturise the whole system. This limitation is overcome in the proposed device since it requires any general TM emitter. Also, the proposed device may have a detector just under it. This is useful for miniaturisation. In contrast, Kretschmann's structures may have the detector far from the structure mainly due to the uncertainty of where the different rays from the multiple reflections will reach the detector. This is also a disadvantage to integrating Kretschmann's sensors in photonic integrated circuits, which is not in the proposed device.

The other option is the use of sensors based on optical fibres. This category groups a huge number of techniques including fibre Bragg grating sensors (FBGs), Fabry–Perot sensors, interferometric sensors and Raman scattering-based sensors. The working principle is the variation of a certain optical signal property (e.g.: intensity, phase, polarisation) from a certain stimulus that changes the refractive index of the optical fibre's surrounding media. However, only some of these sensors are based on SPP excitation and propagation: the ones with metallic layers. Since both signal properties and working principles are similar, the sensitivities of SPP optical fibre sensors and nanoantennas' are identical. However, the use of optical fibre is the main issue to the device's miniaturisation, due to their dimensions and bend issues. Also, due to the fibre's acceptance angle, there are higher losses in comparison with the proposed device. In the proposed scenario, the radiation that is reflected by the device is totally due to its working principle. The acceptance angle of optical fibres generates high losses in the system and even more uncertainty in the results since references are not only affected by the emission distribution but also by the number of photons accepted by the fibre and their angles.

4.9 Discussion about Detectable Analytes

Based on the presented results, the proposed device may act as a biosensor considering at least 3 different approaches: (i) the variation of the output signal intensity; (ii) the variation of the settling time middle point; (iii) the variation of the settling time width near its maxima. Moreover, the device becomes more sensitive if one uses EOT effect correctly, namely, it is possible to increase the sensitivity in (i) by stopping the emission before the response settles. Also, correct sizing considering the similarity between EOT and slit photons near the maxima time in (ii) and (iii) lead to the increase of the device sensitivity. In the worst cases, devices may also present a null sensitivity if the EOT photons are much greater than the slit ones.

As stated at the beginning of this chapter, this section presents some examples of analytes that are differentiable considering the proposed device and the deep review reported in the state-of-the-art.

A possibility to monitor the glucose concentration in an aqueous solution presented in figure 2.19 is to use the proposed nanoantenna and analyse the results near 633 nm. There, the solution's refractive index has a linear behaviour with the glucose concentration. Also, its values ranged between 1.33 and 1.49, which means that the proposed device is sensible both in the frequency and time domains. Also, sweeping the wavelength, it is possible to detect these variations considering the middle point and the width of the settling time response. This means that for just one pulse, one has at least three different indicators.

By similarity, the glucose concentration in the blood may also be detectable. However, as discussed in table 2.2 and figures 2.19, 2.20 and 2.21, it is only valid in a spectral region where the blood's refractive index does not vary with other quantities, for instance, oxygen levels. It occurs between 500-650nm, which is quite interesting since it is also the region where the three indicators present valid results. Thus, the proposed device works as a biosensor to mark diabetes or pre-diabetes stages in that working region.

Discussing the determination of the oxygen level in the blood, it is verifiable that this stimulus produces a huge variation around 400-450 nm, as illustrated in figure 2.20. Then, the proposed device only works for this application at this wavelength considering the variation of the settling time response. However, near 350 nm the refractive index has some variations that may be detectable by the three markers (1.33-1.35).

Figure 2.22 presents the refractive index of breast tissues with different conditions. From that figure, it is observed that for wavelengths higher than 550 nm, the refractive index of normal, fibroadenoma and cancer breast cells are quite different (1.33-1.36). This is also the working region where the three proposed marks are valid. Then, the proposed structure may act as a marker to detect breast diseases.

The same is valid for liver diseases, whose refractive index is presented in figure 2.23. The liver cancerous cells produce variations in the refractive index between 1.35 and 1.39. The refractive indexes are different from 400 nm to 1600 nm. This means that the proposed device can monitor liver cells around 600 nm, presenting the three indicators. Also, around 400-450nm, the device is sensible but only 2 indicators present non-null sensitivity.

Figure 2.24 presents other diseases that affect the refractive index of the biological tissue. Many have variations between 1.3 and 1.41 and consequently the proposed device can monitor them considering at least 2 of the 3 proposed markers.

Figure 2.18 also presents some analytes that can act as references. For instance, to increase sensitivity, one may like to compare the results with some known samples. For example, if a diseases produce variations between 1.33 and 1.35, but the device is more sensible between 1.33 and 1.37, one may like to use any 1.37-reference to test the unknown analyte.

5

Conclusion

Contents

5.1 Conclusions

The discovery of Extraordinary Optical Transmission (EOT) questioned all the classical diffraction theories. None of them explain the new phenomenology, because they assume the existence of ideal materials, namely metals. The light patterns on targets are only influenced by the unobstructed points (slits). This means that the metal is assumed as opaque, leading to the total reflection of light on the metal surface. Consequently, these theories do not describe situations where radiation passes through the metal. Classical diffraction theories do not consider the excitation and propagation of evanescent waves such as Surface Plasmon Polaritons (SPP) and creeping waves in the metal and consequently, they are not accurate in the ultraviolet, visible and near-infrared spectral regions. The appearance of these kinds of waves is totally connected to the consideration of the electrical and optical properties of real materials, through correct modelling of the dielectric function and refractive index, which are complex entities in these regions.

The propagation of SPP and creeping waves are the origin of EOT and can be analysed from Maxwell's equations. The novel methodology introduced in this research shows that near the SPP resonances, there are high transmission angles, transmission probability values, and a nanometric propagation length in a given interface.

Kretschmann structures are analysed to validate the new methodology. The operating principle of this structure results from the propagation of SPP waves. Thus, the transmission increases at wavelengths near the SPP resonances or at incidence angles near the perfect wavevector match condition, leading to the decrease of the structure reflectance. These structures are commonly used as biosensors, due to their simplicity and considerable sensibility values.

Using the proposed methodology it is possible to analyse the excitation and propagation of SPP. The development of the semi-classical and semi-analytic model on the time domain led to the analysis of EOT. After the model validation, the main conclusion is that it is possible to quantify the amount of radiation on the target that passes through the metal, or in other words, this model led to the possibility of quantising EOT. Then, combining it with the geometric intuition brought by the proposed model, a novel paradigm of SPP and EOT-based biosensors appears.

A novel device is proposed to detect refractive index variations between 1.30 and 1.41. This working range represents some important biological events, namely the appearance of diseases in human tissues. Based on the proposed and novel model, the device is designed and due to the variation of SPP resonances on analyte-gold interfaces, three indicators are defined. Since the analysis directly in the time domain may be expensive and with low precision, an algorithm to obtain pulse responses is proposed. Thus, the indicators are the variation of the steady-state intensity, the variation of the settling time middle point and its width around the maximum. The pulse settling time is around 4.5-8 fs. This reveals an ultrafast biosensor since 10^{16} tests may be executed in just one second. This huge value must be used to improve the results by averaging the optical response.

First, it is concluded that the best metal to analyse human tissues variations is gold, not only due to its chemical stability but also due to the refractive index contrast with the analytes.

The settling time middle point variation has a sensitivity around 30-60 %/RIU, whereas the maximum width sensitivity takes values around 600-800 nm/RIU. The intensity output varies around 10-40 %/RIU, namely for wavelengths near 350 nm and 600 nm. In other words, outside the main resonance region (near 450 nm), where R_p tends to be null and, it also has a small variation with the refractive index. From the proposed model it is also concluded that the intensity sensitivity increases a lot if one stops the emission before the response settles. In these cases, the values increase to 50-100 nm/RIU and the use of the 450 nm band is also possible.

A new paradigm is established since novel ways of measuring these stimuli are proposed. These novel figures of merit allow us to have higher sensitivity values in the visible and near-infrared than the ones reviewed in the State-of-the-Art.

Several biological events are detectable, such as glucose concentration in blood, oxygen concentration in blood or the presence of breast, liver, lungs thyroid, pancreas or colon cancerous cells in tissues. All of them may be monitored considering the variations of the optical response settling time. In terms of output intensity, it may vary around 350 nm or 600 nm to exploit all the biosensor indicators.

5.2 Future Work

Considering the presented research, one intends to carry out developing work in the field of optics and optoelectronics. These results suggest some paths of possible innovations.

First, Kretschmann's structures may be projected using the same used PDK. This is a simpler structure that may allow us to start obtaining experimental results and acquiring the experimental equipment to measure the pretended signals. This experimental setup may also be used to measure the complex electrical permittivity of different materials. Then, one may consider to obtain the own parameters of Drude-Lorentz models for the metals provided may the manufacture. After that, more complex devices such as nanoantennas may be fabricated and experimental analysed. However, this first experimental work should be started considering a non-integrated emitter and detector.

Since the detector seems to have a simpler design (both theoretical and practical), one may start the integration of the detector. Thus, considering the same application field (biosensors), one may start the theoretical analysis of different detectors and the optimisation of one for our purposes. After that, considering the same PDK as the one used for the nanoantenna, one may design the detector.

The same might be done for the emitter. However, one may study the hypothesis of using a suspended emitter. Once again, using the same PDK one may design it. After that, it is possible to integrate and design the whole system, which is going to be manufactured and experimentally tested using the set-up created.

Regarding the innovative model, one also would like to carry on developing it. For instance, other emitters than plane waves might be implemented, considering real LASER and LED. Then, the user may choose a certain emission pattern, wavelength bandwidth (combination of wavelengths) and light intensity. Moreover, one may think about developing a graphical interface. Then, it may be available for other users in a simpler software environment. This will increase the scientific outreach as well as extend the range of applications of this tool. Some of this applications may be the ones already tested and presented in the appendix that may benefit from the geometry intuition and from the radiation quantisation brought by the model.

Bibliography

[1] I. M. Pinheiro Caetano, J. P. N. Torres, and **Ricardo A. Marques Lameirinhas**, "Simulation of solar cells with integration of optical nanoantennas," *Nanomaterials*, vol. 11, no. 11, p. 2911, 2021. [Online]. Available: https://doi.org/10.3390/nano11112911

[2] **Ricardo A. Marques Lameirinhas**, J. P. N. Torres, and J. P. de Melo Cunha, "A photovoltaic technology review: History, fundamentals and applications," *Energies*, vol. 15, no. 5, p. 1823, 2022. [Online]. Available: https://doi.org/10.3390/en15051823

[3] F. Duarte, J. P. N. Torres, A. Baptista, and **Ricardo A. Marques Lameirinhas**, "Optical nanoantennas for photovoltaic applications," *Nanomaterials*, vol. 11, no. 2, p. 422, 2021. [Online]. Available: https://doi.org/10.3390/nano11020422

[4] R. D. F. R. Gomes, M. Martins, A. Baptista, and J. P. N. Torres, "Study of a nano optical antenna for intersatellite communications," *Optical and Quantum Electronics*, vol. 49, no. 4, pp. 1–22, 2017. [Online]. Available: https://doi.org/10.1007/s11082-017-0966-y

[5] L. Novotny and N. Van Hulst, "Antennas for light," *Nature photonics*, vol. 5, no. 2, pp. 83–90, 2011. [Online]. Available: https://doi.org/10.1038/nphoton.2010.237

[6] **Ricardo A. Marques Lameirinhas**, J. P. N. Torres, A. Baptista, and M. J. M. Martins, "The impact of nanoantennas on ring resonators' performance," *Optics Communications*, vol. 490, p. 126906, 2021. [Online]. Available: https://doi.org/10.1016/j.optcom.2021.126906

[7] **Ricardo A. Marques Lameirinhas**, J. P. N. Torres, A. Baptista, and M. J. M. Martins, "A new method to determine the response of kretschmann's structure-based biosensors," *IEEE Sensors Journal*, vol. 22, no. 21, pp. 20 421–20 429, 2022. [Online]. Available: https://doi.org/10.1109/JSEN.2022.3207896

[8] **Ricardo A. Marques Lameirinhas**, J. P. N. Torres, A. Baptista, and M. J. Marques Martins, "The effect of the nanoantenna slit geometry in the optical response: Applications on sensors," *IEEE 2021 Telecoms Conference (ConfTELE)*, pp. 1–6, 2021. [Online]. Available: https://doi.org/10.1109/ConfTELE50222.2021.9435596

[9] **Ricardo A. Marques Lameirinhas**, J. P. N. Torres, and A. Baptista, “A sensor based on nanoantennas,” *Applied Sciences*, vol. 10, no. 19, p. 6837, 2020. [Online]. Available: https://doi.org/10.3390/app10196837

[10] **Ricardo A. Marques Lameirinhas**, J. P. N Torres, and A. Baptista, “The influence of structure parameters on nanoantennas’ optical response,” *Chemosensors*, vol. 8, no. 2, p. 42, 2020. [Online]. Available: https://doi.org/10.3390/chemosensors8020042

[11] **Ricardo A. Marques Lameirinhas**, J. P. N. Torres, and A. Baptista, “Sensors based on nanoantennas: Fundamentals,” *European Journal of Applied Physics*, vol. 2, no. 3, 2020. [Online]. Available: https://doi.org/10.24018/ejphysics.2020.2.3.6

[12] R. Gordon, D. Sinton, K. L. Kavanagh, and A. G. Brolo, “A new generation of sensors based on extraordinary optical transmission,” *Accounts of chemical research*, vol. 41, no. 8, pp. 1049–1057, 2008. [Online]. Available: https://doi.org/10.1021/ar800074d

[13] R. Gordon, “Extraordinary optical transmission for surface-plasmon-resonance-based sensing,” *Society of Photo-optical Instrumentation Engineers*, 2008. [Online]. Available: https://doi.org/10.1117/1.3013629

[14] M. D. Wissert, A. W. Schell, K. S. Ilin, M. Siegel, and H.-J. Eisler, “Nanoengineering and characterization of gold dipole nanoantennas with enhanced integrated scattering properties,” *Nanotechnology*, vol. 20, no. 42, p. 425203, 2009. [Online]. Available: https://doi.org/10.1088/0957-4484/20/42/425203

[15] **Ricardo A. Marques Lameirinhas**, J. P. N. Torres, A. Baptista, and M. J. M. Martins, “Analysis of a plasmonic slit nanoantenna as a high sensitivity tilt sensor,” *IEEE Sensors Journal*, vol. 23, no. 17, pp. 19 232–19 238, 2023. [Online]. Available: https://doi.org/10.1109/JSEN.2023.3296270

[16] **Ricardo A. Marques Lameirinhas**, J. P. N. Torres, A. Baptista, and M. J. M. Martins, “A novel analysis for light patterns in nano structures,” *IEEE Photonics Journal*, vol. 14, no. 6, pp. 1–6, 2022. [Online]. Available: https://doi.org/10.1109/JPHOT.2022.3227429

[17] S. Klinghammer, T. Uhlig, F. Patrovsky, M. Bohm, J. Schutt, N. Putz, L. Baraban, L. M. Eng, and G. Cuniberti, “Plasmonic biosensor based on vertical arrays of gold nanoantennas,” *ACS sensors*, vol. 3, no. 7, pp. 1392–1400, 2018. [Online]. Available: https://doi.org/10.1021/acssensors.8b00315

[18] J. Guang, M. Lu, R. Li, C. Wang, M. Lin, R. Fan, and W. Peng, “Visible light-illuminated gold nanohole arrays with tunable on-chip plasmonic sensing properties,” *Photonic Sensors*, vol. 14, no. 3, pp. 1–15, 2024. [Online]. Available: https://doi.org/10.1007/s13320-024-0717-1

[19] A. Portela, O. Calvo-Lozano, M.-C. Estevez, A. M. Escuela, and L. M. Lechuga, "Optical nanogap antennas as plasmonic biosensors for the detection of mirna biomarkers," *Journal of Materials Chemistry B*, vol. 8, no. 19, pp. 4310–4317, 2020. [Online]. Available: https://doi.org/10.1039/D0TB00307G

[20] Y.-C. Lu, B.-H. Chen, T.-Y. Yung, Y.-C. Tzeng, C.-Y. Fang, R.-J. Chung, and P.-T. Chen, "Nano-diamond-enhanced integrated response of a surface plasmon resonance biosensor," *Sensors*, vol. 23, no. 11, p. 5216, 2023. [Online]. Available: https://doi.org/10.3390/s23115216

[21] H. Fischer and O. J. F. Martin, "Engineering the optical response of plasmonic nanoantennas," *Opt. Express*, vol. 16, no. 12, pp. 9144–9154, Jun 2008. [Online]. Available: https://doi.org/10.1364/OE.16.009144

[22] Y. Zhao, K. Mukherjee, K. D. Benkstein, L. Sun, K. L. Steffens, C. B. Montgomery, S. Guo, S. Semancik, and M. E. Zaghloul, "Miniaturized nanohole array based plasmonic sensor for the detection of acetone and ethanol with insights into the kinetics of adsorptive plasmonic sensing," *Nanoscale*, vol. 11, no. 24, pp. 11 922–11 932, 2019. [Online]. Available: https://doi.org/10.1039/C9NR03578H

[23] S. K. Sahu and M. Singh, "Plasmonic elliptical nanohole array for on-chip human blood group detection," *IEEE Sensors Journal*, 2023. [Online]. Available: https://doi.org/10.1109/JSEN.2023.3323556

[24] F. Kurul, Z. A. Yazici, Z. A. Kocer, S. N. Topkaya, and A. E. Cetin, "Low-cost and portable plasmonic biosensor for label-free detection of viruses in resource-limited settings," in *European Conference on Biomedical Optics*. Optica Publishing Group, 2023, p. 126272O. [Online]. Available: https://doi.org/10.1117/12.2671001

[25] A. E. Cetin, Z. A. Kocer, S. N. Topkaya, and Z. A. Yazici, "Handheld plasmonic biosensor for virus detection in field-settings," *Sensors and Actuators B: Chemical*, vol. 344, p. 130301, 2021.

[26] Y. Liu and X. Zhang, "Chapter 10 - microfluidic-based plasmonic biosensors," in *Microfluidic Biosensors*, W. C. Mak and A. H. Pui Ho, Eds. Academic Press, 2023, pp. 287–312. [Online]. Available: https://doi.org/10.1016/B978-0-12-823846-2.00017-1

[27] H. Kurt, P. Pishva, Z. S. Pehlivan, E. G. Arsoy, Q. Saleem, M. K. Bayazıt, and M. Yüce, "Nanoplasmonic biosensors: Theory, structure, design, and review of recent applications," *Analytica Chimica Acta*, vol. 1185, p. 338842, 2021. [Online]. Available: https://doi.org/10.1016/j.aca.2021.338842

[28] A. Minopoli, A. Acunzo, B. Della Ventura, and R. Velotta, “Nanostructured surfaces as plasmonic biosensors: A review,” *Advanced Materials Interfaces*, vol. 9, no. 2, p. 2101133, 2022. [Online]. Available: https://doi.org/10.1002/admi.202101133

[29] S. Verma, A. K. Pathak, and B. A. Rahman, “Review of biosensors based on plasmonic-enhanced processes in the metallic and meta-material-supported nanostructures,” *Micromachines*, vol. 15, no. 4, p. 502, 2024. [Online]. Available: https://doi.org/10.3390/mi15040502

[30] A. S. M. Z. Kausar, A. W. Reza, T. A. Latef, M. H. Ullah, and M. E. Karim, “Optical nano antennas: State of the art, scope and challenges as a biosensor along with human exposure to nano-toxicology,” *Sensors*, vol. 15, no. 4, pp. 8787–8831, 2015. [Online]. Available: https://doi.org/10.3390/s150408787

[31] Y. Gu, L. Zhang, J. K. Yang, S. P. Yeo, and C.-W. Qiu, “Color generation via subwavelength plasmonic nanostructures,” *Nanoscale*, vol. 7, no. 15, pp. 6409–6419, 2015. [Online]. Available: https://doi.org/10.1039/C5NR00578G

[32] N. Anscombe, “Attosecond analysis,” *Nature Photonics*, 2008. [Online]. Available: https://doi.org/10.1038/nphoton.2008.177

[33] A. Ananthaswamy, “Particle, wave, both or neither? the experiment that challenges all we know about reality,” *Nature*, no. 618, pp. 454–456, 2023. [Online]. Available: https://doi.org/10.1038/d41586-023-01938-6

[34] J. Deus, M. Pimenta, A. Noronha, T. Peña, and P. Brogueira, *Introdução à Fisica*, 3rd ed. Porto Editora, 2014.

[35] E. Hecht, *Optica*. Fundação Calouste Gulbenkian, 2012.

[36] J. Mahan, N. Vinh, V. Ho, and N. Munir, “Monte carlo ray-trace diffraction based on the huygens-fresnel principle,” *Applied Optics*, vol. 57, 02 2018. [Online]. Available: https://doi.org/10.1364/AO.57.000D56

[37] H. A. Bethe, “Theory of diffraction by small holes,” *Physical review*, vol. 66, no. 7-8, p. 163, 1944.

[38] C. Bouwkamp, “On bethe’s theory of diffraction by small holes,” *Philips Research Reports*, vol. 5, pp. 321–332, 1950. [Online]. Available: https://doi.org/10.1103/PhysRev.66.163

[39] C. J. Bouwkamp, “Diffraction theory,” *Reports on progress in physics*, vol. 17, no. 1, p. 35, 1954. [Online]. Available: https://doi.org/10.1088/0034-4885/17/1/302

[40] T. Ebbesen, H. Lezec, H. Ghaemi, and et al, “Extraordinary optical transmission through sub-wavelength hole arrays,” *Nature*, vol. 391, pp. 667–669, 1998. [Online]. Available: https://doi.org/10.1038/35570

[41] P. Lalanne and H. Liu, “The elementary interactions in the extraordinary optical transmission phenomenon,” in *Journal of Physics: Conference Series*, vol. 139, no. 1. IOP Publishing, 2008, p. 012001. [Online]. Available: https://doi.org/10.1088/1742-6596/139/1/012001

[42] H. J. Lezec and T. Thio, “Diffracted evanescent wave model for enhanced and suppressed optical transmission through subwavelength hole arrays,” *Optics express*, vol. 12, no. 16, pp. 3629–3651, 2004. [Online]. Available: https://doi.org/10.1364/OPEX.12.003629

[43] G. Gay, O. Alloschery, B. Viaris de Lesegno, C. O’Dwyer, J. Weiner, and H. Lezec, “The optical response of nanostructured surfaces and the composite diffracted evanescent wave model,” *Nature Physics*, vol. 2, no. 4, pp. 262–267, 2006. [Online]. Available: https://doi.org/10.1038/nphys264

[44] H. Raether, “Surface plasmons on smooth surfaces,” *Surface plasmons on smooth and rough surfaces and on gratings*, pp. 4–39, 1988. [Online]. Available: https://doi.org/10.1007/BFb0048317

[45] R. H. Ritchie, “Plasma losses by fast electrons in thin films,” *Physical review*, vol. 106, no. 5, p. 874, 1957. [Online]. Available: https://doi.org/10.1103/PhysRev.106.874

[46] R. H. Ritchie, E. Arakawa, J. Cowan, and R. Hamm, “Surface-plasmon resonance effect in grating diffraction,” *Physical review letters*, vol. 21, no. 22, p. 1530, 1968. [Online]. Available: https://doi.org/10.1103/PhysRevLett.21.1530

[47] J. Pitarke, V. Silkin, E. Chulkov, and P. Echenique, “Theory of surface plasmons and surface-plasmon polaritons,” *Reports on progress in physics*, vol. 70, no. 1, p. 1, 2006. [Online]. Available: https://doi.org/10.1088/0034-4885/70/1/R01

[48] N. Sharma, A. Joy, A. K. Mishra, and R. K. Verma, “Fuchs sondheimer–drude lorentz model and drude model in the study of spr based optical sensors: A theoretical study,” *Optics Communications*, vol. 357, pp. 120–126, 2015. [Online]. Available: https://doi.org/10.1016/j.optcom.2015.08.092

[49] J. Zhang, J. B. Pendry, and Y. Luo, “Transformation optics from macroscopic to nanoscale regimes: a review,” *Advanced Photonics*, vol. 1, no. 1, pp. 1 – 15, 2019. [Online]. Available: https://doi.org/10.1117/1.AP.1.1.014001

[50] C. Sauvan, C. Billaudeau, S. Collin, N. Bardou, F. Pardo, J.-L. Pelouard, and P. Lalanne, “Surface plasmon coupling on metallic film perforated by two-dimensional rectangular hole array,” *Applied Physics Letters*, vol. 92, no. 1, p. 011125, 2008. [Online]. Available: https://doi.org/10.1063/1.2830333

[51] K. Xu, M. Fang, and Z. Huang, "Compact vertical-cavity surface-emitting laser based on all-dielectric metasurfaces," *Optics Communications*, vol. 475, p. 126257, 2020. [Online]. Available: https://doi.org/10.1016/j.optcom.2020.126257

[52] A. D. Rakić, A. B. Djurišić, J. M. Elazar, and M. L. Majewski, "Optical properties of metallic films for vertical-cavity optoelectronic devices," *Applied optics*, vol. 37, no. 22, pp. 5271–5283, 1998. [Online]. Available: https://doi.org/10.1364/AO.37.005271

[53] M. N. Polyanskiy. Refractive index database. [Online]. Available: https://refractiveindex.info

[54] M. Hosseinzadeh Sani and S. Khosroabadi, "Optimizing detection performance of disease by high-sensitivity biosensor with the urine sample," *13th international conference on engineering & technology*, 01 2020. [Online]. Available: https://isn.ac/XBKC-EBAZF

[55] A. Gemta, "Concentration, wavelength and temperature dependent refractive index of sugar solutions and methods of determination contents of sugar in soft drink beverages using laser lights," *Journal of Lasers, Optics & Photonics*, vol. 05, 07 2018. [Online]. Available: https://doi.org/10.4172/2469-410X.1000187

[56] M. Misto, E. Purwandari, S. ., A. Arkundato, L. Rohman, and B. Cahyono, "Analyses of concentration and wavelength dependent refractive index of sugar solution using sellmeier equation," *Journal of Physics: Conference Series*, vol. 1825, p. 012030, 02 2021. [Online]. Available: https://doi.org/10.1088/1742-6596/1825/1/012030

[57] L. Bi and P. Yang, "Modeling of light scattering by biconcave and deformed red blood cells with the invariant imbedding t-matrix method," *Journal of biomedical optics*, vol. 18, no. 5, pp. 055 001–055 001, 2013. [Online]. Available: https://doi.org/10.1117/1.JBO.18.5.055001

[58] C. Clinic. A1c. [Online]. Available: https://my.clevelandclinic.org/health/diagnostics/9731-a1c?fbclid=IwAR0qOvhGFsr0blAeexkOAmXJLYwW7dWwuBvWu-gRA4Xzr2_V-hiOE3hHflw

[59] Forbes. Normal blood sugar levels by age (chart). [Online]. Available: https://www.forbes.com/health/wellness/normal-blood-sugar-levels/?fbclid=IwAR3UdMfam8r3ZduucNENMeIzUamhCl88cNUYkMuvpyZqaRBeJzBg4z_SnjI

[60] M. Matiatou, P. Giannios, S. Koutsoumpos, N. V. Michalopoulos, K. G. Toutouzas, G. C. Zografos, and K. Moutzouris, "Complex refractive index of freshly excised human breast tissue as a marker of disease," *Lasers in Medical Science*, vol. 37, no. 6, pp. 2597–2604, 2022. [Online]. Available: https://doi.org/10.1007/s10103-022-03524-0

[61] P. Giannios, K. G. Toutouzas, M. Matiatou, K. Stasinos, M. M. Konstadoulakis, G. C. Zografos, and K. Moutzouris, "Visible to near-infrared refractive properties of freshly-excised human-liver tissues:

marking hepatic malignancies," *Scientific reports*, vol. 6, no. 1, pp. 1–10, 2016. [Online]. Available: https://doi.org/10.1038/srep27910

[62] R. Khan, B. Gul, S. Khan, H. Nisar, and I. Ahmad, "Refractive index of biological tissues: Review, measurement techniques, and applications," *Photodiagnosis and Photodynamic Therapy*, vol. 33, p. 102192, 2021. [Online]. Available: https://doi.org/10.1016/j.pdpdt.2021.102192

[63] J. E. Roy, "New results for the effective propagation constants of nonuniform plane waves at the planar interface of two lossy media," *IEEE Transactions on Antennas and Propagation*, vol. 51, no. 6, pp. 1206–1215, 2003. [Online]. Available: https://doi.org/10.1109/TAP.2003.812247

[64] S. Zhang, L. Liu, and Y. Liu, "Generalized laws of snell, fresnel and energy balance for a charged planar interface between lossy media," *Journal of Quantitative Spectroscopy and Radiative Transfer*, vol. 245, p. 106903, 2020. [Online]. Available: https://doi.org/10.1016/j.jqsrt.2020.106903

[65] P. C. Chang, J. Walker, and K. Hopcraft, "Ray tracing in absorbing media," *Journal of Quantitative Spectroscopy and Radiative Transfer*, vol. 96, no. 3-4, pp. 327–341, 2005. [Online]. Available: https://doi.org/10.1016/j.jqsrt.2005.01.001

[66] M. Dupertuis, M. Proctor, and B. Acklin, "Generalization of complex snell–descartes and fresnel laws," *JOSA A*, vol. 11, no. 3, pp. 1159–1166, 1994. [Online]. Available: https://doi.org/10.1364/JOSAA.11.001159

[67] **Ricardo A. Marques Lameirinhas**, J. P. N. Torres, A. Baptista, and M. J. M. Martins, "A new method to analyse the role of surface plasmon polaritons on dielectric-metal interfaces," *IEEE Photonics Journal*, vol. 14, no. 4, pp. 1–9, 2022. [Online]. Available: https://doi.org/10.1109/JPHOT.2022.3181967

[68] H. Weber, "The fresnel equations for lossy dielectrics and conservation of energy," *Journal of Modern Optics*, vol. 61, no. 15, pp. 1219–1224, 2014. [Online]. Available: https://doi.org/10.1080/09500340.2014.928375

[69] R. De Roo and C.-T. Tai, "Plane wave reflection and refraction involving a finitely conducting medium," *IEEE Antennas and Propagation Magazine*, vol. 45, no. 5, pp. 54–61, 2003. [Online]. Available: https://doi.org/10.1109/MAP.2003.1252810

[70] S. Mostufa, A. K. Paul, and K. Chakrabarti, "Detection of hemoglobin in blood and urine glucose level samples using a graphene-coated spr based biosensor," *OSA Continuum*, vol. 4, no. 8, pp. 2164–2176, 2021. [Online]. Available: https://doi.org/10.1364/OSAC.433633

[71] T. Treebupachatsakul, A. Boosamalee, K. Chaithatwanitch, and S. Pechprasarn, "Generalized figure of merit for plasmonic dip measurement-based surface plasmon resonance sensors,"

Biomedical Optics Express, vol. 13, no. 4, pp. 1784–1800, 2022. [Online]. Available: https://doi.org/10.1364/BOE.451023

[72] M. S. Rahman, M. S. Anower, M. R. Hasan, M. B. Hossain, and M. I. Haque, "Design and numerical analysis of highly sensitive au-mos2-graphene based hybrid surface plasmon resonance biosensor," *Optics Communications*, vol. 396, pp. 36–43, 2017. [Online]. Available: https://doi.org/10.1016/j.optcom.2017.03.035

[73] S. Mostufa, A. K. Paul, and K. Chakrabarti, "Detection of hemoglobin in blood and urine glucose level samples using a graphene-coated spr based biosensor," *OSA Continuum*, vol. 4, no. 8, pp. 2164–2176, 2021. [Online]. Available: https://doi.org/10.1364/OSAC.433633

[74] M. Dupertuis, B. Acklin, and M. Proctor, "Generalized energy balance and reciprocity relations for thin-film optics," *JOSA A*, vol. 11, no. 3, pp. 1167–1174, 1994. [Online]. Available: https://doi.org/10.1364/JOSAA.11.001167

[75] F. Jutzi, D. Wicaksono, G. Pandraud, N. de Rooij, and P. French, "Far-infrared sensor with lpcvd-deposited low-stress si-rich nitride absorber membrane: Part 2: thermal property, and sensitivity," *Sensors and Actuators A: Physical*, vol. 152, no. 2, pp. 126–138, 2009. [Online]. Available: https://doi.org/10.1016/j.sna.2008.12.024

[76] M. B. Hossain, I. M. Mehedi, M. Moznuzzaman, L. F. Abdulrazak, and M. A. Hossain, "High performance refractive index spr sensor modeling employing graphene tri sheets," *Results in Physics*, vol. 15, p. 102719, 2019. [Online]. Available: https://doi.org/10.1016/j.rinp.2019.102719

[77] N. R. Mohamad, M. F. M. R. Wee, M. A. Mohamed, A. A. Hamzah, and P. S. Menon, "Multi-response optimization of chromium/gold-based nanofilm kretschmann-based surface plasmon resonance glucose sensor using finite-difference time-domain and taguchi method," *Nanomaterials and Nanotechnology*, vol. 10, p. 1847980420982119, 2020. [Online]. Available: https://doi.org/10.1177/1847980420982119

[78] R. E. Nistor, I.-I. Popescu, and N. Ionescu-Pallas, "A schrödinger type explanation of fresnel formulas," *Journal of Optoelectronics and Advanced Materials*, vol. 9, no. 8, pp. 2408–2412, 2007. [Online]. Available: https://old.joam.inoe.ro/index.php?option=magazine&op=view&idu=836&catid=16

[79] F. R. Tangherlini, "Particle approach to the fresnel coefficients," *Phys. Rev. A*, vol. 12, pp. 139–147, Jul 1975. [Online]. Available: https://doi.org/10.1103/PhysRevA.12.139

[80] A. M. Fox, *Quantum optics: an introduction*. Oxford University Press, USA, 2006, vol. 15.

[81] A. Herguth, “On the meaning(fullness) of the intensity unit ‘suns’ in light induced degradation experiments,” *Energy Procedia*, vol. 124, pp. 53–59, 09 2017. [Online]. Available: https://doi.org/10.1016/j.egypro.2017.09.339

[82] P. Gonçalves, T. Christensen, N. Rivera, A.-P. Jauho, N. A. Mortensen, and M. Soljačić, “Plasmon–emitter interactions at the nanoscale,” *Nature communications*, vol. 11, no. 1, p. 366, 2020. [Online]. Available: https://doi.org/10.1038/s41467-019-13820-z

[83] **Ricardo A. Marques Lameirinhas**, J. P. N. Torres, A. Baptista, and M. J. M. Martins, “High sensitivity sensors based on slit plasmonic gold nanoantennas,” in *2024 IEEE 28th Workshop on Signal and Power Integrity (SPI)*, 2024, pp. 1–4.

[84] NobelPrize.org. The nobel prize in physics 2023. [Online]. Available: https://www.nobelprize.org/prizes/physics/2023/popular-information/

[85] **Ricardo A. Marques Lameirinhas**, J. P. N. Torres, A. Baptista, and M. J. M. Martins, “Exploiting extraordinary optical transmission in plasmonic slit nanoantennas for sensor applications,” *IEEE Photonics Journal*, vol. 16, no. 2, pp. 1–7, 2024. [Online]. Available: https://10.1109/JPHOT.2024.3376641

[86] C. G. Littlejohns, D. J. Rowe, H. Du, K. Li, W. Zhang, W. Cao, T. Dominguez Bucio, X. Yan, M. Banakar, D. Tran, S. Liu, F. Meng, B. Chen, Y. Qi, X. Chen, M. Nedeljkovic, L. Mastronardi, R. Maharjan, S. Bohora, A. Dhakal, I. Crowe, A. Khurana, K. C. Balram, L. Zagaglia, F. Floris, P. O’Brien, E. Di Gaetano, H. M. Chong, F. Y. Gardes, D. J. Thomson, G. Z. Mashanovich, M. Sorel, and G. T. Reed, “Cornerstone’s silicon photonics rapid prototyping platforms: Current status and future outlook,” *Applied Sciences*, vol. 10, no. 22, 2020. [Online]. Available: https://doi.org/10.3390/app10228201

[87] D. Bai, T. Wu, X. Li, X. Gao, Y. Xu, Z. Cao, H. Zhu, and Y. Wang, “Suspended gan-based nanostructure for integrated optics,” *Applied Physics B*, vol. 122, pp. 1–7, 2016. [Online]. Available: https://doi.org/10.1007/s00340-015-6293-8

[88] W. Cai, Y. Yang, X. Gao, J. Yuan, W. Yuan, H. Zhu, and Y. Wang, “On-chip integration of suspended ingan/gan multiple-quantum-well devices with versatile functionalities,” *Optics express*, vol. 24, no. 6, pp. 6004–6010, 2016. [Online]. Available: https://doi.org/10.1364/OE.24.006004

[89] J. Yuan, W. Cai, X. Gao, G. Zhu, D. Bai, H. Zhu, and Y. Wang, “Monolithic integration of a suspended light-emitting diode with a y-branch structure,” *Applied Physics Express*, vol. 9, no. 3, p. 032202, 2016. [Online]. Available: https://doi.org/10.7567/APEX.9.032202

[90] K. R. Hiremath, *Coupled mode theory based modeling and analysis of circular optical microresonators*. Kirankumar R. Hiremath, 2005.

[91] J. P. N. Torres, V. M. Machado, and A. Baptista, "A new hybrid finite element method: Electromagnetic propagation in bent waveguides," *IEEE Photonics Journal*, vol. 12, no. 1, pp. 1–13, 2020. [Online]. Available: https://doi.org/10.1109/JPHOT.2020.2966256

[92] J. P. N. Torres, V. M. Machado, A. Baptista *et al.*, "Supermode analysis of ring waveguide," *Optoelectronics and Advanced Materials-Rapid Communications*, vol. 11, no. July-August 2017, pp. 405–408, 2017.

[93] G. Alves Cavaco, **Ricardo A. Marques Lameirinhas**, C. P. Correia V. Bernardo, J. P. N. Torres, and A. Baptista, "Wavelength multiplexing system based on ring resonators," *Results in Optics*, vol. 15, p. 100651, 2024. [Online]. Available: https://doi.org/10.1016/j.rio.2024.100651

[94] M. J. Martins and I. V. Neves, "Propagação e radiação de ondas eletromagnéticas," *Lisboa: LIDEL*, 2015.

[95] M. Bazgir and F. B. Zarrabi, "A switchable split ring resonator nanoantenna design with organic material composite as a refractive index sensor," *Optics Communications*, vol. 475, p. 126211, 2020. [Online]. Available: https://doi.org/10.1016/j.optcom.2020.126211

[96] C.-C. Hu, W. Yang, Y.-T. Tsai, and Y.-F. Chau, "Gap enhancement and transmittance spectra of a periodic bowtie nanoantenna array buried in a silica substrate," *Optics Communications*, vol. 324, pp. 227–233, 2014. [Online]. Available: https://doi.org/10.1016/j.optcom.2014.03.062

[97] L. Ali, M. U. Mohammed, M. Khan, A. H. B. Yousuf, and M. H. Chowdhury, "High-quality optical ring resonator-based biosensor for cancer detection," *IEEE Sensors Journal*, vol. 20, no. 4, pp. 1867–1875, 2019. [Online]. Available: https://doi.org/10.1109/JSEN.2019.2950664

[98] A. Yalcin, K. C. Popat, J. C. Aldridge, T. A. Desai, J. Hryniewicz, N. Chbouki, B. E. Little, O. King, V. Van, S. Chu *et al.*, "Optical sensing of biomolecules using microring resonators," *IEEE Journal of Selected Topics in Quantum Electronics*, vol. 12, no. 1, pp. 148–155, 2006. [Online]. Available: https://doi.org/10.1109/JSTQE.2005.863003

[99] L. Ali, M. Khan, M. U. Mohammed, A. H. B. Yousuf, and M. H. Chaudhry, "High quality silicon photonics optical ring resonator biosensor design," in *2018 IEEE Nanotechnology Symposium (ANTS)*. IEEE, 2018, pp. 1–3. [Online]. Available: https://doi.org/10.1109/NANOTECH.2018.8653557

A

Approach to Implement an Algorithm to Characterise the Wavevector at an Interface

In this appendix the idea to implement the algorithm that determines the new wavevector angles and directions is presented.

Before moving, the implemented photon has a fictitious move in the same direction of propagation. If the refractive index before and after moving is the same, the movement is valid and it occurs. If there is any change on the complex refractive index (the photon reached an interface), the movement is cancelled and new wavevector angles and directions are computed. However, the wavevector components should be referenced to the interface normal and not to the general reference used to impose a propagation direction.

Then, the first step of this algorithm is to determine in which direction there is the refractive index change. It is assumed vertical and horizontal possible variations, since every shape must be decomposed into these ones when amplified. Figures A.1 and A.2 illustrate vertical and horizontal interfaces, respectively, using the example of the wavevector real part (constant phase plane normal vector). In each figure there are four different situations, representative of the combinations regarding the incident, reflected and refracted (or transmitted) radiation quadrants.

The algorithm must convert the incident direction into the incident angle referenced to the surface normal. The incident direction is denoted as θ_{i0} since it is referenced to the null angle, pointing to the right side. After that, knowing the incident angle θ_i, it is possible to determine the reflected and refracted angles, using the appropriated methodology presented in chapter 3. However, the output of this algorithm must be again a direction referenced to the zero and not to the surface normal, since the photon might reach other interface with other normal. Then, the algorithm should perform this conversion.

In figures A.1 and A.2 are presented the reflection and refraction (or transmission) angles for each incident angle. Also, the expressions in these figures suggest the performed conversions from these angles referenced to the surface normal to the angles referenced to the zero.

The same algorithm is used to compute the wavevector imaginary part (constant amplitude plane normal vector). Every step in this algorithm is performed, using a different equation to compute the reflection and refracted angles ψ, accordingly to the proposed methodology, on chapter 3.

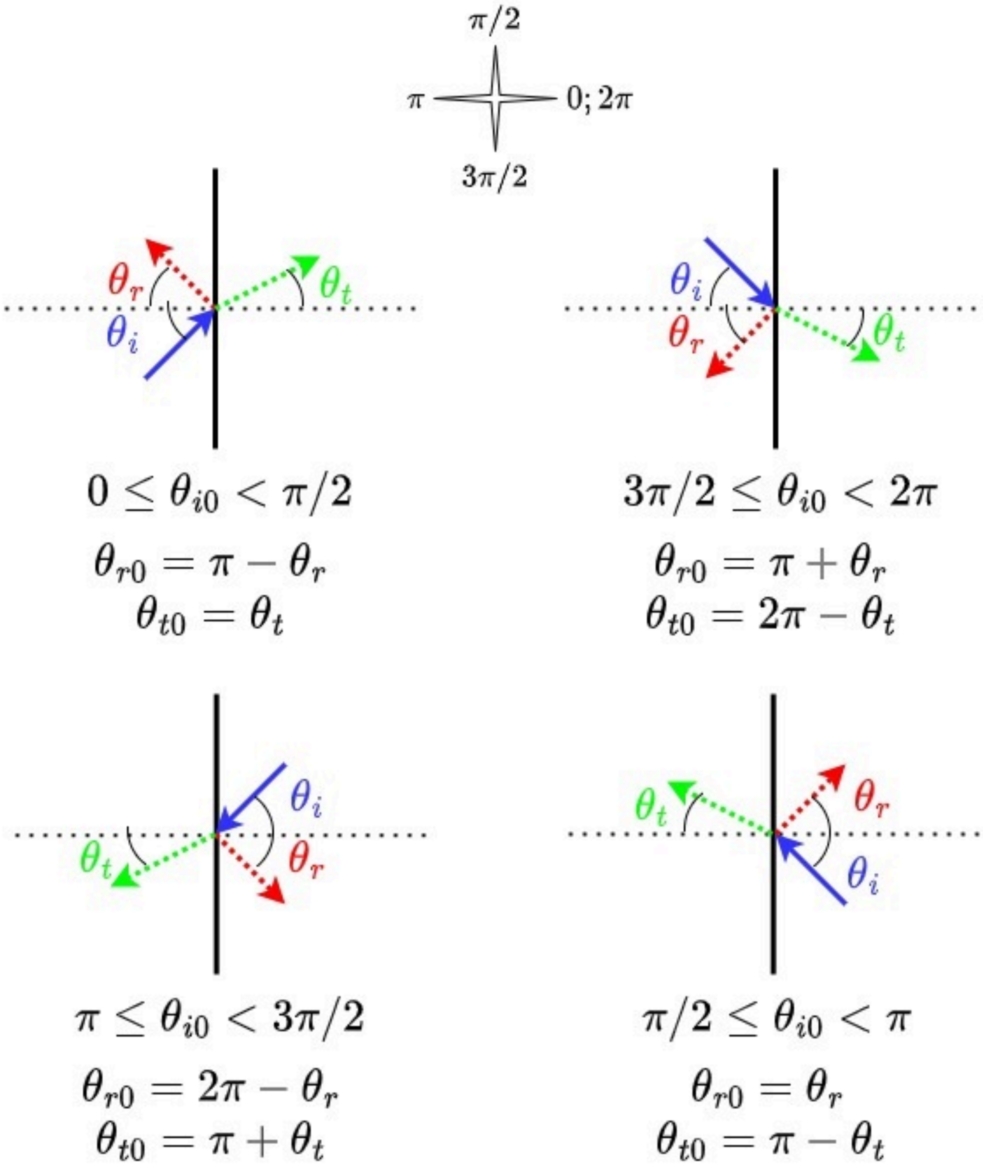

Figure A.1: Vertical interfaces: incident angle (blue, θ_i), reflection angle (red, θ_r) and transmission/refraction angle (green, θ_t) referenced to the surface normal. Conversion from these angles into its directions referenced to zero: incident direction (blue, θ_{i0}), reflection direction (red, θ_{r0}) and transmission/refraction direction (green, θ_{t0}).

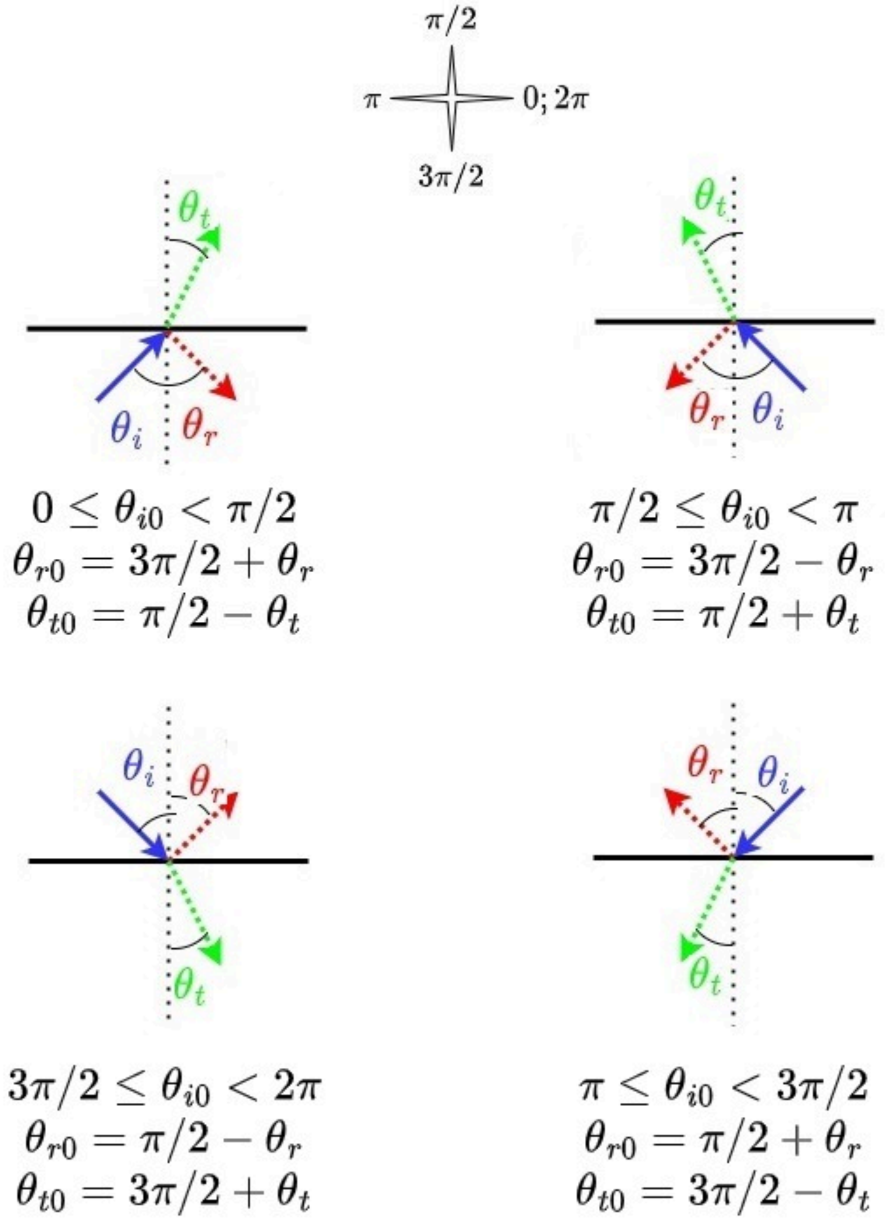

Figure A.2: Horizontal interfaces: incident angle (blue, θ_i), reflection angle (red, θ_r) and transmission/refraction angle (green, θ_t) referenced to the surface normal. Conversion from these angles into its directions referenced to zero: incident direction (blue, θ_{i0}), reflection direction (red, θ_{r0}) and transmission/refraction direction (green, θ_{t0}).

B

Metallic Nanostructures Inclusion to Improve Energy Harvesting in Silicon

The research aims to analyse the role of surface plasmon polaritons in the increase of transmittance of this kind of nanostructures. Furthermore, there is also the research goal of verifying in which wavelengths the structure transmits more energy to the semiconductor layer, which is excellent for harvesting energy. Then, the inclusion of nanoparticles on the top of solar cells is going to be discussed based on the illustrated results.

The analysed semiconductors are the amorphous silicon (a-Si) and the crystalline silicon (c-Si), respectively modelled by Schinke et al. and Gao et al. Gold, silver, aluminium and copper are the used metals, which are modelled by the Rakic's complex electrical permittivity model based on Drude-Lorentz model. All of these models are obtained from the refractive index database [53]. Air is used as dielectric as $\epsilon_{air} = 1 + j0$.

B.1 Results

Both a-Si and c-Si are going to be analysed. For that reason, the first subsection is to describe the differences between their optical responses. Only after that, the inclusion of metal layers on top of the semiconductor ones is going to be analysed, being presented and discussed in the second subsection.

B.1.1 Air-Semiconductor Interface

Figure B.1 illustrates the analysed structure, where $\hat{\boldsymbol{s}}$ is the surface normal vector, $\bar{\boldsymbol{k}}$ is the complex wavevector, and θ and ψ are respectively the angles of the vectors of equal phase and amplitude referenced with $\hat{\boldsymbol{s}}$. The analysed wavevectors represent TM waves, due to the fact that SPP are only excited by polarised waves [7, 16, 65, 67].

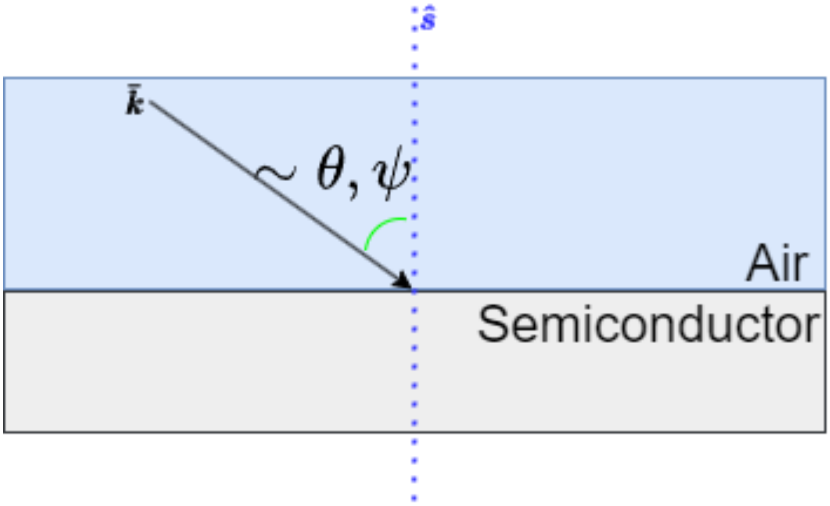

Figure B.1: Air-semiconductor interface.

Even though the a-Si absorbs for wavelengths higher than 800 nm and c-Si than 1100 nm, the aim of this research work is to analyse if the inclusion of metals on top of silicon layers may decrease its reflectance and consequently increase the absorption probability.

Figure B.2 illustrates the reflectance of silicon layers as a function of the incident angle and wavelength. It is observable that both a-Si and c-Si have small reflectance values at the infrared region. Also, both have an abrupt transition at the infrared: around 2000 nm for a-Si and around 1500 for c-Si.

Furthermore, a-Si presents small reflectance for incident angles between 60º and 80º along all the analysed ranges, being that angle's range increases in the microwave regime where a-Si transmits approximately 80% of the radiation that is incident with an angle between 20º and 80º.

On the other hand, in general, c-Si reflects more light than a-Si in all the analysed ranges. Additionally, it is possible to verify that at the visible spectral region, the reflection of c-Si tends to have high values, 10% to 20% higher than the ones obtained for the a-Si.

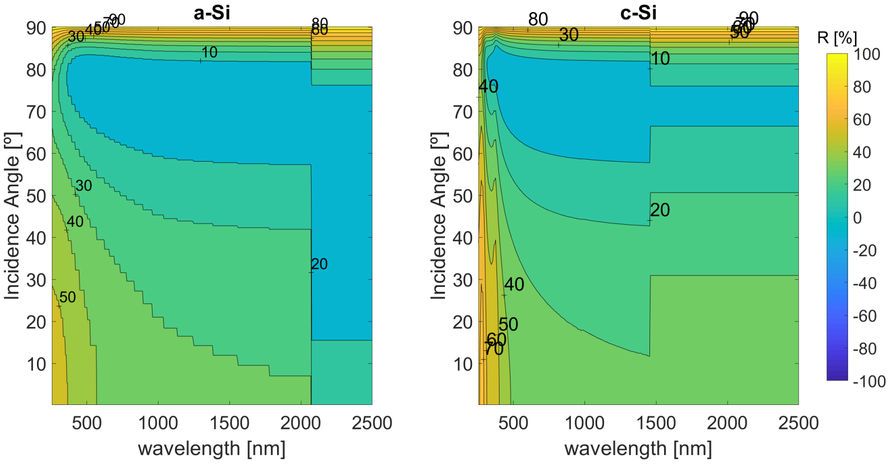

Figure B.2: Reflectance in function of the wavelength and incident angle for Air-(a-Si) and Air-(c-Si) interfaces.

This illustrates the fact that most of the radiation that is incident on a silicon solar cell is reflected back, decreasing the energy harvesting and (external) efficiencies.

However, the main conclusion to point out is that by decreasing the silicon reflectance, more light is available for absorption processes. That reflectance is huge where silicon has an excellent absorption coefficient, which is the reason to exploit novel methods to reduce it (or equivalently, to increase silicon transmittance).

B.1.2 Air-Metal-Semiconductor Structures

One possibility is to place nanostructures on top of the silicon layers. In this research work, the multilayer structure composed of air-metal-silicon is analysed in order to understand the possibility of increasing the radiation on the silicon layer. In figure B.3 is presented the structure under analysis, which is similar to figure B.1 with the inclusion of the metal layer.

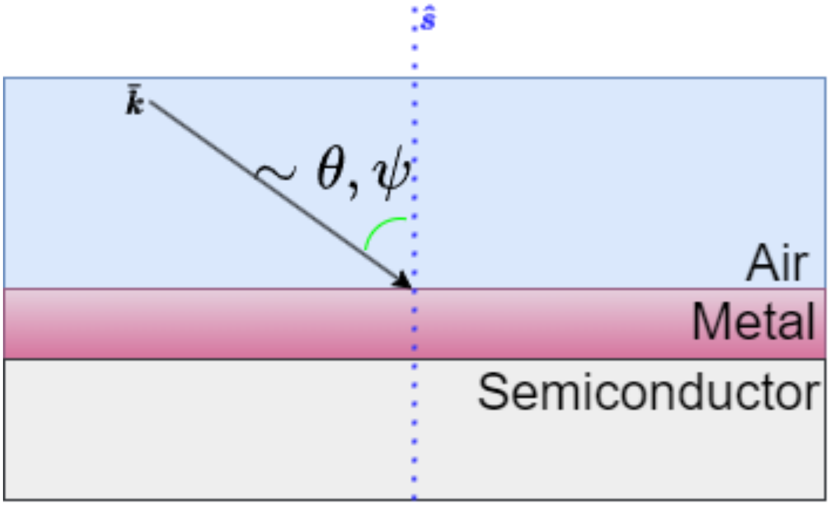

Figure B.3: Air-Metal-Semiconductor structure.

The main hypothesis is to increase the structure transmittance to the silicon layer, taking into account the surface plasmon polaritons excitation and propagation [7, 16, 67], similar to what is done in Kretschmann's structures [7].

To analyse the role and the hypothesis to increase transmittance into silicon, four metals are going to be analysed: gold, silver, aluminium and copper. All of them are characterised by the Rakic's Drude-Lorentz model, where the complex electrical permittivity is a function of wavelength [53]. Furthermore, four different metal thicknesses are considered in order to verify the influence of it on the transmittance to the silicon layer.

This research aims to analyse in which regions the inclusion of nanoparticles or nanostructures on top of silicon layers brings optical benefits and to clarify some useful optical mechanisms to increase solar cell efficiencies. For that purpose, the variation of reflectance is analysed considering the values in B.2 as a reference. It means that, for instance, the higher the variation (between 100% and -100%), the more radiation is transmitted to the silicon layer, i.e., less reflectance.

B.1.2.A Air-metal-(a-Si) Structures

The first analysed multi-layer structures are the air-metal-(a-Si), being the gold, silver, aluminium and copper results in figures B.4, B.5, B.6, B.7, respectively.

In all these figures it is observable that the reflectance tends to increase, being the graphics being more bluish than yellowish. However, the exception is in the visible spectral region, where light is much more transmitted to the silicon layer.

The results in figure B.4 suggest that in the visible region, the structure's reflectance decreases 10% to 20%, meaning that it is possible to reach values around 20%. It is verified with thicknesses of 20 and 50 nm and this effect is lost for small thicknesses, as 5 nm and 10 nm. Then, it is also pointed out that structure optical behaviour is quite influenced by the metal thickness

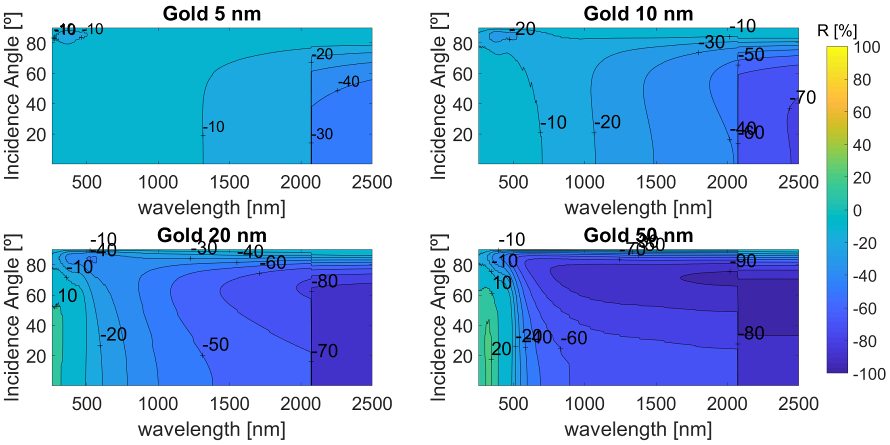

Figure B.4: Reflectance in function of the wavelength and incident angle for the Air-Gold-(a-Si) structure.

On the other hand, using silver, the results in figure B.5 suggest much higher positive variations, meaning that the structure's reflectance decreases. These values are around 40% indicating that the reflectance takes values around 10%. Also, comparing them with the gold ones, one should note that the wavelength range of this effect is tighter, but the incident angle range is wide. This means that it is possible to transmit to the silicon layer more photons with the same energy but fewer photons with different energy.

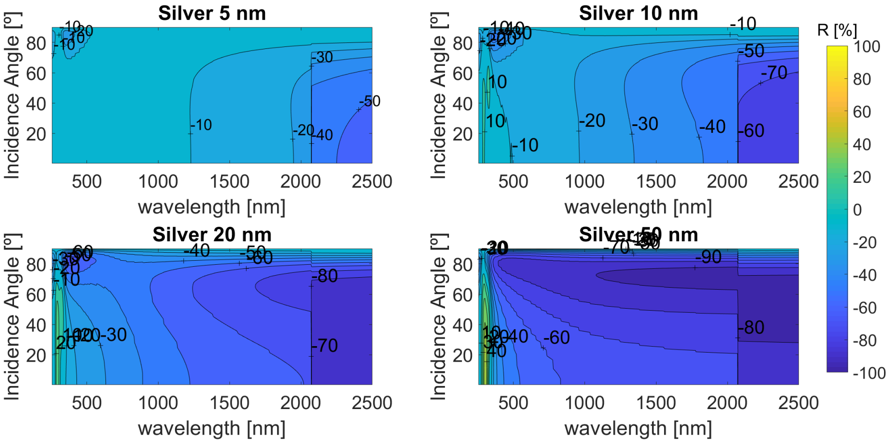

Figure B.5: Reflectance in function of the wavelength and incident angle for the Air-Silver-(a-Si) structure.

The aluminium analysis is more peculiar. It is possible to verify the aluminium's resonance near 800 nm [67]. Nonetheless, the transmission to the silicon layer is only conceivable for huge incident angles but in contrast with the previous examples, it happens at the infrared spectral region and for thinner metals. Furthermore, the values are not as huge as the ones verified before, around 10%. Moreover, this reflectance improvement is observed where its reference value is huge, meaning that the use of aluminium does not allow us to increase the radiation on the silicon layer, by transmission.

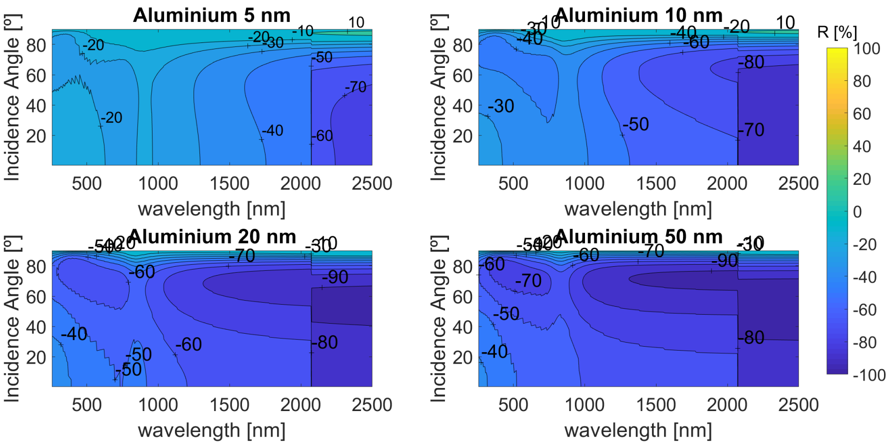

Figure B.6: Reflectance in function of the wavelength and incident angle for the Air-Aluminium-(a-Si) structure.

The last tested metal is copper, which is quite similar to gold in terms of its complex electrical permittivity. For that reason, it is expected to present similar optical responses. These expectations are confirmed by the results in figure B.7, from which one may take similar conclusions to the ones presented in figure B.4.

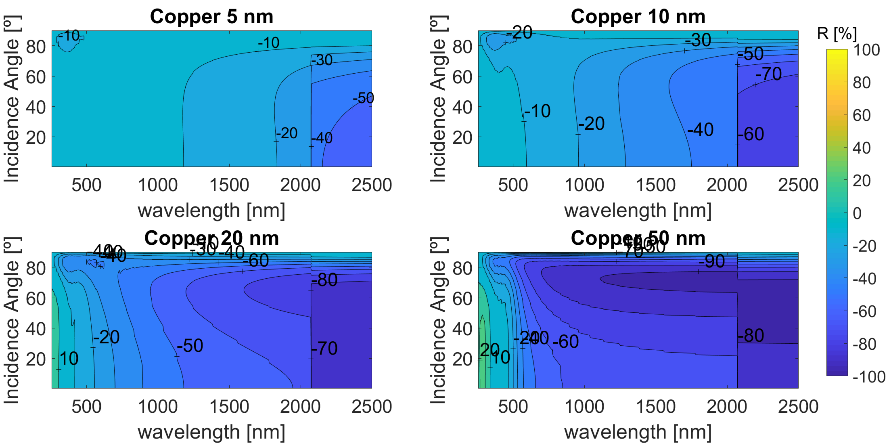

Figure B.7: Reflectance in function of the wavelength and incident angle for the Air-Copper-(a-Si) structure.

B.1.2.B Air-metal-(c-Si) Structures

Next, it is intended to perform a similar analysis but with c-Si in the semiconductor layer, considering the same metals as before. The results are presented in figures B.8, B.9, B.10 and B.11 respectively for gold, silver, aluminium and copper.

For the gold scenario, presented in figure B.8, it is possible to verify that the reflectance improvements occur at the visible, allowing the energy harvesting in the semiconductor layer. These results also show that the wave interference dominates the reflectance in contrast with the metals' absorption. In this case, the decrease on the metal's thickness led to low reflectance due to the phase of the waves after the metal-semiconductor interface.

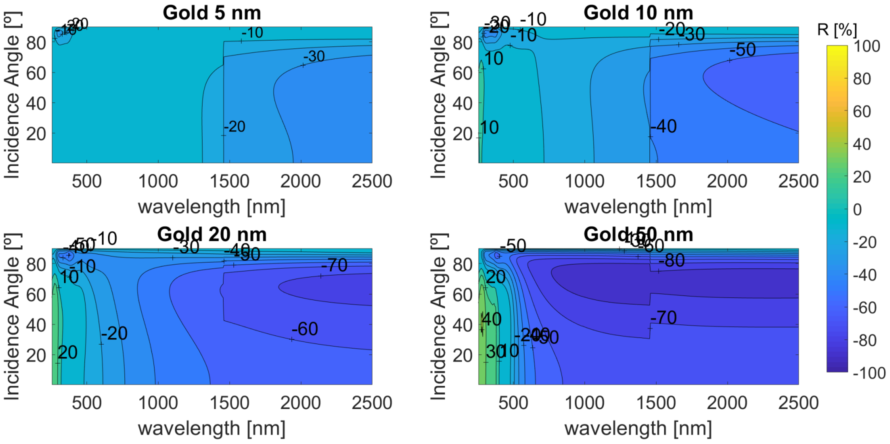

Figure B.8: Reflectance in function of the wavelength and incident angle for the Air-Gold-(c-Si) structure.

Figure B.9 presents the results for silver, which tends to be higher than the gold ones. As shown for 20 nm and 50 nm, silver suggests to have lower reflectance than gold (high results) however, for small thicknesses this effect also tends to be more neglectable.

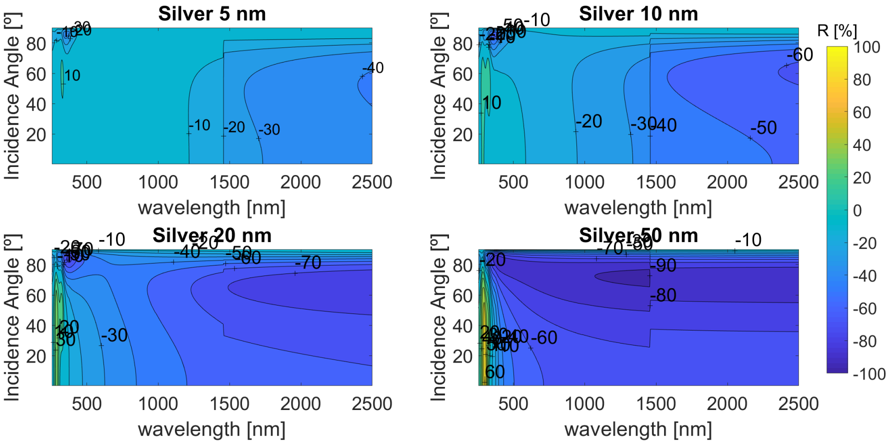

Figure B.9: Reflectance in function of the wavelength and incident angle for the Air-Silver-(c-Si) structure.

The differences between aluminium to the other simulated metals are already observed in the previous structure. It is stated that the structure with aluminium allows it to transmit more energy at high incident angles. The resonance near 800 nm is detected in figure B.10 but it does not allow to increase energy on the semiconductor in comparison to the case without metal.

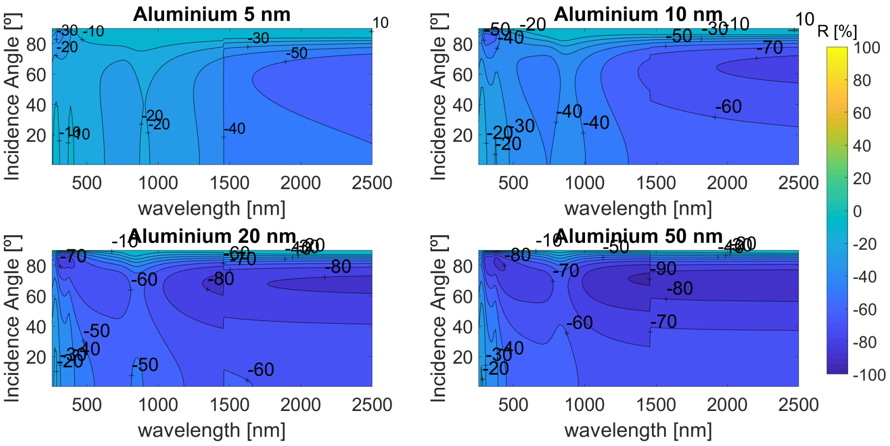

Figure B.10: Reflectance in function of the wavelength and incident angle for the Air-Aluminium-(c-Si) structure.

In figure B.11 are the copper results. As previously suggested, copper and gold have identical results due to their similar complex electrical permittivity. Nonetheless, it is visible that in the highest improvements, copper performance occurs for a wide incident angle range. It is quite visible for 20 nm and 50 nm, for short wavelengths.

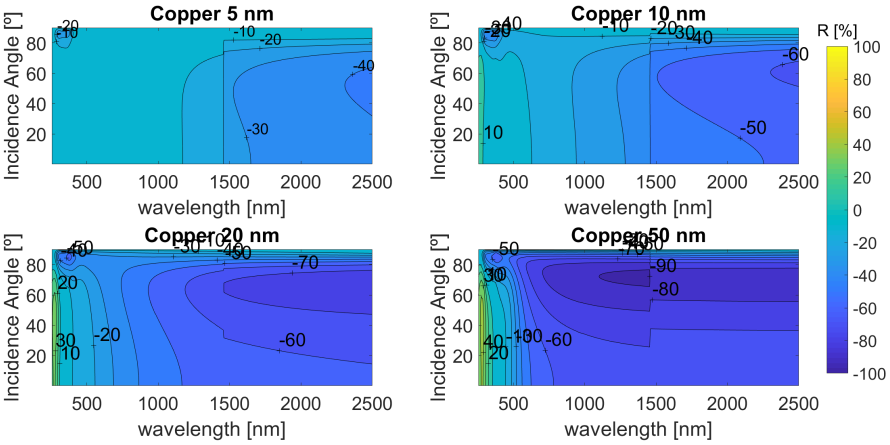

Figure B.11: Reflectance in function of the wavelength and incident angle for the Air-Copper-(c-Si) structure.

B.2 Discussion

This article aims to contribute to the understanding of the nanostructures' placement on semiconductor layers. For 4 different metals, dielectric-metal-semiconductor structures are studied according to a novel methodology capable of better modelling the energy propagation in absorbing media.

The inclusion of metallic nanostructures on silicon layers is been studied to improve energy harvesting in semiconductor layers. The results presented in the previous section allow us to analyse the importance of the excitation and propagation of surface plasmon polaritons. The inclusion of these metal layers on top of silicon ones allows it to divide its benefits into two different regions. First, the most common and expected one is, that metal can reflect radiation for long wavelengths, meaning that it is possible to concentrate radiation using reflection. On the other hand, for short wavelengths, the propagation of surface plasmon polaritons on the metal leads to the increase of its transmissivity and consequently the caption of energy after the metal-semiconductor interface. Thus, the other working region is near the metal resonances, where the structures have huge transmittance and consequently, it is possible to concentrate radiation on the semiconductor layer near its interface with the metal.

It is similar to characterising the performance of these structures as an optical window or filter, adjustable by changing the metal and its thickness. Regarding the metal thicknesses, it is suggested that for small values the structure reflects more energy. It must be useful to concentrate radiation based on the metal's reflectivity. On the other hand, the 20 nm and 50 nm metals presented results that besides the reflectance improvement in the infrared region, allow for the transmission of energy in the visible and ultraviolet spectral regions.

The random introduction of metallic nanostructures (for instance, nanoparticles) on top of the absorbing layer might be optimised considering results like the ones presented in this article. Taking into account a geometrical approach as proposed, it is possible to analyse and optimise structures placement and dimensions.

Regarding the differences between gold and copper, it is stated that their results are quite similar due to their identical electrical permittivity. However, as verified in the previous study [67], copper has 4 resonances with non-neglectable strength, whereas gold has only 3. For that reason, the copper response seems to have better results, namely on the incident angle range. Gold is more chemically stable, leading to more feasibility and reproducibility. However, copper has a lower cost, which gives us another perspective on the problem.

Aluminium seems to be the more indicated metal to reflect energy. Nonetheless, it might transmit energy that is incident on the perpendicular, which is also a quite important specification, for instance, to collimate light.

Silver allows us to have higher transmissivity in a small spectral region. Its resonances are closer than the gold or copper ones and consequently, the wavelength range is more restricted.

The inclusion of the metal layer may decrease the reflectance by at least 10%, reaching values higher than 60%. The presented charts allow us to analyse the materials, wavelengths and incident angles where reflectance is decreased.

Considering these reasons, and generically speaking, gold seems to be the best metal to transmit more energy and design optical windows in UV-Visible range, whereas aluminium may be useful to reflect radiation and concentrate it in a smaller area.

The inclusion of metal layers brings benefits to the photodetection since more energy is available in the absorbing layer. Considering this approach, the detection of specific wavelengths may be improved by introducing metals in the detectors.

C

The Impact of Nanoantennas on Ring Resonators' Performance

From Maxwell's equations it is possible to determine the electromagnetic field profile in the waveguides, being them straight or rings.

The coupling analysis is a well-known field. The coupling between two waveguides (straight or rings) is discussed in [6, 90–93].

This research work aims to analyse the performance of ring resonators and how nanoantennas may be included to improve it. As illustrated in figure C.1, the optical device is formed by one input (port 1) and three different outputs (port 2, 3 and 4) [90]. The straight waveguides are characterised by a height h_s, a width w_s and a complex refractive index n_s. In the same way, the ring is defined by a radius R, a width w_c and a complex refractive index n_c. R and h_s are unrelated parameters, despite of in yhe figure they seems to be related. The minimum distance between the straight and the ring waveguides is given by the distance, g. The substrate is characterised by a complex refractive index n_{sub} [90].

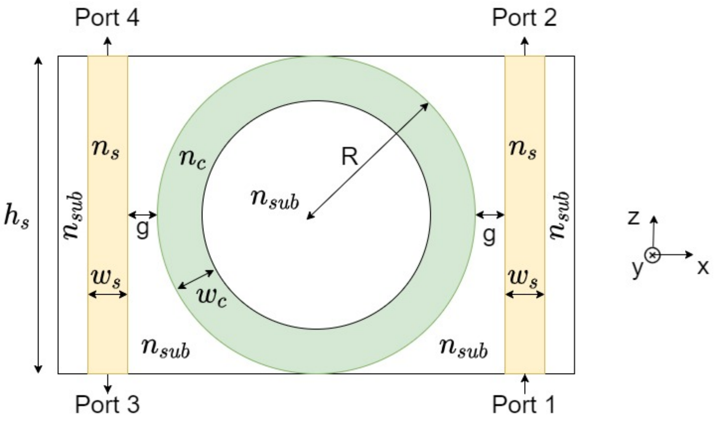

Figure C.1: Illustration of simulated problem.

An electromagnetic field input at the straight waveguide creates a sinusoidal profile along all the waveguide's height. Helmholtz equation, shown in equation C.1, describes the propagation inside the straight waveguide, where ϕ is $\bar{E}_z$ at TM modes (and $\bar{H}_z = 0$) and it is $\bar{H}_z$ for TE modes (and $\bar{E}_z = 0$) [6, 90–92, 94]. The spacial phase constant k (propagation constant) is decomposed regarding $k^2 = k_x^2 + k_y^2 + k_z^2$ and ∇_T is the transversal Laplacian. The solutions of Helmholtz equations are presented in equation C.2, where $\bar{A}_c$, $\bar{B}_c$, $\bar{C}_c$ and $\bar{D}_c$ are complex constants, ω the angular frequency and t the time variable [6, 90–94].

$$\nabla_T^2 \phi + (k^2 - k_z^2)\phi = 0 \tag{C.1}$$

$$\phi = \left(\bar{A}_c \, cos\left(k_x x\right) + \bar{B}_c \, sin\left(k_x x\right)\right) \left(\bar{C}_c \, cos\left(k_y y\right) + \bar{D}_c \, sin\left(k_y y\right)\right) e^{j(\omega t - k_z z)} \tag{C.2}$$

Evanescent waves propagate from straight waveguide walls, according to expression C.3, where $\bar{E}_c$

is a complex constant and $d = x, y$ that should be the perpendicular direction of the wall [90, 93, 94]. Also, α_d is the attenuation constant along the direction d [90, 93, 94].

$$\phi = \bar{E}_c e^{-\alpha_d |d|} e^{j(\omega t - k_z z)} \tag{C.3}$$

The ring's electromagnetic field profile is also well-known, being characterised by Bessel equations [6, 90, 93]. First, the characteristic equation is given by the equation C.4, where r is the radial variable, n is the refractive index and k the propagation constant. In this case, $\phi = \bar{E}_y$ for TE modes and $\phi = \bar{H}_y$ for TM modes. Also, γ is the complex propagation constant. The solutions of this characteristic equation is presented in equation C.5, being $\nu = \gamma R$ the angular number modes [6, 90, 93]. Thus, it is possible to analyse the electromagnetic field profile, that is described by Bessel functions of the first kind J, second kind Y and Hankel functions of second kind, $H^{(2)}$ [6, 90, 93]. Similarly to the previous analysis, $\bar{F}_c$, $\bar{G}_c$, $\bar{L}_c$ and $\bar{N}_c$ are complex constants [6, 90, 93].

$$\frac{\partial^2 \phi}{\partial r^2} + \frac{1}{r}\frac{\partial \phi}{\partial r} + (n^2 k^2 - \frac{\gamma^2 R^2}{r^2})\phi = 0 \tag{C.4}$$

$$\begin{cases} \bar{F}_c J_\nu \left(n_{sub} kr\right), \, 0 \leqslant r \leqslant R^- \\ \bar{G}_c J_\nu \left(n_c kr\right) + \bar{L}_c Y_\nu \left(n_c kr\right), \, R^- \leqslant r \leqslant R^+ \\ \bar{N}_c H_\nu^{(2)} \left(n_{sub} kr\right), \, R^+ \leqslant r \end{cases} \tag{C.5}$$

Thus, to obtain the coupled electromagnetic field profile, all the complex constants should be determined and the coordinate system should be uniformed (the straight profile should be analysed twice, since there are two different straight waveguides in different positions) [6, 90, 93]. One of the complex constants should be the input field value (usually on one straight waveguide). The others should be obtained imposing the boundary conditions of Maxwell's equations along all the space.

Published in [93] is a deeper analytical and numerical analysis for the Ring Resonator performance, with several topologies and for different materials. Nonetheless, the focus of this appendix is the inclusion of nanoantennas in Ring Resonators, which is analysed in [93].

Analysing the previous equations, it is verified that there are two possible regions to place the nanoantenna: on the coupling region between the straight waveguide and the ring and inside the ring. It is intended to compare the output spectra when varying the nanoantenna's structure parameters (periodicity, hole diameter, and thickness). The set of parameters' values is called configuration. Moreover, each nanoantenna placement region is here defined as topology. Thus, there will be three topologies: parallel to the straight waveguide on the coupling region, perpendicular to the straight waveguide on the coupling region and radially displaced inside the ring.

Since the coupling region is defined by evanescent waves, both waveguides need to be close. Placing the nanoantenna between them, it is possible to amplify and concentrate the electromagnetic field, increasing the coupling effects.

The response of this kind of devices is typically presented as a relation between the output spectrum and the input one. Hiremath's structure only considered active power, analysing the ratio between the transmitted and the incident one. In this article, scattering parameters (S-parameters) are used. Each port is related on port 1 (input) by its S_{p1}, being p the number of the output port. Then, it is possible to observe magnitude spectra (absolute value of the power ratio), but also to trace the phase spectrum, which is very important to telecommunications applications.

Moreover, internal losses are analysed using S-parameters, regarding expression C.6. Mainly, internal losses on the device are due to the ring's curvature (leading to complex propagation constants) and dielectric losses. The inclusion of nanoantennas are an attempt to diminish the total losses and even to create gain (not in just one port, but in the complete device).

$$|S_{internal}| = 1 - |S_{21}| - |S_{31}| - |S_{41}| \tag{C.6}$$

C.1 Results

C.1.1 Optical Response Without Nanoantenna

Using a Finite Element Tool, simulations are performed. Port 1 is excited with 1 W power and a single wavelength/frequency. To obtain the spectra on the other ports, this generated wavelength is swept with a step of 0.1 nm, for all the wavelength intervals presented on the following figures. For the substrate the mesh is described by a maximum element size of 85.1 nm and a minimum of 0.28 nm, with a maximum curvature factor of 0.2 and a maximum element growth factor of 1.1. For the ring and straight waveguide, the values are the same, except the maximum element size that is 35.4 nm. These mesh values are typically associated to an extremely fine mesh description. Moreover, all the external boundary conditions are scattering boundary conditions, in order not to consider internal reflections.

Considering the structure analysed by Hiremath [90], presented in figure C.1, described by $R = 2.5\text{µm}$, $g = 0.232\text{µm}$, $w_c = w_s = 0.3\text{µm}$ and $h_s = 14\text{µm}$, it is possible to verify that the designed model corroborate with his simulations based on analytical bent modes and couple model theories. Both obtained results are presented in figure C.2 and C.3. To obtain these responses, both straight and ring waveguides have a real refractive index of $n_s = n_c = 3.2$ and the substrate has $n_{sub} = 1$.

Hiremath's simulation method only consider a small area around the coupling region. Thus, there are differences in the values, despite of the resonant peaks are at the same wavelengths. In this article it is considered all the device, analysing field profiles as presented on figure C.4.

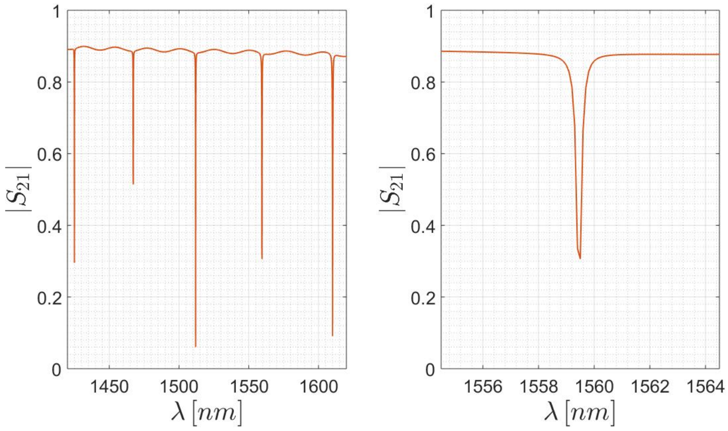

Figure C.2: Resonant spectra from $|S_{21}|$ for a wavelength range of [1420;1620] nm.

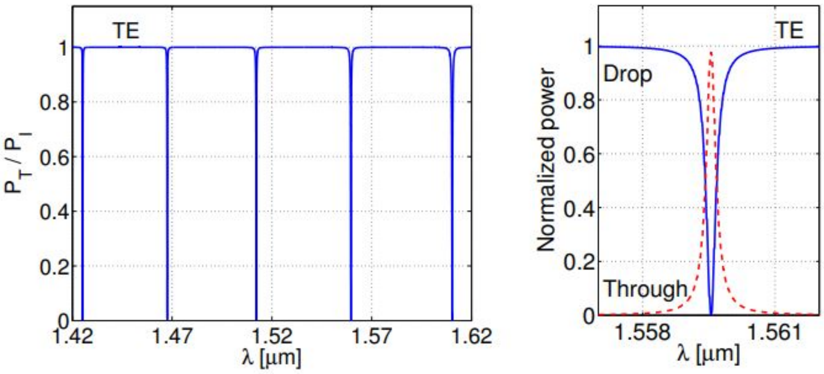

Figure C.3: Resonant spectra took by Hiremath from $|S_{21}|$ for a wavelength range of [1420;1620] nm [90].

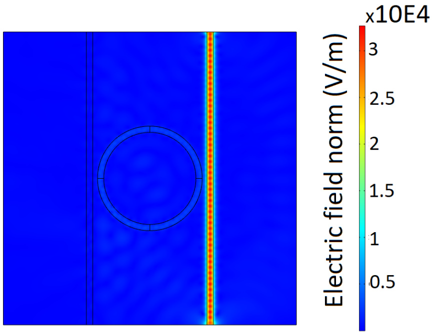

Figure C.4: Electric field profile (without nanoantenna for $\lambda = 1600\mathrm{nm}$).

C.1.2 Optical Response With Nanoantenna

Materials can be optically described by their complex refractive index. Furthermore, the complex refractive index, both real and imaginary part, depend of the frequency (or wavelength). In order to improve simulations' results, taking more realistic results, all materials are characterised by a frequency-dependent complex refractive index. To follow Hiremath's results, it is considered silicon (Si, modelled by Pierce and Spicer in 1972) waveguides and quartz (SiO_2, modelled by Lemarchand in 2013), since their complex refractive index has a quite small imaginary part and a real part around the previous simulations values. Moreover, it is studied the impact of a metal-made nanoantenna. It is decided to use gold (Au, modelled by Rakic using Drude-Lorentz equations), since it is a chemically stable metal.

The ring resonator performance is analysed with and without the gold nanoantenna. As referred before, three different nanoantennas' topologies are simulated, not simultaneously but as suggested on figure C.5: (i) in the substrate between the straight waveguide and the ring, in both sides of the ring and parallel to the straight waveguide (blue circle on figure C.5, but on both sides); (ii) in the substrate between the straight waveguide and the ring, in both sides of the ring and perpendicular to the straight waveguide (green circle on figure C.5, but on both sides); (iii) on the ring, radially distributed according to an angle θ of displacement (yellow circle on figure C.5).

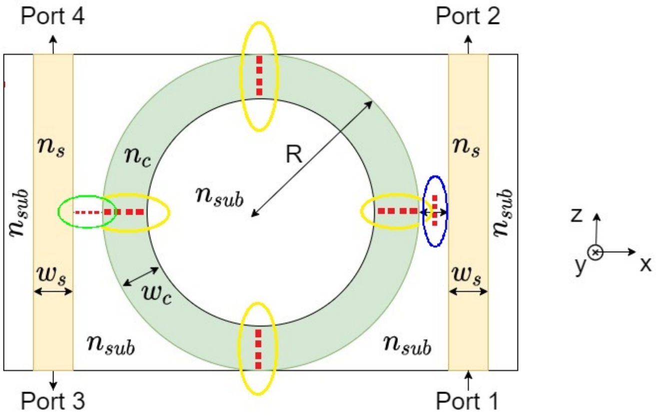

Figure C.5: Illustration of simulated problem with nanoantenna: Gold Nanoantenna Parallel to the Rectangular Waveguide (blue, but on both sides of the ring); Gold Nanoantenna Perpendicular to the Rectangular Waveguide (green, but on both sides of the ring); Gold Nanoantenna on the Ring (yellow, with an displacement angle θ).

C.1.2.A Gold Nanoantenna Parallel to the Rectangular Waveguide

The nanoantenna is placed between the straight waveguide and the ring. Several topologies are analysed, regarding the nanoantennas' periodicity, hole diameter, thickness and number of holes/slits.

In figure C.6 is showed the absolute value of S_{21}. Based on this figure it is possible to verify that there are only three configurations at seven with a better resonant response than the one obtained without nanoantenna, in terms of peak magnitude. Furthermore, for this port, this improvement is only observed for one resonance wavelength. Moreover, it is quite visible that the nanoantenna's parameters can be tuned to adjust the wavelength resonance.

When analysed the phase of S_{21} it is possible to visualised significant improvements on it, since several applications, namely on telecommunications, need to guarantee a constant group delay. Once again, nanoantenna's parameters can tune the phase response of port 2 and consequently the group delay. The group delay is the time envelope amplitude delay of several sinusoidal components. A non-constant group delay means that a signal characterised by several components at different frequencies will suffer distortion, since each component will be delayed for different amount of time. The group delay is mathematically defined as $\tau_g(\omega_0 = 2\pi f_0) = -\frac{d\phi}{d\omega}|_{\omega=\omega_0}$. Thus, if the phase is more linear, this means that the group delay will be more constant. As verified in the phase response without nanoantenna presented in figure C.7, the phase around the resonant wavelength has a huge variation. Based on the same figure, it is possible to observe that nanoantenna configuration can tune the phase spectrum and in all the studied situation, the phase response became more linear on port 2.

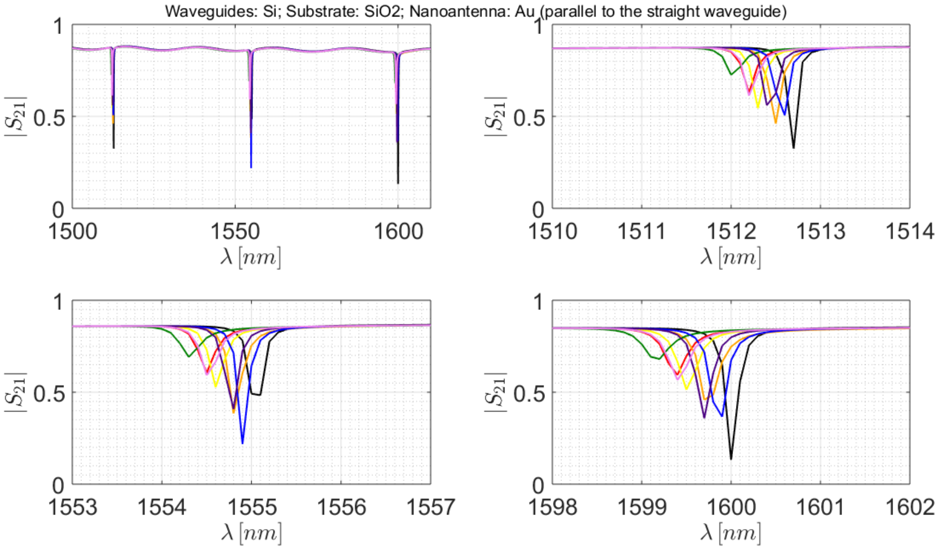

Figure C.6: Resonant spectra of $|S_{21}|$: without nanoantenna (black); $a_0 = 100\text{nm}$, $d = 25\text{nm}$, $t = 20\text{nm}$ and $n = 7$ (red); $a_0 = 100\text{nm}$, $d = 50\text{nm}$, $t = 20\text{nm}$ and $n = 3$ (orange); $a_0 = 100\text{nm}$, $d = 50\text{nm}$, $t = 20\text{nm}$ and $n = 7$ (yellow); $a_0 = 100\text{nm}$, $d = 50\text{nm}$, $t = 50\text{nm}$ and $n = 7$ (green); $a_0 = 100\text{nm}$, $d = 75\text{nm}$, $t = 20\text{nm}$ and $n = 3$ (blue);$a_0 = 100\text{nm}$, $d = 75\text{nm}$, $t = 20\text{nm}$ and $n = 7$ (purple); $a_0 = 100\text{nm}$, $d = 75\text{nm}$, $t = 50\text{nm}$ and $n = 7$ (lilac).

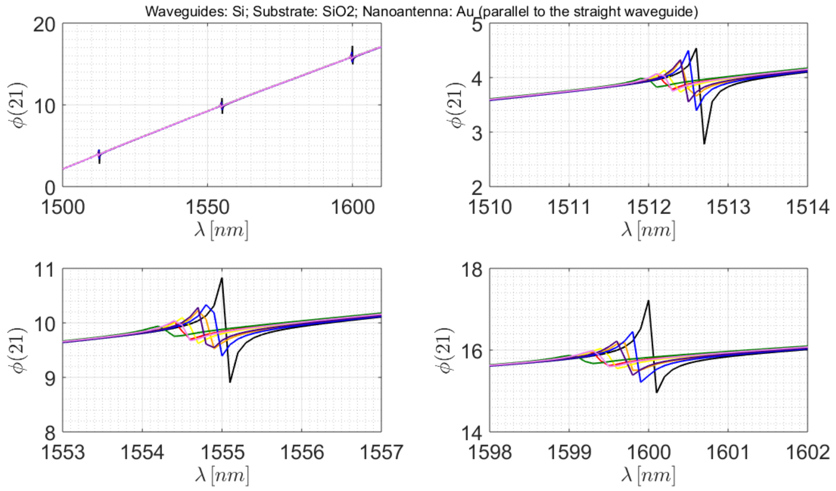

Figure C.7: Resonant spectra of the phase of S_{21} in degree: without nanoantenna (black); $a_0 = 100\text{nm}$, $d = 25\text{nm}$, $t = 20\text{nm}$ and $n = 7$ (red); $a_0 = 100\text{nm}$, $d = 50\text{nm}$, $t = 20\text{nm}$ and $n = 3$ (orange); $a_0 = 100\text{nm}$, $d = 50\text{nm}$, $t = 20\text{nm}$ and $n = 7$ (yellow); $a_0 = 100\text{nm}$, $d = 50\text{nm}$, $t = 50\text{nm}$ and $n = 7$ (green); $a_0 = 100\text{nm}$, $d = 75\text{nm}$, $t = 20\text{nm}$ and $n = 3$ (blue);$a_0 = 100\text{nm}$, $d = 75\text{nm}$, $t = 20\text{nm}$ and $n = 7$ (purple); $a_0 = 100\text{nm}$, $d = 75\text{nm}$, $t = 50\text{nm}$ and $n = 7$ (lilac).

Similarly to the port 2 analysis, port 3 response is worst with nanoantenna than without it, regarding the comparison between the absolute values of S_{31} resonant peaks illustrated in figure C.8. On the other hand, it is notorious even the phase response does not improve, since it is only observed a shift of phase spectra in figure C.9.

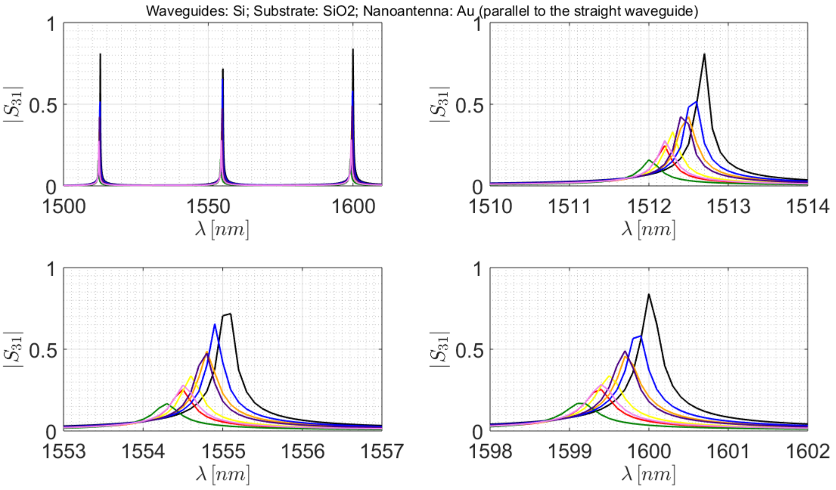

Figure C.8: Resonant spectra of $|S_{31}|$: without nanoantenna (black); $a_0 = 100\text{nm}$, $d = 25\text{nm}$, $t = 20\text{nm}$ and $n = 7$ (red); $a_0 = 100\text{nm}$, $d = 50\text{nm}$, $t = 20\text{nm}$ and $n = 3$ (orange); $a_0 = 100\text{nm}$, $d = 50\text{nm}$, $t = 20\text{nm}$ and $n = 7$ (yellow); $a_0 = 100\text{nm}$, $d = 50\text{nm}$, $t = 50\text{nm}$ and $n = 7$ (green); $a_0 = 100\text{nm}$, $d = 75\text{nm}$, $t = 20\text{nm}$ and $n = 3$ (blue);$a_0 = 100\text{nm}$, $d = 75\text{nm}$, $t = 20\text{nm}$ and $n = 7$ (purple); $a_0 = 100\text{nm}$, $d = 75\text{nm}$, $t = 50\text{nm}$ and $n = 7$ (lilac).

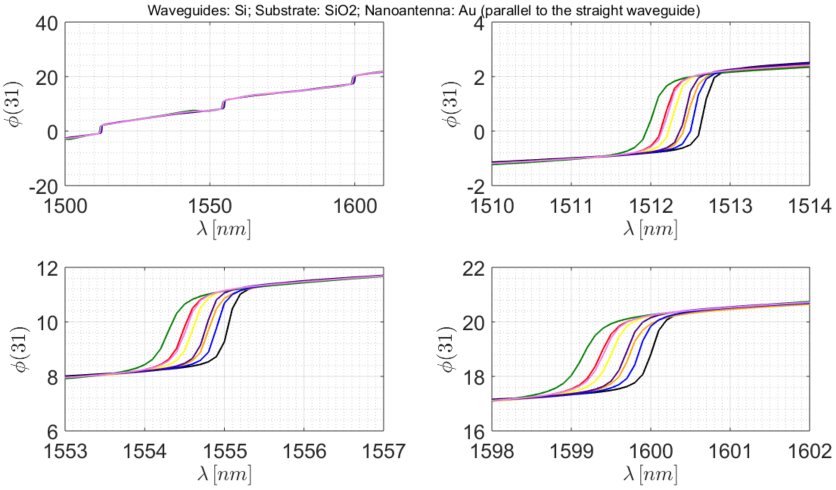

Figure C.9: Resonant spectra of the phase of S_{31} in degree: without nanoantenna (black); $a_0 = 100\text{nm}$, $d = 25\text{nm}$, $t = 20\text{nm}$ and $n = 7$ (red); $a_0 = 100\text{nm}$, $d = 50\text{nm}$, $t = 20\text{nm}$ and $n = 3$ (orange); $a_0 = 100\text{nm}$, $d = 50\text{nm}$, $t = 20\text{nm}$ and $n = 7$ (yellow); $a_0 = 100\text{nm}$, $d = 50\text{nm}$, $t = 50\text{nm}$ and $n = 7$ (green); $a_0 = 100\text{nm}$, $d = 75\text{nm}$, $t = 20\text{nm}$ and $n = 3$ (blue);$a_0 = 100\text{nm}$, $d = 75\text{nm}$, $t = 20\text{nm}$ and $n = 7$ (purple); $a_0 = 100\text{nm}$, $d = 75\text{nm}$, $t = 50\text{nm}$ and $n = 7$ (lilac).

For the nanoantenna parallel to the straight waveguide leads to huge improvements on port 4, as observed in figures C.10 and C.11. It is visible that there are at least two at seven configurations with better resonant peak magnitudes. Even more, phase response has not a general rule: there are nanoantenna's configurations leading to improvements as well as others with less benefits.

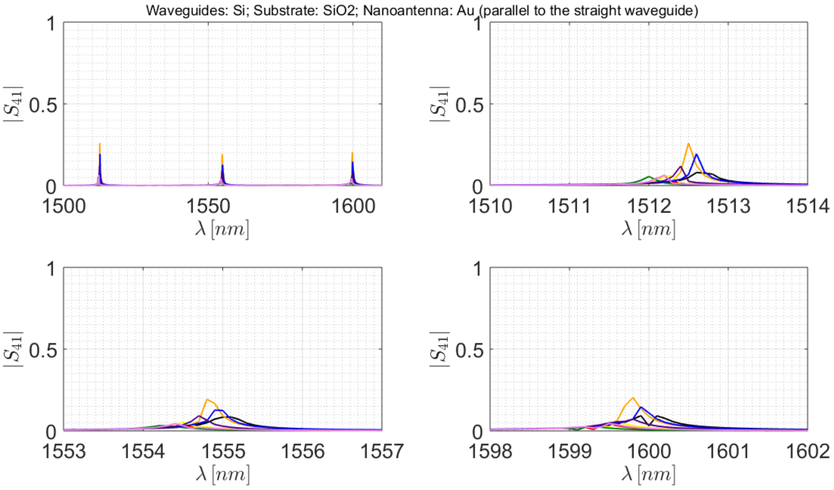

Figure C.10: Resonant spectra of $|S_{41}|$: without nanoantenna (black); $a_0 = 100\text{nm}$, $d = 25\text{nm}$, $t = 20\text{nm}$ and $n = 7$ (red); $a_0 = 100\text{nm}$, $d = 50\text{nm}$, $t = 20\text{nm}$ and $n = 3$ (orange); $a_0 = 100\text{nm}$, $d = 50\text{nm}$, $t = 20\text{nm}$ and $n = 7$ (yellow); $a_0 = 100\text{nm}$, $d = 50\text{nm}$, $t = 50\text{nm}$ and $n = 7$ (green); $a_0 = 100\text{nm}$, $d = 75\text{nm}$, $t = 20\text{nm}$ and $n = 3$ (blue);$a_0 = 100\text{nm}$, $d = 75\text{nm}$, $t = 20\text{nm}$ and $n = 7$ (purple); $a_0 = 100\text{nm}$, $d = 75\text{nm}$, $t = 50\text{nm}$ and $n = 7$ (lilac).

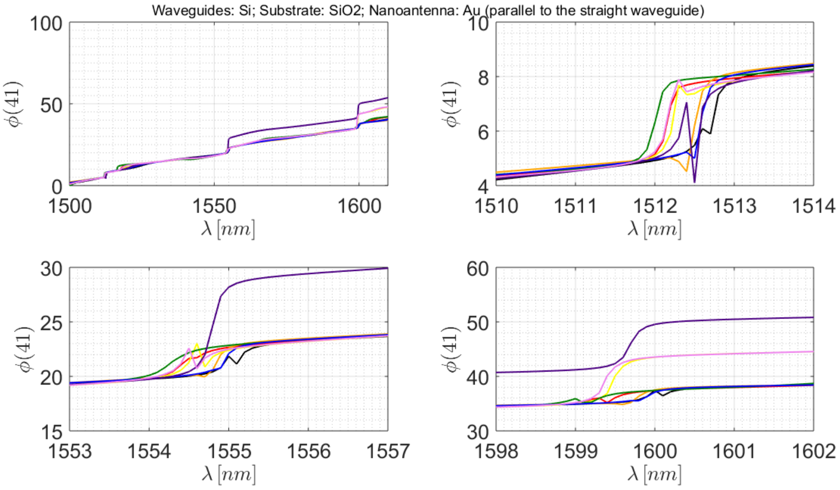

Figure C.11: Resonant spectra of the phase of S_{41} in degree: without nanoantenna (black); $a_0 = 100\mathrm{nm}$, $d = 25\mathrm{nm}$, $t = 20\mathrm{nm}$ and $n = 7$ (red); $a_0 = 100\mathrm{nm}$, $d = 50\mathrm{nm}$, $t = 20\mathrm{nm}$ and $n = 3$ (orange); $a_0 = 100\mathrm{nm}$, $d = 50\mathrm{nm}$, $t = 20\mathrm{nm}$ and $n = 7$ (yellow); $a_0 = 100\mathrm{nm}$, $d = 50\mathrm{nm}$, $t = 50\mathrm{nm}$ and $n = 7$ (green); $a_0 = 100\mathrm{nm}$, $d = 75\mathrm{nm}$, $t = 20\mathrm{nm}$ and $n = 3$ (blue);$a_0 = 100\mathrm{nm}$, $d = 75\mathrm{nm}$, $t = 20\mathrm{nm}$ and $n = 7$ (purple); $a_0 = 100\mathrm{nm}$, $d = 75\mathrm{nm}$, $t = 50\mathrm{nm}$ and $n = 7$ (lilac).

Lastly, it is analysed the internal power losses according to expression C.6. Based on figure C.12, it is observed that there are power losses on the device almost along all the spectrum (positive value of losses). However, at the three resonant peaks the total losses are negative, i.e., the output spectra (the sum of all output ports) have more energy/power than the input one. The impact of nanoantennas on port spectra has influence on this one. Thus, it is possible to verify that there are configurations for what the nanoantenna spoil the performance of the device, since there are losses along all the spectrum, including in the resonances. Nonetheless, there are configurations with a similar losses spectrum than without nanoantenna. Since the overall contribution of nanoantennas placement in terms of magnitude is not better than the topology without nanoantenna, it can be concluded that nanoantennas (placed parallel to the straight waveguide) can be helpful at least to adjust the resonance wavelengths, to level the linearity of the phase and consequently to impose a more constant group delay and to increase the peaks magnitude of port 4, as a consequence of a decrease of it on ports 2 and 3.

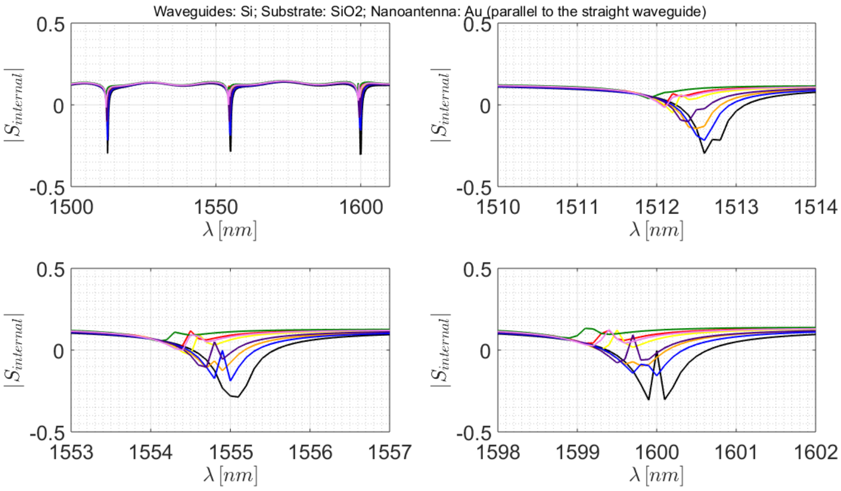

Figure C.12: Internal dissipated power, $|S_{internal}|$: without nanoantenna (black); $a_0 = 100\text{nm}$, $d = 25\text{nm}$, $t = 20\text{nm}$ and $n = 7$ (red); $a_0 = 100\text{nm}$, $d = 50\text{nm}$, $t = 20\text{nm}$ and $n = 3$ (orange); $a_0 = 100\text{nm}$, $d = 50\text{nm}$, $t = 20\text{nm}$ and $n = 7$ (yellow); $a_0 = 100\text{nm}$, $d = 50\text{nm}$, $t = 50\text{nm}$ and $n = 7$ (green); $a_0 = 100\text{nm}$, $d = 75\text{nm}$, $t = 20\text{nm}$ and $n = 3$ (blue);$a_0 = 100\text{nm}$, $d = 75\text{nm}$, $t = 20\text{nm}$ and $n = 7$ (purple); $a_0 = 100\text{nm}$, $d = 75\text{nm}$, $t = 50\text{nm}$ and $n = 7$ (lilac).

C.1.2.B Gold Nanoantenna Perpendicular to the Rectangular Waveguide

After analysing nanoantenna's configurations parallel to the straight waveguide, it is decided to analysed perpendicular configurations.

On figures C.13 and C.14 are presented the same optical response as analysed before for the topology without nanoantenna as well as two other spectra for two different nanoantenna configurations. For the set of results concerning the perpendicular topologies, it is assume that the nanoantenna is covering all the distance g, between the ring and the straight waveguide. Thus, just adjusting the number of holes, both periodicity and hole diameter will be defined. For this reason, it is only specified the number of holes, n.

Both configurations lead to a very similar absolute value spectrum. The conclusions for port 2 are quite identical than the previous state. In this case, resonant peaks magnitudes are worst with nanoantenna than without it and the phase response became more linear when nanoantennas are placed on the device. Nonetheless, it is visible that for this configurations, the variation of the nanoantenna's parameter (number of slits) does not influence the spectrum, as analysed before in figure C.6.

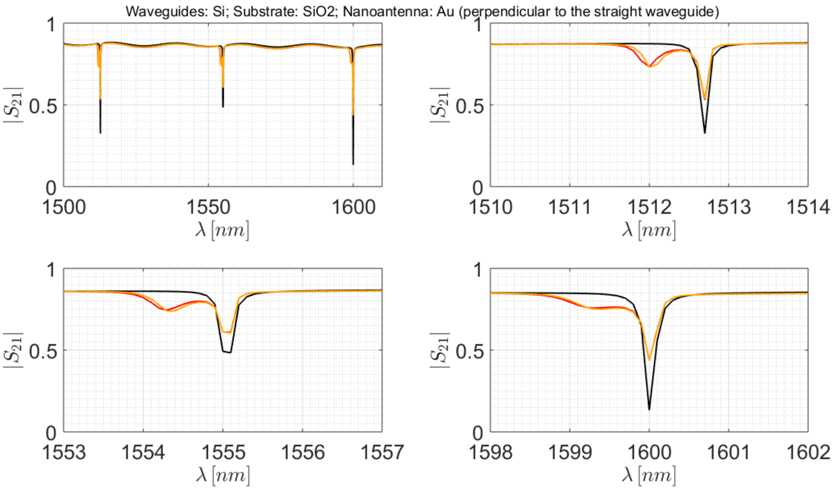

Figure C.13: Resonant spectra of $|S_{21}|$: without nanoantenna (black); $d = a_0/2$, $t = 20\mathrm{nm}$ and $n = 5$ (red); $d = a_0/2$, $t = 20\mathrm{nm}$ and $n = 3$ (orange).

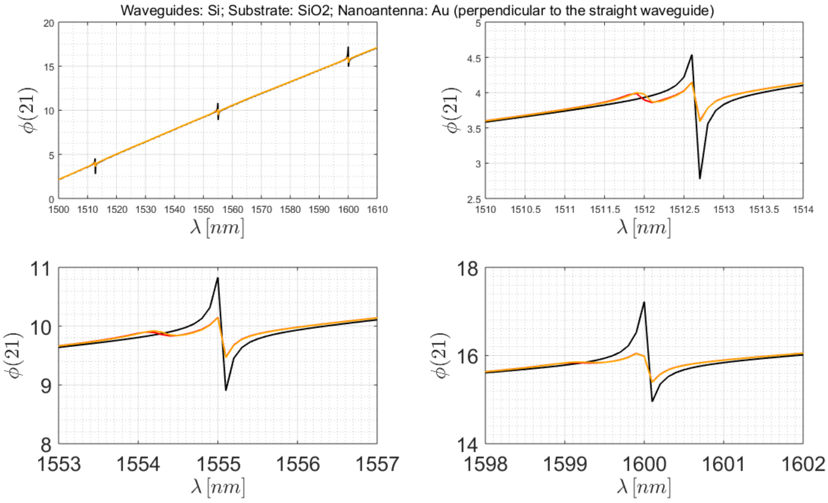

Figure C.14: Resonant spectra of the phase of S_{21} in degree: without nanoantenna (black); $d = a_0/2$, $t = 20\mathrm{nm}$ and $n = 5$ (red); $d = a_0/2$, $t = 20\mathrm{nm}$ and $n = 3$ (orange).

Surprises start to appear when analysed port 3. Based on the spectrum presented in figure C.15 it is obvious that peaks magnitudes decrease when comparing the situations with nanoantenna to the situations without it. However, a new behaviour is observed on port 3, leading to two resonant peaks instead of just one. This behaviour is also analysed in terms of phase response, as visualised on figure C.16.

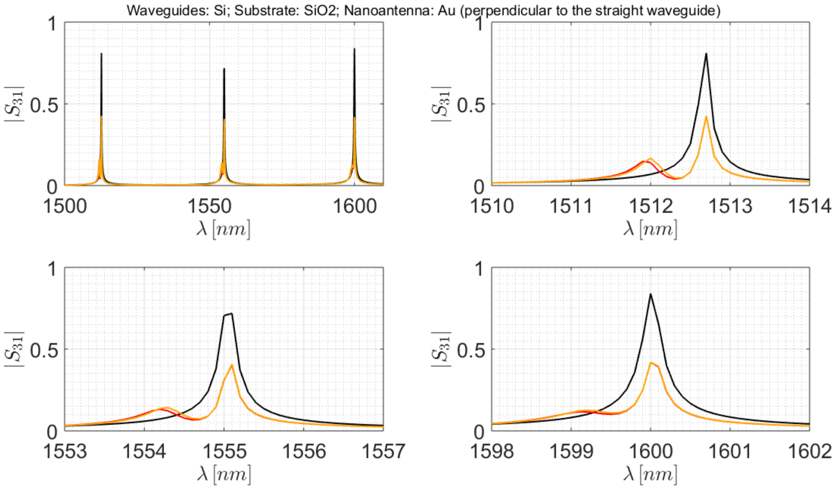

Figure C.15: Resonant spectra of $|S_{31}|$: without nanoantenna (black); $d = a_0/2$, $t = 20\text{nm}$ and $n = 5$ (red); $d = a_0/2$, $t = 20\text{nm}$ and $n = 3$ (orange).

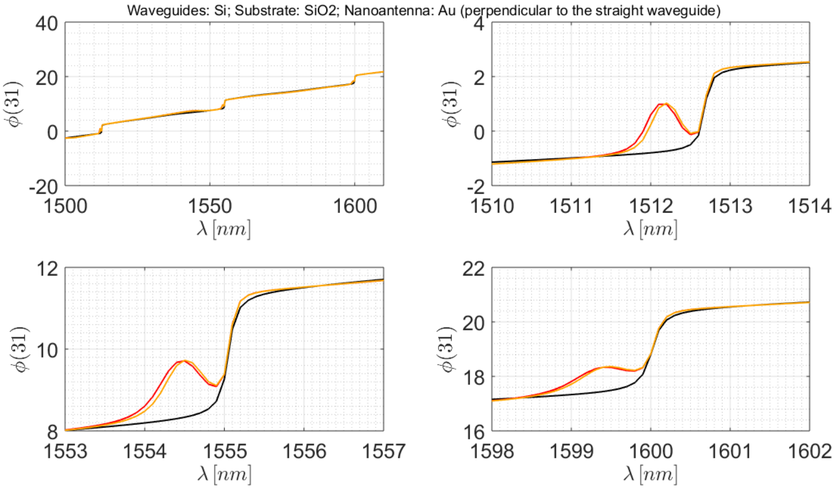

Figure C.16: Resonant spectra of the phase of S_{31} in degree: without nanoantenna (black); $d = a_0/2$, $t = 20\text{nm}$ and $n = 5$ (red); $d = a_0/2$, $t = 20\text{nm}$ and $n = 3$ (orange).

If port 4 response in a parallel topology has some identical or even better results to the ones without nanoantenna (leading to a thought that other configurations can create more significant improvements), with perpendicular topology it is quite obvious that port 4 response improve a lot with the nanoantenna. It is observed in figure C.17, where it is possible to verify that both studied nanoantennas' configurations guarantee a higher peak magnitude and even a second resonance peak close to the main one. On the other hand, in terms of phase, presented on figure C.18 it is verified identical profiles, even that values can increase in comparison with the device response without nanoantenna.

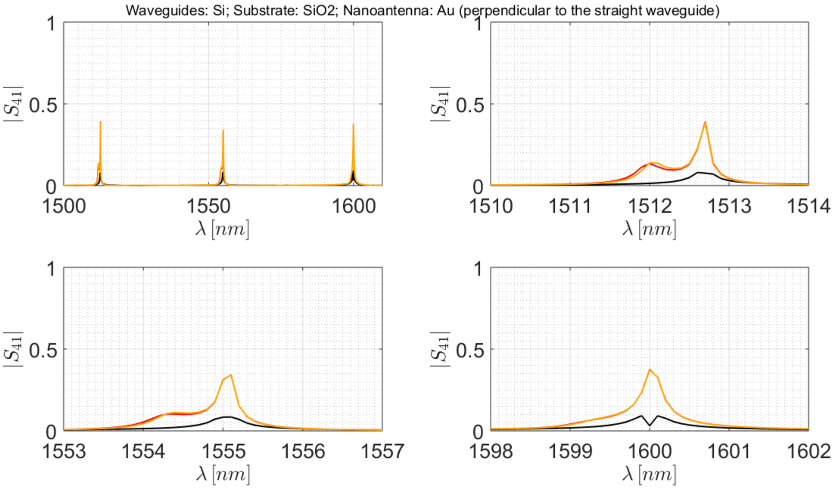

Figure C.17: Resonant spectra of $|S_{41}|$: without nanoantenna (black); $d = a_0/2$, $t = 20\text{nm}$ and $n = 5$ (red); $d = a_0/2$, $t = 20\text{nm}$ and $n = 3$ (orange).

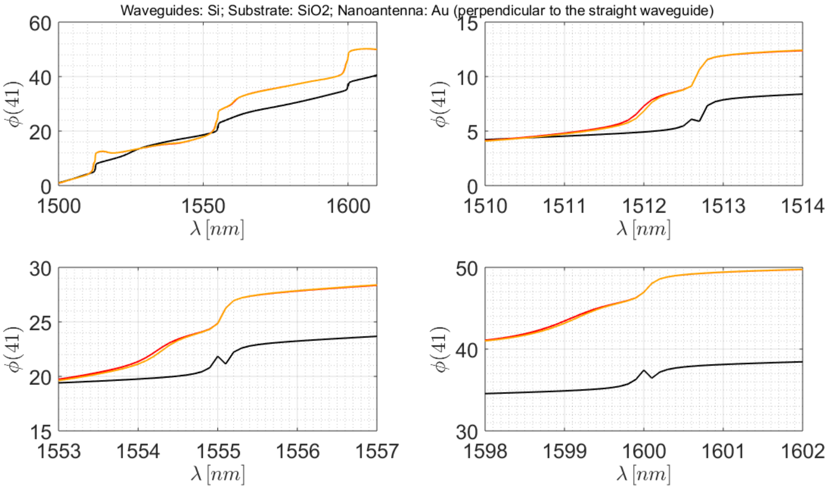

Figure C.18: Resonant spectra of the phase of S_{41} in degree: without nanoantenna (black); $d = a_0/2$, $t = 20\text{nm}$ and $n = 5$ (red); $d = a_0/2$, $t = 20\text{nm}$ and $n = 3$ (orange).

Regarding the previous analysis, it is expected that the device performance is characterised to have less losses (on non-resonant wavelengths) and higher gains (on resonant wavelengths) when compared with the performance of the device without nanoantenna. Analysing the figure C.19 it is visible that the overall device performance is better with nanoantennas. First, because all spectra are similar, but the spectra obtained with nanoantennas lead to a smaller losses value, but negative, which is a higher gain. Even more, another resonant peak near the main one is created. Thus, there are not one but two gain regions per main resonant peak.

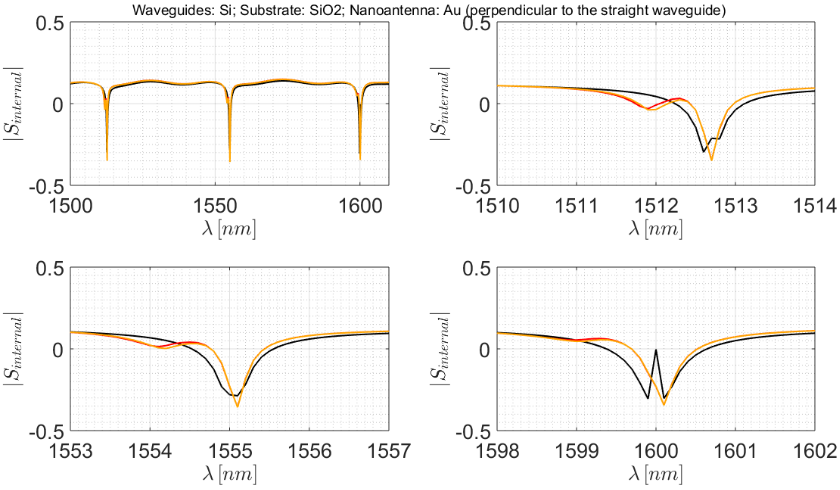

Figure C.19: Internal dissipated power, $|S_{internal}|$: without nanoantenna (black); $d = a_0/2$, $t = 20\text{nm}$ and $n = 5$ (red); $d = a_0/2$, $t = 20\text{nm}$ and $n = 3$ (orange).

C.1.2.C Gold Nanoantenna on the Ring

Lastly nanoantennas are placed inside the ring equally separated by an angle θ, being the periodicity direction according to the ring's radius. In this results set is considered a nanoantenna characterised by a thickness $t = 20\text{nm}$ and a total width equal to the guide width, $w_c = 0.3\mu\text{m}$. Moreover, it is assumed a hole number $n = 7$, that leads to a complete definition of the nanoantennas configuration, because it is also assumed $d = a_0/2$, just as done on the previous set. Thus, this section's results will allow us to concluded about the spectral response variations under a θ sweep concerning the values $\{5°, 15°, 30°, 45°, 90°\}$.

It is verified, as possible to analysing in figure C.20, that the higher the number of nanoantennas displaced inside the ring, less is the peaks magnitudes. In other words, the port 2 absolute values are lower when parts of the guide are replaced by gold, leading to almost null spectra for low values of θ. However, it is observed that it is possible to adjust the resonant wavelength just including more or less gold nanoantennas over the ring. The window to visualised the second peak is kept on the same range, just to compare the results with the previous ones. It is possible to verify that the resonant peak that is associated to this window without the nanoantenna position is shifted to lower wavelengths (out of the window range), when analysing the device with nanoantenna.

Even more, the phase response becomes more linear, as presented in figure C.21. Nonetheless, it is quite important to inform that only the non-null magnitude spectra should be analysed on the phase response. If the magnitude response is null, the phase one will be too. Thus, phase became more linear at port 2, for the resonant wavelengths that actually exist.

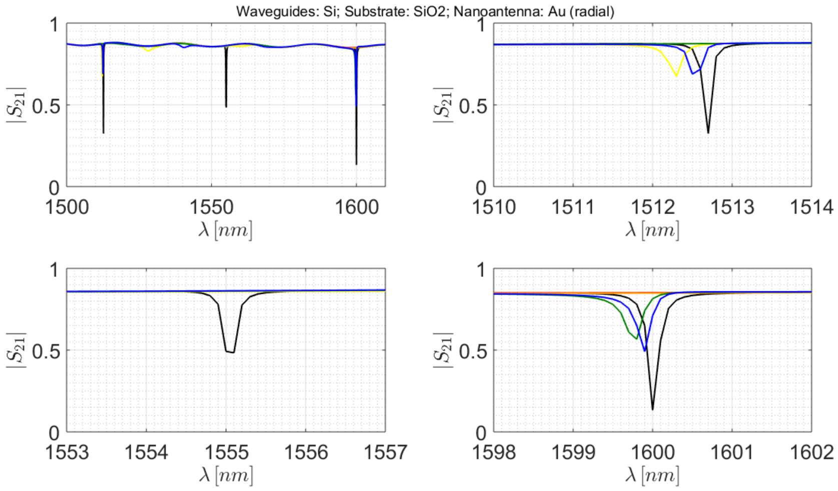

Figure C.20: Resonant spectra of $|S_{21}|$: without nanoantenna (black); $d = a_0/2\text{nm}$, $t = 20\text{nm}$, $n = 7$ and $\theta = 5°$ (red); $d = a_0/2\text{nm}$, $t = 20\text{nm}$, $n = 7$ and $\theta = 15°$ (orange); $d = a_0/2\text{nm}$, $t = 20\text{nm}$, $n = 7$ and $\theta = 30°$ (yellow); $d = a_0/2\text{nm}$, $t = 20\text{nm}$, $n = 7$ and $\theta = 45°$ (green); $d = a_0/2\text{nm}$, $t = 20\text{nm}$, $n = 7$ and $\theta = 90°$ (blue).

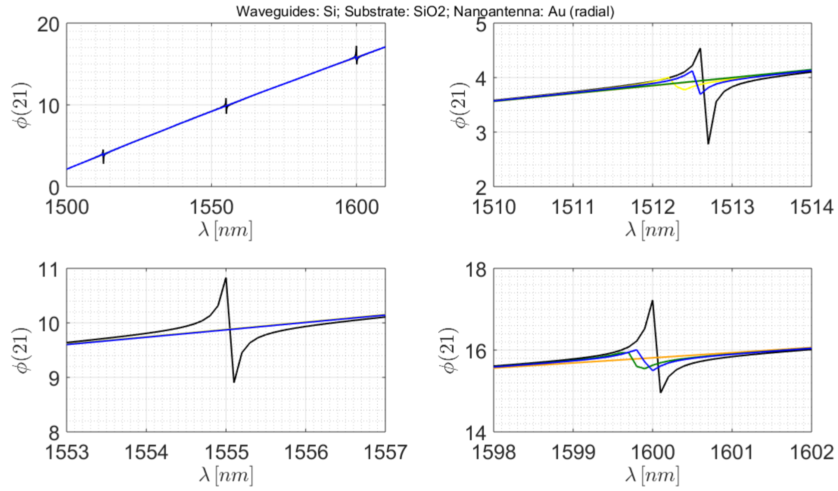

Figure C.21: Resonant spectra of the phase of S_{21} in degree: without nanoantenna (black); $d = a_0/2\text{nm}$, $t = 20\text{nm}$, $n = 7$ and $\theta = 5°$ (red); $d = a_0/2\text{nm}$, $t = 20\text{nm}$, $n = 7$ and $\theta = 15°$ (orange); $d = a_0/2\text{nm}$, $t = 20\text{nm}$, $n = 7$ and $\theta = 30°$ (yellow); $d = a_0/2\text{nm}$, $t = 20\text{nm}$, $n = 7$ and $\theta = 45°$ (green); $d = a_0/2\text{nm}$, $t = 20\text{nm}$, $n = 7$ and $\theta = 90°$ (blue).

The same conclusions can be taken for the absolute values and for the phase of S_{31}, respectively represented in figures C.22 and C.23.

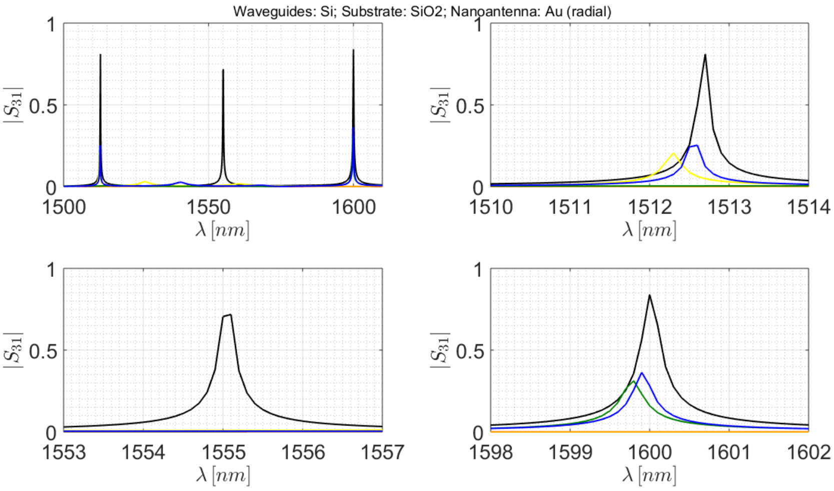

Figure C.22: Resonant spectra of $|S_{31}|$: without nanoantenna (black); $d = a_0/2\text{nm}$, $t = 20\text{nm}$, $n = 7$ and $\theta = 5°$ (red); $d = a_0/2\text{nm}$, $t = 20\text{nm}$, $n = 7$ and $\theta = 15°$ (orange); $d = a_0/2\text{nm}$, $t = 20\text{nm}$, $n = 7$ and $\theta = 30°$ (yellow); $d = a_0/2\text{nm}$, $t = 20\text{nm}$, $n = 7$ and $\theta = 45°$ (green); $d = a_0/2\text{nm}$, $t = 20\text{nm}$, $n = 7$ and $\theta = 90°$ (blue).

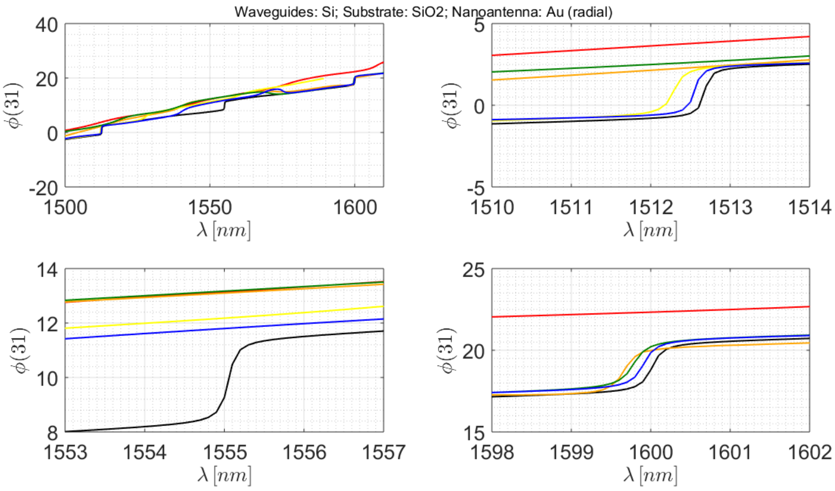

Figure C.23: Resonant spectra of the phase of S_{31} in degree: without nanoantenna (black); $d = a_0/2\text{nm}$, $t = 20\text{nm}$, $n = 7$ and $\theta = 5°$ (red); $d = a_0/2\text{nm}$, $t = 20\text{nm}$, $n = 7$ and $\theta = 15°$ (orange); $d = a_0/2\text{nm}$, $t = 20\text{nm}$, $n = 7$ and $\theta = 30°$ (yellow); $d = a_0/2\text{nm}$, $t = 20\text{nm}$, $n = 7$ and $\theta = 45°$ (green); $d = a_0/2\text{nm}$, $t = 20\text{nm}$, $n = 7$ and $\theta = 90°$ (blue).

As already expected, port 4 has the greatest improvement in terms of its power absolute values, which are presented in figure C.24. In the first and third visualisation sub-range, there are at least two configurations that lead to higher peaks magnitudes. Only in the second sub-range, there are no resonant peaks. Some of them are shifted to lower wavelengths, but also with small magnitudes. In terms of phase, that is in figure C.25, it seems to be more linear, even that there is not any global rule, and also that all the results are very identical to straightly compare linearity.

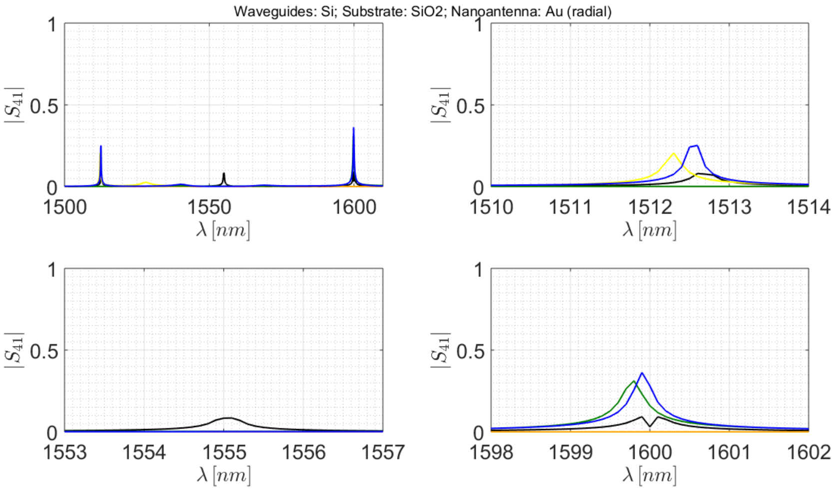

Figure C.24: Resonant spectra of $|S_{41}|$: without nanoantenna (black); $d = a_0/2\text{nm}$, $t = 20\text{nm}$, $n = 7$ and $\theta = 5°$ (red); $d = a_0/2\text{nm}$, $t = 20\text{nm}$, $n = 7$ and $\theta = 15°$ (orange); $d = a_0/2\text{nm}$, $t = 20\text{nm}$, $n = 7$ and $\theta = 30°$ (yellow); $d = a_0/2\text{nm}$, $t = 20\text{nm}$, $n = 7$ and $\theta = 45°$ (green); $d = a_0/2\text{nm}$, $t = 20\text{nm}$, $n = 7$ and $\theta = 90°$ (blue).

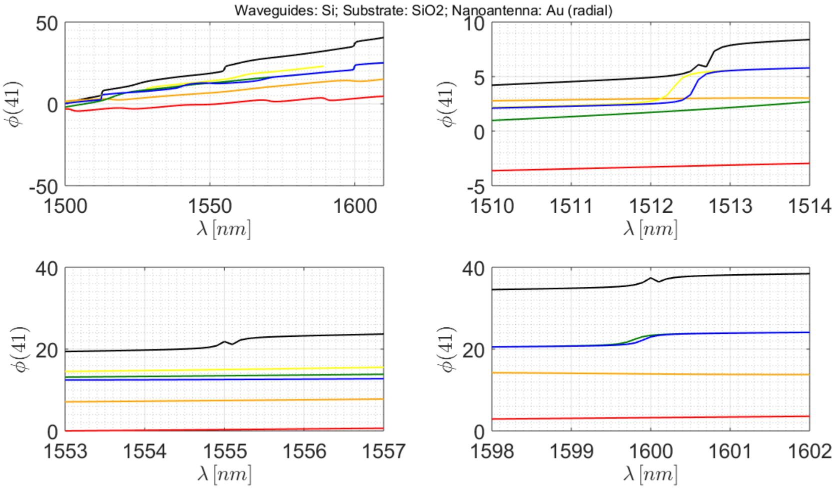

Figure C.25: Resonant spectra of the phase of S_{41} in degree: without nanoantenna (black); $d = a_0/2\text{nm}$, $t = 20\text{nm}$, $n = 7$ and $\theta = 5°$ (red); $d = a_0/2\text{nm}$, $t = 20\text{nm}$, $n = 7$ and $\theta = 15°$ (orange); $d = a_0/2\text{nm}$, $t = 20\text{nm}$, $n = 7$ and $\theta = 30°$ (yellow); $d = a_0/2\text{nm}$, $t = 20\text{nm}$, $n = 7$ and $\theta = 45°$ (green); $d = a_0/2\text{nm}$, $t = 20\text{nm}$, $n = 7$ and $\theta = 90°$ (blue).

Globally, the device performance is null along all the spectrum, when a large number of nanoantennas are inside the ring. However, for a small number of nanoantennas, it is possible to adjust the resonant wavelength but also to choose the number of resonances at port 4: there are θ values for which two at three expected resonances are null and θ values for which one at three are null, being possible to choose it regarding θ.

Since ports 2 and 3 have worst responses along all the spectrum with nanoantennas than without them, internal losses will be highly dependent on port 4 (as already expected, regarding previous analysis), because the response at this port can have higher magnitudes with the nanoantennas position. This is observable on figure C.26. According to the analysis of the previous paragraph, it is predictable that it is possible to have similar losses profiles for different values of θ, but at most on two analysed sub-ranges.

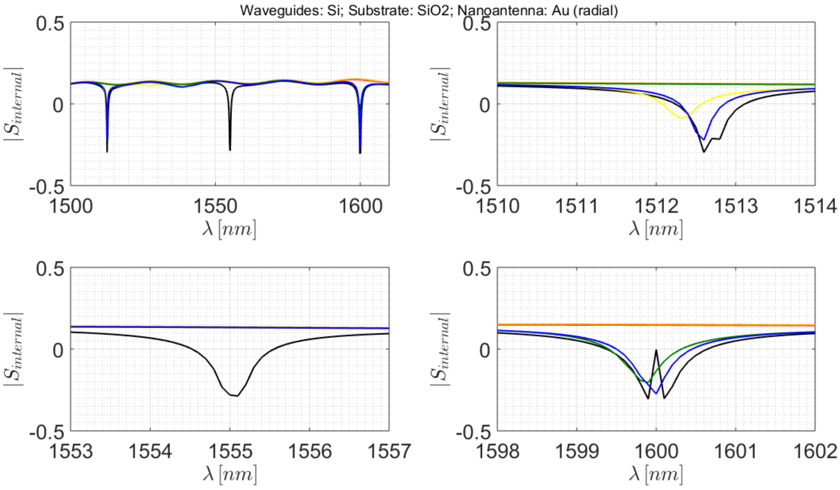

Figure C.26: Internal dissipated power, $|S_{internal}|$: without nanoantenna (black); $d = a_0/2\text{nm}$, $t = 20\text{nm}$, $n = 7$ and $\theta = 5°$ (red); $d = a_0/2\text{nm}$, $t = 20\text{nm}$, $n = 7$ and $\theta = 15°$ (orange); $d = a_0/2\text{nm}$, $t = 20\text{nm}$, $n = 7$ and $\theta = 30°$ (yellow); $d = a_0/2\text{nm}$, $t = 20\text{nm}$, $n = 7$ and $\theta = 45°$ (green); $d = a_0/2\text{nm}$, $t = 20\text{nm}$, $n = 7$ and $\theta = 90°$ (blue).

In the same conditions, other simulations are performed for $n = 5$. Similarly to the analysis done on the perpendicular topology, it is found that the variation of the number of holes, n, do not influence the output spectra.

C.2 Applications

This kind of resonators is quite used in optical telecommunications as amplifier, filter, repeater, multiplexer/switch and even as modulator [6, 90–93, 95, 96]. Different responses, for different applications, can be obtained just tuning parameters as the ring radius, the distance between the straight waveguide and the ring, the height of the straight waveguide and the used materials [6, 90–93, 96].

Also, recently, there performance as biosensors are being highly study [95, 97–99]. The device performance as sensor consists on a variable refractive index, for example leaving the core inside the ring or any other part of the substrate not be fixed (for example, let it be a sample of a tissue or blood) [95, 97–99]. Thus, depending on this variable refractive index, the optical responses of the four ports will change and it can be useful to monitor or detect diseases. In this case, port 1 should has always the same input, and the true input of the sensor will be the variation of the refractive index of the sample.

In any of these applications (both on telecommunications or on biosensoring), there are two important factors that give us the perception if the proposed structure is better in comparison with others. The Quality Factor, Q, is mathematically presented on expression C.7, where λ_{res} is the resonant wavelength and $\Delta\lambda$ is the bandwidth of the resonant peak, in terms of wavelength (can be measure for different power decays, but in this article is used the half power (peak bandwidth) [97–99].

If the higher Q is, the resonant peak is more thinner, i.e., less different wavelengths pass on the filter, amplifier, repeater, multiplexer, modulator or the sensor [97–99]. Other quantitative results dependent on the quality factor could be analysed, for example the Purcell factor, quite used on quantum computing and photons mutual coupling. Nonetheless, their analysis will be based on Q-factor results, and then, generally the analysis done for Q is also valid for them, namely about its increase and consequently, the benefits the nanoantennas incorporation.

$$Q = \frac{\lambda_{res}}{\Delta\lambda} \tag{C.7}$$

The other parameter is the Extinction Ratio, E (also known by ER), which measure the difference between the lower and the higher magnitude of the spectrum (one of them is the peak magnitude) [97–99]. This value is usually presented in decibel and calculated according expression C.8. For the applications point of view it give us the idea of the output signal if the output signal will be weak or strong [97–99].

$$E = \left| 10log_{10}\left(\frac{P_L}{P_H}\right) \right| \tag{C.8}$$

If the resonator will work as a sensor, an analysis of these parameters will help us to study at first sight sensitivities, ranges and bandwidths [97–99]. Among resonators, the one with higher Q and E is expected to have higher sensitivity. A small variation of the input (refractive index) will be easily detected as the resonant peak is thinner and higher [97–99].

In the following tables, from table C.1 to C.6, it is possible to compare the values of this factors for different topologies and configurations. Previously, only the magnitudes of the peaks and the linearity of the phase were compared. Nonetheless, it is also quite important to analyse these factors. It was decided just to compare the values for the parallel and perpendicular topology, since the radial one leads to different conclusions: only a few number of displacement angle θ leads to resonant peaks and on different sub-ranges (that affects directly the measured factors).

Analysing these tables, it is observable that placing nanoantennas it is possible to tune every factor mentioned before, which is an advantage since it give us more degrees of freedom (parameters) to tune the device response.

However, most of the times, it is better to have the lowest bandwidth, $\Delta\lambda$, the highest Q and E possible. Two different E values are analysed: E_p that considered the peak value and the highest difference value (maximum or minimum, depending if the own peak is the minimum or the maximum) on the range $[1500, 1620]\mathrm{nm}$ and E_3 that divide the range into three equal sub-ranges and measure the highest difference between power values the sub-range of the resonant peak.

Based on these tables, it is possible to verify that a small number of nanoantennas' configuration on parallel topology lead to improvement on E values of S_{21} absolute values spectrum, but only for one of the three resonant peaks. Even more, Q is always lower when comparing the topology without nanoantenna with any nanoantenna configuration as well as $\Delta\lambda$ is always higher. For the S_{31} analysis at parallel topology, there are quite visible improvements in $\Delta\lambda$ and consequently on Q. Otherwise, on E values, just on nanoantenna configuration reveals better results that the topology without nanoantenna but only for one resonant sub-range. On the opposite, based on the analysis done for S_{41} it is possible to verify that, generically, any nanoantenna configuration leads to better results in any of the aforementioned factors (the ones that are not better, are at least close to the topology without nanoantenna).

When analysed the performance with a perpendicular topology, similar conclusions can be taken. Despite some values of these factors are quite similar, both nanoantenna's configurations on the perpendicular topology provide improvements on the device's performance at one resonant peak of S_{21}, in all the calculated factors, $\Delta\lambda$, Q, and both E values. On S_{31}, both configurations lead to benefits in $\Delta\lambda$ and Q for two at three analysed resonant peaks and, as expected, the improvements are quite visible for S_{41}, leading to better performances with nanoantennas in terms of $\Delta\lambda$, Q and E values in two of three peaks and just on E values on the last one. Furthermore, it is important to verify that these two configurations are quite similar in terms of these determined factors, because, as aforementioned, their spectra are also identical.

Table C.1: Quantitative analysis of $|S_{21}|$, when the nanoantenna is parallel to the straight waveguide. Results are divided per resonant peak (sub-range) and green cells are expressing the improvements related to the same factors of the same resonance.

Topology				λ_{res}	$\Delta\lambda$	Q	ER_p	ER_3
a_0	d	t	N	[nm]	[nm]		[dB]	[dB]
–	–	–	–	1512.7	0.878	1723.0	4.324	4.314
100	25	20	7	1512.2	1.467	1030.8	1.445	1.437
100	50	20	3	1512.5	1.085	1393.9	2.793	2.787
100	50	20	7	1512.3	1.265	1195.5	2.066	2.057
100	50	50	7	1512.0	1.974	766.1	0.813	0.805
100	75	20	3	1512.6	1.123	1347.2	2.384	2.377
100	75	20	7	1512.4	1.196	1264.8	1.946	1.937
100	75	50	7	1512.2	1.425	1061.4	1.550	1.542
–	–	–	–	1555.1	1.494	1041.2	2.251	2.184
100	25	20	7	1554.5	1.704	912.3	3.398	3.334
100	50	20	3	1554.8	1.888	823.8	1.468	1.411
100	50	20	7	1554.6	1.719	904.4	2.617	2.551
100	50	50	7	1554.3	1.759	883.4	4.469	4.404
100	75	20	3	1554.9	2.609	596.0	0.437	0.376
100	75	20	7	1554.8	2.593	599.6	1.649	1.582
100	75	50	7	1554.5	1.709	909.5	3.258	3.191
–	–	–	–	1600.0	1.287	1242.9	8.096	8.175
100	25	20	7	1599.4	2.387	670.1	1.555	1.635
100	50	20	3	1599.7	1.712	934.2	2.663	2.755
100	50	20	7	1599.5	1.965	814.0	2.189	2.269
100	50	50	7	1599.2	3.911	408.9	0.964	1.040
100	75	20	3	1599.9	1.764	907.1	3.658	3.745
100	75	20	7	1599.7	1.629	982.0	3.762	3.842
100	75	50	7	1599.4	2.176	735.1	1.766	1.845

Table C.2: Quantitative analysis of $|S_{31}|$, when the nanoantenna is parallel to the straight waveguide. Results are divided per resonant peak (sub-range) and green cells are expressing the improvements related to the same factors of the same resonance.

Topology				λ_{res} [nm]	$\Delta\lambda$ [nm]	Q	ER_p [dB]	ER_3 [dB]
a_0	d	t	N					
–	–	–	–	1512.7	1.513	999.9	16.812	23.5826
100	25	20	7	1512.2	1.347	1122.7	14.150	23.378
100	50	20	3	1512.5	1.498	1009.4	14.643	22.341
100	50	20	7	1512.3	1.388	1089.4	14.764	22.972
100	50	50	7	1512.0	1.321	1144.6	12.999	25.032
100	75	20	3	1512.6	1.534	986.1	15.241	22.608
100	75	20	7	1512.4	0.314	4820.4	15.060	22.535
100	75	50	7	1512.2	1.353	1118.1	14.224	22.863
–	–	–	–	1555.1	2.924	531.8	13.800	21.533
100	25	20	7	1554.5	0.531	2926.8	13.211	19.738
100	50	20	3	1554.8	1.216	1278.2	13.126	20.789
100	50	20	7	1554.6	0.4502	3452.8	13.474	20.207
100	50	50	7	1554.3	0.638	2437.4	12.680	19.271
100	75	20	3	1554.9	1.195	1300.8	13.868	21.611
100	75	20	7	1554.8	0.516	3012.0	13.658	20.650
100	75	50	7	1554.5	0.505	3078.0	13.172	19.779
–	–	–	–	1600.0	1.318	1214.1	13.090	21.620
100	25	20	7	1599.4	1.045	1530.3	12.270	19.654
100	50	20	3	1599.7	0.557	2872.4	12.231	19.858
100	50	20	7	1599.5	0.611	2618.3	12.524	20.161
100	50	50	7	1599.1	0.739	2163.4	11.745	18.681
100	75	20	3	1599.9	1.286	1244.2	12.535	20.536
100	75	20	7	1599.7	0.596	2685.5	12.812	20.760
100	75	50	7	1599.4	0.707	2261.9	12.286	19.770

Table C.3: Quantitative analysis of $|S_{41}|$, when the nanoantenna is parallel to the straight waveguide. Results are divided per resonant peak (sub-range) and green cells are expressing the improvements related to the same factors of the same resonance.

Topology				λ_{res}	$\Delta\lambda$	Q	ER_p	ER_3
a_0	d	t	N	[nm]	[nm]		[dB]	[dB]
–	–	–	–	1512.6	1.750	864.3	13.920	20.879
100	25	20	7	1512.2	1.275	1186.3	14.920	27.114
100	50	20	3	1512.5	1.402	1079.2	18.029	24.873
100	50	20	7	1512.3	0.642	2356.3	14.338	23.882
100	50	50	7	1512.0	1.179	1282.2	16.824	31.749
100	75	20	3	1512.6	1.458	1037.5	17.182	23.872
100	75	20	7	1512.4	1.291	1172.0	16.675	24.081
100	75	50	7	1512.2	1.202	1258.3	15.143	25.288
–	–	–	–	1555.1	3.634	427.9	11.630	17.221
100	25	20	7	1554.4	0.700	2221.4	12.329	20.144
100	50	20	3	1554.8	1.191	1305.1	14.492	25.480
100	50	20	7	1554.5	0.560	2777.9	13.162	19.573
100	50	50	7	1554.2	0.760	2046.1	12.011	24.049
100	75	20	3	1554.9	0.417	3733.5	12.958	20.803
100	75	20	7	1554.7	1.172	1326.3	14.518	19.994
100	75	50	7	1554.4	0.636	2442.5	12.782	19.826
–	–	–	–	1599.9	0.808	1979.8	10.302	18.386
100	25	20	7	1599.5	0.588	2719.4	13.018	18.243
100	50	20	3	1599.8	1.206	1327.0	14.458	25.842
100	50	20	7	1599.3	0.503	3178.8	12.559	19.389
100	50	50	7	1599.3	0.598	2675.6	14.500	17.257
100	75	20	3	1599.9	0.422	3792.7	12.950	22.240
100	75	20	7	1599.8	0.647	2473.8	12.027	19.999
100	75	50	7	1599.5	0.567	2821.8	12.866	18.744

Table C.4: Quantitative analysis of $|S_{21}|$, when the nanoantenna is perpendicular to the straight waveguide. Results are divided per resonant peak (sub-range) and green cells are expressing the improvements related to the same factors of the same resonance.

Topology				λ_{res} [nm]	$\Delta\lambda$ [nm]	Q	ER_p [dB]	ER_3 [dB]
a_0	d	t	N					
–	–	–	–	1512.7	0.878	1723.0	4.324	4.314
$0.232/5$	$a_0/2$	20	5	1512.7	0.987	1533.1	2.181	2.158
$0.232/7$	$a_0/2$	20	7	1512.7	0.993	1522.9	2.128	2.106
–	–	–	–	1555.1	1.494	1041.2	2.251	2.184
$0.232/5$	$a_0/2$	20	5	1555.1	1.365	1139.6	3.444	3.350
$0.232/7$	$a_0/2$	20	7	1555.1	1.368	1137.0	3.392	3.301
–	–	–	–	1600.0	1.287	1242.9	8.096	8.175
$0.232/5$	$a_0/2$	20	5	1600.0	1.495	1069.9	2.883	2.954
$0.232/7$	$a_0/2$	20	7	1600.0	1.495	1070.5	2.888	2.960

Table C.5: Quantitative analysis of $|S_{31}|$, when the nanoantenna is perpendicular to the straight waveguide. Results are divided per resonant peak (sub-range) and green cells are expressing the improvements related to the same factors of the same resonance.

Topology				λ_{res} [nm]	$\Delta\lambda$ [nm]	Q	ER_p [dB]	ER_3 [dB]
a_0	d	t	N					
–	–	–	–	1512.7	1.513	999.9	16.812	23.583
$0.232/5$	$a_0/2$	20	5	1512.7	1.541	981.6	13.923	21.802
$0.232/7$	$a_0/2$	20	7	1512.7	1.540	982.0	13.981	21.707
–	–	–	–	1555.1	2.924	531.8	13.800	21.533
$0.232/5$	$a_0/2$	20	5	1555.1	1.344	1157.0	12.083	19.509
$0.232/7$	$a_0/2$	20	7	1555.1	1.340	1160.6	12.093	19.486
–	–	–	–	1600.0	1.318	1214.1	13.090	21.620
$0.232/5$	$a_0/2$	20	5	1600.0	0.452	3537.3	11.518	18.782
$0.232/7$	$a_0/2$	20	7	1600.0	0.453	3530.8	11.481	18.792

Table C.6: Quantitative analysis of $|S_{41}|$, when the nanoantenna is perpendicular to the straight waveguide. Results are divided per resonant peak (sub-range) and green cells are expressing the improvements related to the same factors of the same resonance.

Topology				λ_{res}	$\Delta\lambda$	Q	ER_p	ER_3
a_0	d	t	N	[nm]	[nm]		[dB]	[dB]
–	–	–	–	1512.6	1.750	864.3	13.920	20.879
$0.232/5$	$a_0/2$	20	5	1512.6	1.487	1017.2	19.399	26.818
$0.232/7$	$a_0/2$	20	7	1512.6	1.486	1017.9	19.492	27.115
–	–	–	–	1555.1	3.634	427.9	11.630	17.221
$0.232/5$	$a_0/2$	20	5	1555.1	0.673	2310.4	18.498	29.925
$0.232/7$	$a_0/2$	20	7	1555.1	0.634	2453.8	18.693	29.249
–	–	–	–	1599.9	0.808	1979.8	10.302	18.386
$0.232/5$	$a_0/2$	20	5	1599.9	1.296	1234.9	14.902	25.152
$0.232/7$	$a_0/2$	20	7	1599.9	1.295	1235.2	14.943	25.161

C.3 Discussion

Having a initial structure of the ring resonator without nanoantenna and performing 2D simulations on a Finite Element Tool is possible to verify the impact of nanoantennas at different positions and with different configurations. In this research work, a gold nanoantenna is studied.

Placing the gold nanoantenna in the coupling region, parallel to the straight waveguide, it is possible to observe a few configurations where the optical response of $|S_{21}|$ and $|S_{31}|$ improved. When analysing $|S_{41}|$ it is even more notorious that nanoantennas can improve the optical response of this device. Since nanoantennas can concentrate and amplify electromagnetic waves, the evanescent wave between guides can be replace by other type of waves and thus, improve the coupling. However, EOT is not a phenomenon that occurs for every frequency, configuration or topology and consequently, only few of them lead to better responses. On the opposite, a huge number of configurations and topologies will led to worst spectra. Nonetheless, when phase spectra are analysed, it is observable that nanoantennas will benefit a lot this response. Without nanoantenna, the phase spectrum has a huge variation on the resonant wavelength. Placing nanoantennas in parallel to the straight waveguide led to a more linear phase, which allow us to have a more constant group delay, that is very important to optical telecommunications.

On the other hand, placing the nanoantenna on the coupling region but perpendicular to the straight waveguide, two configurations are analysed. Both create identical spectral responses that led to similar quantitative results. Comparing to previous analysis, same conclusions can be taken, in this case the variation of the number o holes for a constant relation between the periodicity and the hole diameter of the nanoantenna do not have significant influence. Both configurations lead to a supermode response and therefore, there are quite visible improvements in terms of spectral responses.

Lastly, the gold nanoantennas are placed inside the ring, varying the angular distance between them, θ. It is analysed that as lower is θ (more nanoantennas are placed inside the guide), more null will be the responses in all the ports. Just for $\theta = 90°$ two of the three expected resonant peaks are visible (on the first and third sub-range). For $\theta = 45°$ and $\theta = 30°$, just one resonance is reveal and in different sub-ranges: on the first sub-range and on the third, respectively. This property can be useful at least on multiplexing and switching applications. Huge improvements are visible on the response of port 4, that are balanced with the decrease of magnitude observed on ports 2 and 3. These results are for $n = 5$ and $n = 7$, keeping constant the relation between the nanoantennas' periodicity and hole diameter.

Based on the previous paragraphs analysis, it is pointed out that if the nanoantenna periodicity is in the same direction that the electric field propagation direction, the variation of the number of holes (keeping constant the nanoantennas' total width and the relation between the periodicity and the diameter) do not have significant influence. It is visible on the simulations where the nanoantenna is perpendicular to the straight waveguide and when nanoantennas are radially displaced.

To sum it up, nanoantennas can help on the phase linearity of any output port when placed on the coupling region. Nanoantennas behaviour is due to the generation and propagation of surface plasmon polaritons and creeping waves. Their generation is dependent on the wave vector that is on the nanoantennas front, and its relation to the nanoantennas structure parameters. The resultant wave vector can be different, and it will influence all the coupling effects. The variation of the angular frequency regarding the wave vector will tend to be constant since the wavelength will be dependent on the output of the nanoantenna and not about its input (which depends on the resonator input). This led to a constant phase and group velocities and linear phases. Some configurations led to similar responses on ports 2 and 3 and to huge improvements on the power magnitude spectrum on port 4. It is clear not only visualising the spectra but also when quantitative results are compared. It can be helpful not only in telecommunications but also on biosensing, since these improvements can be related to sensors specifications as sensitivities, bandwidths and ranges. Radial nanoantennas displacement can be helpful on multiplexing ideas.

Nanoantennas improved results from a well-studied structure of the ring resonator, by Hiremath [90]. Some of these improved results are now more close or better to others reported on recent literature [6,90,93,97–99]. Even that, it is shown that ring resonators' response can be improved using nanoantennas.